

Structural basis of eukaryotic phosphate transport mechanisms

Dissertation
zur Erlangung des Doktorgrades
der Naturwissenschaften (Dr. rer. nat.)

vorgelegt beim Fachbereich 14 - Biochemie, Chemie und Pharmazie
der Johann Wolfgang Goethe-Universität
in Frankfurt am Main

von
Simon Joshua Rainer Schneider
aus Hanau

Frankfurt, 2024
(D 30)

Diese Arbeit wurde vom Fachbereich 14 - Biochemie, Chemie und Pharmazie der Johann Wolfgang Goethe-Universität als Dissertation angenommen.

Dekan: Prof. Dr. Clemens Glaubitz

1. Gutachter: Prof. Dr. Clemens Glaubitz
2. Gutachter: Prof. Dr. Werner Kühlbrandt

Datum der Disputation: 04.07.2024

Contents

Abstract	1
Zusammenfassung	5
List of Abbreviations	11
List of Figures	15
List of Tables	19
1 Introduction	21
1.1 Membrane proteins	21
1.2 Phosphate homeostasis	24
1.2.1 Phosphate regulation in yeast	24
1.2.2 Phosphate import in yeast	26
1.2.3 Phosphate export in yeast	27
1.2.4 Human phosphate homeostasis	29
1.2.5 Human phosphate export by Xpr1	29
1.3 Electron cryo-microscopy	31
1.3.1 Microscope structure	31
1.3.2 Sample preparation	34
1.3.3 Data processing	35
1.4 Project motivation	37
2 Material and Methods	39
2.1 Media and competent cell buffers	39
2.2 Cloning and vector design	40
2.3 Preparation and transformation of competent cells	41
2.3.1 Preparation and transformation of competent <i>E. coli</i> cells	41
2.3.2 Preparation and transformation of competent <i>S. cerevisiae</i> cells	42
2.4 Protein analysis	43
2.4.1 Sodium dodecyl sulfate polyacrylamide gel electrophoresis	43

2.4.2	Blue native PAGE	43
2.4.3	Coomassie staining and Western Blotting	44
2.4.4	Protein quantification	44
2.5	Protein expression and membrane preparation	45
2.5.1	Protein expression in <i>S. cerevisiae</i>	45
2.5.2	Expression of HsXpr1 in HEK293 GnTI- cells	46
2.5.3	Membrane isolation	46
2.5.4	Screening of detergents for solubilization	47
2.6	Protein purification	48
2.6.1	Purification of proteins expressed in <i>S. cerevisiae</i>	48
2.6.2	Purification of HsXpr1 expressed in HEK293 GnTI- cells	48
2.7	Electron microscopy and data processing	49
2.7.1	Preparation and imaging of negative-stain EM grids	49
2.7.2	Cryo-EM sample vitrification	50
2.7.3	Cryo-EM data acquisition	50
2.7.4	Cryo-EM image processing	51
2.7.5	Model building and refinement	53
2.8	Biochemical analysis	54
2.8.1	Thin layer chromatography	54
2.8.2	Microscale thermophoresis	54
2.8.3	Reconstitution of ScPho90 into liposomes	54
2.8.4	ScPho90 transport assays	55
2.8.5	ScSyt1/HsXpr1 reconstitution into liposomes	55
2.8.6	ScSyt1/HsXpr1 transport assays	55
3	Results	57
3.1	The eukaryotic low-affinity phosphate importer Pho90	57
3.1.1	Expression and purification	57
3.1.2	Electron microscopy screening	60
3.1.3	High-resolution cryo-EM data acquisition of ScPho90	60
3.1.4	Structure of phosphate-bound ScPho90	62
3.1.5	Structure of phosphate-free ScPho90	64
3.1.6	Structural basis for phosphate binding	67
3.1.7	Co-purified lipids	68
3.1.8	The SPX domain	69
3.1.9	Functional analysis	70
3.2	The eukaryotic phosphate exporters Syt1 and Xpr1	72

3.2.1	Expression and purification of Syg1 proteins	72
3.2.2	Electron microscopy screening	74
3.2.3	High-resolution cryo-EM data acquisition of ScSyg1	75
3.2.4	Structure of substrate-free ScSyg1	78
3.2.5	Structural details of ScSyg1	80
3.2.6	Structure of substrate-bound ScSyg1	83
3.2.7	Phosphate binding	85
3.2.8	The SPX domain of ScSyg1	87
3.2.9	Expression and purification of HsXpr1	92
3.2.10	High-resolution cryo-EM data acquisition of HsXpr1	93
3.2.11	Structures of HsXpr1	94
3.2.12	Structural details of HsXpr1 and comparison to ScSyg1	97
3.2.13	The SPX domain of HsXpr1	101
3.2.14	The HsXpr1 dimer with inverted monomers	102
3.2.15	Phosphate transport mediated by HsXpr1 and ScSyg1	102
4	Discussion	105
4.1	Electron cryo-microscopy in structural biology of membrane proteins . .	105
4.2	The eukaryotic low-affinity phosphate importer Pho90	111
4.2.1	Overall structure	111
4.2.2	Phosphate binding and comparison with known phosphate trans- porter structures	113
4.2.3	Pho90 phosphate translocation mechanism	116
4.3	The eukaryotic phosphate exporters Syg1 and Xpr1	120
4.3.1	Overall structure of ScSyg1/HsXpr1	120
4.3.2	Dimerization interface of phosphate exporters	121
4.3.3	Effect of bound lipids	122
4.3.4	Substrate translocation pathway	123
4.3.5	Phosphate binding	124
4.3.6	Regulatory role of the SPX domain	126
4.3.7	Proposed mechanism of phosphate export in eukaryotes	129
4.3.8	Conserved function of EXS domain proteins	130
4.3.9	Sequence conservation and disease mutations in HsXpr1	133
4.3.10	Physiological impact	136
4.4	Concluding remarks and outlook	138
	Bibliography	139

Supplement	155
Acknowledgements	163
Additional information	165
Declaration of scientific collaboration	165
Permission rights for figures, tables and illustrations	165
Eidesstaatliche Erklärung	166
Curriculum vitae	167

Abstract

Inorganic phosphate is one of the most abundant and essential nutrients in living organisms. It plays an indispensable role in energy metabolism and serves as a building block for major cellular components such as the backbones of DNA and RNA, headgroups of phospholipids and in posttranslational modifications of many proteins. Disturbances in cellular phosphate homeostasis have a detrimental effect on the viability of cells. Therefore, both the import and export of phosphate is strictly regulated in eukaryotic cells. In the eukaryotic model organism *Saccharomyces cerevisiae*, the uptake of phosphate is carried out either by transporters with high affinity or by transporters with low affinity, depending on the cytosolic phosphate concentration. While structures are available for homologues of the high-affinity transporters, no structures of low-affinity transporters have been solved so far. Interestingly, only the low-affinity transporters have a regulatory SPX domain, which is found in various proteins involved in phosphate homeostasis.

In this work, structures of Pho90 from *Saccharomyces cerevisiae*, a low-affinity phosphate transporter, were solved by cryo-EM, providing insights into its transport mechanism. The dimeric structure resembles the structures of proteins of the divalent anion symporter superfamily (DASS) and of mammalian transporters of the solute carrier 13 (SLC13) family. The transmembrane domain of each protomer consists of 13 helical elements and can be subdivided into scaffold and transport domains. The structure of ScPho90 in the presence of phosphate shows the phosphate binding site within the transporter domain in an outward-open conformation with a bound phosphate ion and two sodium ions. In the absence of phosphate, an asymmetric dimer structure was determined, with one protomer adopting an inward-open conformation. While the dimer contact and the scaffold domain are identical in both conformations, the transport domain is rotated by about 30° and shifted by 11 Å towards the cytoplasmic side, leading to the accessibility of the binding pocket from the cytoplasm. Based on these findings and by comparison with known structures, a phosphate transport mechanism is proposed in the present work that involves substrate binding on the extracellular side, conformational change by a rigid-body motion of the transport domain, in an "elevator-like" motion, and substrate release into the cytoplasm. The regulatory SPX domain is not well

resolved in the ScPho90 structures, so that no direct conclusions were drawn about its regulatory mechanism. The findings provide new insights into the function and mechanism of eukaryotic low-affinity phosphate transporters.

While eukaryotic cells express various phosphate import proteins, most eukaryotes have only a single highly conserved and essential phosphate exporter. These exporters show no sequence homology to other transporters of known structure, but also possess a regulatory SPX domain. In this work, the structural basis for eukaryotic phosphate export is investigated by elucidating the structures of the homologous phosphate exporters Syg1 from *Saccharomyces cerevisiae* and Xpr1 from *Homo sapiens*, using cryo-EM. The structures of ScSyg1 and HsXpr1 show a conserved homodimeric structure and the transmembrane part of each protomer consists of 10 TM helices. Helix TM1 establishes the dimer contact by means of a glycine zipper motif, which is a known oligomerization motif. Helices TM2-5 form a hydrophobic pocket that has density for a lipid molecule. Whether the lipid binding into the hydrophobic pocket has an allosteric effect on the phosphate export activity or only serves protein stabilization is not known. Helices TM5-10 form a six-helix bundle, which constitutes a putative phosphate translocation pathway in its center. This bundle is formed by the protein sequence annotated as EXS domain.

The respective phosphate translocation pathways of ScSyg1 and HsXpr1 show structural differences. While the translocation pathway in HsXpr1 is accessible from the cytoplasm, in ScSyg1 it is closed by a large loop of the SPX domain. Interestingly, this loop is not conserved in higher eukaryotes and is therefore not present in HsXpr1. Another difference are distinct conformations of helix TM9. In ScSyg1, TM9 adopts a kinked conformation, which results in the translocation pathway being open to the extracellular side. In contrast, TM9 adopts a straight conformation in HsXpr1, resulting in the placement of a highly conserved tryptophane residue in the middle of the translocation pathway. As a result, the translocation pathway in HsXpr1 is closed to the extracellular side. In addition, different phosphate binding sites have been identified in the translocation pathway of ScSyg1 and HsXpr1 likely caused by the different conformations. Based on these structural findings and on the highly conserved sequence of eukaryotic phosphate transporters, a general phosphate export mechanism is proposed. Intracellular phosphate can bind into the translocation pathway of the exporter in an inward-open conformation, in which helix TM9 is straight. After phosphate binding, the transport pathway closes towards the cytoplasm. This favors the kinking of TM9, which leads to an outward-open conformation of the exporter. In this conformation, phosphate ions can leak into the extracellular space, after which the exporter transitions back into an

inward-open conformation for a new transport cycle.

The SPX domain is poorly resolved in most structures, but addition of its substrate InsP_6 enabled me to elucidate the structure of the ScSyt1 SPX domain. This revealed its three-helix bundle structure, InsP_6 binding sites and interactions with the transmembrane part. *In vitro* transport assays show that InsP_6 addition significantly increases the transport activity of phosphate exporters. These findings provide insights into the regulatory mechanism of eukaryotic phosphate exporters. Overall, these results reveal the first insights into the three-dimensional structure of ScSyt1 and HsXpr1, and consequently into the mechanism of eukaryotic phosphate export. These insights provide valuable information for the development of new therapeutic strategies to combat various diseases associated with impaired cellular phosphate homeostasis.

Zusammenfassung

Anorganisches Phosphat ist einer der am häufigsten vorkommenden und wichtigsten Nährstoffe in lebenden Organismen. Es spielt eine unverzichtbare Rolle im Energiestoffwechsel und ist ein elementarer Baustein vieler Zellbestandteile. Es findet sich zum Beispiel im Rückgrat von DNA- und RNA-Molekülen, in Kopfgruppen von Phospholipiden und dient als posttranslationale Modifikation vieler Proteine. Die zelluläre Phosphatkonzentration muss streng reguliert werden, da ein Phosphatmangel zu Wachstumsproblemen führt, was wiederum zelluläre Autophagie auslöst. Andererseits führen überhöhte Phosphatkonzentrationen zu Störungen im Energiestoffwechsel von Zellen und somit zu einer verminderten Lebensfähigkeit, was mit der Entstehung verschiedener Krankheiten in Verbindung gebracht wird.

Die Phosphathomöostase auf zellulärer Ebene ist am besten in dem eukaryotischen Modellorganismus *Saccharomyces cerevisiae* charakterisiert. Ein gemeinsames Merkmal der an der Phosphatregulierung in Hefe beteiligten Proteine, ist das Vorhandensein einer SPX-Domäne. Vorausgegangene Studien lösten die 3D-Struktur dieser Domäne und zeigten, dass sie Inositolhexakisphosphat (InsP₆) sowie dessen Pyrophosphatderivate (InsPPs) bindet, die vermutlich als Signalmoleküle für die intrazelluläre Phosphatkonzentration dienen. In Hefe wird die Aufnahme von Phosphat in Abhängigkeit von der zytosolischen Phosphatkonzentration entweder durch Transporter mit hoher Affinität oder durch Transporter mit niedriger Affinität durchgeführt. Während für Homologe der Hochaffinitätstransporter Strukturen verfügbar sind, wurden bisher keine Strukturen von Transportern mit niedriger Affinität gelöst. Interessanterweise besitzen nur die Transporter mit niedriger Affinität eine zusätzliche SPX-Domäne, die nachweislich den Phosphattransport *in vivo* inhibiert. Wie diese Domäne den Phosphattransport auf mechanistischer Ebene hemmt, ist jedoch noch unbekannt.

Im Vergleich zu den zahlreichen Phosphatimportern ist im Genom von *S. cerevisiae* nur ein einziger bekannter Phosphatexporter kodiert, der Suppressor of Yeast Gpa1 (Syg1). Sequenzanalysen zeigen, dass dieser keine Homologie zu anderen Transportern mit bekannter Struktur aufweist, jedoch ist die Familie der Phosphatexporter in allen Eukary-

oten hochkonserviert. Syg1 besitzt ebenfalls eine regulatorische SPX-Domäne, aber wie diese sowohl den Phosphatimport als auch den Phosphatexport in Hefe reguliert, ist noch nicht erforscht. Das Ortholog in Säugetieren heißt Xenotropher und Polytropher Retrovirus Rezeptor 1 (Xpr1) und wurde vor etwa 10 Jahren als Phosphatexporter identifiziert. Im Gegensatz zu Hefe ist Xpr1 das einzige bekannte Säugerprotein, welches eine regulatorische SPX-Domäne besitzt. Frühere Studien haben gezeigt, dass der von Xpr1 vermittelte Phosphat-Efflux von der Bindung von InsPPs an die SPX-Domäne abhängig ist. Mutationen im *Xpr1*-Gen führen außerdem zu verschiedenen Krankheiten, die alle mit Defekten in der Phosphathomöostase in Verbindung stehen. Des Weiteren wurde festgestellt, dass Xpr1 bei bestimmten Krebsarten überexprimiert wird und es wurde gezeigt, dass die Hemmung oder das Ausschalten von Xpr1 zu toxisch hohen intrazellulären Phosphatspiegeln und anschließendem Zelltod führt, was Xpr1 zu einem interessanten therapeutischen Ziel macht.

Der erste Teil dieser Arbeit verfolgte das Ziel, die Strukturen von eukaryotischen Phosphattransportern mit niedriger Affinität aufzuklären, um ihren Transportmechanismus und die Regulierung des Phosphatimports zu verstehen. Zu diesem Zweck wurde die Expression und Reinigung mehrerer Transporter getestet und Pho90 aus *S. cerevisiae* wurde schließlich als geeignetes Protein für die Strukturbestimmung mittels Kryo-EM identifiziert. Die Strukturen von ScPho90 wurden in An- und Abwesenheit von Phosphat durch Kryo-EM mit nominalen Auflösungen von 2,3 Å, 2,6 Å und 3,1 Å bestimmt. Die dimere Struktur ähnelt den Strukturen von Proteinen der Divalenten Anionen Symporter Superfamilie (DASS) und von Säugetier-Transportern der SLC13-Familie. Die Transmembrandomäne eines jeden Protomers besteht aus 13 helikalen Elementen (H1-H13). Beide Protomere interagieren durch hydrophobe Wechselwirkungen der Gerüst-Domäne, die aus den Helices H1-H4 und H8-H10 besteht. Die Transport-Domäne ist ein Helixbündel mit zwei helikalen Hairpins (H5A/B und H11A/B), zwei teilweise entfalteten Helices (H6 und H12) und den Helices H7 und H13. Die Struktur von ScPho90 in Gegenwart von Phosphat zeigt die Phosphatbindungsstelle innerhalb der Transporterdomäne in einer nach außen offenen Konformation. Das Phosphat-Ion wird durch die Seitenketten Asn556, Gln605, His779 und Ser815 innerhalb der Bindungstasche und in der Nähe von zwei gebundenen Natrium-Ionen koordiniert. Die Natrium-Ionen werden von den Sauerstoffatomen des Peptidrückgrats und den Seitenketten der Reste Ser603, Asn606, Thr775, Ala811, Ser815, Gly817 und Leu820 koordiniert. Transportstudien an ScPho90-Mutanten zeigten, dass zumindest Gln605 und Ser815 für den Phosphattransport wichtig sind. In Abwesenheit von Phosphat nehmen die meisten ScPho90-Partikel die gleiche nach außen offene Konformation an, wie sie in der phosphatgebundenen

Struktur zu sehen ist. Mit Hilfe von 3D-Variabilitätsanalyse konnte jedoch eine zweite asymmetrische Dimerstruktur aufgeklärt werden, in der ein Protomer in einer nach innen offenen Konformation vorliegt. Während der Dimerkontakt und die Gerüst-Domäne in beiden Konformationen identisch sind, ist die Transport-Domäne um ca. 30° gedreht und um 11 Å in Richtung der zytoplasmatischen Seite verschoben. Dies führt dazu, dass die Bindungstasche vom Zytoplasma aus zugänglich ist und Substrat entlassen werden kann.

Auf der Grundlage dieser Befunde und durch Vergleiche mit bekannten Strukturen wird in der vorliegenden Arbeit ein Phosphattransport-Mechanismus vorgeschlagen, der die Substratbindung auf der extrazellulären Seite, die Konformationsänderung durch eine Starrkörperbewegung der Transportdomäne, in einer Aufzug-ähnlichen Bewegung und die Substratfreisetzung in das Zytoplasma umfasst. Die regulatorische SPX-Domäne ist in allen ScPho90-Strukturen nur niedrig aufgelöst, so dass keine strukturellen Rückschlüsse auf ihre regulatorische Funktion gezogen werden konnten. Die Deletion der SPX-Domäne verändert die Phosphattransportraten in *in vitro* Transportassays nicht, aber weitere Untersuchungen sind notwendig, um ihre regulatorische Funktion im Detail aufzuklären.

Im zweiten Teil dieser Arbeit sollten die strukturellen Grundlagen für den eukaryotischen Phosphatexport untersucht werden, indem die Strukturen der homologen Phosphatexporter Syg1 aus *S. cerevisiae* und Xpr1 aus *H. sapiens* aufgeklärt wurden. Die Expression und Reinigung von ScSyg1 und HsXpr1 wurde für die Strukturaufklärung mittels Kryo-EM optimiert. Kryo-EM Strukturen von ScSyg1 wurden in Abwesenheit von Substraten und mit gebundenem Phosphat und InsP_6 mit nominalen Auflösungen von 2,3 Å und 2,2 Å bestimmt. Die bestimmten Kryo-EM Dichten ermöglichten den Bau eines Atommodells für den gesamten Transmembranteil, einschließlich mitgereinigter Lipide und mehrerer Wassermoleküle. In Anwesenheit von Substraten ist auch die SPX-Domäne von ScSyg1 gut aufgelöst und das typische Drei-Helix-Bündel der SPX-Domäne konnte modelliert werden. Kryo-EM Dichten von HsXpr1 wurden in Anwesenheit und Abwesenheit von Phosphat mit nominalen Auflösungen von 3,4 Å und 3,0 Å bestimmt, was die Modellierung der kompletten Transmembrandomäne ermöglichte.

Die Strukturen von ScSyg1 und HsXpr1 weisen eine konservierte homodimere Struktur auf. Der transmembrane Teil jedes Protomers besteht aus 10 TM-Helices. Helix TM1 stellt den Dimerkontakt in einer Glycin-Zipper-ähnlichen Weise her, ein bekanntes Dimerisierungsmotiv, das auch in TM-Helices von Rezeptortyrosinkinasen zu finden ist.

Die physiologische Bedeutung der Dimerisierung des Exporters ist nicht verstanden und auch die zytoplasmatische SPX-Domäne könnte dabei eine wichtige ungeklärte Rolle spielen. Helices TM2-5 bilden eine hydrophobe Tasche, die Dichte für ein Lipidmolekül aufweist. Die TLC-Analyse der mit den Proteinen gereinigten Lipide zeigte, dass hauptsächlich Phosphatidylcholin (PC) und Phosphatidylethanolamin (PE) an ScSyt1 gebunden sind. Ob die Lipidbindung in die hydrophobe Tasche einen allosterischen Effekt auf die Phosphatexportaktivität hat oder nur der Proteinstabilisierung dient, muss durch weitere Untersuchungen geklärt werden.

Die Helices TM5-10 bilden ein Sechs-Helix-Bündel, welches in seiner Mitte den mutmaßlichen Phosphat-Translokationsweg aufweist. In dem Helixbündel von ScSyt1 sind die Helices TM5 und TM9 nach außen geknickt. Der Translokationsweg in ScSyt1 ist hydratisiert, was durch mehrere zusätzliche Dichten innerhalb des Translokationsweges deutlich wird, die als Wassermoleküle interpretiert wurden. An seiner engsten Stelle beträgt der Durchmesser des Translokationswegs 1,3 Å, was eine freie Diffusion von Wasser verhindert. Der Translokationsweg ist von der extrazellulären Seite her zugänglich (daher in einer nach außen offenen Konformation), wird aber vom Zytoplasma aus durch eine Schleife der SPX-Domäne verschlossen, die sich um das Helixbündel wickelt und von der Zytoplasmaseite aus in dieses inseriert (Reste Glu236 und Phe238). Interessanterweise ist diese SPX-Schleife in Metazoen nicht konserviert und ist daher in der Struktur von HsXpr1 auch nicht vorhanden. Daher ist der Translokationsweg von HsXpr1 vom Zytoplasma aus zugänglich (also in einer nach innen geöffneten Konformation), aber von der extrazellulären Seite aus aufgrund einer Konformationsänderung in TM9 geschlossen. Die Helix TM9 von HsXpr1 nimmt eine ungeknickte Konformation an, die zu ihrer Ausdehnung in den Translokationsweg führt. Hauptsächlich der konservierte Rest Trp573 sitzt innerhalb des Translokationsweges und verschließt ihn zur extrazellulären Seite hin.

Die Seitenketten innerhalb des Translokationsweges sind in allen eukaryotischen Phosphatexporteuren hoch konserviert, was ihre Bedeutung für die Proteinfunktion unterstreicht. In Anwesenheit von Phosphat wurden unterschiedliche Phosphatbindestellen im Translokationsweg von ScSyt1 und HsXpr1 identifiziert. In den Translokationsweg von ScSyt1 wurden zwei Phosphat-Ionen modelliert, eine am zytoplasmatischen Ende (P1) und eine weitere zur extrazellulären Seite hin (P2), die von den Resten Glu236, Arg633, His643, Asn646 beziehungsweise Ser564, Arg745, Glu772, Arg775, Arg776 koordiniert werden. In HsXpr1 wurde nur ein Phosphat-Ion identifiziert, das von Lys482, Asp529, Arg570 und Arg603 koordiniert wird. Es ist ca. 4 Å von der P2-Bindestelle in

ScSyg1 entfernt, wird aber von zwei der korrespondierenden Argininreste koordiniert (Arg570 und Arg603 in HsXpr1 entsprechen Arg745 und Arg775 in ScSyg1). Interessanterweise ist die P2-Bindestelle in HsXpr1 durch Trp573 von TM9 besetzt, wodurch die Phosphatbindung an dieser Position verhindert wird. Zusätzliche *in vitro* Transportassays bestätigen die Phosphattransportaktivität von ScSyg1 und HsXpr1 und zeigen eine erhöhte Aktivität nach Bindung von InsP_6 an die SPX-Domäne.

Auf der Grundlage dieser Erkenntnisse kann ein allgemeiner eukaryotischer Phosphatexportmechanismus vorgeschlagen werden. Intrazelluläres Phosphat kann in den Translokationsweg des Exporters in einer nach innen offenen Konformation binden, wobei TM9 gerade ist. Nach der Phosphatbindung schließt sich das intrazelluläre Gate (SPX-Schleife in ScSyg1), um den Transportweg zum Zytoplasma zu verschließen. Dies begünstigt das Abknicken von TM9, was zu einer nach außen offenen Konformation des Exporters führt. In dieser Konformation können Phosphat-Ionen in den extrazellulären Raum austreten, wonach der Exporter für einen neuen Transportzyklus in eine nach innen geöffnete Konformation zurückkehrt.

Aufgrund ihrer inhärenten Flexibilität ist die SPX-Domäne in den meisten Strukturen nur schlecht aufgelöst, Zugabe ihres Substrats InsP_6 ermöglichte jedoch die Strukturaufklärung der SPX-Domäne von ScSyg1. Dabei wurden die Drei-Helix-Bündelstruktur, InsP_6 -Bindestellen und Interaktionen mit dem transmembranen Teil sichtbar. Diese Erkenntnisse erlauben es, einen Regulationsmechanismus vorzuschlagen. Durch die InsP_6 -Bindung rückt die SPX-Domäne näher an die Membranebene heran, was zu einer Interaktion der SPX-Helix $\alpha 3$ mit dem intrazellulären Loop 4 (ICL4) führt. Da ICL4 direkt mit TM9 verbunden ist, könnte diese Interaktion Änderungen in der Konformation von TM9 erleichtern und dadurch die Phosphatexportaktivität erhöhen.

Neben neuen Erkenntnissen über den Mechanismus des eukaryotischen Phosphatexports sind die Strukturen von ScSyg1 und insbesondere von HsXpr1 wichtig für die Entwicklung neuer therapeutischer Strategien zur Bekämpfung von Krankheiten, die mit einer gestörten Phosphathomöostase zusammenhängen. So hilft beispielsweise die Lokalisierung von krankheitsverursachender Mutationen, bei Patienten mit primärer familiärer Basalganglien-Kalzifikation (PFBC), anhand der aufgeklärten Strukturen um den pathogenen Mechanismus der Mutationen zu verstehen. Mithilfe von struktur-basierten Wirkstoffdesigns könnten neue pharmakologische Wirkstoffe entwickelt werden, die auf HsXpr1 einwirken und dessen Phosphatexportaktivität modulieren und somit zur Behandlung von gestörter Phosphathomöostase eingesetzt werden können.

List of Abbreviations

°C	degree Celsius
2D	2-dimensional
3D	3-dimensional
Å	Ångström, 1 Å = 0.1 nm
<i>A. thaliana</i>	<i>Arabidopsis thaliana</i>
ABC	ATP binding cassette
AFIS	aberration-free image shift
ATP	adenosine triphosphate
BN	blue native
BSA	bovine serum albumin
<i>C. thermophilum</i>	<i>Chaetomium thermophilum</i>
CHS	cholesterol hemi succinate
cryo-EM	electron cryo-microscopy
CTF	contrast transfer function
<i>D. rerio</i>	<i>Danio rerio</i>
Da	Dalton, 1 Da = 1 g/mol
DASS	divalent anion symporter superfamily
DDM	n-dodecyl-β-D-maltopyranoside
DM	n-decyl-β-D-maltopyranoside
DNA	deoxyribonucleic acid
dNTP	deoxy nucleic triphosphate
e ⁻	electrons
ECL	extracellular loop
EER	electron-event representation
Erd1	ER retention defective 1
Ex/Em	excitation/emission
EXS	Erd1, Xpr1, Syg1
Fos-8	fluorinated foscholine 8
FEG	field emission gun
FFT	fast Fourier Transform

List of Abbreviations

FSC	Fourier shell correlation
FSEC	fluorescence size exclusion chromatography
GDN	glycol-diosgenin
GFP	green fluorescent protein
H	helical element
<i>H. sapiens</i>	<i>Homo sapiens</i>
HEK	human embryonic kidney
ICL	intracellular loop
IMAC	immobilized metal affinity chromatography
InsP ₆	inositol hexakisphosphate
InsPP	inositol pyrophosphates
IPTG	isopropyl β-d-1-thiogalactopyranoside
kV	kilo Volt
LMNG	lauryl maltose neopentyl glycol
M	molar
MST	microscale thermophoresis
<i>N. crassa</i>	<i>Neurospora crassa</i>
NMR	nuclear magnetic resonance
NTA	nitrilotriacetic acid
NU	non-uniform
<i>O. sativa</i>	<i>Oryza sativa</i>
OD	optical density
<i>P. pastoris</i>	<i>Pichia pastoris</i>
PA	phosphatidic acid
PAGE	polyacrylamide gel electrophoresis
PC	phosphatidylcholine
PCR	polymerase chain reaction
PDB	Protein Data Bank
PE	phosphatidylethanolamine
PFBC	primary familial brain calcification
PG	phosphatidylglycerol
Pho	phosphate transporter
PI	phosphatidylinositol
P _i	inorganic phosphate
PS	phosphatidylserine
PVDF	polyvinylidene fluoride
RMSD	root-mean-square deviation

RNA	ribonucleic acid
RT	room temperature
RTK	receptor tyrosine kinase
<i>S. cerevisiae</i>	<i>Saccharomyces cerevisiae</i>
SDS	sodium dodecyl sulfate
SEC	size exclusion chromatography
SEM	scanning electron microscopy
SLC	solute carrier
SNR	signal-to-noise ratio
SPA	single particle analysis
SPX	Syg1, Pho, Xpr1
Syg1	Suppressor of Yeast Gpa1
TBS	Tris buffered saline
TEM	transmission electron microscopy
TLC	thin layer chromatography
TM	transmembrane
Tris	tris hydroxymethyl aminomethane
w/v	weight per volume
w/w	weight per weight
WT	wild-type
<i>X. laevis</i>	<i>Xenopus laevis</i>
Xpr1	Xenotropic and Polytropic Retrovirus Receptor 1
<i>Y. lipolytica</i>	<i>Yarrowia lipolytica</i>
YNB	yeast nitrogen base
YPD	yeast extract peptone dextrose
YPL	yeast polar lipids

List of Figures

1	Schematic overview of different types of protein-mediated transport across membranes	22
2	Phosphate homeostasis in <i>S. cerevisiae</i>	25
3	Sequence alignment of Pho1, Syg1 and Xpr1	28
4	AlphaFold model of human Xpr1	30
5	Overview of cryo-EM SPA workflows	32
6	Structure of a transmission electron microscope	33
7	Plunge freezing of cryo-EM samples	35
8	Expression and purification tests of low-affinity phosphate transporters .	58
9	Purification of ScPho90	59
10	Screening of ScPho90 grids	61
11	Processing scheme of ScPho90 in the presence of phosphate	62
12	Structure of phosphate-bound ScPho90	63
13	Processing scheme of ScPho90 in the absence of phosphate	65
14	Structure of the symmetric and asymmetric ScPho90 dimer in the absence of phosphate	66
15	Conformational change of ScPho90 between outward-open and inward-open states	67
16	Insights into substrate coordination by ScPho90	68
17	Co-purified lipids of ScPho90	69
18	Low-resolution density maps of ScPho90 SPX domains	70
19	Functional characterization of ScPho90 and its mutants	71
20	Expression and FSEC analysis of different Syg1 constructs	72
21	Small-scale purifications of Syg1 constructs	73
22	Purification of ScSyg1	75
23	ScSyg1 sample screening by electron microscopy	76
24	Processing scheme of ScSyg1 without phosphate	77
25	Overall structure of ScSyg1	78
26	ScSyg1 dimerization interface	79
27	Lipid binding pocket of ScSyg1	80

28	Putative translocation pathway	81
29	The SPX domain and its interaction with the TM domain	82
30	Processing scheme of substrate-bound ScSyt1	84
31	Comparison of ScSyt1 in presence and absence of substrates	85
32	Structure of ScSyt1 in the presence of phosphate and InsP ₆	86
33	Putative phosphate binding sites	87
34	Different conformations of the ScSyt1 extracellular loop 5 (ECL5)	88
35	Comparison of SPX domains in the presence and absence of substrates	89
36	SPX domain structure and InsP ₆ binding site	90
37	Contacts between TM and SPX domain and a putative additional InsP ₆ binding site	91
38	Expression and purification of HsXpr1 from HEK293 GnTI- cells	92
39	Processing scheme of HsXpr1 in the presence of phosphate	94
40	Processing scheme of HsXpr1 in the absence of phosphate	95
41	Overall structure of HsXpr1	96
42	Comparisons of HsXpr1 structures	97
43	HsXpr1 dimerization interface and lipid binding pocket	98
44	Putative phosphate translocation pathway in HsXpr1	99
45	Different conformations of TM9 in HsXpr1 and ScSyt1	100
46	Phosphate binding site in HsXpr1	101
47	SPX density of HsXpr1	102
48	Alternative conformation of HsXpr1 dimer with inverted topologies	103
49	Functional characterization of HsXpr1 and ScSyt1	104
50	Determination of B-factors	108
51	High resolution features of cryo-EM maps	109
52	Comparison of ScPho90 with known homologous structures	112
53	Comparison of ScPho90 with human sulfate transporters	114
54	Comparison of phosphate coordination in phosphate transporters	115
55	Putative phosphate translocation mechanism by low-affinity phosphate transporters	118
56	Comparison of dimer interfaces	122
57	Comparison of phosphate coordination in ScSyt1 and HsXpr1	126
58	Structural comparison of SPX domains	127
59	Proposed model of eukaryotic phosphate export	131
60	Comparison of EXS-domain helix bundles	132
61	Multiple sequence alignment of eukaryotic phosphate exporters	134

62	Mapping of PFBC-linked mutations onto HsXpr1 and ScSyt1	135
S1	Comparison of ScPho90 models	158
S2	Map and model of the TM part of ScSyt1 in the presence of phosphate/InsP ₆	158
S3	HsXpr1 sample screening by electron microscopy	159
S4	Alignment of yeast low-affinity phosphate transporter	160
S5	Alignment of yeast Pho87/90 and human NaS1/2	161
S6	Comparison of experimental and AlphaFold predicted ScPho90 structures	161
S7	Comparison of experimental and AlphaFold predicted HsXpr1 structures .	162

List of Tables

1	Cultivation media and competent cell buffers	39
2	Composition of PCR reactions	40
3	Pho87/Pho90 plasmids used for protein expression	41
4	Syg1/Xpr1 plasmids used for protein expression	42
5	<i>E. coli</i> and <i>S. cerevisiae</i> strains used in this thesis	43
6	Buffers used for SDS-PAGE, Western Blotting, BN-PAGE, Coomassie staining and agarose gels	45
7	Cryo-EM parameters of ScPho90 datasets	51
8	Cryo-EM parameters of ScSyg1 datasets	51
9	Cryo-EM parameters of HsXpr1 datasets	52
S1	Processing and refinement statistics of ScPho90 datasets	155
S2	Processing and refinement statistics of ScSyg1 datasets	156
S3	Processing and refinement statistics of HsXpr1 datasets	157

1 Introduction

1.1 Membrane proteins

Compartmentalization in biological systems is a prerequisite for life and is mainly achieved by lipid membranes, which separate cells from their surroundings and cellular organelles from the cytoplasm. The semipermeable characteristics of these membranes allow for a certain diffusion of small non-polar molecules across them (Finkelstein, 1976). To facilitate the transport of larger and polar molecules across cellular membranes, proteins are incorporated into the lipid bilayer. Of all human genes, approximately 10 % encode for transporters or transport-related proteins, highlighting their importance for cellular function (Hediger et al., 2013). These integral membrane proteins catalyze the transport of specific substrates across the membrane, either passively or actively against their electrochemical gradient (Figure 1).

Passive transport is mediated by channels or carriers that transport their substrates along their concentration gradient. The concentration gradient alone drives the transport of uncharged molecules, while charged molecule transport is also influenced by the electrical gradient across the membrane (Yang et al., 2015). Channel proteins allow the diffusion of specific substrates across the membrane through a hydrophilic channel. A typical characteristic for protein channels is that they exist in open and closed states, mediated by the opening and closing of a single gate within the protein (Gadsby, 2009). In the open state, the channel is accessible from both sides of the membrane, allowing for very fast diffusion of the substrate across the membrane. In contrast, carrier proteins are only accessible to the substrates from one side of the membrane at a time. This is ensured by the presence of two gates within the protein which must not be open at the same time. After substrate binding, the carrier undergoes a reversible conformational change that closes one gate and opens the other and therefore exposes the substrate to the other side of the membrane where it is released. This transport mechanisms usually results in slower transport rates compared to protein channels. Most glucose transporters, like GLUT1, are an example for passive carriers, while water channels such as Aquaporins are well-characterized examples for channels (Agre et al., 1993; Deng et al., 2014).

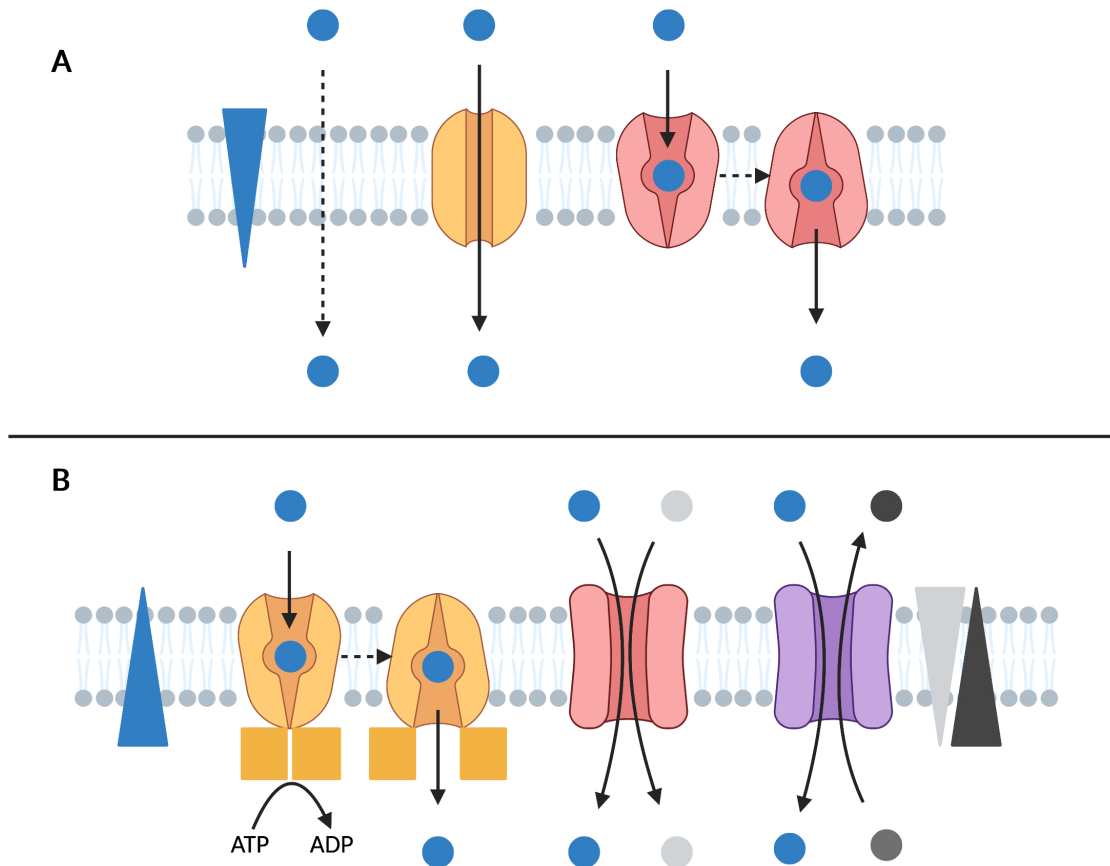


Figure 1: Schematic overview of different types of protein mediated transport across membranes. (A) Passive transport. Molecules can transverse biological membranes along their concentration gradient either by simple or facilitated diffusion without external energy being required. Facilitated diffusion is mediated by protein channels or carriers. (B) Active transport. Primary active transporters use the energy liberated from ATP hydrolysis to drive substrate transport against their electrochemical gradient. Secondary active transporter use electrochemical gradients of co-substrates to drive the transport of the substrate against the gradient. These transporters can be symporters or antiporters. Concentration gradients are indicated by triangles. (Figure created with BioRender.com)

Contrary to passive transport, active transporters can transport their respective substrates against electrochemical gradients through the use of external energy. Like passive carriers, these transporters undergo conformational changes during the transport cycle to translocate substrates across the lipid bilayer. Primary-active transporters couple transport to the hydrolysis of ATP, delivering the energy needed for substrate translocation. The ABC transporter family and F-, P- and V-type ATPases are typical members of this group (Dietz et al., 2001; Kühlbrandt, 2004; Kühlbrandt, 2019; Locher, 2009).

These transporters are also responsible for establishing specific ion gradients, which can then be used to drive the transport of other molecules, like for example sodium (Na^+)-potassium (K^+) ATPases which maintain high intracellular K^+ levels and low Na^+ levels (Jorgensen et al., 2003). Transporters that use the energy of an electrochemical gradient of one substrate to drive the transport of another substrate are classified as secondary active transporters. Sodium-calcium (Ca^{2+}) exchanger 1 (NCX1) for example uses the Na^+ gradient to actively export Ca^{2+} ions (Blaustein et al., 2008). Depending on the transport direction of the co-substrate, these transporters can be divided into symporters or antiporters. Throughout all domains of life, the action of these transporters keeps intracellular concentrations of small molecules at physiological levels, which is a prerequisite for the proper function of all cellular processes.

Even though these transporters and membrane proteins in general play crucial roles in all cellular processes, many are still scantily characterized and their mechanisms are poorly understood. One limiting factor in understanding these proteins is the limited number of membrane protein structures, as only a fraction (approximately 3 %) of all published structures in the protein data bank (PDB) represent membrane proteins (September 2023). The limited number of structures is due to intrinsic properties of membrane proteins: Outside of the hydrophobic membrane bilayer most membrane proteins are unstable, so they have to be kept in a hydrophobic environment after extraction from the membrane (Helenius et al., 1975). Different types of detergent and membrane-mimicking substances have proven capable of keeping membrane proteins in a functional state (Denisov et al., 2004; Frauenfeld et al., 2016; Knowles et al., 2009). However, extensive screening and optimization are often necessary to find the optimal conditions. Additionally, expression levels of membrane proteins are usually low, thereby limiting the amount of protein for structural studies. Recent advances in the field of electron cryo-microscopy have made it the method of choice for membrane protein structure determination (Chua et al., 2022; Frank, 2017; Kühlbrandt, 2014). Major advantages are the low amount of protein needed, the omission of protein crystallization (required for X-ray crystallography) and its ability to deal with structural heterogeneity of the sample. But even with these recent advances, the number of published membrane protein structures remains low.

1.2 Phosphate homeostasis

Phosphate is an essential nutrient in all living organisms and is a building block for all major cellular components. The backbone of both DNA and RNA molecules is composed of phosphate, connecting deoxyribonucleotides and ribonucleotides, respectively. Additionally, it is a main component in the headgroup of all phospholipids and phosphorylation of proteins is one of the most common posttranslational modifications. Protein phosphorylation is also one of the main mechanisms in cellular signaling, as phosphorylation and dephosphorylation by specific kinases and phosphatases can act as a switch between active and inactive protein states (Ardito et al., 2017). Furthermore, phosphate plays an indispensable role in cellular energy conversion, as energy is mainly stored in and liberated from the phosphoanhydride bonds of adenosine tri-phosphate (ATP). While the need for intracellular phosphate is high during growth and proliferation phases, excessive phosphate levels lead to an impaired metabolism and decreased cell viability (Yamada et al., 2014; He et al., 2020). Particularly for microorganisms and plants, inorganic phosphate (P_i) availability is often one of the most limiting factors for growth and proliferation (Cridland et al., 2020; Vicent et al., 2015). In humans, imbalances of phosphate levels can lead to numerous health issues, including diabetes, heart and kidney diseases as well as different tumors (Brown et al., 2018; Kalantar-Zadeh et al., 2010; Mancini et al., 2018; Tonelli et al., 2005). Moreover, elevated phosphate levels (hyperphosphatemia) were found to accelerate ageing but the underlying mechanism is largely unknown (Komaba et al., 2016).

1.2.1 Phosphate regulation in yeast

In eukaryotes regulation of phosphate homeostasis at a cellular level is best characterized in the model organism *Saccharomyces cerevisiae* (Figure 2). The phosphate-responsive regulatory pathway, known as the PHO pathway (named after the multiple Pho proteins involved in this pathway), is the main regulator of intracellular phosphate levels in yeast (Ogawa et al., 2000; Wykoff et al., 2001). It controls import and export of P_i as well as intracellular phosphate recycling and storage as polyphosphate (polyP) (Secco et al., 2012b).

A common feature of proteins involved in the PHO pathway is the presence of an N-terminal regulatory SPX domain. This domain is named after its presence in the proteins Suppressor of yeast *gpa1* (Syg1), Phosphatase 81 (Pho81) and the human Xenotropic and polytropic retrovirus receptor 1 (Xpr1). The SPX domain can be found in proteins of all major eukaryotes and the identified proteins are generally all linked to phosphate home-

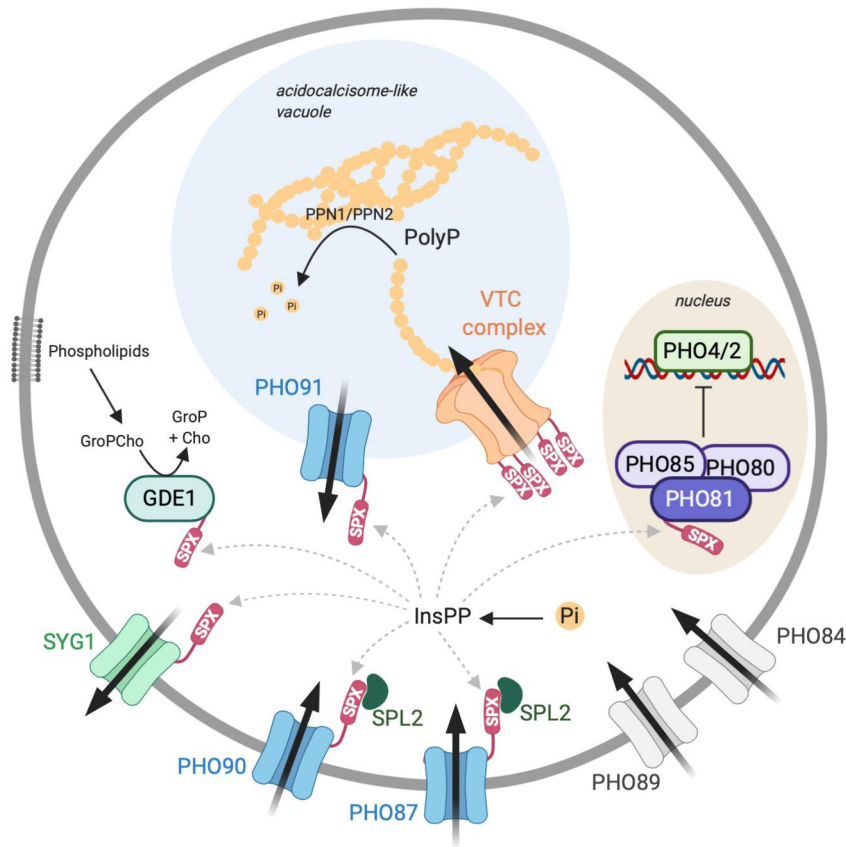


Figure 2: Phosphate homeostasis in *S. cerevisiae*. In yeast, inorganic phosphate (P_i) is imported into the cytosol by high-affinity (Pho84/89) and low-affinity (Pho87/90) transporters. Cytosolic P_i can be transported and stored as polyphosphate (PolyP) in acidocalcisome-like vacuoles by the action of VTC complexes. Upon phosphate starvation PolyP is reconverted into P_i and imported into the cytosol by Pho91. Export of P_i into the extracellular space is facilitated by the phosphate exporter Syg1 upon elevated cytosolic P_i concentrations. Many proteins of this pathway have a regulatory SPX domain. These domains bind inositol pyrophosphates (InsPP) which are produced when cytosolic P_i levels are high, leading to the activation or inactivation of specific transporters or enzymes. The protein kinase Pho80/Pho81/Pho85 is also regulated by an SPX domain and phosphorylates transcription factors Pho4/2 upon phosphate starvation which leads to the expression of Pho84, Pho89, Gde1 and other proteins involved in phosphate accumulation (Figure from Austin et al., 2020).

ostasis (Secco et al., 2012a). Especially in plants and microorganisms numerous proteins with an SPX domain have been identified, likely due to limited phosphate availability in the environment of these organisms and therefore tight regulation of phosphate homeostasis (Ågren et al., 2012).

Crystal structures of different SPX domains revealed a three-helix bundle formation (Wild et al., 2016). An additional N-terminal helical hairpin forms a conserved basic sur-

face cluster and it was shown that this cluster binds inositol hexakisphosphate (InsP₆) and its pyrophosphate variants (InsPPs) with affinities in the nanomolar range. It has been proposed that InsP₆ and especially InsPPs are evolutionarily conserved cellular signaling molecules conveying sufficient intracellular P_i concentration, while their absence signals a need for P_i (Gu et al., 2017). Consequently, the binding of these signaling molecules to SPX domains has regulatory effects on the respective proteins which are involved in phosphate homeostasis. The InsPPs, mainly 5-diphosphoinositol 1,2,3,4,6-pentakisphosphate (5 – InsP₇) and 1,5-bis-diphosphoinositol 2,3,4,6-tetrakisphosphate (InsP₈) are produced by diphosphoinositol pentakisphosphate kinases (PPIP5Ks) and inositol hexakisphosphate kinases (IP6Ks). These enzymes were shown to be directly regulated by intracellular P_i and ATP concentrations and thereby couple InsPPs production to P_i and ATP levels (Mulugu et al., 2007). Interestingly, PPIP5Ks also possess a phosphatase domain which was reported to be activated upon phosphate starvation, thereby leading to decreased cellular InsPPs levels (Gu et al., 2017). It was also suggested that different InsPPs isomers exhibit specific signaling functions but further studies are necessary to validate this hypothesis (Azevedo et al., 2017; Shears, 2018).

1.2.2 Phosphate import in yeast

Phosphate uptake in yeast is facilitated by four distinct phosphate importers (Pho84, Pho87, Pho89 and Pho90), which are located in the yeast plasma membrane (Persson et al., 2003). These transporters can be categorized into high-affinity (Pho84 and Pho89) and low-affinity type transporters (Pho87 and Pho90). High-affinity transporters are expressed under phosphate limiting conditions through the action of transcription factors Pho4/2 and kinases Pho80/Pho81/Pho85 and are responsible for phosphate accumulation (Persson et al., 1998). Under these conditions, low-affinity transporters are degraded by targeting them to the vacuole through a Spl2-dependent mechanism (Wykoff et al., 2007). When intracellular phosphate levels are sufficient, low-affinity transporter become the primary phosphate transporter to maintain a constant cytoplasmic phosphate concentration. The advantages of these dual-type transporter systems include more effective and faster responses to changing environmental nutrient concentrations (Levy et al., 2011).

Pho84 functions as a proton/phosphate symporter and acts as the main transporter during phosphate starvation. It has been demonstrated that Pho84 can activate protein kinase A (PKA), suggesting that Pho84 is also involved in sensing and signaling of extracellular phosphate levels (Giots et al., 2003; Popova et al., 2009). When cytoplasmic phosphate levels are high, Pho84 is internalized and degraded in the vacuole. The crys-

tal structure of a Pho84 homologue from the fungus *Piriformospora indica* showed a monomeric assembly of 12 TM helices and suggests a "rocker-switch" mechanism of phosphate translocation (Pedersen et al., 2013). Pho89, a sodium/phosphate symporter, is a homologue of mammalian SLC20 transporters and exhibits a 100-fold lower transport activity compared to Pho84 (Pattison-Granberg et al., 2000). Recently, structures of a homologous transporter from *Thermotoga maritima* have been published, revealing a dimeric structure with similarities to the leucine transporter superfamily (Tsai et al., 2020).

The low-affinity transporters Pho87 and Pho90 are both sodium/phosphate symporters and share a high sequence identity of 66 %. In contrast to high-affinity transporters both contain a regulatory SPX domain. Based on sequence analysis, their TM domain is predicted to differ from that of high-affinity transporters and instead shows similarities to transporters of the divalent anion sodium symporter (DASS) family, especially mammalian SLC13 transporters like NaS1 (SLC13A1) and NaS2 (SLC13A4) which are sodium/sulfate symporters (Bergeron et al., 2013). Malfunctions of these transporters in humans lead to conditions like hyposulfatemia and hypersulfaturia (Dawson et al., 2003; Lee et al., 2006). Although Pho87 and Pho90 have a high sequence identity, previous studies have shown that Pho90 is the main phosphate transporter under high cellular phosphate levels, whereas Pho87 is more involved in phosphate sensing (Ghillebert et al., 2011). *S. cerevisiae* encodes another close homologue, called Pho91, a vacuolar phosphate transporter which is able to transport phosphate from acidocalcisome-like vacuoles into the cytoplasm under low cytoplasmic phosphate levels (Hürlimann et al., 2007). The SPX domain of Pho90 was shown to act as a suppressor of phosphate transport, as its removal increases the phosphate uptake rate *in vivo* (Hürlimann et al., 2009). The mechanism of how the SPX domain interacts with transmembrane regions to regulate transport activity and the exact role of InsPPs within this mechanism remain still unknown.

1.2.3 Phosphate export in yeast

For precise control of intracellular P_i concentrations, not only the uptake but also the export of phosphate needs to be tightly regulated. Compared to the presence of multiple different importers, most eukaryotic organisms express only a single phosphate exporter (Austin et al., 2020). In *S. cerevisiae* this protein is named Syg1 based on its first identification in yeast pheromone signaling (Spain et al., 1995). It is conserved throughout all eukaryotic organisms and its homologous mammalian proteins are classified into its own SLC53 family. In plants, the exporter is known as Phosphate transporter 1 (Pho1), while

1.2. Phosphate homeostasis

the mammalian orthologue is named Xpr1 as it was initially identified as a receptor for xenotropic and polytropic murine leukemia retroviruses (Battini et al., 1999; Hamburger et al., 2002). Yeast Syg1 shares a sequence identity and similarity of 24.1 % and 36.1 % with human Xpr1 and 21.6 % and 36.5 % with Pho1 from *Arabidopsis thaliana* (Figure 3). In yeast, Syg1 is one of multiple proteins possessing a N-terminal SPX domain. How the same domain is able to regulate phosphate import and phosphate export, and its role in the regulation of several soluble enzymes remains poorly understood. The TM domain of Syg1 shows no sequence homology to any known transporter structure. The C-terminal part of the protein is annotated as an EXS-domain, named after its presence in Erd1 (ER retention defective 1), Xpr1 and Syg1 proteins (Wang et al., 2004). This domain covers parts of the TM domain and the soluble C-terminal end of Syg1 but its function remains elusive with only studies of Pho1 from *Arabidopsis thaliana* showing an essential role for phosphate export (Wege et al., 2016). So far, most studies of eukaryotic phosphate export have focused on human Xpr1, making it the best-characterized phosphate exporter.

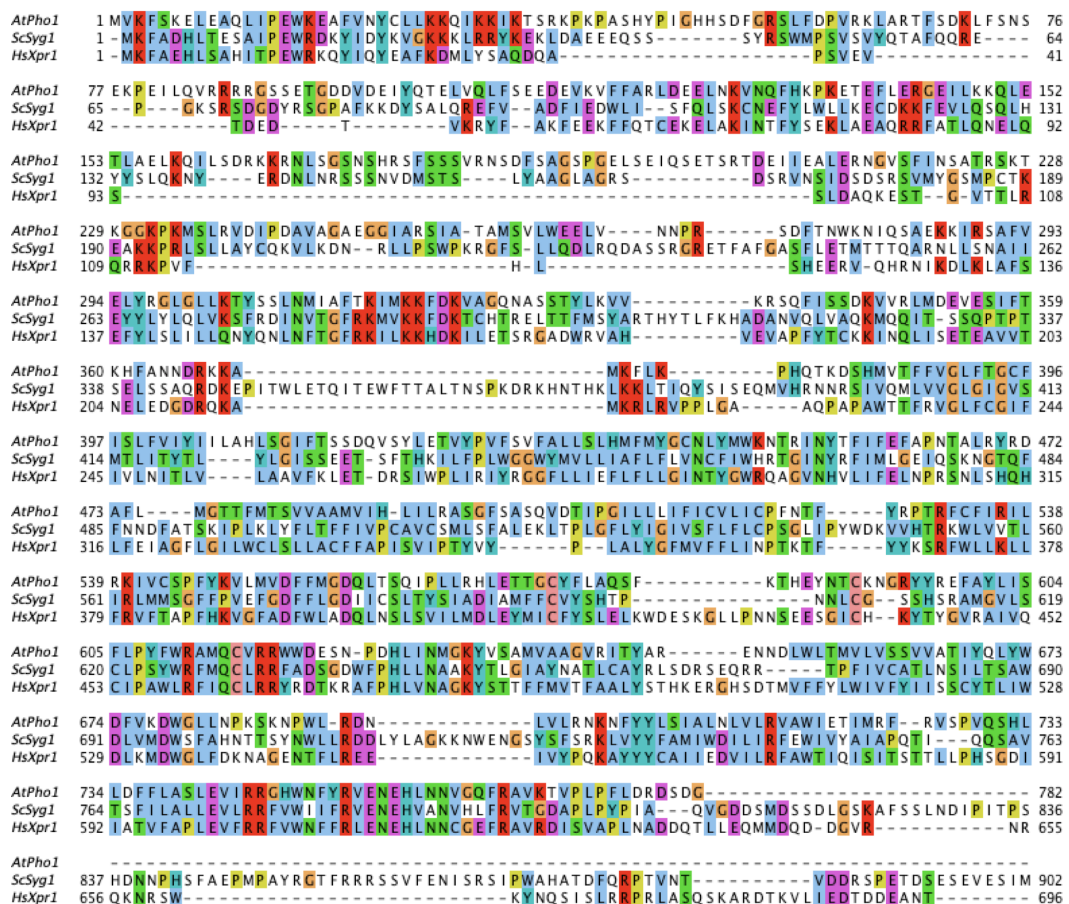


Figure 3: Sequence alignment of Pho1, Syg1 and Xpr1. Sequence homology between AtPho1 (*A. thaliana*), ScSyg1 (*S. cerevisiae*) and HsXpr1 (*H. sapiens*) is shown. Sequences are colored according to the Clustal X color scheme and gaps are shown as minus (-) symbols. Sequences were aligned using Clustal Omega (Madeira et al., 2022).

1.2.4 Human phosphate homeostasis

In multicellular eukaryotes, phosphate is not only regulated at the level of individual cells but also at an organismal level. In humans, phosphate is the most abundant anion, making up 1 % of the total body weight (Farrow et al., 2011). Approximately 85 % of total phosphate is present as hydroxyapatite in bones and teeth (Penido et al., 2012). Phosphate is absorbed with food and taken up in the intestine from where it is transferred into the blood. It is also actively reabsorbed or excreted in renal tubes based on the organismal phosphate demand. Absorption, re-absorption and excretion are regulated by the action of different hormones, especially fibroblast growth factor 23 (FGF23) and parathyroid hormone (PTH) (Bergwitz et al., 2010).

Phosphate homeostasis at the cellular level is poorly understood in higher eukaryotes. It is partially regulated by the action of different sodium/phosphate importers. Transporters of the SLC34 family are the main transporters in phosphate absorption in intestine (SLC34A2) and reabsorption in kidneys (SLC34A1 and SLC34A3) (Forster et al., 2013). However, SLC34A2 is also expressed in other cell types where it is also responsible for phosphate uptake. The other class of phosphate transporters are SLC20 family members (PiT1 and PiT2). They are ubiquitously expressed and were suggested as “housekeeping” importers, keeping cellular phosphate levels constant in most cell types (Collins et al., 2004). The interplay of these transporters and how they are regulated based on intracellular phosphate levels remains elusive.

1.2.5 Human phosphate export by Xpr1

In mammals, Xpr1 is the only known phosphate export protein and is ubiquitously expressed in all cell types. After its first identification as a virus receptor, it was later found to be an inorganic phosphate exporter (Giovannini et al., 2013). Xpr1 has the same predicted domain architecture as Syg1, including SPX and EXS domains (Figure 4). In contrast to fungi and plants, Xpr1 is the only human protein with a regulatory SPX domain. Previous studies revealed that Xpr1-mediated P_i efflux is specifically dependent on $InsP_8$ and that $InsP_8$ binds to the SPX domain with high affinity (180 nM) (Li et al., 2020). Moreover, knock-outs of inositol hexakisphosphate kinases I and II (IP6K1/2) were shown to result in significantly diminished phosphate export by Xpr1 due to the absence of $InsPPs$ in general (Wilson et al., 2019). It has also been reported that Xpr1 can interact with the β -subunit of G-proteins, leading to increased cellular cyclic-AMP (cAMP) levels but the function of this signaling pathway is still unknown (Vaughan et al., 2012).

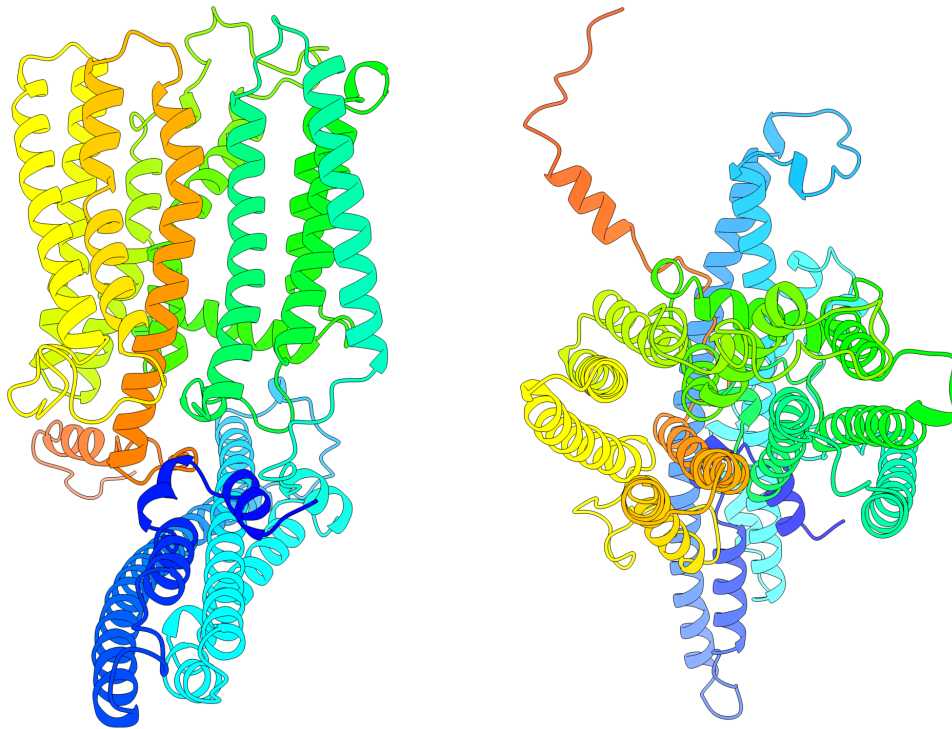


Figure 4: AlphaFold model of human Xpr1. The AlphaFold model (Jumper et al., 2021) is shown along the presumed membrane plane (left) and perpendicular to the membrane plane (right). The predicted structure of HsXpr1 shows 10 predicted TM helices and the typical three-helix bundle of the SPX domain. The SPX domain lies parallel to the membrane plane at the cytosolic side. The model is rainbow colored from the N- to the C-terminus.

The *Xpr1* gene is essential and its knock-out was shown to be embryonically lethal in mice (Vaughan et al., 2012). Mutations lead to several disorders that are all linked to defects in phosphate homeostasis: Primary familial brain calcification (PFBC) is a neurodegenerative disorder characterized by calcium phosphate deposits in the basal ganglia of the brain. Faulty Xpr1-mediated phosphate export is one of the main reasons for the formation of these calcium phosphate deposits (Legati et al., 2015). Xpr1 is also responsible for basolateral phosphate efflux in renal tubes and its inactivation led to impaired renal phosphate reabsorption (Ansermet et al., 2017). This condition also leads to impaired reabsorption of glucose and amino acids in renal tubes, which is known as Fanconi syndrome. Additionally, Xpr1 was found to be overexpressed in ovarian cancers and it was shown that inhibition or knock-out of Xpr1 leads to toxicologically high intracellular P_i levels in these cancer cells, leading to increased cell death, making Xpr1 an interesting therapeutic target (Akasu-Nagayoshi et al., 2022; Bondeson et al., 2022). Xpr1 was also found to be overexpressed in different squamous cell carcinoma and was suggested as a potential biomarker and immunotherapy target (Wang et al., 2022; Chen et al., 2019).

1.3 Electron cryo-microscopy

Electron cryo-microscopy (cryo-EM) has emerged as a revolutionary technique in the field of structural biology (Kühlbrandt, 2014), enabling structure determination of biological macromolecules with unprecedented levels of detail and complexity.

Cryo-EM is a microscopy technique used to visualize structures of frozen biological samples with electrons (Henderson, 2018). The samples must be frozen to withstand the high vacuum within the microscope, while preserving their natural aqueous environment. Single-particle analysis (SPA) in cryo-EM is a predominant technique for determining structures of biological macromolecules (Figure 5). In this technique, multiple 2D projections of the specimen in random orientations are recorded and later computationally classified, averaged and reconstructed into a 3D volume. In the last decade, advances in detector technology, new image processing algorithms and increased computing capabilities have led to near-atomic resolution of protein structures determined by cryo-EM (Kühlbrandt, 2014).

1.3.1 Microscope structure

Electron microscopes are indispensable instruments for capturing high-resolution images of small biological and non-biological specimens. They can be classified into two classes: scanning electron microscopes (SEM) and transmission electron microscopes (TEM). While a SEM detects back-reflected electrons and is primarily used for analyzing surface structures, a TEM detects electrons that have passed through the sample and thereby reveals the inner structure of the specimen. This represents the predominant technique used to image biological samples (Orlova et al., 2011).

The overall architecture of a transmission electron microscope (TEM) is similar to that of a light microscope (Figure 6). Instead of a light source, an electron source is installed at the top of the microscope. Common electron sources are tungsten filaments, LaB₆ crystals or field emission guns (FEG). The electrons emitted from these sources are accelerated by an electric field. The wavelength of the electrons depends on the voltage of the applied electric field with typical values ranging between 100 – 300 kV. For example, an accelerating voltage of 300 kV results in a wavelength of 0.02 Å. Since the maximal theoretic resolution of a microscope is directly correlated to the wavelength (Abbe's diffraction limit) very high-resolution can be achieved (Abbe, 1873). The electron beam is focused by electromagnetic lenses (condenser lens) onto the specimen at the cooled stage and gets scattered by the specimen atoms. The scattered electrons are then re-focused

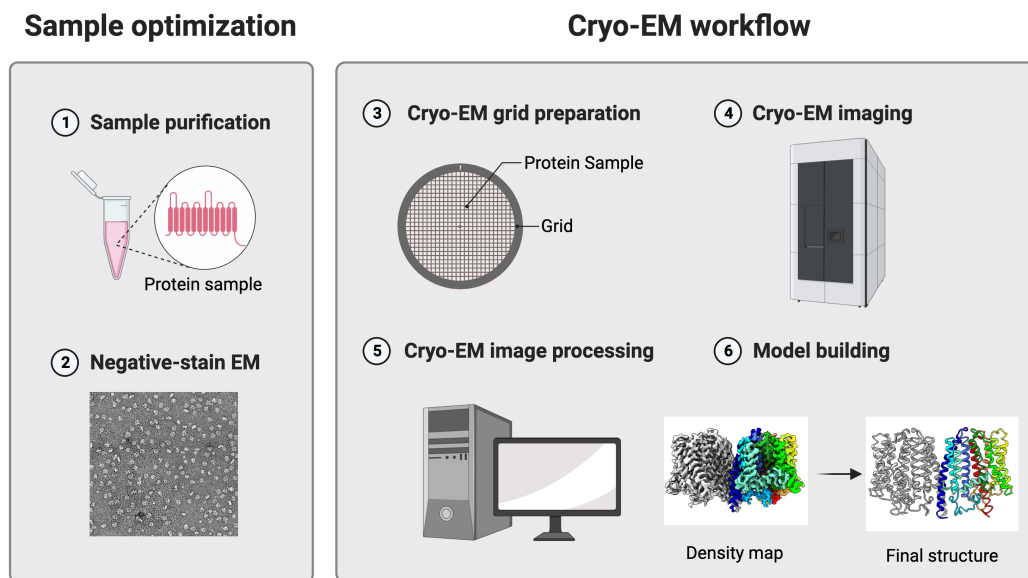


Figure 5: Overview of cryo-EM SPA workflows. Protein specimen for cryo-EM should be optimized for purity, stability and homogeneity. This can be verified by different biochemical assays or by negative-stain EM. Optimized samples are applied to a cryo-EM grid and plunge frozen in a thin amorphous ice layer. Thousands of images are recorded on an electron microscope and computationally processed to obtain 3D density maps. These maps are then used to build an atomic model of the protein. (Figure created with BioRender.com)

onto the detector at the bottom of the microscope by the objective and projector lenses, thereby forming a magnified image of the illuminated area. The entire microscope column must be kept under high vacuum since the emitted electrons are scattered by any atom within the beam path. For the same reason, the specimen must also be very thin to allow electrons to pass through. Most electrons pass through thin specimens without interactions. When electrons interact with the specimen, they are scattered either elastically or inelastically. Elastically scattered electrons are deflected without any energy loss and contribute to the image formation in TEM. Conversely, inelastically scattered electrons transfer energy to the specimen and exit with a reduced energy. The deposited energy of inelastically scattered electrons causes radiation damage to the sample and thereby limits the electron dose that can be used to image biological samples (Glaeser, 1971). Moreover, inelastically scattered electrons contribute to noise in TEM images. To reduce this effect, energy filters are placed in front of the detector to filter out inelastically scattered electrons and improve image contrast (Schröder et al., 1990).

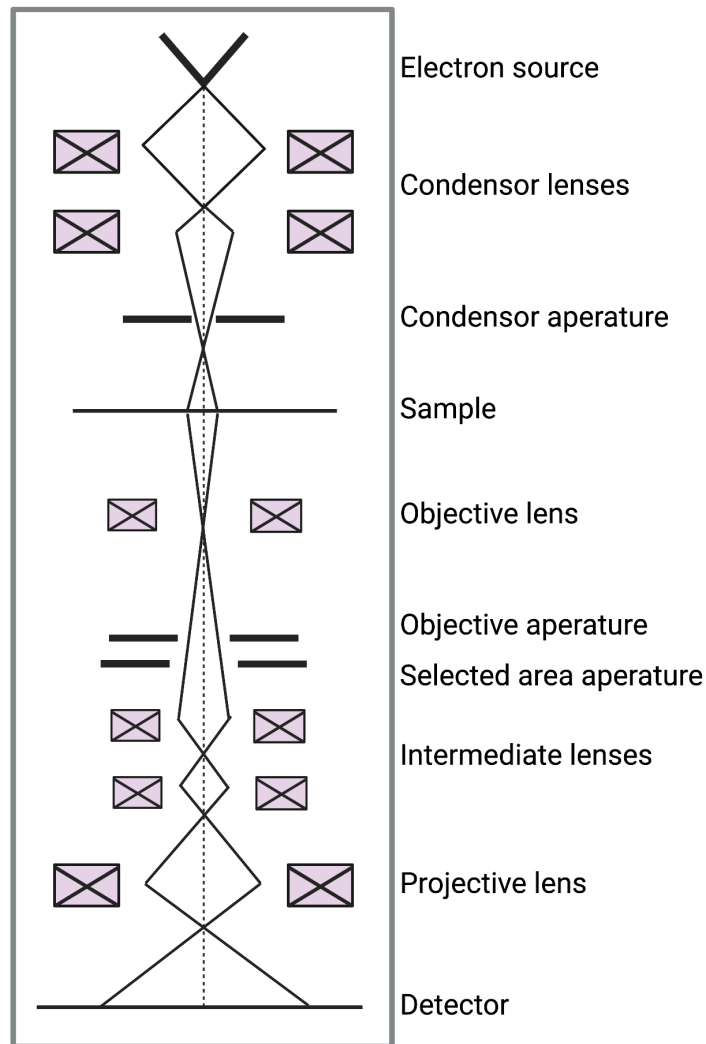


Figure 6: Structure of a transmission electron microscope. Electrons are emitted from the electron source on top of the column and accelerated by an electric field towards the sample. A condenser lens system focuses the coherent electron beam onto the sample. Different apertures within the column filter electrons with a large angular spread. After interaction with the sample the beam is focused by different lens systems onto the detector resulting in a magnified image. (Figure created with BioRender.com)

Image formation in cryo-EM depends on the amplitude and phase contrast generated by electrons on the detector. Since protein specimens consist mainly of light atoms like hydrogen, carbon, oxygen and nitrogen, the amplitude contrast in cryo-EM images is low. Phase contrast arises from the different path lengths of scattered and unscattered electron waves which subsequently show constructive and destructive interference leading to detectable contrast on the detector. However, the scattering angles of electrons interacting with protein specimens are only small, resulting in weak phase contrast. Stronger

phase contrast can be achieved by recording under-focused images since this increases the difference in path lengths and thus phase differences between scattered and unscattered electrons (Frank, 2006). The interference of electron waves is also dependent on their spatial frequency, resulting in some frequencies being more strongly represented in the image than others, with some even missing or flipped in sign. This phenomenon is mathematically described by the Contrast Transfer Function (CTF). The CTF is a quasi-periodic sine function that indicates which spatial frequencies are represented in the recorded image (for example frequencies where the values are zero, do not contribute to the image) (Cheng et al., 2015). The oscillations of the CTF are visualized by Fourier Transformation (FT) of the image, where the amplitudes are represented by Thon rings in the FT. The CTF is modulated by changing the defocus values of the recorded image. In fact, it is essential to record cryo-EM datasets over a defined defocus range to include information of all spatial frequencies in later 3D reconstructions (Nogales et al., 2015). The CTF is also modulated by an envelope function resulting from microscope lens aberrations, underfocus and spatial and temporal electron incoherence, leading to a dampening of high-frequency information and thus attenuation of high-resolution information (Penczek, 2010).

1.3.2 Sample preparation

Protein samples for cryo-EM should be pure and homogeneous, since structure determination by single-particle cryo-EM relies on thousands of identical particles to be recorded and computationally averaged (Thompson et al., 2016). A useful method for assessing sample homogeneity is imaging the sample by negative-stain EM. Negative-staining is a technique to stain protein samples by using heavy atom salts (e.g. uranyl formate) and thereby increasing image contrast. However, due to the grain size of the stain, negative-stain EM does not provide high-resolution information (Ohi et al., 2004).

Once sample homogeneity is confirmed, protein samples for cryo-EM must be frozen in a thin amorphous layer of ice, so that it can survive the vacuum inside an electron microscope, but still remains transparent to electrons (Dubochet et al., 1988). Such a thin layer of amorphous ice is obtained by applying a small sample volume (usually 3 μ l) to an EM grid and blotting away excess liquid, leaving only a very thin layer of solution within the small holes of the grid (Figure 7). The grid is then rapidly plunge-frozen in liquid ethane to obtain a thin layer of amorphous ice (McDowell et al., 1983). These grids can be stored at liquid nitrogen temperature until used for data acquisition.

Vitrification is essential for specimens to withstand the high vacuum in the microscope,

while preserving their natural aqueous environment. Another advantage of imaging under cryogenic conditions is the reduction of radiation damage, a major limitation when working with biological specimens (Baker et al., 2010). Incident electrons ionize the sample and break chemical bonds of the biomolecules. This also causes the production of secondary electrons and free radicals that migrate through the sample, further damaging the specimen. These reactions lead to the production of hydrogen gas, which can be seen as "bubbling" on the specimen at high electron exposures. In order to minimize beam-induced radiation damage, cryo-EM images are recorded with low electron doses, which however results in noisy micrographs with a low signal-to-noise ratio (SNR). Consequently, structure determination of high-resolution structures by cryo-EM depends on the computational alignment and averaging of thousands of particles.

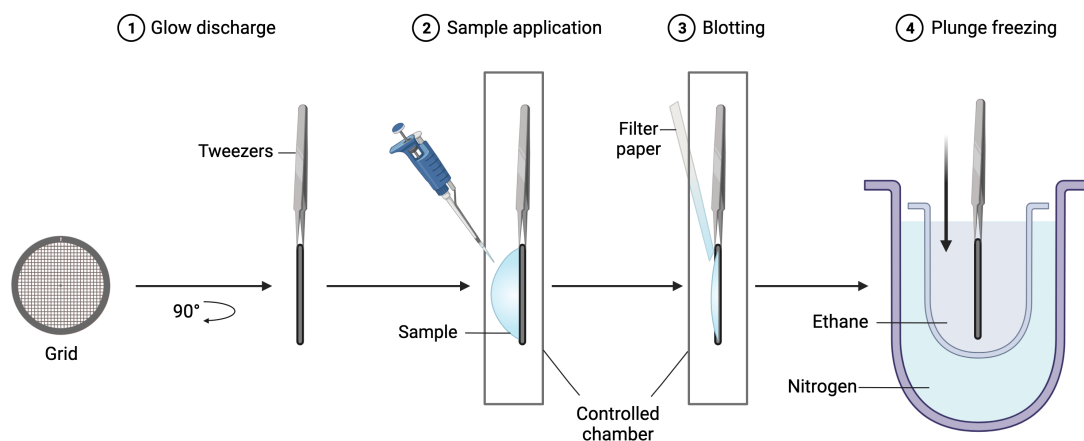


Figure 7: Plunge freezing of cryo-EM samples. Cryo-EM grids are glow discharged to render the grid surface hydrophobic. A small droplet of sample is applied to the glow discharged grid in a chamber with controlled temperature and humidity. Excess liquid is blotted off using filter papers so that only a thin layer of sample remains. The grids are then rapidly plunge-frozen in liquid ethane to generate vitreous ice. Frozen grids are transferred to liquid nitrogen for storage until data acquisition. (Figure created with BioRender.com)

1.3.3 Data processing

Since cryo-EM datasets typically require a large storage capacity, extensive computing capacities are needed to apply complex processing algorithms. Therefore, the data is

best processed on powerful computers or computing clusters.

Cryo-EM micrographs are not recorded as single images but as movies with multiple individual frames. This allows to computationally correct for particle motion during data acquisition caused by the phenomenon of beam-induced motion (Brilot et al., 2012). Correcting for particle movement by individual frame alignment is necessary to recover high-resolution information in the images which is lost unless particle movement is corrected (Zheng et al., 2017). This motion correction is usually the first step in data processing. After motion correction the second step typically is CTF estimation. The CTF is a mathematical function to describe how EM images are distorted by microscope optics and aberrations. CTF estimation determines defocus and astigmatism, so that the CTF function approximates the Thon rings in the power spectrum of a respective EM image (Rohou et al., 2015). Once images have been corrected, particles are picked, either manually or automatically. Automated particle picking algorithms can be based on previously generated templates, on Gaussian “blob” recognition or on deep neural networks (Scheres, 2015; Wagner et al., 2019).

After particles are picked and extracted with sufficient box sizes, they are averaged and classified in 2D space, which is called 2D classification. In cryo-EM particles are recorded as 2D projections of the 3D Coulomb potential of the specimen. Since freezing is very rapid, the proteins are ideally caught in various orientations, thereby yielding 2D projections from different angular orientations. These 2D projections are aligned and classified into a number of 2D classes (Joyeux et al., 2002). In an ideal case, different classes show the target protein in different angular views, while classes containing image artifacts or invalid particles can be excluded from subsequent processing steps. Selected 2D classes are used to calculate an *ab initio* 3D map using a back-projection algorithm, if no previous initial model of the target protein is available (Levin et al., 2017). The initial map is then iteratively refined, a process that is referred to as 3D refinement. During this procedure, the orientation parameters of the particles are optimized to better match computed reprojections of the initial density map. These optimized parameters are then used to improve the resolution of the map. Refinement algorithms often use a so called “gold standard” approach, in which two independent half-maps are refined, each from half of the available particles (Scheres et al., 2012). The two half-maps are cross-correlated in Fourier space and the resulting Fourier Shell Correlation (FSC) is used as a criterion to assess the nominal resolution of the reconstructed map (Rosenthal et al., 2003). To further improve the quality of the final map CTF refinement, Bayesian polishing or density modification are common strategies (Terwilliger et al., 2020; Zivanov et al., 2019).

1.4 Project motivation

The low-affinity phosphate transporters of yeast represent a unique class of phosphate importers. The TM domain, showing homology to proteins from the DASS superfamily along with the regulatory SPX domain, suggests a distinct phosphate transport mechanism compared to other known phosphate transporters. Additionally, the closest homologues of these transporters in mammals are sodium sulfate symporters NaS1 and NaS2, which lack an SPX domain, but display sequence similarities in the TM part. To understand the mechanism of phosphate translocation and the regulatory role of the SPX within this mechanism, high-resolution structures in combination with functional analysis are crucial. Since structural information is so far limited to isolated SPX domains, this thesis focused on obtaining high-resolution structures of Pho90 by cryo-EM, with a particular emphasis on the TM domain. This approach aimed to unveil the overall architecture of this phosphate transporter class and identify important residues involved in substrate binding, translocation and regulation. Combining these structural findings with functional studies will shed light on the translocation mechanism of low-affinity phosphate transporters.

In contrast to the multiple phosphate importers in yeast, there is only one known class of phosphate exporters, which is conserved throughout all eukaryotes. Despite their pivotal role in eukaryotic phosphate homeostasis, structural information on these phosphate exporters is currently lacking. This thesis sought to optimize the expression and purification of yeast Syg1 and human Xpr1, aiming to obtain high-resolution structures by cryo-EM of both, preferably in different states of the translocation cycle. Together with biochemical experiments, these findings should elucidate aspects of the conserved eukaryotic phosphate export mechanism at an atomistic level. These insights also bear medical relevance, since mutations in Xpr1 are linked to the neurodegenerative disorder PFBC and Fanconi Syndrome. Additionally, Xpr1 has been shown to be overexpressed in different cancer types and its knock-out has been associated with increased cancer cell death, rendering it a potentially important cancer marker and drug target.

2 Material and Methods

2.1 Media and competent cell buffers

The composition of media and buffers used to cultivate cells or prepare competent cells can be found in Table 1. When individual media or buffers were used it is referenced in the respective sections.

Table 1: Cultivation media and competent cell buffers.

Medium	Specification
LB Medium	10 g/L Bacto tryptone 5 g/L Yeast extract 10 g/L NaCl
RF1 Competent Cells buffer	30 mM KAc pH 5.8 100 mM RbCl 50 mM MnCl ₂ 10 mM CaCl ₂ 15 % glycerol
RF2 Competent Cells buffer	10 mM MOPS pH 6.8 10 mM RbCl 75 mM CaCl ₂ 15 % glycerol
YPD Medium	20 g/L Peptone 10 g/L Yeast extract 20 g/L Glucose
Yeast drop-out medium (Pre-culture)	6.7 g/L Yeast nitrogen base 2 % (w/v) Glucose 1.65 g/L -Leu or 1.92 g/L -Ura amino acid mix
Yeast drop-out medium (Expression)	6.7 g/L Yeast nitrogen base 2 % (w/v) Lactate pH 5.5 1.65 g/L -Leu or 1.92 g/L -Ura amino acid mix
Sf-900 III SFM medium	<i>see</i> Thermo Fisher F12658019
FreeStyle 293 Expression Medium	<i>see</i> Thermo Fisher 12338026

2.2 Cloning and vector design

Unless otherwise stated, all Kits were used according to the manufacturer's protocol.

All genes were ordered from Genscript as codon optimized constructs for either bacterial or yeast expression and were flanked by N-terminal NdeI and C-terminal XhoI restriction sites. The genes and corresponding expression vectors were digested using the restriction enzymes NdeI and XhoI (Thermo Fisher) for 2 h at 37 °C. The reaction mixtures were then loaded onto a 1 % agarose gel and separated in TAE buffer (40 mM Tris pH 7.0, 20 mM acetic acid, 1 mM EDTA) for 30 – 60 min at 100 V. The gel was stained using Midori Green DNA Stain (Biozym) and the DNA bands were extracted from the gel using the QIAquick Gel Extraction Kit (Qiagen). The digested inserts and respective expression vectors were then ligated overnight at 16 °C using T4 DNA ligase (Thermo Fisher). *E. coli* DH5 α cells were transformed with 10 μ l of the reaction mixture and cultivated at 37 °C (see 2.3.1). After isolation of plasmid DNA using a QIAprep Spin Miniprep Kit (Qiagen) the correct sequences were confirmed by Sanger sequencing (Microsynth).

Table 2: Composition of PCR reactions.

Component	Amount
10x Pfu Ultra II buffer	5 μ l
DNA template	50 ng
Primer forward (10 μ M)	1.5 μ l
Primer reverse (10 μ M)	1.5 μ l
dNTPs (10 mM)	2 μ l
Pfu Ultra II polymerase	0.5 μ l
Water	up to 50 μ l

Genes encoding for Pho90, Syg1 or Xpr1 were subcloned into the yeast expression vector pDD containing either an N- or C-terminal His10-tag (pDD-His) or into a pDD vector containing C-terminal GFP and His10-tags (pDD-GFP). Xpr1 was also subcloned into the BacMam expression vector pEZT using NheI and XhoI restriction sites after amplification of the gene with these restriction sites by PCR. The pEZT vector contained C-terminal GFP and His10 tags. Mutations were introduced by site-directed mutagenesis using quick-change PCR reactions. All PCR reactions were set up as described in Table 2 and ran according to the protocol of Pfu Ultra II polymerase (Agilent). PCR products were purified using a PCR Purification Kit (Qiagen), digested with DpnI for 1 h and transformed into *E. coli* DH5 α cells. Correct mutations were confirmed by Sanger sequencing (Microsynth). A list of all vectors can be found below in Table 3 and 4.

Table 3: Pho87/Pho90 plasmids used for protein expression.

Name	Backbone	Protein	Tags
pDD-CtPho87-His	pDD	CtPho87	N-term. His10
pDD-CtPho87-CHis	pDD	CtPho87	C-term. His10
pDD-CtPho87-CGFP	pDD	CtPho87	C-term. GFP and His10
pDD-ScPho87-His	pDD	ScPho87	N-term. His10
pDD-ScPho87-CHis	pDD	ScPho87	C-term. His10
pDD-ScPho87-CGFP	pDD	ScPho87	C-term. GFP and His10
pDD-ScPho90-His	pDD	ScPho90	N-term. His10
pDD-ScPho90-CHis	pDD	ScPho90	C-term. His10
pDD-ScPho90-CGFP	pDD	ScPho90	C-term. GFP and His10
pDD-ScPho90N566A-His	pDD	ScPho90 with point mutation N566A	N-term. His10
pDD-ScPho90S815A-His	pDD	ScPho90 with point mutation S815A	N-term. His10
pDD-ScPho90d390-His	pDD	ScPho90 with deletion of residues 1-390	N-term. His10
pDD-ScPho90d355-377-His	pDD	ScPho90 with deletion of residues 355-377	N-term. His10
pDD-ScPho90d355-408-His	pDD	ScPho90 with deletion of residues 355-408	N-term. His10
pDD-ScPho90d363-377-His	pDD	ScPho90 with deletion of residues 363-377	N-term. His10
pDD-ScPho90d363-408-His	pDD	ScPho90 with deletion of residues 363-408	N-term. His10

2.3 Preparation and transformation of competent cells

2.3.1 Preparation and transformation of competent *E. coli* cells

All competent *E. coli* cells were prepared according to the RbCl protocol (Promega). An overnight culture was inoculated with a single colony and grown in LB medium. This culture was used to inoculate 100 mL LB medium and grown at 37 °C to an OD600 of 0.5 - 0.8. After centrifugation at 2700 xg for 10 min the cell pellet was resuspended in RF1 buffer and incubated on ice for 15 min. The cell slurry was centrifuged again at 590 xg for 15 min and the cell pellet resuspended in 4 mL RF2 buffer. Aliquots of 100 µl were prepared, flash frozen in liquid nitrogen and stored at -80 °C. For transformations, a single aliquot was thawed, mixed with plasmid DNA and incubated on ice for 10 min. The cells were heat shocked at 42 °C for 45 s and placed back on ice for 5 min. 750 µl

2.3. Preparation and transformation of competent cells

Table 4: Syg1/Xpr1 plasmids used for protein expression.

Name	Backbone	Protein	Tags
pDD-CtSyt1-NHis	pDD	CtSyt1	N-term. His10
pDD-CtSyt1-His	pDD	CtSyt1	C-term. His10
pDD-CtSyt1-GFP	pDD	CtSyt1	C-term. GFP and His10
pDD-YlSyt1-NHis	pDD	YlSyt1	N-term. His10
pDD-YlSyt1-His	pDD	YlSyt1	C-term. His10
pDD-YlSyt1-GFP	pDD	YlSyt1	C-term. GFP and His10
pDD-ScSyt1-NHis	pDD	ScSyt1	N-term. His10
pDD-ScSyt1-His	pDD	ScSyt1	C-term. His10
pDD-ScSyt1-GFP	pDD	ScSyt1	C-term. GFP and His10
pDD-HsXpr1-His	pDD	HsXpr1	C-term. His10
pDD-HsXpr1-GFP	pDD	HsXpr1	C-term. GFP and His10
pEZT-HsXpr1-GFP	pEZT	HsXpr1	C-term. GFP and His10

LB medium were added and cells were incubated at 37 °C for 30 min. The cells were streaked onto antibiotic selection plates and incubated overnight at 37 °C.

2.3.2 Preparation and transformation of competent *S. cerevisiae* cells

S. cerevisiae BJ5460 cells were streaked onto YPD agar plates and incubated for 2 days at 30 °C. A single colony was used to inoculate 5 ml of YPD medium and incubated overnight at 30 °C shaking. 100 ml YPD were inoculated with the overnight culture to a final titer of 5×10^6 cells/mL and incubated at 30 °C shaking. When the titer reached 2×10^7 cells/mL, the cells were centrifuged for 5 min at 3000 xg. The cell pellet was washed with sterile water, centrifuged again and resuspended in 4 mL of sterile water. 100 µl aliquots were prepared and placed in an air-tight Styrofoam box at -80 °C to slowly freeze the cells. For yeast transformations the lithium-acetate method was used (Gietz et al., 2007). In brief, a single yeast aliquot was thawed and centrifuged for 5 min at 3000 xg. The cell pellet was resuspended in 400 µl of 100 mM lithium acetate and centrifuged for 15 s at 8000 xg. The cell pellet was resuspended in 50 µl lithium acetate and placed on ice. 240 µl of freshly prepared 50 % PEG3350 was added and mixed briefly. Then 25 µl of 2 mg/mL ss carrier DNA and 1 µg plasmid DNA was added and mixed again briefly. The cells were incubated at 30 °C for 30 min, then heat shocked for 30 min at 42 °C, plated on -Ura

drop-out plates and incubated at 30 °C for 2 days. If -Leu was used as drop-out marker the cells were re-streaked on -Leu drop-out plates and incubated at 30 °C for 2 days.

Table 5: *E. coli* and *S. cerevisiae* strains used in this thesis.

Strain	Genotype
<i>E. coli</i> DH5 α	F ⁻ endA1 glnV44 thi-1 recA1 relA1 gyrA96 deoR nupG purB20 φ 80dlacZ δ M15 δ lacZYA-argF)U169, hsdR17 λ ⁻
<i>E. coli</i> Top10	F ⁻ mcrA δ (mrr-hsdRMS-mcrBC) φ 80dlacZ δ M15 δ lacX74 nupG recA1 araD139 δ (ara-leu)7697 galE15 galK16 rpsL(StrR) endA1 λ ⁻
<i>E. coli</i> DH10Bac	F ⁻ mcrA δ (mrr-hsdRMS-mcrBC) φ 80dlacZ δ M15 δ lacX74 recA1 araD139 δ (ara-leu)7697 galU galK nupG λ ⁻ rpsL/bMON14272 / pMON7124
<i>S. cerevisiae</i> BJ2168	MATa prc1-407 prb1-1122 pep4-3 leu2 trp1 ura3-52 gal2
<i>S. cerevisiae</i> BJ5460	MATa ura3-52 trp1 lys2-801 leu2-delta1 his3-delta200 pep4::HIS3 prb1-delta1.6R can1 GAL

2.4 Protein analysis

2.4.1 Sodium dodecyl sulfate polyacrylamide gel electrophoresis

Sodium dodecyl sulfate polyacrylamide gel electrophoresis (SDS-PAGE) is a method for separating proteins depending on their molecular size within an applied electric field (Laemmli, 1970). Protein samples were mixed with SDS-PAGE sample buffer and applied onto an SDS-PAGE gel. Precasted SDS-PAGE gels (Bio-Rad) consisted of two different layers with different concentrations of polyacrylamide - 12 % for the resolving gel and 4 % for the stacking gel. Electrophoresis was performed at 160 V for 40 min or until the gel front reached the bottom of the gel. PageRuler™ Plus Prestained Protein Ladder, 10 to 250 kDa (Thermo Fisher) was used as marker.

2.4.2 Blue native PAGE

Blue native PAGE (BN-PAGE) is an electrophoresis technique that preserves the native structure of proteins and protein complexes, while separating according to their molecular weight (Reisinger et al., 2006). All samples were mixed with BN sample buffer in a

1:3 ratio before being applied to a NativePAGE 4-16 % Bis-Tris Gel (Invitrogen). The inner gel chamber was filled with cathode buffer and the outer chamber with anode buffer. The gel was run for 1 h at 100 V before the cathode buffer was exchanged to cathode buffer without Coomassie and the gel was run for another 3 h at 200 V. NativeMark™ Unstained Protein Standard (Thermo Fisher) was used as marker.

2.4.3 Coomassie staining and Western Blotting

Coomassie staining of gels was prepared by incubating the gel for 10 min in Coomassie fixative buffer. To stain all protein bands, the gel was incubated for 30 min in Coomassie staining buffer, which contained 0.025 % Coomassie G250. The unspecific staining was removed by washing with water or destaining buffer. Western blotting was used to determine expression levels in cell lysates and solubilization assays. The separated protein samples were transferred to a polyvinylidene fluoride (PVDF) membrane by electroblotting with a Bio-Rad Trans-Blot Turbo for 30 min, 200 mA, 15 V. The method is based on Towbin et al., 1979. The membranes were incubated in 5 % BSA in TBST for 1 h and washed 2 times with TBS. Then they were incubated overnight at 4 °C with the primary antibody (Monoclonal Anti-polyHistidine antibody produced in mouse (Sigma); 1:2000 in TBS with 1 % milk powder). The membranes were washed 3 times with TBS and incubated for 2 h with the secondary antibody (Anti-mouse IgG-Peroxidase antibody produced in goat (Sigma); 1:1000 in TBS). The membrane was again washed 3 times with TBS, then incubated for 30 s with Amersham ECL WB Detection Reagents (GE Healthcare) and imaged using a Bio-Rad ChemiDoc MP imager.

2.4.4 Protein quantification

The protein concentrations of membrane fractions were determined by Bradford assays (Bradford, 1976). 5 µl of membrane fractions in different dilutions were mixed with 250 µl Bradford reagent (Sigma) and incubated for 5 min. The absorbance at 595 nm was measured in microplates and compared to a BSA standard curve.

Protein concentrations of purified proteins were determined by measuring the absorbance at 280 nm using a Nanodrop spectrometer (Thermo Fisher).

Table 6: Buffers used for SDS-PAGE, Western Blotting, BN-PAGE, Coomassie staining and agarose gels.

Buffer	Components	Concentration
SDS-PAGE sample buffer	Tris pH 6.8	20 mM
	Glycerol	5 %
	SDS	0.4 %
	Mercaptoethanol	1 %
	Bromphenol Blue	0.05 %
SDS-PAGE buffer	SDS	1 g/L
	Tris	3 g/L
	Glycine	14.4 g/l
TBS	Tris pH 7.5	10 mM
	NaCl	150 mM
WB transfer buffer	Tris	3 g/L
	Glycine	14.4 g/L
	Methanol	20 %
Coomassie fixative buffer	Ethanol	50 %
	Acetic acid	10 %
Coomassie staining buffer	Ethanol	5 %
	Acetic acid	7.5 %
	Coomassie G250	0.1 %
BN-PAGE sample buffer	Bis-Tris pH 7.0	100 mM
	6-aminocaproic acid	500 mM
	Glycerol	10 %
BN-PAGE anode buffer	Bis-Tris pH 7.0	50 mM
BN-PAGE cathode buffer	Bis-Tris pH 7.0	15 mM
	Tricine	50 mM
	Coomassie G250	0.02 %

2.5 Protein expression and membrane preparation

2.5.1 Protein expression in *S. cerevisiae*

The expression of yeast constructs was adapted from Parker et al., 2014. A single yeast clone was used to inoculate 10 ml of yeast drop-out medium (-Ura or -Leu) including 2 % (w/v) glucose and yeast nitrogen base (YNB) and the culture was grown for 18 h at 30 °C. This culture was used to inoculate a 1L culture of yeast drop-out medium (-Ura or -Leu) including 2 % (w/v) glucose and YNB and the culture was grown for 24 h at 30 °C again. 10 L of yeast drop-out expression medium (-Ura or -Leu) with YNB and 2 % (w/v) lactate pH 5.5 instead of glucose were inoculated and grown for 18 h at 30 °C. Expression was induced by the addition of galactose to a final concentration of 2 % (w/v) and protein expression was conducted for 24 h at 25 °C (for Pho90 and Syg1 constructs) or at 20 °C

2.5. Protein expression and membrane preparation

(for HsXpr1). All Pho90 constructs used for subsequent experiments were expressed in -Ura drop-out medium while final Syg1 and Xpr1 constructs were expressed in -Leu drop-out medium.

2.5.2 Expression of HsXpr1 in HEK293 GnTI- cells

The expression of HsXpr1 in HEK293 GnTI- (ATCC CRL3022) cells using baculovirus transduction of mammalian cells (BacMam) was adapted from previous studies (Goehring et al., 2014). The optimization of expression conditions and large-scale expressions were performed together with Sabine Häder (MPI of Biophysics). First, the plasmid pEZT-HsXpr1-GFP was transferred into competent *E. coli* DH10Bac cells (see 2.3.1). Cells were incubated at 37 °C for 4 h, streaked on LB agar plates (containing 50 µg/mL kanamycin, 7 µg/mL gentamicin, 10 µg/mL tetracycline, 100 µg/mL Bluo-Gal and 40 µg/mL IPTG) and incubated at 37 °C for 48 h. A single white colony was picked and used to inoculate 5 ml LB (containing 50 µg/mL kanamycin, 7 µg/mL gentamicin and 10 µg/mL tetracycline). Bacmid DNA was isolated by a QIAprep Spin Miniprep Kit (Qiagen) but using isopropanol for DNA extraction instead of spin columns.

For baculovirus generation 1×10^6 *Spodoptera frugiperda* Sf9 (Novagen T71104) cells were seeded in 2 mL of SF 900 III medium and transfected using Cellfectin II (Gibco) and 5 µl Bacmid DNA. After incubation at 27 °C for 72 h the supernatant containing P1 virus was harvested, sterile filtered and stored at 4 °C. For P2 virus generation 800 ml Sf9 suspension culture with a density of 1.5×10^6 cells/mL were infected with 400 µl P1 virus and incubated at 27 °C for 5 days, shaking. The P2 virus was harvested by removing Sf9 cells by centrifugation at 5,000 xg for 5 min. The supernatant was then ultracentrifuged at 30,000 xg for 60 min and the virus pellet was resuspended in 6 ml medium and sterile filtered. 800 mL HEK293 GnTI- suspension cells in FreeStyle293 medium + 2% FBS were grown to a density of 3×10^6 cells/mL in baffled plastic flasks (Corning) and infected with 500 µl P2 virus. The cultures were cultivated for 24 h at 37 °C and 5 % CO₂ before the addition of sodium butyrate to a final concentration of 10 mM to induce protein expression. The cultures were cultivated for another 72 h at 30 °C and 8 % CO₂.

2.5.3 Membrane isolation

Yeast cells were harvested by centrifugation for 5 min at 5,000 xg. Cell pellets were washed once with sterile water and either stored at -20 °C or directly used for membrane isolations. Cell pellets were resuspended in lysis buffer (50 mM KP_i pH 8.0, 100 mM NaCl, 1 µg/mL DNase I, Complete protease inhibitor (Roche)) and stirred for 60 min at 4 °C.

Cell lysis was accomplished using a cell disruptor (Constant System) at 2.3 bar and three passes of the cell suspension. The cell lysate was centrifuged at 20,000 xg for 30 min to discard cell debris. The supernatant was then again centrifuged at 200,000 xg for 75 min to harvest membranes. Membrane pellets were resuspended in membrane buffer (50 mM KPi pH 8.0, 100 mM NaCl, 10 % glycerol) and homogenized using a Dounce homogenizer. The membrane aliquots were then flash frozen in liquid nitrogen and stored at $-80\text{ }^{\circ}\text{C}$.

HEK cell pellets were harvested by centrifugation for 10 min at 4,000 xg. Cell pellets were washed with sterile PBS and either stored at $-20\text{ }^{\circ}\text{C}$ or directly used for membrane isolations. Cell pellets were resuspended in lysis buffer (50 mM KPi pH 8.0, 100 mM NaCl, 0.5 mM PMSF, 1 $\mu\text{g}/\text{mL}$ DNase I, Complete protease inhibitor (Roche)) and homogenized using a dounce homogenizer. The suspension was briefly sonicated for 1 min (20 % amplitude, 2 sec pulse, 2 sec pause) and membrane pellets were harvested by ultracentrifugation for 60 min at 200,000 xg and $4\text{ }^{\circ}\text{C}$. Membrane pellets were resuspended in membrane buffer (50 mM KPi pH 8.0, 100 mM NaCl, 10 % glycerol) and homogenized using a Dounce homogenizer. Aliquots with a total protein concentration of 10 mg/mL were frozen in liquid nitrogen and stored at $-80\text{ }^{\circ}\text{C}$.

2.5.4 Screening of detergents for solubilization

To determine solubilization efficiencies of His-tagged proteins by different detergents, 100 μl membrane samples were solubilized by the addition of various detergents. Final detergent concentration was 1 % (w/v) and solubilization was conducted for 2 h at $4\text{ }^{\circ}\text{C}$. Samples were centrifuged for 30 min at 100,000 xg and samples of the supernatant and pellet were loaded onto a SDS-PAGE gel and separated. His-tagged proteins were detected by Western Blotting (see 2.4.3).

To determine solubilization efficiencies and homogeneity of GFP fusion constructs in different detergents, 100 μl membrane samples were solubilized by the addition of various detergents. Final detergent concentration was 1 % (w/v) and solubilization was conducted for 2 h at $4\text{ }^{\circ}\text{C}$. Samples were centrifuged for 30 min at 100,000 xg and the supernatant was directly analyzed by FSEC. 50 μl of sample were injected by an autosampler onto an Agilent ProSEC 300 column (flow rate: 3 mL/min) and GFP fluorescence (Ex/Em: 480/520 nm) was measured. Resulting chromatograms were compared and analyzed.

2.6 Protein purification

2.6.1 Purification of proteins expressed in *S. cerevisiae*

Pho90-containing yeast membrane fractions were thawed and either LMNG/CHS or DDM/CHS were added to final concentrations of 0.75 %/ 0.075 % or 1 %/ 0.1 %, respectively and incubated for 2h at 4 °C (if DDM/CHS was used it was present in all buffers at 0.02 %/ 0.002 % instead of LMNG/CHS). Unsolubilized material was discarded by ultracentrifugation at 200,000 xg for 60 min. To the supernatant 20 mM imidazole was added, mixed with Ni-NTA beads (Sigma-Aldrich) and incubated for 1h at 4°C. The slurry was loaded into a gravity-flow column and washed with wash buffer 1 (20 mM KP_i pH 8.0, 250 mM NaCl, 10 % glycerol, 2 mM MgSO₄, 50 mM imidazole, 0.005 %/0.0005 % LMNG/CHS) followed by wash buffer 2 (20 mM KP_i pH 8.0, 100 mM NaCl, 2 mM MgSO₄, 10 % glycerol, 0.005 %/0.0005 % LMNG/CHS). Bound protein was eluted with elution buffer (20 mM KP_i pH 8.0, 100 mM NaCl, 2 mM MgSO₄, 250 mM imidazole, 0.005 %/0.0005 % LMNG/CHS) and concentrated using a 100 kDa cut-off spin concentrator (Amicon). The concentrated protein solution was applied to a Superdex 200 Inc column equilibrated with SEC buffer (20 mM KP_i pH 8.0, 100 mM NaCl, 0.005 %/0.0005 % LMNG/CHS). Elution fractions containing Pho90 were pooled for subsequent experiments and protein concentration was determined by absorbance at 280 nm. In phosphate-free purifications KP_i was replaced with Tris pH 8.0 in all purification buffers.

Syg1 proteins were purified as described for Pho90 with minor variations. No MgSO₄ was present in any purification buffer. For purifications in the presence of InsP₆, 5 mM InsP₆ was added during membrane solubilization and included in all wash and elution buffers. InsP₆ concentration in the final SEC buffer was 1 mM.

HsXpr1 expressed in *S. cerevisiae* was purified as described for Syg1 and Pho90 (see 2.6.1). Since the protein was unstable in solution the duration of all purification steps was minimized. The protein was solubilized for 1 h at 4 °C, the ultracentrifugation time was shortened to 40 min and batch binding to Ni-NTA beads was performed for 30 min.

2.6.2 Purification of HsXpr1 expressed in HEK293 GnTI- cells

The optimization of purification conditions and cryo-EM sample preparations of HsXpr1 were performed in collaboration with Julian Schneider (Goethe University, Frankfurt). HsXpr1-containing HEK293 membrane aliquots were thawed and homogenized briefly using a dounce homogenizer. Solubilization was achieved by the addition of DDM/CHS

to a final concentration of 1.5 %/0.15 % and incubation for 90 min at 4 °C. Unsolubilized material was discarded by ultracentrifugation at 200,000 xg for 60 min. The supernatant was mixed with 15 mM imidazole and Ni-NTA beads and incubated for 30 min at 4 °C. The slurry was loaded into a gravity-flow column and washed with wash buffer 1 (20 mM KP_i pH 8.0, 250 mM NaCl, 10 % glycerol, 50 mM imidazole, 0.03 %/0.003 % DDM/CHS) followed by wash buffer 2 (20 mM KP_i pH 8.0, 100 mM NaCl, 10 % glycerol, 0.03 %/0.003 % DDM/CHS). For cryo-EM samples detergent exchange was performed by washing with wash buffer 2 containing 0.01 %/0.001% LMNG/CHS instead of DDM/CHS. Bound protein was eluted with elution buffer (20 mM KP_i pH 8.0, 100 mM NaCl, 250 mM imidazole, 0.005 %/0.0005 % LMNG/CHS) and concentrated using a 100 kDa cut-off spin concentrator (Amicon). The concentrated protein sample was applied to a Superdex 200 Inc column equilibrated with SEC buffer (20 mM KP_i pH 8.0, 100 mM NaCl, 0.005 %/0.0005 % LMNG/CHS). Peak fractions were pooled for subsequent experiments and protein concentration was determined by measuring the absorbance at 280 nm. HsXpr1 used for reconstitution and transport measurements no detergent exchange to LMNG/CHS was performed but 0.03 %/0.003 % DDM/CHS was present in all final purification and SEC buffers.

2.7 Electron microscopy and data processing

2.7.1 Preparation and imaging of negative-stain EM grids

For all negative-stain experiments SPI Cu, 3mm 400 MESH TEM regular grids were used. Grids were washed in acetone and water before carbon coating. A 4 nm carbon layer was produced by a carbon coater (Leica) and gently flowed onto the grids. Grids were dried and stored under controlled humidity at room temperature until further use. Before application of protein samples, grids were glow-discharged using a PELCO easiGlow glow discharger (15 mA for 90 s). 3 μl of the protein sample (0.02 mg/mL) were applied to the grid and blotted manually using Whatman filter paper. Then 3 μl uranyl formate (2 % w/v; pH 4) or sodium silicotungstate (3 % w/v; pH 7) were added and blotted again three times. The grids were stored under controlled humidity at room temperature. Images were recorded on a Tecnai Spirit electron microscope, operating at 120 kV accelerating voltage and equipped with a Gatan Rio camera. Images were collected manually at a pixel size of 1.2 Å (52,000x magnification), an exposure time of 3 s and defocus values of 2.0 - 3.0 μm .

2.7.2 Cryo-EM sample vitrification

3 μL of purified ScSyt1, ScPho90 or HsXpr1 at a concentration of 2.5 - 5 mg/mL were applied to glow-discharged (15 mA for 90 s) C-flat 1.2/1.3 300 mesh copper grids (Science Services GmbH) and plunge-frozen in liquid ethane using a Vitrobot (Thermo Fischer) operated at 4 °C and 100 % humidity. The blotting force was kept at a constant value of 2 while the blotting time was varied between 4 – 10 s. Whatman 595 was used as filter paper. Vitrified grids were clipped into auto-grid cartridges and kept under liquid nitrogen until use.

2.7.3 Cryo-EM data acquisition

For grid screening, a 200 kV Glacios microscope equipped with a Falcon3 camera, operating in linear mode was used. All images were collected at a nominal magnification of 150,000x, corresponding to a pixel size of 0.955 Å. The total dose was 70 $\text{e}^-/\text{Å}^2$ and defocus range varied from -1.0 μm to -3.0 μm .

High-resolution datasets were collected using a Tecnai KriosG4i microscope equipped with a cold field emission gun (cold-FEG), a Falcon4 camera operating in counting mode and a Selectris energy filter (Slit width: 8 eV). Acquisition parameters of all datasets are summarized in Tables 7 - 9. 4,942 movies were collected for the phosphate-bound dataset of ScPho90 and 13,845 were collected for the phosphate-free dataset, both at 215,000x magnification corresponding to a pixel size of 0.573 Å. The total dose was 65 $\text{e}^-/\text{Å}^2$ in both datasets and defocus values ranged from -0.6 μm to -2.3 μm and from -0.5 μm to -2.1 μm , respectively. For ScSyt1 16,970 exposures were collected for the phosphate-free dataset and 13,902 were collected for the phosphate/InsP₆ dataset, both at 215,000x magnification corresponding to a pixel size of 0.573 Å. In the phosphate-free dataset the total dose was 65 $\text{e}^-/\text{Å}^2$ and in the phosphate/InsP₆ dataset 70 $\text{e}^-/\text{Å}^2$. The defocus ranges varied from -0.6 μm to -2.3 μm and from -0.5 μm to -2.2 μm , respectively. For HsXpr1 purified from *S. cerevisiae* the dataset was composed of 15,249 images collected at 215,000x magnification, corresponding to a pixel size of 0.573 Å. The total dose was 70 $\text{e}^-/\text{Å}^2$ and defocus values ranged from -0.8 μm to -2.3 μm . HsXpr1 purified from HEK293 GnTI- cells was imaged in the presence and absence of phosphate. The dataset in the presence of phosphate comprised 15,329 exposures that were collected at 215,000x magnification corresponding to a pixel size of 0.573 Å. The total dose was 65 $\text{e}^-/\text{Å}^2$ and defocus values ranged from -0.8 μm to -2.0 μm . The phosphate-free dataset comprised 21,128 exposures also collected at 215,000x magnification corresponding to a pixel size of 0.573 Å. The total dose was 65 $\text{e}^-/\text{Å}^2$ and defocus values ranged from -0.8 μm to -2.1 μm .

Table 7: Cryo-EM parameters of ScPho90 datasets.

Data acquisition	ScPho90 phosphate	ScPho90 phosphate-free
Microscope	Titan Krios G4i	
Detector	Falcon 4	
Magnification	215,000	
Pixel size	0,573 Å	
Voltage	300 kV	
Energy filter slit width	8 eV	
Total dose	65 e ⁻ / Å ²	
Defocus range	-0.6 - -2.3 µm	-0.5 - -2.1 µm
Movies collected	4,942	13,845

Table 8: Cryo-EM parameters of ScSyg1 datasets.

Data acquisition	ScSyg1 phosphate-free	ScSyg1 phosphate/InsP ₆
Microscope	Titan Krios G4i	
Detector	Falcon 4	
Magnification	215,000	
Pixel size	0,573 Å	
Voltage	300 kV	
Energy filter slit width	8 eV	
Total dose	65 e ⁻ / Å ²	70 e ⁻ / Å ²
Defocus range	-0.6 - -2.3 µm	-0.5 - -2.2 µm
Movies collected	16,970	13,902

2.7.4 Cryo-EM image processing

Processing of individual datasets was similar, but differed at certain steps between projects. Processing workflows for individual datasets can be found in the Results section.

Collected movies of ScPho90 and ScSyg1 datasets were imported into RELION and motion-corrected using the RELION algorithm (Scheres, 2012). CTF estimation was done using Gctf (Zhang, 2016). Particles were picked by training a model in crYOLO on manually picked particles from approximately 30 micrographs (Wagner et al., 2019). The coordinate files were imported into RELION and particles were extracted at individual box sizes and binning factors. The particle stacks were then imported into CryoSPARC and multiple rounds of 2D classification were used to clean the particle stacks (Punjani et al.,

Table 9: Cryo-EM parameters of HsXpr1 datasets.

Data acquisition	HsXpr1 phosphate	HsXpr1 phosphate-free	HsXpr1 (yeast)
Microscope	Titan Krios G4i		
Detector	Falcon 4		
Magnification	215,000		
Pixel size	0,573 Å		
Voltage	300 kV		
Energy filter slit width	8 eV		
Total dose	65 e ⁻ / Å ²		70 e ⁻ / Å ²
Defocus range	-0.8 - -2.0 μm	-0.8 - -2.1 μm	-0.8 - -2.3 μm
Movies collected	15,339	21,128	15,249

2017). After 3D *ab initio* reconstruction different 3D refinement strategies were used to obtain high-resolution maps.

For the ScPho90 phosphate dataset, 3 different classes were generated by 3D *ab initio* reconstruction and subsequent heterogeneous refinement yielded one good class of ScPho90. This class was refined by non-uniform refinement (NU) (Punjani et al., 2020), first without symmetry and then with C2-symmetry applied. The final map was further optimized using Phenix density modification (Terwilliger, 2020). In the phosphate-free dataset, six *ab initio* classes were generated that were used as inputs for subsequent heterogeneous refinement. The best class was again further refined using NU refinements with and without C2-symmetry applied. The final symmetric map was optimized using density modification. 3D variability analysis (Punjani et al., 2021) of the non-symmetrized map revealed distinct structural heterogeneity of one of the transport domains and displayed different conformations of the protein. 3D classification was used to classify particles into the different conformations. Particles classified into the asymmetric conformation were further refined using NU-refinement and yielded the final map of the asymmetric structure. The final map was again density-modified using Phenix density modification.

For the ScSyg1 dataset without phosphate, 3D *ab initio* reconstruction was conducted with 4 different classes. After heterogeneous refinement particles of the best reconstruction were used for subsequent NU refinement and NU refinement with C2-symmetry applied. The final symmetric map was sharpened using the software deepEMenhancer (Sanchez-Garcia et al., 2021). For ScSyg1 with phosphate/InsP₆, 6 initial volumes were

generated by 3D *ab initio* reconstruction. Heterogeneous refinement was used to further separate all particles into the different classes. Particles from the best reconstruction were used for subsequent NU refinement and NU refinement with C2-symmetry applied. The final symmetric map was sharpened using the software deepEMenhancer. Additionally, particles from the final refinement were analyzed by 3D variability analysis. This revealed a subset of particles that showed a better refined SPX domain. These particles were isolated and again refined by NU refinement with C2-symmetry and local refinement and yielded a map with well-defined density for the SPX domain.

Movies of HsXpr1 datasets were directly imported into CryoSPARC and motion-correction and CTF estimation was done using CryoSPARC's implemented algorithms. Initial particles were picked using the blob picker tool and extracted with a box size of 512 pixels that was binned to 256 pixels. 2D classification was used to identify HsXpr1 particles and good 2D classes were used to pick particles using the template picker tool or train a Topaz model that was then also used to pick particles again (Bepler et al., 2019). Multiple rounds of 2D classification yielded a clean HsXpr1 particle stack. These particles were used to generate multiple 3D *ab initio* models that were refined using heterogeneous refinements. Particles from the best 3D reconstructions were combined, duplicates removed and refined using NU-refinement without and with C2-symmetry applied. Final maps were sharpened using deepEMenhancer.

2.7.5 Model building and refinement

Dr. Özkan Yildiz (direct supervisor) assisted in model building and refinement of the atomic models. Initial models were obtained from AlphaFold and rigid-body fitted into the respective cryo-EM maps or created *de novo* and manually corrected in Coot (Emsley et al., 2004). Models were finalized by iterative manual model building in Coot and refined against the full map using Phenix real-space-refinement (Adams et al., 2010). Models were validated by MolProbity (Chen et al., 2010). Model and refinement statistics for each model can be found in the Supplement (Table S1-S3). Protein cavities were calculated and visualized using Hollow-1.3 with a 1.4 Å probe radius (Ho et al., 2008). All figures of protein models were created with either ChimeraX or Chimera (Goddard et al., 2018; Pettersen et al., 2004).

2.8 Biochemical analysis

2.8.1 Thin layer chromatography

50 µg of purified protein were precipitated in a 2:1 methanol:chloroform mixture. Another 100 µl chloroform and 100 µl water were added, samples were mixed vigorously and then centrifuged for 15 min at 4,000 xg to separate organic and aqueous phases. The organic phase was isolated, evaporated under a nitrogen stream and resuspended in 10 µl of chloroform. Small amounts of sample and lipid standards were applied to a silica plate. The silica plate was put into a preequilibrated TLC chamber and run for 25 min (Running buffer: 39 ml chloroform, 15 ml methanol, 2.4 ml water). The silica plate was dried and lipid bands were visualized using either elemental iod or Molybdenum Blue (Müthing et al., 1998).

2.8.2 Microscale thermophoresis

The phosphate binding affinity of ScPho90 was measured by microscale thermophoresis using a Monolith NT.115 instrument (NanoTemper). ScPho90 (50 nM) was labeled with RED-tris-NTA dye in 20 mM HEPES pH 8.0, 100 mM NaCl and 0.005 %/0.0005 % LMNG/CHS. 10 µl of labeled ScPho90 was mixed with 10 µl of ligand (10 µM – 30 mM) in the same buffer. Samples were loaded into premium capillaries and MST traces were recorded for 25 s at 25 °C with 60 % LED power and high MST power. All concentrations were measured in triplicates and normalized fluorescence values at 20 s were used for binding curve analysis. The binding curve was fitted with a one-site binding model.

2.8.3 Reconstitution of ScPho90 into liposomes

A lipid mixture (55 % POPC, 35 % DOPE, 10 % POPG) was mixed with Ergosterol in chloroform to give a final concentration of 15 % (w/w) and dried under a gentle flow of nitrogen overnight. The dried lipids were resuspended in lipid buffer (20 mM Tris pH 8.0, 150 mM KCl) by sonication and heating. The lipid suspension was diluted to 5 mg/ml and freeze-thaw cycles were applied to produce unilamellar vesicles. The suspension was extruded through a 400 nm sized membrane to get liposomes with diameter of approximately 400 nm. The suspension was further diluted to 2.5 mg/ml and stored at -80 °C until further use. For reconstitution, liposomes were mixed with ScPho90 (purified in DDM/CHS) in a 50:1 ratio (w/w), destabilized by Triton-X-100 addition and incubated for 30 min at room temperature. Then they were supplemented with 80 mg Bio-beads and incubated at 4 °C. After 1 h, another 80 mg fresh Bio-beads were added. On the next day fresh Bio-beads (80 mg) were added and the mixture was incubated for 2 h.

Proteoliposomes were flash-frozen in liquid nitrogen and stored at -80 °C until further use.

2.8.4 ScPho90 transport assays

Proteoliposomes were thawed and ultra-centrifuged for 30 min at 200,000 xg. The supernatant was discarded and liposomes were resuspended in assay buffer (20 mM Tris pH 8.0, 150 mM NaCl) at a final lipid concentration of 2.0 mg/ml. Transport assays were started by adding 50 mM KP_i to 250 μ l liposome suspension and incubated at 30 °C for 30 min. After transport reactions liposomes were ultra-centrifuged for 30 min at 200,000 xg, washed twice with assay buffer and ultra-centrifuged for 30 min at 200,000 xg. Liposomes were resuspended in 25 μ l assay buffer and solubilized by the addition of 0.5 % SDS. The solution was mixed with 25 μ l 40 mM H_2SO_4 and 25 μ l malachite green solution (0.8 mg/ml malachite green, 15 % H_2SO_4 , 5 % Na_2MnO_4) and incubated for 5 min. The absorbance of each sample was measured in a microwell plate at 620 nm using a SpectraMax M2 (Molecular Devices). All measurements were performed in triplicates.

2.8.5 ScSyt1/HsXpr1 reconstitution into liposomes

A lipid mixture (40 % POPC, 30 % DOPE, 30 % POPG) was mixed with 10 % Cholesterol (w/w) in chloroform and dried under a gentle flow of nitrogen stream overnight. The dried lipids were resuspended in lipid buffer (20 mM Tris pH 8.0, 100 mM NaCl) by sonication and heating. The lipid suspension was diluted to 5 mg/ml and freeze-thaw cycles were applied to produce unilamellar vesicles. The suspension was extruded through a 400 nm sized membrane to get liposomes with diameter of 400 nm. The suspension was further diluted to 2.5 mg/ml and stored at -80 °C until further use. For reconstitution liposomes were mixed with ScSyt1 in a 50:1 ratio (w/w) or with HsXpr1 30:1 ratio (w/w) (both purified in DDM/CHS), destabilized by Triton-X-100 addition and incubated for 30 min at 4 °C. Then they were supplemented with 50 mg Bio-beads and incubated at 4 °C. After 1 h, another 100 mg fresh Bio-beads were added. On the next day another 100 mg Bio-beads were added and the mixture was incubated at 4 °C for 2 h. Proteoliposomes were directly used for transport assays.

2.8.6 ScSyt1/HsXpr1 transport assays

All transport measurements were performed using ^{33}P -labeled K_2HPO_4 (BioTrend). The reaction buffer (20 mM KP_i pH 8.0, 100 mM NaCl) contained 2 μ Ci/mL of ^{33}P isotope. For reactions containing InsP6, 5 mM InsP6 were added to the reaction buffer. 100 μ l of

2.8. Biochemical analysis

reaction buffer was added to 100 μ l liposomes solution and incubated for specific time points at either 30°C (ScSyt1 liposomes) or 37°C (HsXpr1 liposomes). After incubation proteoliposomes were transferred to 0.22 μ m nitrocellulose filters (Millipore). Excessive reaction buffer was removed by applying vacuum and the filters were washed three times with 1 mL of cold reaction buffer. The filters were put into counting tubes and 4 mL of scintillation liquid (Rotiszint Eco Plus, Carl Roth) was added. Radioactivity was measured for 5 min in Tri-carb 1500 device (Packard). All measurements were performed in triplicates.

3 Results

The results chapter is divided into two parts. In the first part, results for the yeast low-affinity phosphate importer ScPho90 are reported, while the second part reports findings for the yeast and human phosphate exporters ScSyt1 and HsXpr1. Each section starts with the expression, purification and grid screening of the respective transporters. After that, cryo-EM data acquisition and processing as well as overall structures are shown. Structural details and additional biochemical data are described in the final sections.

3.1 The eukaryotic low-affinity phosphate importer Pho90

3.1.1 Expression and purification

The expression of different low-affinity phosphate transporter homologues in *S. cerevisiae* was evaluated by small-scale expression tests. A list of all tested constructs can be found in the Material and Methods section (Table 3). An exemplary expression test is shown in Figure 8A. ScPho90 in -Ura drop-out medium showed the highest expression levels while CtPho87 and ScPho87 showed only low expression levels under the tested conditions. ScPho90 with a C-terminal His-tag showed a prominent second lower molecular weight band whereas N-terminally His-tagged ScPho90 only showed one band with the expected molecular weight. Further optimization of expression conditions improved expression levels for C-His ScPho87, resulting in sufficient yields for small-scale purifications. All constructs containing either N- or C-terminal GFP fusions did not express well under the tested conditions and were not further analyzed.

After establishing expression conditions that yielded sufficient amounts of protein, different detergents were tested for their solubilization efficiency of the overexpressed transporters (Figure 8B). As expected, SDS showed the highest solubilization efficiency but was not considered for downstream experiments due to its denaturing property. Of the milder detergents tested, GDN only solubilized a small fraction of the protein while all other detergents (DM, DDM, DMNG, LMNG) showed higher and comparable solubi-

3.1. The eukaryotic low-affinity phosphate importer Pho90

lization efficiencies. The results were very similar for ScPho90 and ScPho87. Additional experiments revealed that the addition of CHS improved the stability of proteins after solubilization.

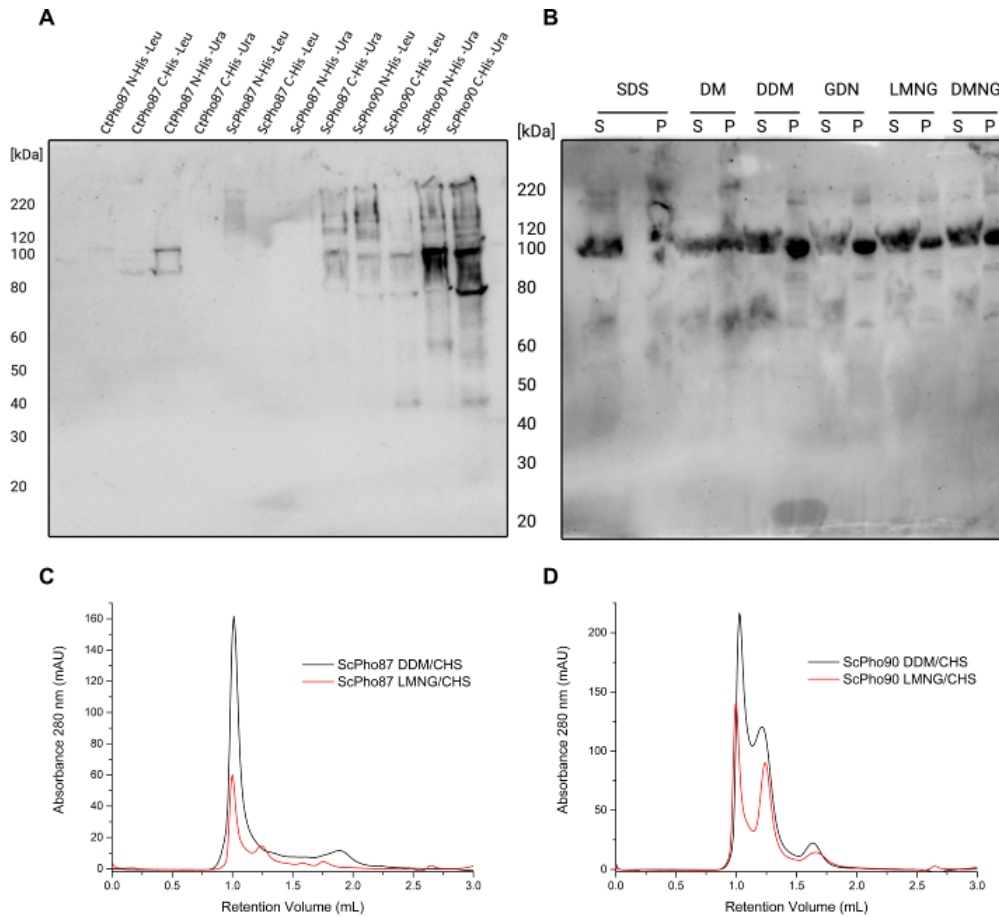


Figure 8: Expression and purification tests of low-affinity phosphate transporters. (A) Expression of CtPho87, ScPho87 and ScPho90 in *S. cerevisiae* was investigated by Western Blot with ScPho90 showing the highest expression levels. (B) Solubilization efficiencies of ScPho90 using different detergents. Samples of the supernatant (S) and the remaining membrane pellet (P) are compared. The solubilization efficiency was highest for SDS and lowest for GDN. DM, DDM, LMNG and DMNG all show comparable efficiencies of approximately 40 %. An anti-His antibody was used for detection in both Western Blots. (C) SEC profile of ScPho87 purified in either DDM/CHS or LMNG/CHS. In both detergents ScPho87 eluted predominantly in the void volume (1.0 mL). (D) SEC profile of ScPho90 purified in either DDM/CHS or LMNG/CHS. Apart from a peak at the void volume, ScPho90 showed a second peak around 1.25 mL in both detergents.

Both ScPho90 and ScPho87 were purified using DDM/CHS or LMNG/CHS as detergents. After solubilization, IMAC using Ni-NTA columns was performed and the quality of the purified protein was assessed by analytical SEC runs (Figure 8C and D). While ScPho90

showed an elution peak at around 1.25 mL in both detergents and a peak at the void volume (1.0 mL), ScPho87 eluted predominantly in the void volume. Further optimization of purification buffer conditions did not improve ScPho87 elution profiles, so ScPho90 was the target of choice for subsequent structural and functional studies.

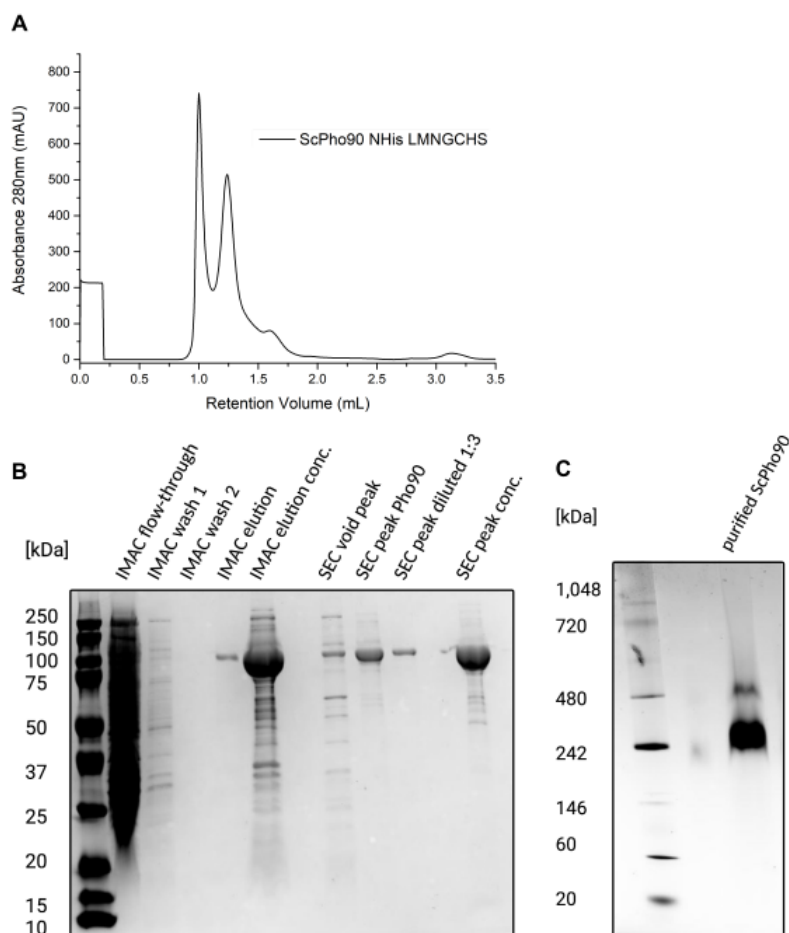


Figure 9: Purification of ScPho90. (A) SEC profile of ScPho90 in LMNG/CHS. The second peak around 1.25 mL corresponds to dimeric ScPho90 that was used for subsequent experiments. (B) Coomassie-stained SDS gel of ScPho90 purification steps. ScPho90 bands appear at 100 kDa in agreement with its molecular weight. IMAC enriches ScPho90, while SEC increases the purity of the final sample. (C) Blue-native PAGE analysis of purified ScPho90. The sample shows a main band at around 242 kDa, indicating that ScPho90 forms dimers in solution.

Upscaling the purification of ScPho90 in LMNG/CHS resulted in a similar SEC profile as before. SDS-PAGE analysis of each purification step revealed a pure protein sample (Figure 9A and B). Comparison of the SEC profile with standards indicated that ScPho90 (97.7 kDa) likely forms dimers in solution. Analysis of purified ScPho90 by BN-PAGE revealed a main band at around 242 kDa, which corresponds to the molecular weight

of ScPho90 dimers plus additional detergent or lipid molecules, confirming that it forms dimers in solution (Figure 9C). Sufficient amounts of monodisperse ScPho90 were purified for subsequent structural and functional studies. ScPho90 was found to be unstable in the absence of phosphate and aggregated if kept in buffers without phosphate for prolonged periods of time. In the presence of phosphate, the protein was stable at room temperature for 24 h and at 4 °C for more than 3 days. However, for cryo-EM grid preparations the protein was freshly purified on the same day and concentrated up to 5 mg/mL. For functional studies the protein was frozen in liquid nitrogen and stored at -80 °C until use.

3.1.2 Electron microscopy screening

Purified ScPho90 samples were analyzed by negative-stain EM using a 120 kV Tecnai Spirit microscope. 3 µl of ScPho90 at a concentration of 0.02 mg/mL were stained with sodium silicotungstate. The sample showed homogeneous, spherical particles as expected for a small membrane protein in detergent micelles (Figure 10A). After confirming particle homogeneity by negative-stain EM, different freezing conditions were tested to obtain evenly distributed particles in a thin layer of amorphous ice. The varying parameters were: protein concentration, blotting parameters, grid type and added secondary detergents. The best grids were obtained using a protein concentration of 4 mg/mL, a blotting time of 8 s at 4 °C and 100 % humidity, C-flat 1.2/1.3 400 mesh grids and no added secondary detergents (Figure 10B). An initial small dataset was recorded using a 200 kV Glacios microscope, equipped with a Falcon 3 camera. Processing of this dataset yielded 2D classes of ScPho90 with twofold symmetry (Figure 10B). Top views of the protein showed densities for transmembrane helices with some helices organized into two helix bundles. 3D reconstructions yielded an initial reconstruction with a resolution of approximately 7 Å (Figure 10C). In this reconstruction, the dimeric arrangement and the two helix bundles are visible, although no symmetry was applied. Additional density, which is present below the micelle likely corresponds to the soluble SPX domain of ScPho90.

3.1.3 High-resolution cryo-EM data acquisition of ScPho90

The ScPho90 grids were used to record a larger dataset on a 300 kV Titan Krios G4i microscope, equipped with a cold-FEG, a Falcon 4 camera and a Selectris energy filter. A total of 4,942 movies were recorded with a total electron dose of 65 e⁻/Å² and a defocus range of -0.6 to -2.3 µm (Table 7, Material and Methods). The dataset was processed in RELION and CryoSPARC (Figure 11). Recorded movies were motion-corrected and Ctf-

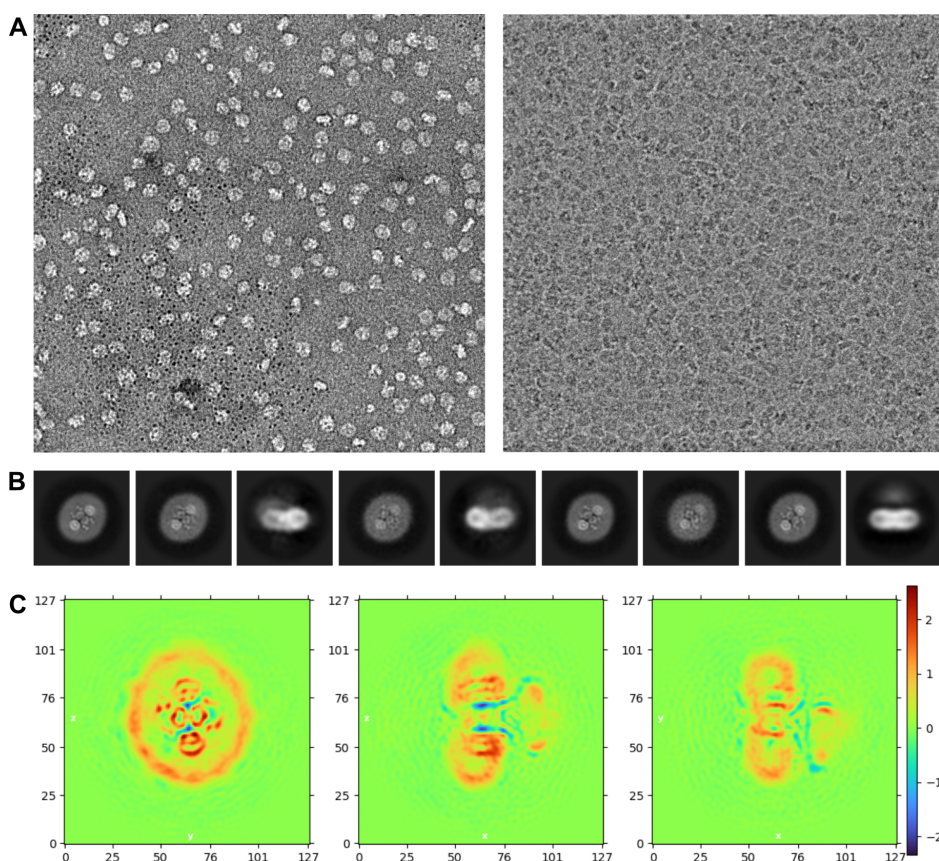


Figure 10: Screening of ScPho90 grids. (A) Images of purified ScPho90 either stained with uranyl formate (left) or embedded in a thin layer of vitreous ice (right). Both images show homogeneously sized particles and good particle distributions. (B) Selected 2D classes of ScPho90 show both top and side views. In top views, individual helices can be seen as well as the twofold symmetry of the dimeric ScPho90 particles. (C) Unidirectional views of a ScPho90 3D reconstruction with an overall resolution of approximately 7 Å.

estimated in RELION. Particle picking by a pre-trained model in crYOLO yielded 476,290 initial particles. After extraction, the particle stacks were imported into CryoSPARC and false-positive picks were removed using 3 rounds of 2D classification. The 2D classes show different angular views of the protein with clear secondary structure elements. *Ab initio* 3D reconstruction of 3 independent classes and subsequent heterogeneous refinement further removed broken particles. Non-uniform refinement of the best class resulted in a map of ScPho90 with a nominal resolution of 2.85 Å. An additional non-uniform refinement with C2-symmetry applied improved the resolution to 2.62 Å. This map was density-modified and sharpened in Phenix to obtain the final map.

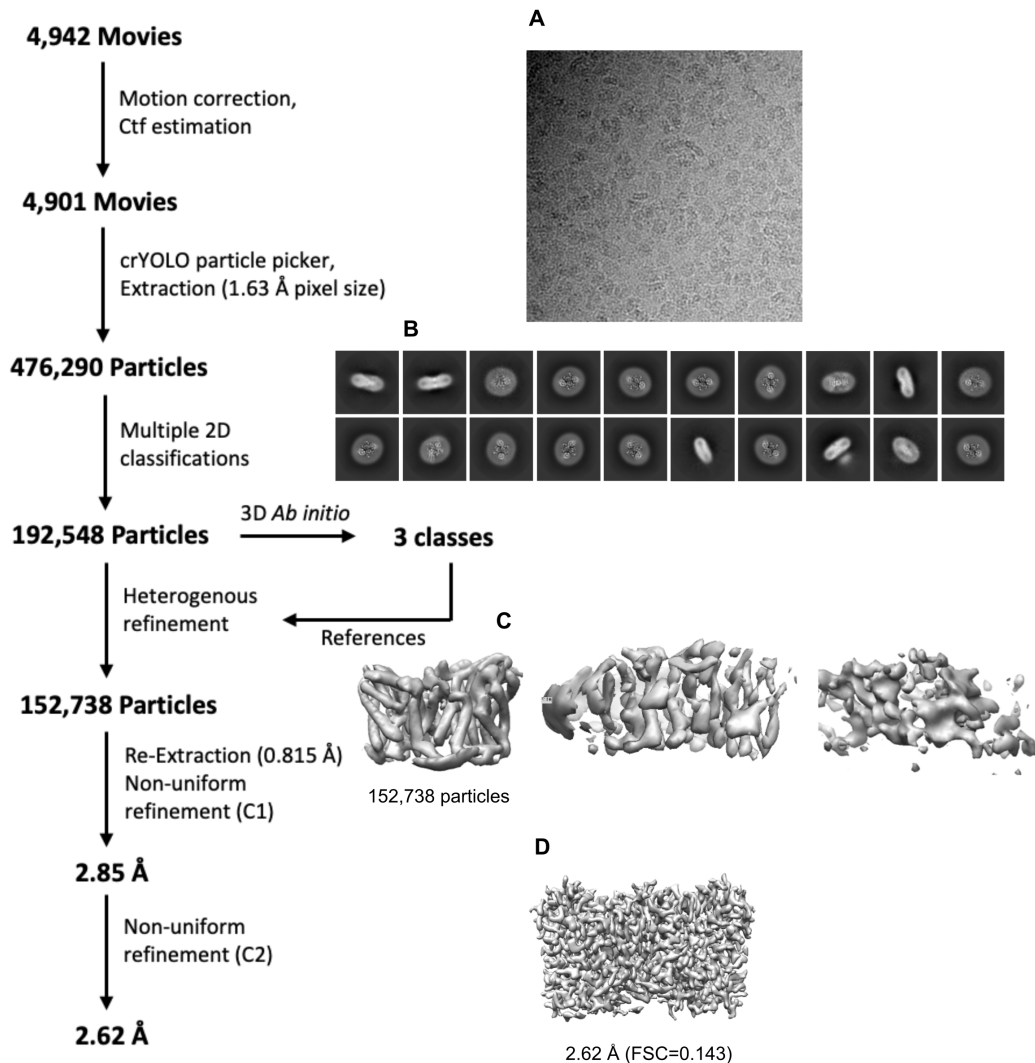


Figure 11: Processing scheme of ScPho90 in the presence of phosphate. The cryo-EM processing pipeline to obtain the final reconstruction of phosphate-bound ScPho90 is shown on the left. A representative micrograph (A), final 2D classes (B) and all *ab initio* models (C) are displayed. The final map after non-uniform refinement is shown at the bottom (D).

3.1.4 Structure of phosphate-bound ScPho90

The final map of the ScPho90 dimer allowed for atomic model building of the complete transmembrane domain (Figure 12). The dimer dimensions are 90 x 60 x 40 Å. Each protomer consists of 13 helical elements (H1-H13) with the N-terminus of H1 connected to the soluble cytoplasmic domain and the C-terminus of H13 located on the extracellular side. Helices H2-H7 and H8-H13 are organized as two repeats with inverted topology. In these inverted repeats H5A/B and H11A/B are helical hairpins, while H4, H6, H10 and H12 are transmembrane helices with unwound stretches (Figure 12C). Each protomer can be divided into two domains, the scaffold and transport domain. The scaffold

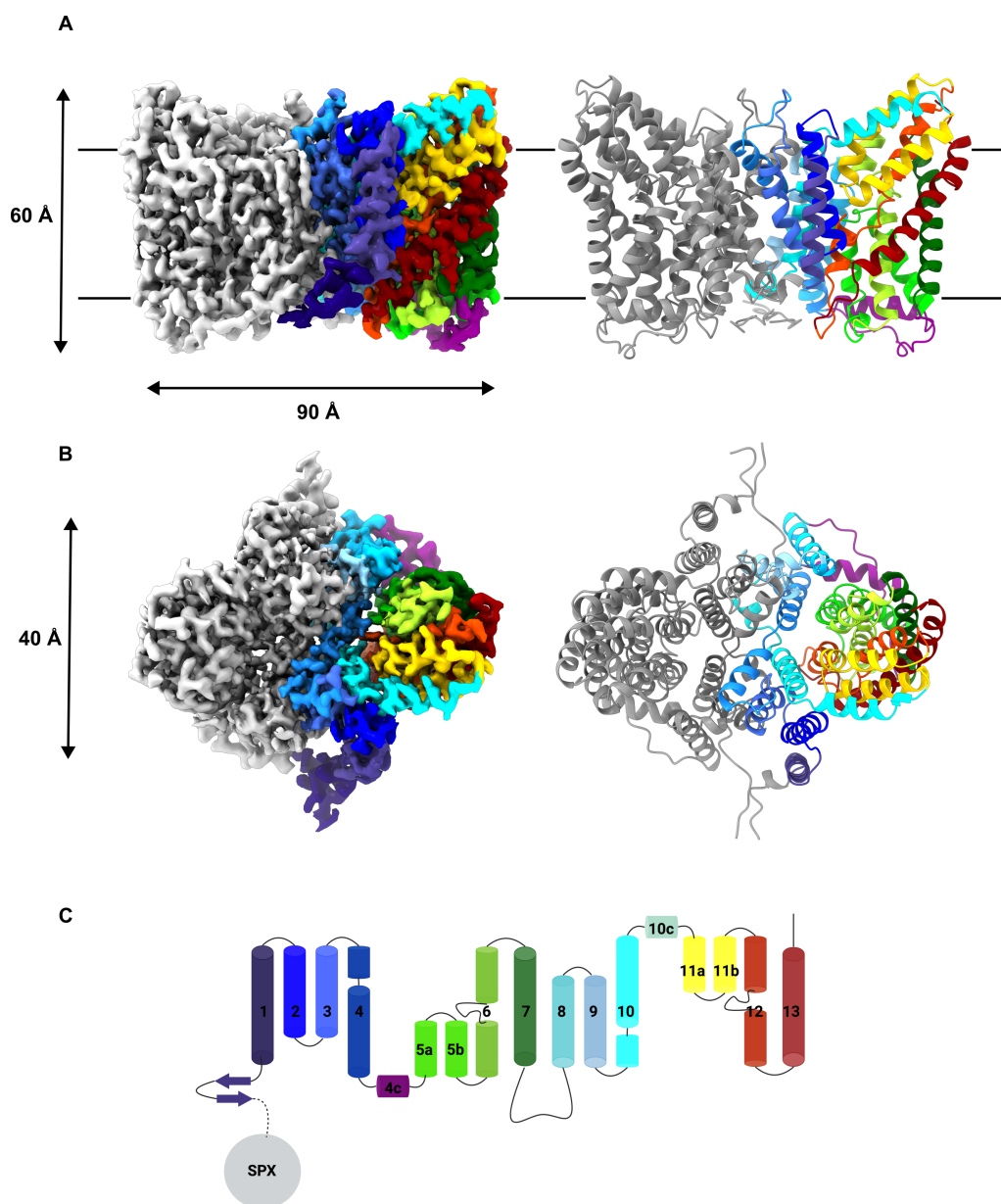


Figure 12: Structure of phosphate-bound ScPho90. (A) Side views of the map (left) and model (right) of ScPho90. One protomer is colored in grey while the other is colored by individual transmembrane helices numbered as in (C). (B) Top views of ScPho90 map (left) and model (right). Both are turned by 90° in relation to (A). (C) Schematic overview of the transmembrane organization of ScPho90.

domain, consisting of seven helices (H1-4, H8-10), forms the dimer interface through extensive hydrophobic interactions. Strikingly, two tryptophan residues (Trp721, Trp498) interact by π -stacking with the same tryptophans of the opposite protomer in the membrane center. The transport domain is a helix bundle formed by the two helical hairpins (H5A/B and H11A/B), two partially unwound helices (H6 and H12) and helices H7 and H13. These helical hairpins and unwound helices are known to be involved in sub-

strate binding of transporters with a similar fold (Garaeva et al., 2020). It has also been shown that the transport domain is responsible for the translocation of substrates into the cytoplasm. The scaffold and transport domain interact mainly through hydrophobic interactions between H2, H4, H6, H8 of the scaffold domain and H5, H6, H11 and H12 of the transport domain. One salt bridge between Glu455 and Arg480 connects the two domains. Both protomers are in an outward-open conformation since both hypothetical substrate binding pockets are accessible from the extracellular site.

3.1.5 Structure of phosphate-free ScPho90

To determine the structure of ScPho90 in a different conformation, cryo-EM samples were prepared in the absence of phosphate (20 mM KP_i pH 8 was replaced by 20 mM Tris pH 8). A total of 13,845 movies were recorded on a Titan Krios G4i microscope with similar acquisition parameters (Table 7, Material and Methods). Processing of the dataset in RELION and CryoSPARC resulted in a final C2-symmetric map with an overall resolution of 2.29 Å (Figure 13). The obtained symmetric map is almost identical to the phosphate-bound map and the resulting model differed only marginally (RMSD of 0.434 Å) from the phosphate-bound structure. However, no phosphate density is found in the binding pocket (Figure 14 and Figure S1). A small N-terminal stretch of helix H1 is better resolved in this map and has been built as a β -hairpin that lies below the membrane plane and ends just below the transporter (Val377-Lys407, 389-401 unresolved).

Since in cryo-EM thousands of individual particles are combined to reconstruct a 3D volume, particle heterogeneity is a common phenomenon in cryo-EM data. 3D Variability Analysis (3DVA), which is implemented in CryoSPARC is a powerful tool to investigate this heterogeneity (Punjani et al., 2021). Analyzing the 3D variability of the map without applied symmetry, revealed that a fraction of particles (approximately 15 %) adopted a different conformation. These particles were separated by 3D classification and refined to a nominal resolution of 3.15 Å. This map shows an asymmetric structure with one side being shifted towards the cytoplasmic side in comparison to previous maps. Atomic model building revealed that one protomer is in the exact same conformation as in the symmetric structures, while the other protomer is in a different conformation (Figure 14). Since the binding pocket of this protomer is accessible from the cytoplasmic side, it represents an inward-open conformation.

Structural comparison of both protomers shows that the scaffold domain is virtually identical in both conformations. The transport domain however, is shifted towards the cytoplasm by approximately 11 Å by a rigid body movement. The helix bundle also

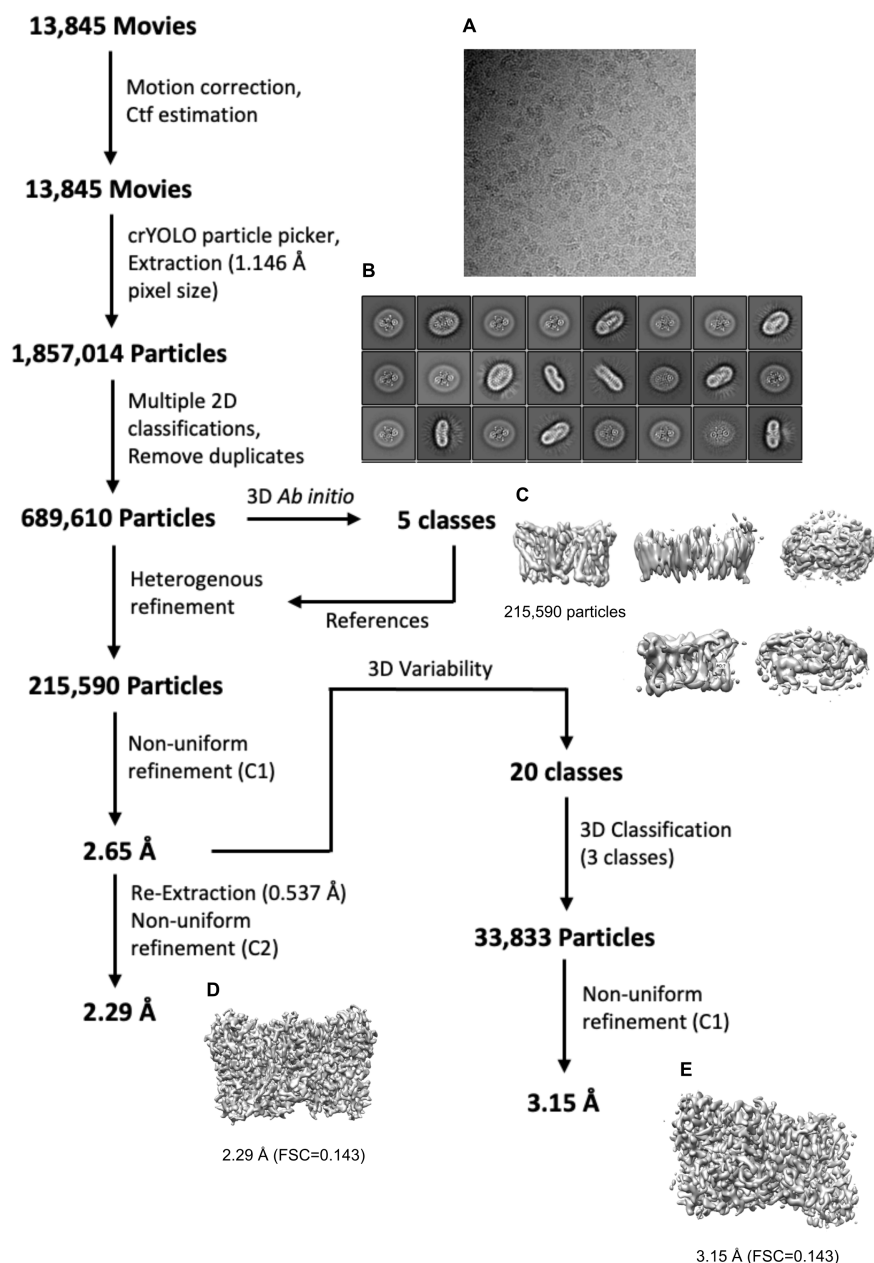


Figure 13: Processing scheme of ScPho90 in the absence of phosphate. The cryo-EM processing pipeline to obtain the final maps of ScPho90 is shown on the left. A subset of particles was isolated by 3D variability analysis and 3D classification and yielded an asymmetric ScPho90 reconstruction. A representative micrograph (A), final 2D classes (B) and all *ab initio* models (C) are displayed. The final symmetric (D) and asymmetric (E) maps after non-uniform refinement are shown at the bottom.

rotated by roughly 30° in relation to the outward-open conformation. The substrate-binding pocket is now accessible from the cytoplasmic side, so that substrates can be released into the cytoplasm in the inward-open conformation. The interface between scaffold and transport domain still mainly consists of hydrophobic interactions. The

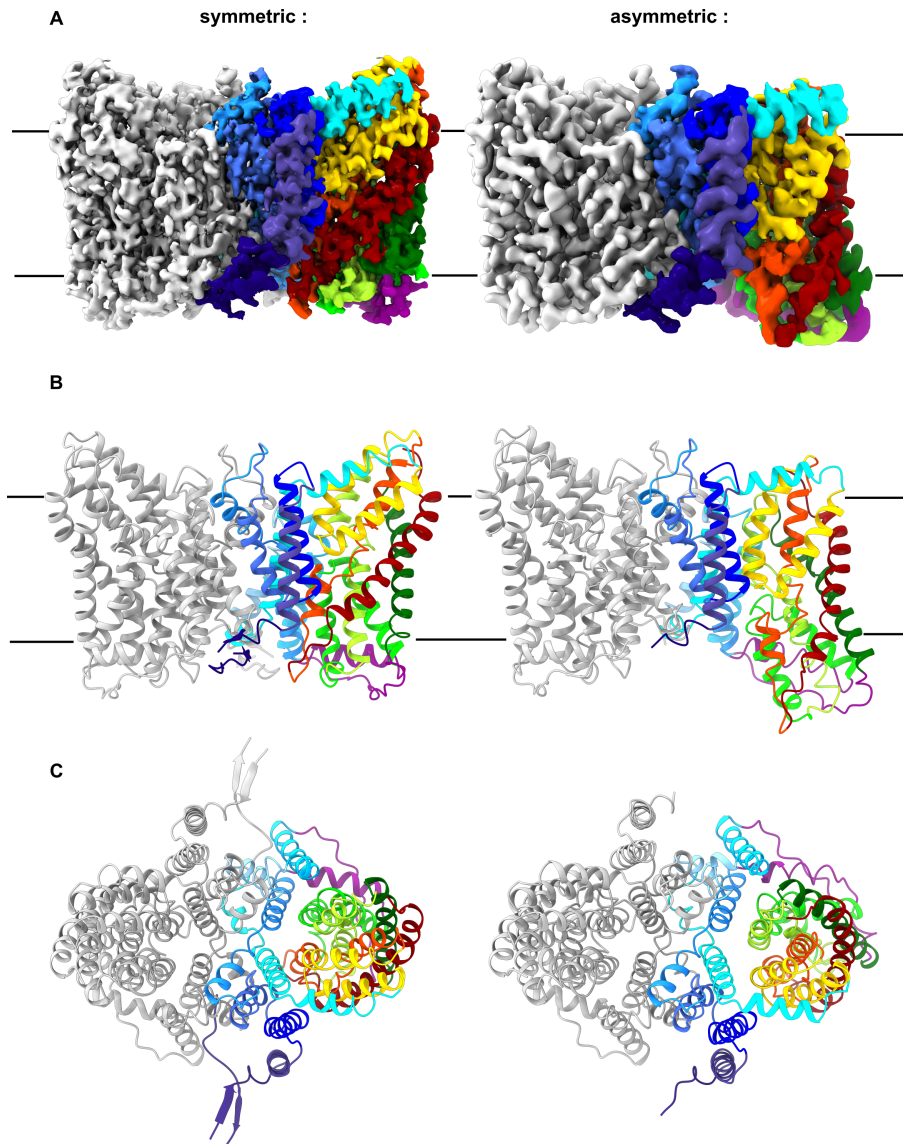


Figure 14: Structure of the symmetric and asymmetric ScPho90 dimer in the absence of phosphate. (A) Side views of the cryo-EM maps of the symmetric (left) and asymmetric (right) ScPho90 dimer. Both protomers were in the outward-open conformation in the symmetric dimer and nearly exactly matched the structure with phosphate. In the asymmetric dimer one protomer adapted an inward-open conformation. (B) Resulting models of symmetric and asymmetric ScPho90 dimer. (C) Top views of both models. Both are turned by 90° in relation to (B).

sidechains provided by the scaffold domain are the same as in the outward-open state, but the interacting sidechains of the transport domain changed due to the inward movement of the domain. The only inter-domain salt bridge present in the outward-open conformation is lost (Glu455-Arg480) but is compensated by the formation of a new one between Lys614 and Glu688 in the inward-open state.

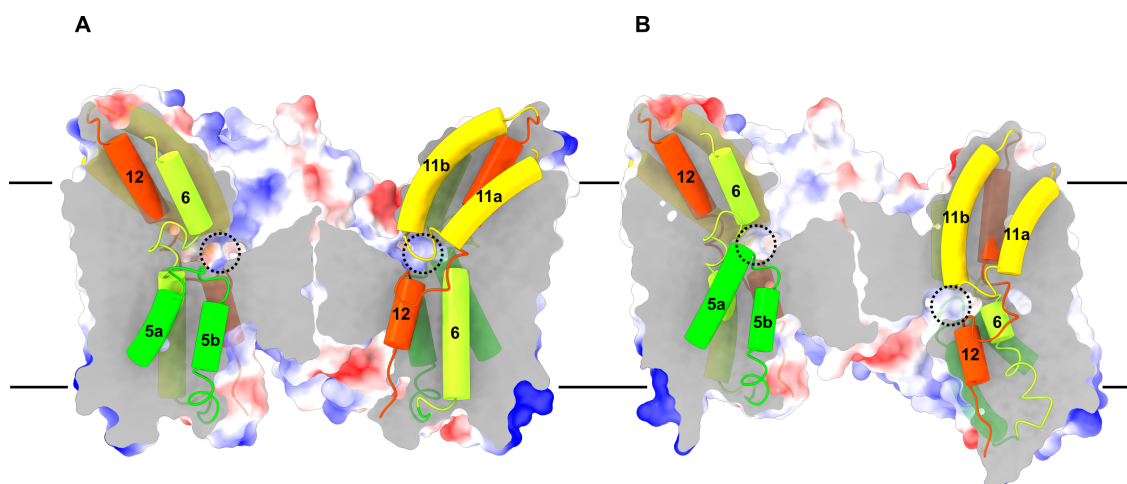


Figure 15: Conformational change of ScPho90 between outward-open and inward-open states. (A) Slice through the symmetric outward-open ScPho90 structure. Helices defining the substrate-binding pocket are shown as colored tubes. Phosphate binding sites are highlighted by black circles and the membrane plane is indicated by black lines. (B) Slice through the asymmetric ScPho90 structure where protomers are in complementary states. Phosphate-binding sites are highlighted by dashed circles.

3.1.6 Structural basis for phosphate binding

The substrate binding pockets of ScPho90 are defined by the tips of hairpins H5A/B and H11A/B and the unwound stretches of helices H6 and H12. In the symmetric structure, both binding pockets are accessible from the extracellular side (Figure 15) and consist mainly of hydrophilic residues, yet no charged residues are present. Additional densities were observed within the binding pocket of the phosphate-bound structure which were interpreted as phosphate and sodium ions based on the knowledge that ScPho90 is a sodium/phosphate co-transporter and both substrates were present in the sample at high concentrations. An overview of the binding sites and the coordination of both substrates within the binding pocket can be seen in Figure 16. Phosphate is coordinated by sidechains of Asn556, Gln605, His779 and Ser815 in the center of the binding pocket between both hairpins and unwound helix stretches. The two sodium ions are located on both sites of the phosphate molecule but are not in direct contact with it. Ser815 is the only residue that directly coordinates phosphate and one sodium ion (Na1). In addition to Ser815, the sidechains of Ser603 and Asn606 also coordinate Na1, as does the main-chain oxygen of Ala811. The second sodium ion (Na2) is coordinated by the sidechain of Thr775 and the mainchain oxygens of Thr775, Gly817 and Leu820. In the absence of phosphate, no density for phosphate was observed in the center of the binding pocket (Figure 16B). However, several weaker densities are present that correspond to either sodium ions (which were present in the sample) or water molecules that are resolved due

3.1. The eukaryotic low-affinity phosphate importer Pho90

to the higher resolution of the symmetric phosphate-free structure. In the inward-open state, residues that are involved in phosphate coordination (Asn556, Gln605, His779 and Ser815) have a similar spatial arrangement as in the outward-open state. No additional density is present within the binding pocket. This may be due to a weaker affinity for sodium ions in this conformation but is more likely a consequence of the overall lower resolution of the asymmetric structure.

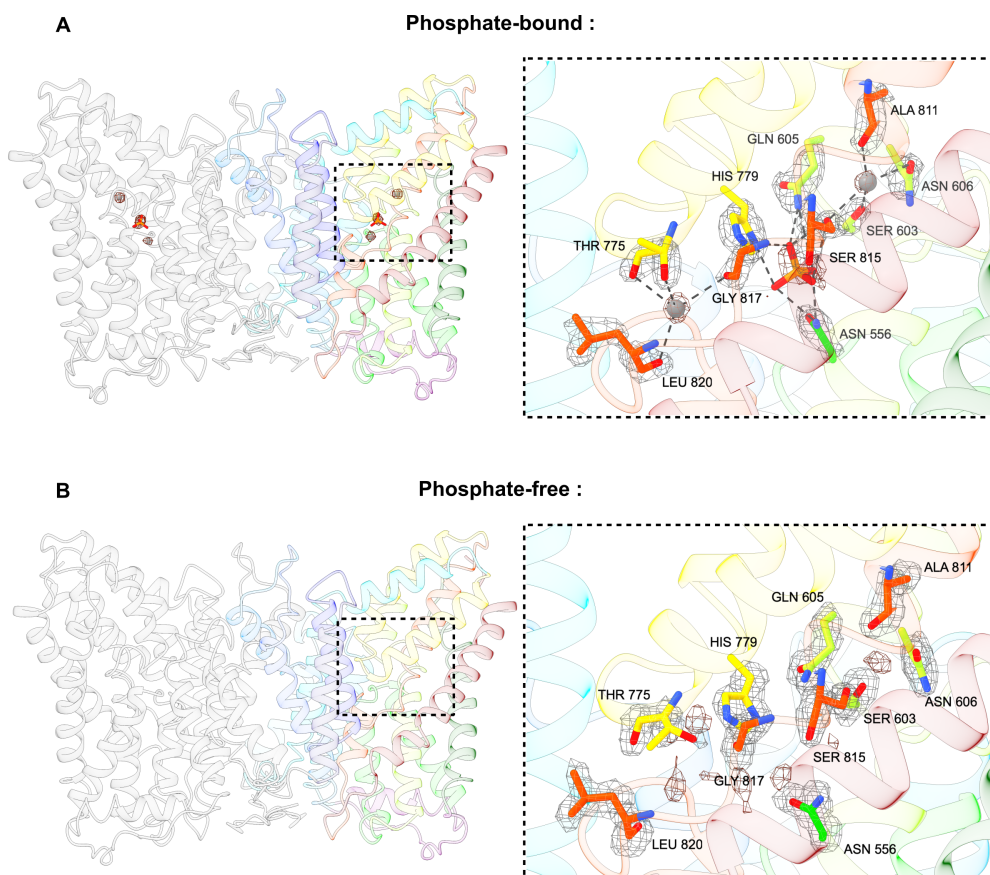


Figure 16: Insights into substrate coordination by ScPho90. (A) Positions of phosphate and sodium ions are shown with their respective densities within the ScPho90 structure (left). The area within the dashed box is shown in detail (right). Residues involved in phosphate and sodium ion coordination are shown and labeled. Phosphate is coordinated by Asn556, Gln605, His779 and Ser815. Two sodium ions are coordinated by Ser603, Asn606, Ala811, Ser815 and Thr775, Gly817, Leu820, respectively. (B) Overview and detailed view of the binding pocket of ScPho90 in the absence of phosphate. Density threshold level is the same as in (A).

3.1.7 Co-purified lipids

All ScPho90 maps show additional elongated densities at the surface of the membrane embedded part of the protein (Figure 17). These densities correspond to detergent mo-

lecules and individual lipids that are retained during the purification process. To determine whether specific lipids bind to ScPho90, thin-layer chromatography was used to identify lipids within the sample. TLC analysis shows that several different types of lipids and sterols are present in the cryo-EM sample. Since the density of individual lipid headgroups is only poorly resolved in the maps, it is not possible to clearly assign specific lipids to them. Into the most prominent lipid densities, phosphatidic acid (PA) was modelled as default lipid molecule.

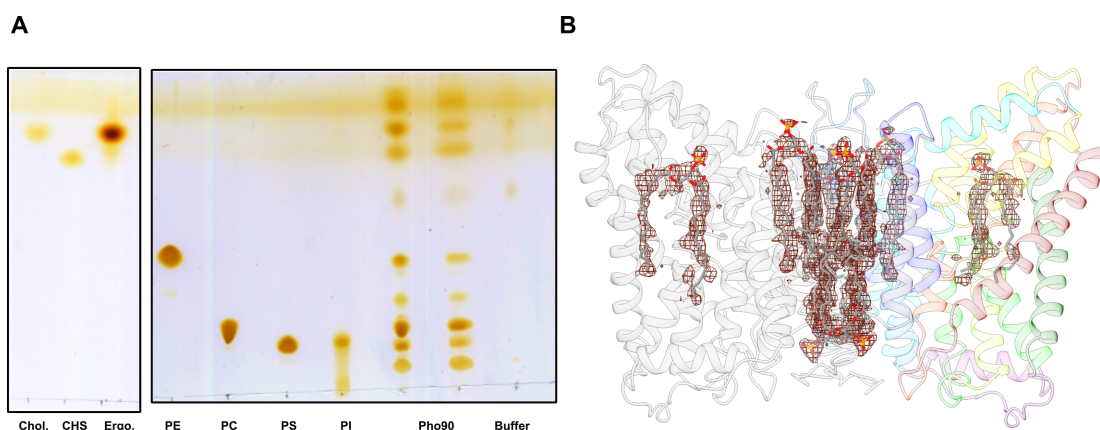


Figure 17: Co-purified lipids of ScPho90. (A) TLC analysis of purified ScPho90 in LMNG/CHS. Several different lipids and sterols were identified in the purified sample. (B) Modelled lipid densities are shown with the ScPho90 structure. All lipids were modelled as phosphatidic acid (PA) as no specific headgroups were identified.

3.1.8 The SPX domain

The soluble SPX domain is not visible in any of the high-resolution maps of ScPho90. However, at low threshold levels of the maps, additional densities are present at the cytoplasmic end of the protein, below the detergent micelles (Figure 18). The SPX domain is connected to the first transmembrane helix via a large flexible linker. Part of this linker is resolved in the cryo-EM structures, in particular in the symmetric map of ScPho90 when no phosphate was present (Figure 14). The linker adopts the fold of a small β -hairpin, running parallel to the membrane plane on the cytoplasmic side. The resolved part of the linker ends beneath the transmembrane part. In the ScPho90 maps at low threshold levels, the SPX domains seem to be connected with the micelle at the cytoplasmic part of both transport domains. However, due to the low resolution of the SPX domain, exact interaction sites remain elusive. The low resolution of the SPX domain compared to the transmembrane part is presumably caused by its high flexibility. Thus, different ScPho90 constructs with linker deletions of different lengths were constructed

($\Delta 355-377$, $\Delta 355-408$, $\Delta 363-377$, $\Delta 363-408$). However, none of the constructs expressed well enough in *S. cerevisiae* for further purification and structural analysis. Also the addition of InsP_6 , which is a known substrate of the SPX domain, did not stabilize a specific conformation of the SPX domain. The SPX domain retained its flexibility and therefore its high-resolution structure was not accurate.

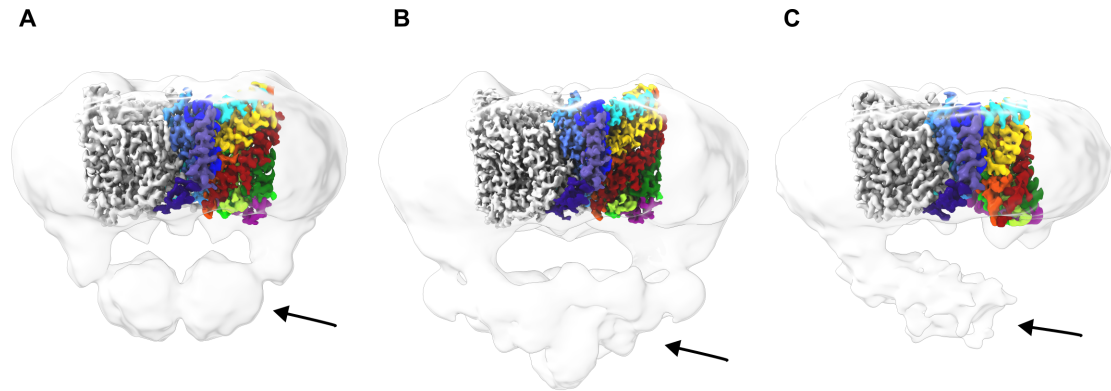


Figure 18: Low-resolution density maps of ScPho90 SPX domains. Cryo-EM density for the cytoplasmic SPX domain is visible at low threshold levels in each ScPho90 map (black arrow). Density at a high threshold level is shown in grey/rainbow and density at a low threshold level is shown in opaque grey. (A) Phosphate-bound map, (B) phosphate-free symmetric map, (C) phosphate-free asymmetric map.

3.1.9 Functional analysis

To determine the affinity of ScPho90 for phosphate, microscale thermophoresis experiments were performed using a Monolith NT.115 instrument (Figure 19). Red tris-NTA labelled ScPho90 was mixed with different concentrations of KP_i and MST traces were measured. All concentrations were measured in triplicates and the data was fitted with a one-site binding model. An experimental K_d value of 1.9 ± 0.7 mM was determined. For the transport measurements, ScPho90 was reconstituted into preformed liposomes with an average diameter of 400 nm. Phosphate transported into the liposomes by ScPho90 was detected and quantified using a malachite green assay. Empty liposomes were used as a control and transported phosphate levels were normalized to the amount transported by wild-type (WT) ScPho90. WT ScPho90 shows a significantly higher phosphate transport activity compared to empty liposomes, but only if a sodium ion gradient is present. The transport activity decreases to nearly background levels without a sodium ion gradient. Deletion of the SPX domain leads to a comparable transport activity *in vitro* as measured for WT ScPho90. The phosphate binding site mutants Asn566Ala and Ser815Ala decrease phosphate transport activity of ScPho90 greatly.

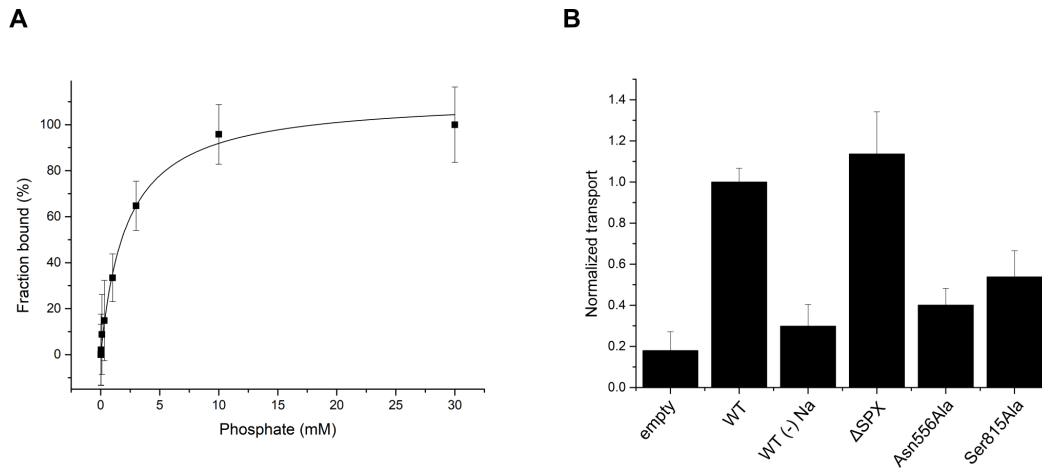


Figure 19: Functional characterization of ScPho90 and its mutants. (A) Phosphate binding to ScPho90 determined by microscale thermophoresis. The experimental K_d value is 1.9 ± 0.7 mM. Mean values and standard deviations are shown ($n=3$). (B) Transport activity measurements of reconstituted ScPho90. WT ScPho90 and ScPho90 lacking the soluble part (Δ SPX) showed similar transport activities. The absence of a sodium gradient ($-$ Na) as well as the mutations Asn556Ala and Ser815Ala show greatly decreased transport activities. Mean values and standard deviations are indicated ($n=3$).

3.2 The eukaryotic phosphate exporters Syg1 and Xpr1

3.2.1 Expression and purification of Syg1 proteins

The expression of different eukaryotic phosphate exporters was evaluated by small-scale expression tests in *S. cerevisiae*. Syg1 proteins from *C. thermophilum* (CtSyg1), *S. cerevisiae* (ScSyg1) and *Y. lipolytica* (YlSyg1) were tested under different expression conditions. A list of all tested constructs can be found in the Materials and Methods section (Table 4).

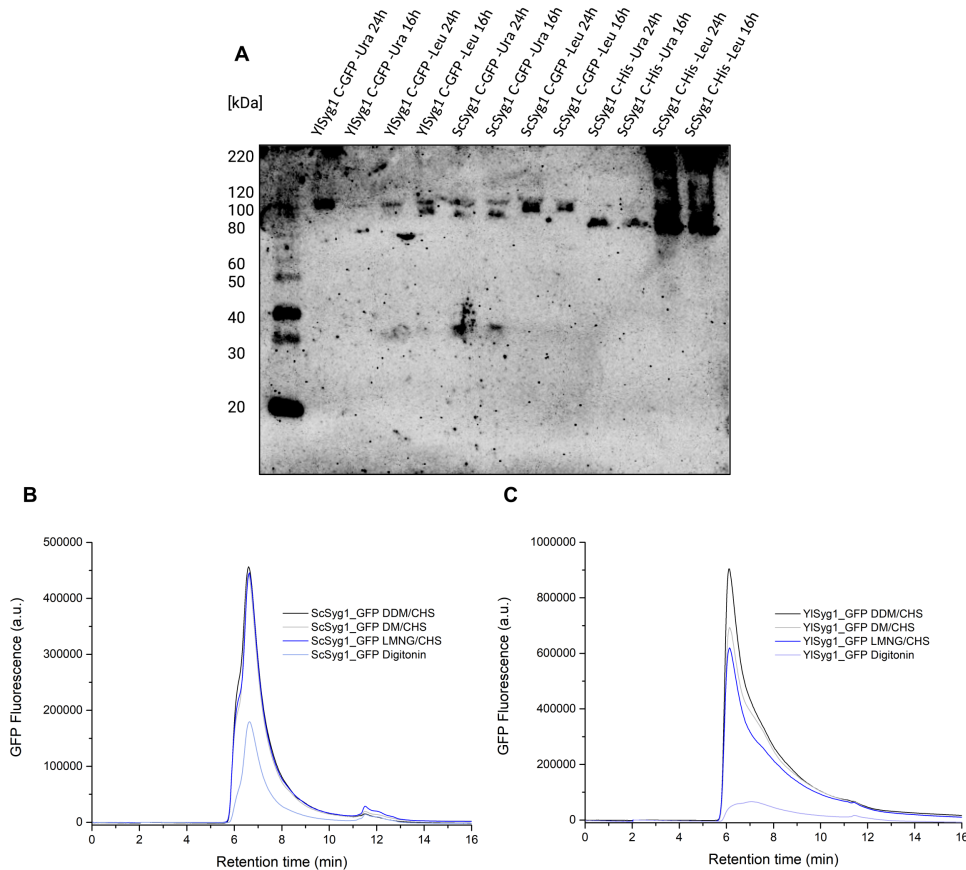


Figure 20: Expression and FSEC analysis of different Syg1 constructs. (A) Expression of YlSyg1 C-GFP, ScSyg1 C-GFP and ScSyg1 C-His in *S. cerevisiae* was investigated by Western Blot. All constructs expressed and showed bands at the expected molecular weight. His-tagged ScSyg1 showed the highest expression levels. An anti-His antibody was used for detection. (B)/(C) Solubilized protein samples were separated using a 300S Pro SEC column (flow rate: 3 mL/min) and GFP fluorescence (Ex/Em: 480/520 nm) was detected. While all YlSyg1 samples eluted mainly in the void volume (6 min), ScSyg1 samples eluted in a main peak around (7 min).

The result of a representative expression test is shown in Figure 20A. The CtSyg1 constructs did not express under any of the tested conditions. Both YISyg1 and ScSyg1 expressed as C-terminal GFP fusion constructs (C-GFP) as well as constructs with only a C-terminal His-tag (C-His). The detected bands corresponded to the expected molecular weight for all constructs. The highest expression levels were observed for ScSyg1 C-His in -Leu drop-out medium. Varying the expression duration (16 or 24 h) did not alter expression levels for most constructs and subsequent expressions were carried out for 24 h.

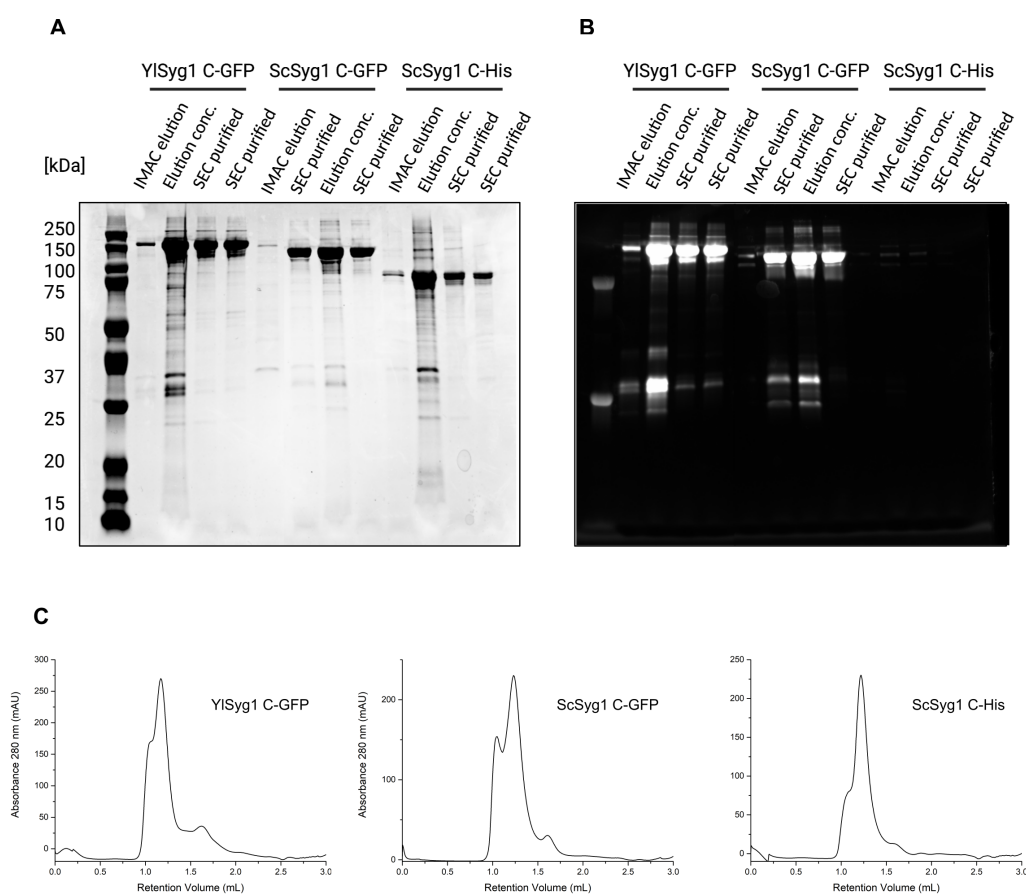


Figure 21: Small-scale purifications of Syg1 constructs. (A) Coomassie-stained SDS gel of Syg1 constructs purified in LMNG/CHS. (B) In-gel fluorescence of the same gel as in (A). YISyg1-GFP, ScSyg1-GFP and ScSyg1 samples showed main bands at the expected molecular weight. (C) SEC runs of Syg1 constructs purified in LMNG/CHS. All SEC runs were performed using a Superdex 200 Inc. 5/150 column. YISyg1-GFP eluted around 1.2 mL, while ScSyg1-GFP and ScSyg1 eluted around 1.25 mL.

GFP fusion constructs were used to evaluate the solubilization efficiencies of different detergents for Syg1 extraction from yeast membranes. Solubilized fractions were separated from unsolubilized material by centrifugation and analyzed by fluorescence size exclusion chromatography (FSEC). GFP fluorescence was measured to specifically detect

Syg1 fusion proteins (Figure 20B and C). Syg1 C-GFP eluted in a peak around 7 min retention time for all tested detergents. Digitonin showed a lower solubilization efficiency compared to the other tested detergents (DDM/CHS, DM/CHS and LMNG/CHS). YlSyg1 C-GFP eluted mainly in a peak around 6 min which corresponds to the void volume of the used column. Digitonin again showed only a low solubilization efficiency.

After testing the solubilization efficiency and protein stability in the respective detergents, small-scale purifications were performed to assess whether the protein remains intact during the purification process. For this LMNG/CHS was used as detergent. Syg1 constructs (ScSyg1 C-His, ScSyg1 C-GFP and YlSyg1 C-GFP) were solubilized, purified by IMAC using Ni-NTA columns, concentrated and analyzed by analytical SEC runs. Samples of IMAC eluates, concentrated eluates and SEC peak fractions were also analyzed by SDS-PAGE (Figure 21). All fractions showed main bands around the expected molecular weight and SEC peak fractions showed pure protein samples. In-gel fluorescence revealed bands for the GFP fusion constructs and weaker bands around 25 kDa corresponding to free GFP. The SEC profiles showed peaks at retention volumes of 1.2 mL for YlSyg1 C-GFP and 1.25 mL for both ScSyg1 constructs. All profiles showed a shoulder or second peak around 1.0 mL which is the void volume of the used column and indicates the presence of some aggregated protein.

The ScSyg1 C-His construct was selected for upscaled purifications since its SEC profile showed the lowest degree of protein aggregation and it is also the most native protein as it does not have an additional GFP fusion protein. ScSyg1 was purified in LMNG/CHS by IMAC and SEC (Figure 22). The SEC profile again showed peaks in the void volume and around 1.25 mL (and an additional small shoulder at 1.35 mL), which were separated sufficiently. SDS-PAGE analysis of different purification steps revealed a pure protein sample with the expected molecular weight (104,2 kDa). BN-PAGE analysis of pure ScSyg1 revealed a main band at around 242 kDa, indicating that ScSyg1 likely forms dimers in solution. The ScSyg1 sample was purified in the absence of phosphate and was stable for several days at 4 °C. ScSyg1 was also purified in the presence of phosphate and InsP₆ and showed comparable SEC profiles and purity on SDS gels.

3.2.2 Electron microscopy screening

Freshly purified ScSyg1 was analyzed by negative-stain EM using a 120 kV Tecnai Spirit microscope. 3 µl of ScSyg1 at a concentration of 0.02 mg/mL were stained using uranyl formate. The sample showed uniformly sized particles, indicating a pure and well-folded protein sample (Figure 23A). After confirming particle homogeneity by negative-stain

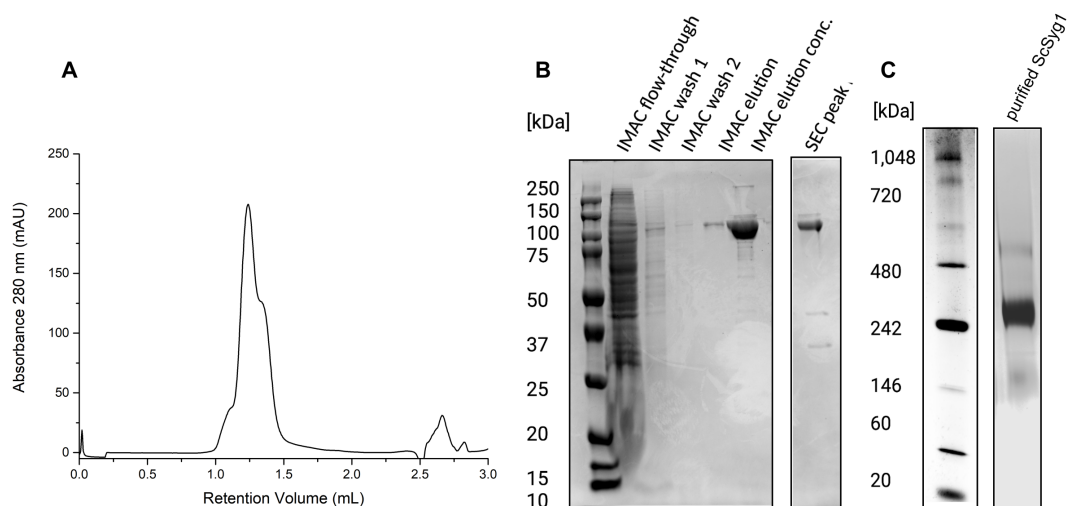


Figure 22: Purification of ScSyg1. (A) SEC profile of ScSyg1 in LMNG/CHS. The peak around 1.25 mL corresponds to dimeric ScSyg1 that was used for subsequent experiments. (B) Coomassie-stained SDS gel of ScSyg1 purification steps. ScSyg1 bands appear around 100 kDa in accordance to its molecular weight. IMAC enriches ScSyg1 while SEC increases the purity of the final sample. (C) BN-PAGE analysis of purified ScSyg1. The sample shows a main band around 242 kDa indicating that ScSyg1 forms dimers in solution.

EM, different vitrification conditions were tested to obtain nicely distributed ScSyg1 particles in a thin layer of amorphous ice. The varying parameters were: protein concentration, blotting parameters, grid type and added secondary detergents. The best grids were obtained using a protein concentration of 3.5 mg/mL, blotting at 4 °C and 100 % humidity, C-flat 1.2/1.3 300 mesh grids and adding 0.05 % of Fos-8. An initial small dataset was recorded using a 200 kV Glacios microscope equipped with a Falcon 3 camera. Processing of this dataset yielded different 2D classes of ScSyg1 (Figure 23B). Top views of the protein indicate a two-fold symmetry and densities for individual transmembrane helices. 3D reconstructions yielded an initial reconstruction with a resolution of approximately 8 Å (Figure 23C). The dimeric arrangement is visible in the 3D reconstruction, as was some density below the micelle density likely corresponding to the soluble SPX domain of ScSyg1.

3.2.3 High-resolution cryo-EM data acquisition of ScSyg1

The same ScSyg1 grids were used to record a larger dataset on a 300 kV Titan Krios G4 microscope equipped with cold-FEG, a Falcon 4 camera and a Selectris energy filter. A total of 16,970 movies were recorded using a total electron dose of $65 \text{ e}^- / \text{Å}^2$ and a defocus range of -0.5 to -2.2 μm (Table 8, Material and Methods). The dataset was processed

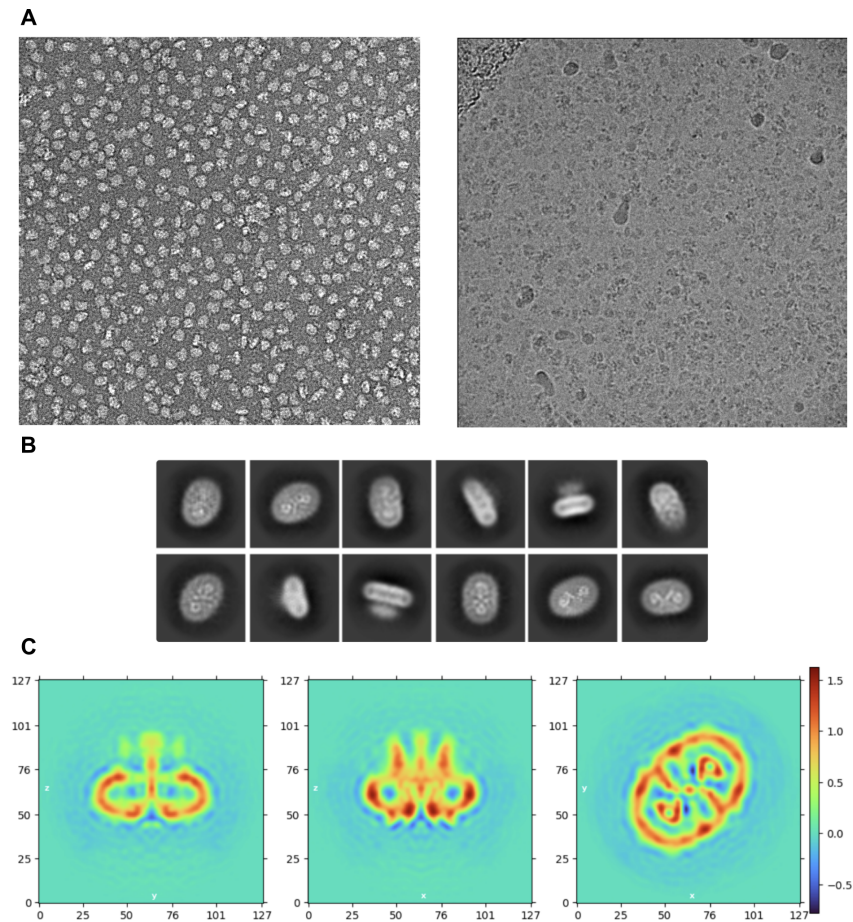


Figure 23: ScSyg1 sample screening by electron microscopy. Images of purified ScSyg1 either stained with uranyl formate (left) or embedded in a thin layer of vitreous ice (right). Both images show homogeneously sized particles and good particle distributions. (B) 2D classes of ScSyg1. 2D classes show both top and side views. In top views, the helix organisation can be seen as well as the twofold symmetry of dimeric ScSyg1 particles. (C) Unidirectional views of a ScSyg1 3D reconstruction with an overall resolution of approximately 8 Å.

in RELION and CryoSPARC (Figure 24). Recorded movies were motion-corrected and Ctf-estimated in RELION. Particle picking using a pre-trained model in crYOLO resulted in 2,796,653 initial particles. After extraction, the particle stacks were imported into CryoSPARC and false-positive picks were removed by three rounds of 2D classification. The 2D classes show different angular views of the protein with clear secondary structure elements. The top views show the organization of the TM helices into two helix bundles and connected by additional helices. Side views also show several TM helices within the micelle and an additional, less defined density below the micelle (Figure 24B).

Ab initio 3D reconstruction of four independent classes and subsequent heterogeneous refinement further removed broken and low resolution particles. Non-uniform refine-

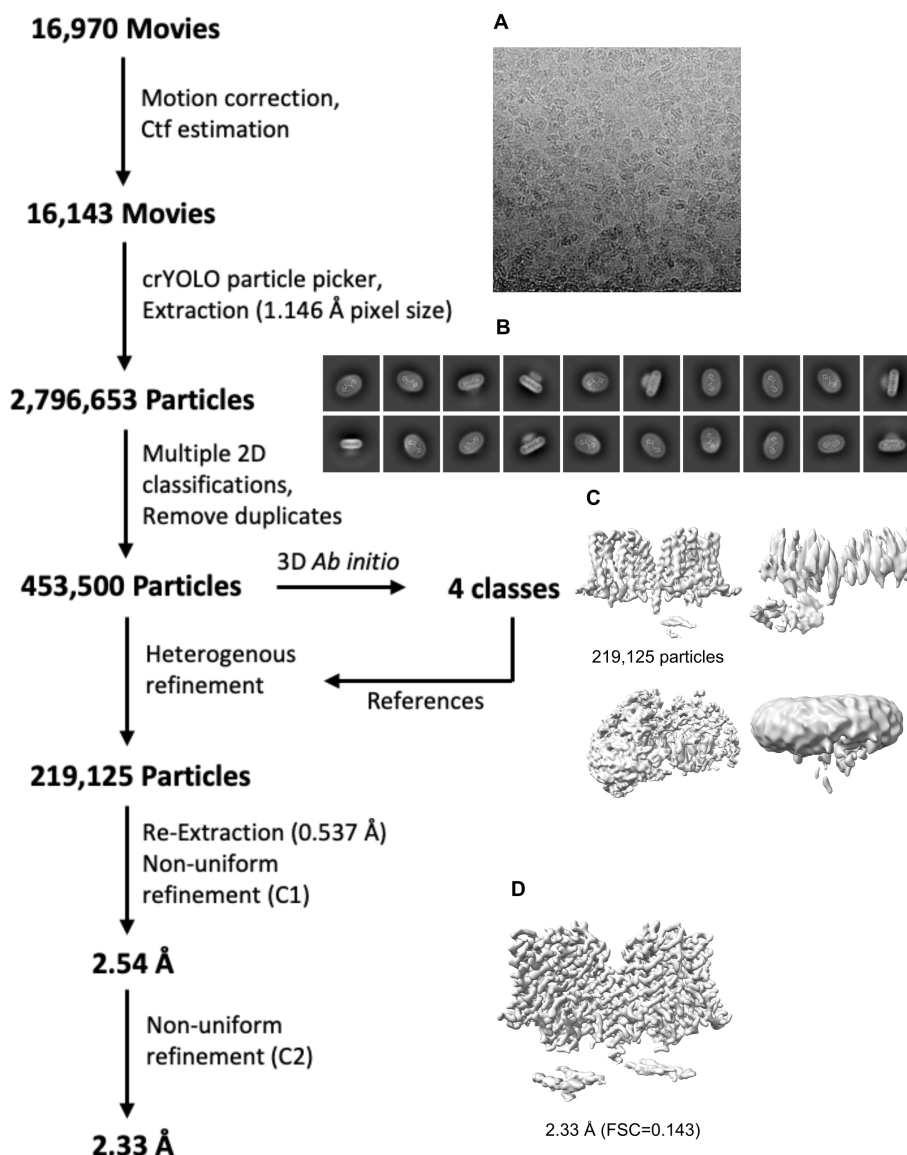


Figure 24: Processing scheme of ScSyg1 without phosphate. The cryo-EM processing pipeline to obtain the final maps of ScSyg1 is shown on the left. A representative micrograph (A), final 2D classes (B) and all *ab initio* models (C) are displayed. The final map after non-uniform refinement with C2-symmetry applied is shown at the bottom.

ment of the best class yielded a map of ScSyg1 with a nominal resolution of 2.53 Å. An additional non-uniform refinement with C2-symmetry applied improved the resolution to 2.33 Å. This map was sharpened using DeepEMenhancer. The final maps reveal the transmembrane part of ScSyg1 in high detail. In addition, density for the soluble SPX domain can be observed. This density is resolved at modest resolution and only covered a fraction of the SPX domain compared to known crystal structures (Wild et al., 2016). Local refinements of this part improved neither the resolution nor the size of the resolved area.

3.2.4 Structure of substrate-free ScSyg1

The cryo-EM map was used to build an atomic model of the transmembrane part of dimeric ScSyg1 (Figure 25). The dimer dimensions are 100 x 60 x 45 Å. Each monomer consists of 10 transmembrane helices (TM1-10), with the N- and C-terminal ends located at the cytoplasmic side. A schematic overview is shown in Figure 25C.

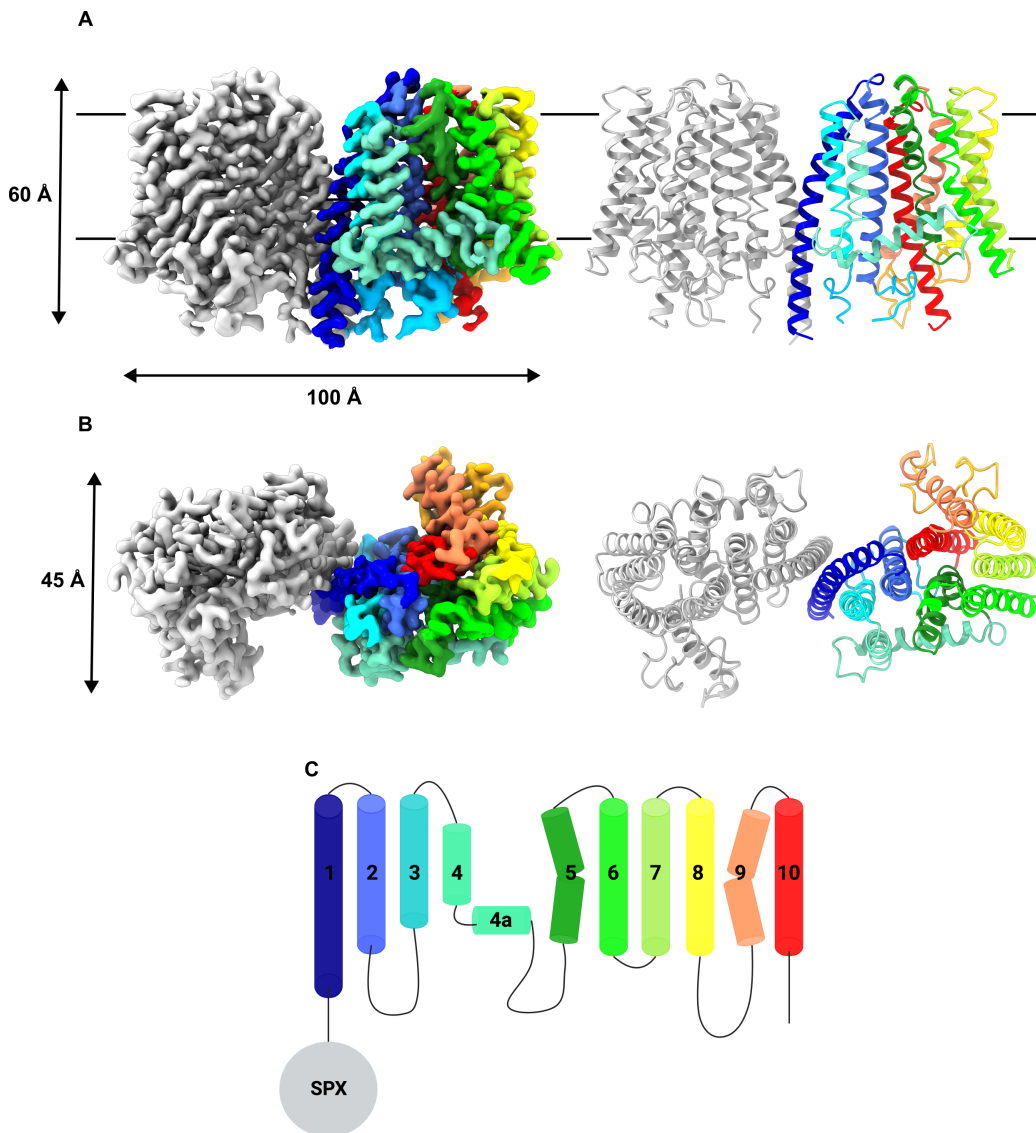


Figure 25: Overall structure of ScSyg1. (A) Side views of the map (left) and model (right) of the transmembrane part of ScSyg1. One protomer is colored in grey while the other one is colored by individual transmembrane helices and numbered as in (C). The membrane plane is indicated by black lines. (B) Top views of the map (left) and the corresponding model (right). Both are turned by 90° in relation to (A). (C) Schematic overview of the transmembrane organization of ScSyg1.

The only helix contributing to the dimer interface is TM1, which interacts with TM1

from the other protomer within the membrane. Helices TM2-4 and parts of TM5 form a hydrophobic pocket within the inner leaflet of the membrane. The lateral helix TM4a connects the first 4 helices with TM5-10, which form a six-helix bundle, constituting a putative translocation pathway in its center. Of these helices TM5 and TM9 are kinked towards the interior of the pathway. ScSyg1 also possesses two larger intracellular loops (ICL1 and ICL4), which were resolved only at lower resolution likely due to their intrinsic flexibility, but were fully modelled outside of the small stretch between residues 478 - 483.

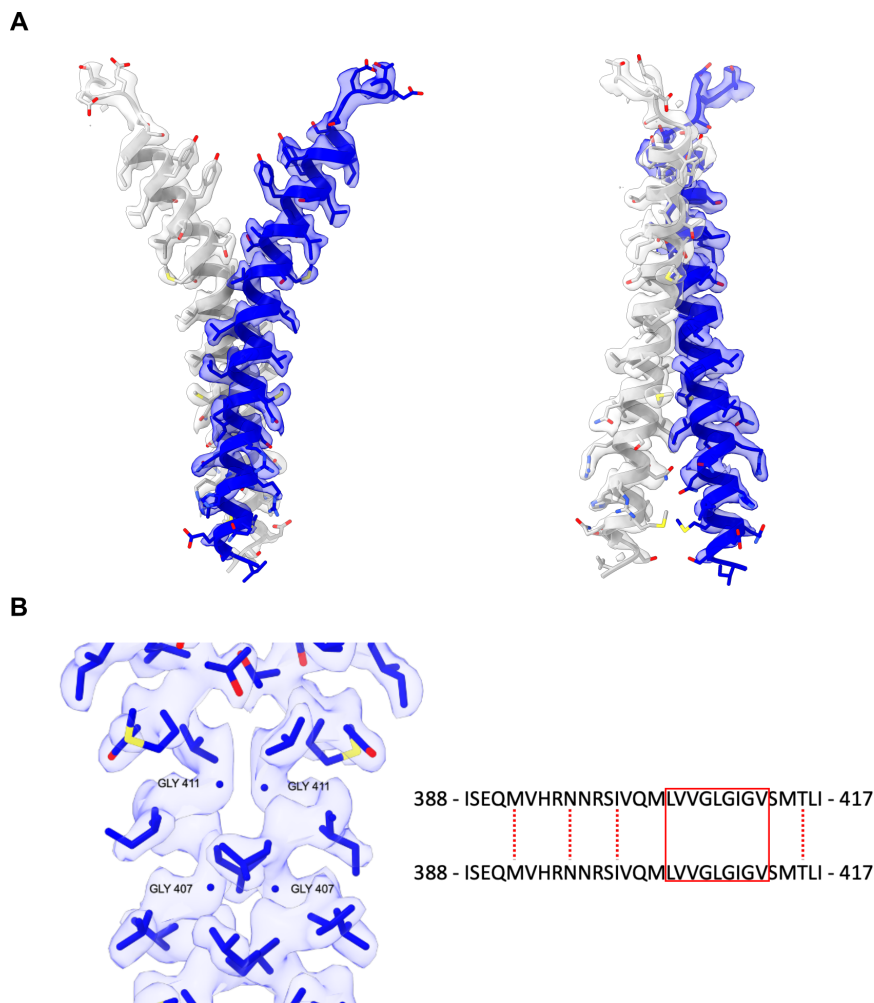


Figure 26: ScSyg1 dimerization interface. (A) The ScSyg1 dimer has a very small dimer interface. Only helix TM1 from each protomer, colored in grey and blue respectively, contributes to the interface. The right view is turned by 90° in relation to the left one. (B) Sequence of the TM1 part that is involved in the interaction. The red box indicates a stretch of the helices that interact in a glycine zipper-like fashion. This stretch is shown in detail (left). Sidechains of residues Met392, Asn396, Ile400 and Thr415 show direct contacts indicated by dotted red lines.

3.2.5 Structural details of ScSyg1

The ScSyg1 dimer shows a very small dimer interface, to which only helix TM1 contributes (Figure 26). The TM1 helices from both protomers cross within the membrane and residues Met392, Asn396, Ile400 and Thr415 interact with the same residues of the opposite protomer (Figure 26B). Additionally, a stretch rich in glycine and hydrophobic residues makes direct helix contacts with the same stretch of the opposite TM1. The small glycines (Gly407 and Gly411) allow the helices to come into close contact (C_{α} distance of 4.0 Å) so that adjacent hydrophobic sidechains interact with opposite ones. This interaction motif and the residues involved show similarities to a glycine zipper motif (GxxxG), which is a common interaction motif between α -helices (Kim et al., 2005).

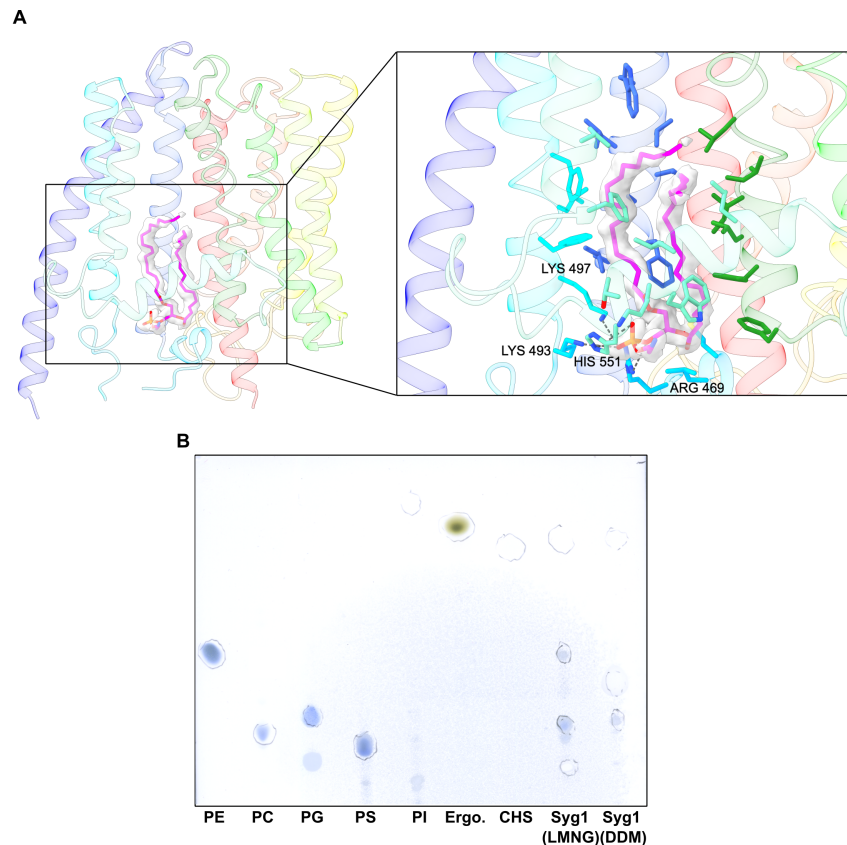


Figure 27: Lipid binding pocket of ScSyg1. (A) Overview of the lipid binding pocket in ScSyg1. The pocket is formed by helices TM2-5 at the inner leaflet of the membrane (left). The lipid density is shown in light grey. A close-up view shows interactions between the PE lipid and ScSyg1 residues (right). The phosphate headgroup is coordinated by the basic sidechains Arg469, Lys493, Lys497 and His551. The lipid tails are buried deep within the hydrophobic pocket. (B) TLC analysis of lipids bound to ScSyg1. Bands were visualized using Molybdenum Blue. In LMNG-purified ScSyg1 both PE and PC lipids were co-purified, while in DDM-purified ScSyg1 only PC was detected.

While TM1 is involved in the formation of the dimer interface, helices TM2-5 form a hydrophobic pocket in which density for a lipid molecule was found (Figure 27). The pocket is located within the inner leaflet of the membrane and is open towards the cytoplasmic side. It also has a lateral opening within the membrane plane above the lateral helix TM4a. The headgroup of the bound lipid is facing the cytoplasmic side and its phosphate group is coordinated by four basic sidechains (Arg469, Lys493, Lys497 and His551). The lipid tails are buried deep inside the hydrophobic pocket, composed of sidechains from helices TM2-5. TLC analysis revealed that phosphatidylcholine (PC) and phosphatidylethanolamine (PE) are present in LMNG-purified ScSyg1. The observed density for the lipid headgroup fits a PE lipid well and was therefore modelled as such into the hydrophobic pocket. However, it is also possible that the pocket is occupied by a mixture of both lipids.

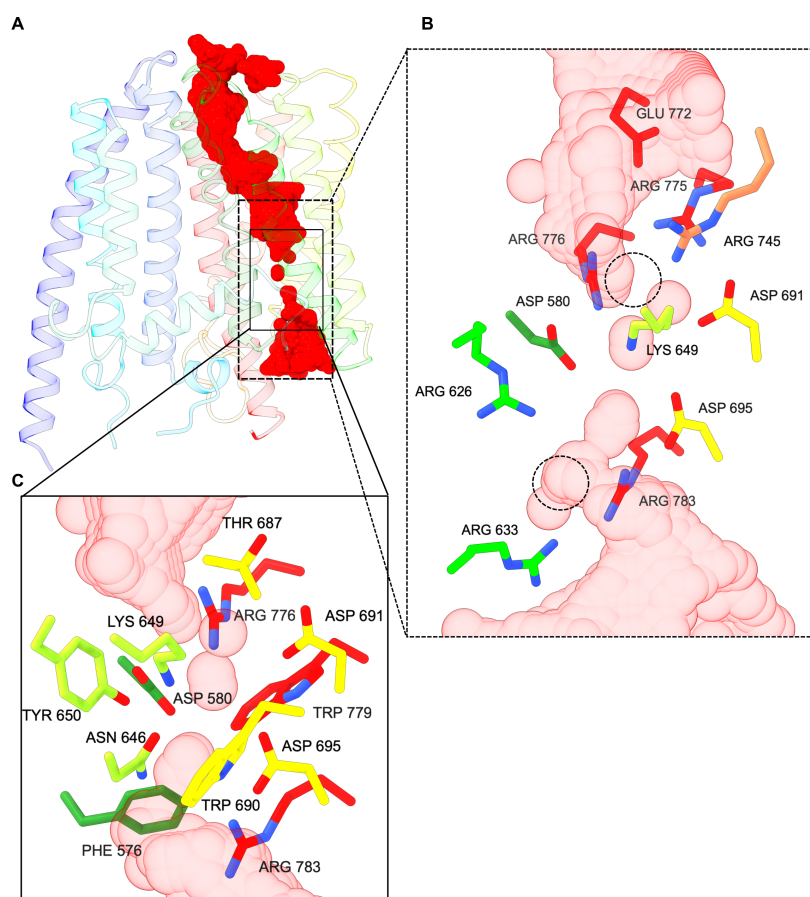


Figure 28: Putative translocation pathway. (A) Overview of the putative translocation pathway spanning the transmembrane part of ScSyg1. The interior surface of the translocation pathway was calculated using Hollow-1.3 (red surface). The translocation pathway shows a narrow stretch close to the cytoplasmic channel exit. (B) Charged residues pointing towards the interior of the pathway near the narrow passage. (C) Sidechains responsible for pathway narrowing include bulky as well as charged residues.

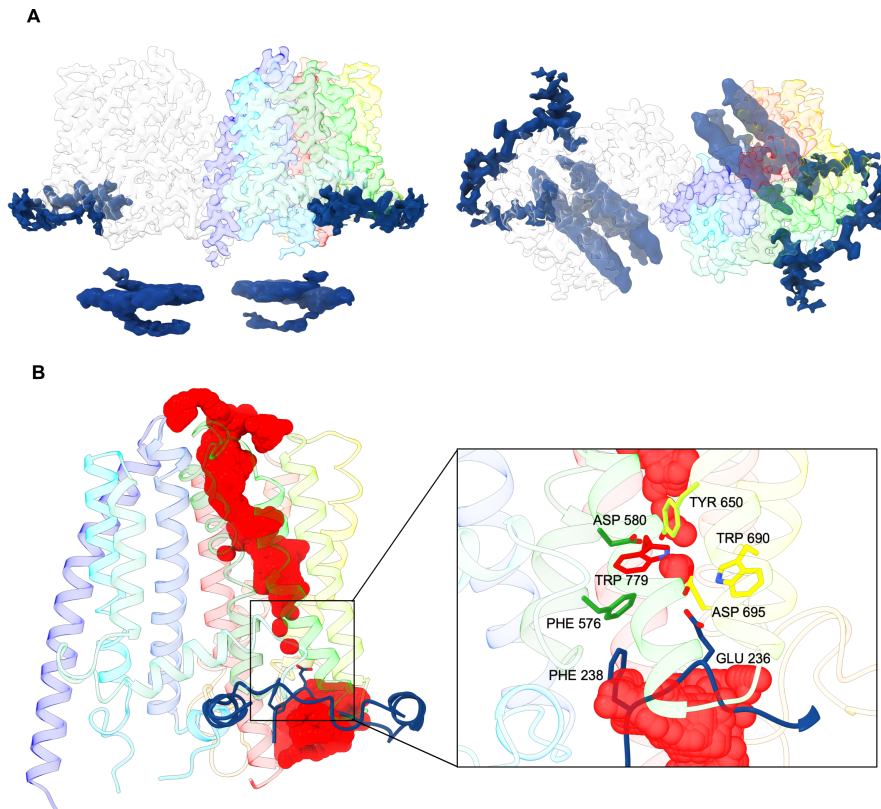


Figure 29: The SPX domain and its interaction with the TM domain. (A) ScSyg1 maps with highlighted SPX domains (dark blue). The SPX domain forms a three-helix bundle below the transmembrane domain. Additional density was observed wrapping around the cytoplasmic end of the helices forming the putative translocation pathway. This density corresponds to residues Leu198 - Ala239 which are part of a long loop between SPX helices. (B) This loop not only wraps around the transmembrane part but also blocks the cytoplasmic entry to the translocation pathway. Phe238 and Glu236 extend into the pathway and block it on the cytoplasmic side.

Helix TM5 is not only involved in the formation of the lipid binding pocket, but is also part of a helix bundle together with helices TM6-10, forming a putative phosphate translocation pathway in the center of the bundle (Figure 28). Its interior surface was calculated using Hollow-1.3 (Ho et al., 2008). This pathway spans the whole transmembrane part and has a narrowed section close to its cytoplasmic end. This constriction is caused by sidechains in close contact within the pathway. Besides four bulky sidechains (Phe576, Tyr650, Trp690 and Trp779) that narrow the inner diameter, two aspartate and one asparagine residues (Asp580, Asn646, Asp695) are in close contact (Asp580-Asp695: 4.9 Å, Asn646-Asp695: 5.4 Å) at the narrowest site of the translocation pathway (Figure 28C). Several other charged residues are present at this constriction, in particular six arginine residues, three of which are clustered directly below (Arg626, Arg633, Arg783) and three above (Arg745, Arg775, Arg776) the constriction.

In the absence of substrates, the SPX domain is only poorly resolved. However, a weak density for a three-helix bundle can be observed below the transmembrane part (Figure 29), in agreement with previously resolved homologous crystal structures (Wild et al., 2016). The cryo-EM map resolved only parts of the SPX domain and no direct contact between the SPX helix bundle and the transmembrane part can be observed. However, additional protein density is found at the cytoplasmic end of the helix bundle that forms the translocation pathway (Figure 29A). Surprisingly, this density corresponds to residues Leu198 - Ala239, which are part of a large loop connecting $\alpha 3$ and $\alpha 4$ -helices of the SPX domain (Figure 29B). This loop wraps around part of the helices that form the translocation pathway. It also passes directly under the cytoplasmic entrance of the translocation pathway and actually closes it from the cytoplasmic side. In particular, residues Phe238 and Glu236 are responsible for closing the translocation pathway, as they are located right inside its opening.

3.2.6 Structure of substrate-bound ScSyg1

In addition to the structure of ScSyg1 in the absence of its substrates, also a substrate-bound state of ScSyg1 was elucidated by recording cryo-EM data in the presence of phosphate and InsP₆. Both substrates were present in all purification steps and the final buffer composition was 20 mM KP_i pH 8, 100 mM NaCl, 1 mM InsP₆, 0.005 % / 0.0005 % LMNG/CHS. The dataset was again recorded on a 300 kV Titan Krios G4 microscope. The dataset was processed in RELION and CryoSPARC (Figure 30). In total, 13,902 movies were recorded using a total electron dose of 65 e⁻ / Å² and a defocus range of -0.5 to -2.2 μ m (Table 8, Material and Methods). Motion correction and Ctf estimation were done in RELION and particles were picked using a pre-trained model in crYOLO, resulting in 2,212,011 picked particles. After extraction, the particle stacks were imported into cryoSPARC and false-positive picks were removed using three rounds of 2D classification. The final 2D classes are similar to those from the substrate-free dataset with secondary structures clearly visible inside the micelles. *Ab initio* 3D reconstruction of four independent classes and subsequent heterogeneous refinement further removed broken particles. Non-uniform refinement of the best class yielded a map of ScSyg1 with a nominal resolution of 2.31 Å. An additional non-uniform refinement with C2-symmetry applied improved the resolution to 2.19 Å for the transmembrane part. Since well-resolved density for the soluble SPX domain has been observed in earlier iterations of refinements, 3D variability analysis was used to analyze the SPX domain for different distinct conformations. Particles that contained a well-defined SPX domain density were identified and isolated. Non-uniform refinement of the isolated particles resulted

3.2. The eukaryotic phosphate exporters Syg1 and Xpr1

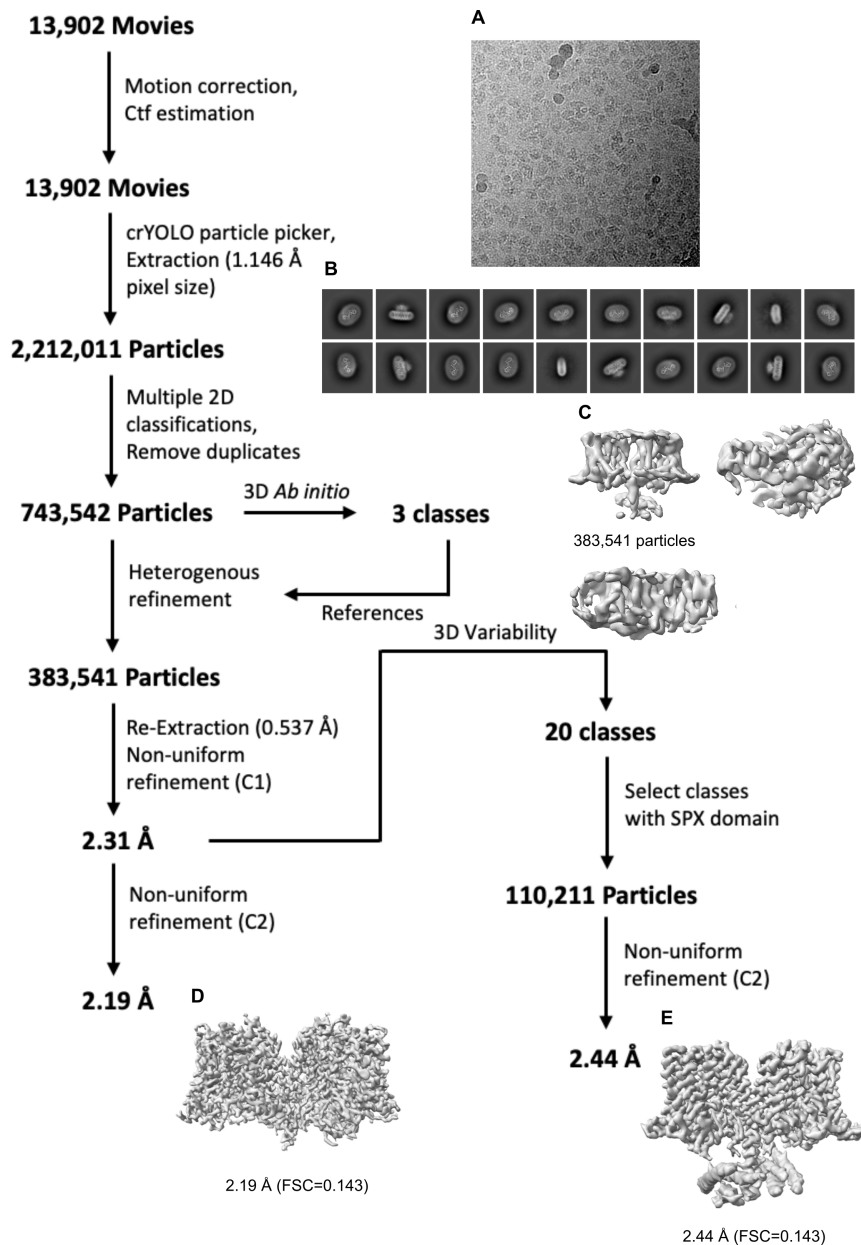


Figure 30: Processing scheme of substrate-bound ScSyg1. The cryo-EM processing pipeline to obtain maps of substrate-bound ScSyg1 is shown on the left. Particles with a well-defined SPX domain were isolated by 3D variability analysis and refined separately. A representative micrograph (A), final 2D classes (B) and all *ab initio* models (C) are displayed. The final consensus map (D) and map with well-defined SPX domains (E) after non-uniform refinement with applied C2-symmetry are shown at the bottom.

in a map with a nominal resolution of 2.44 Å, showing a well-defined density in the soluble part of the protein, although the resolution in this part is only around 4 Å.

The overall structure of the transmembrane part of the substrate-bound ScSyg1 structure is virtually identical to the substrate-free structure. The high-resolution map and model

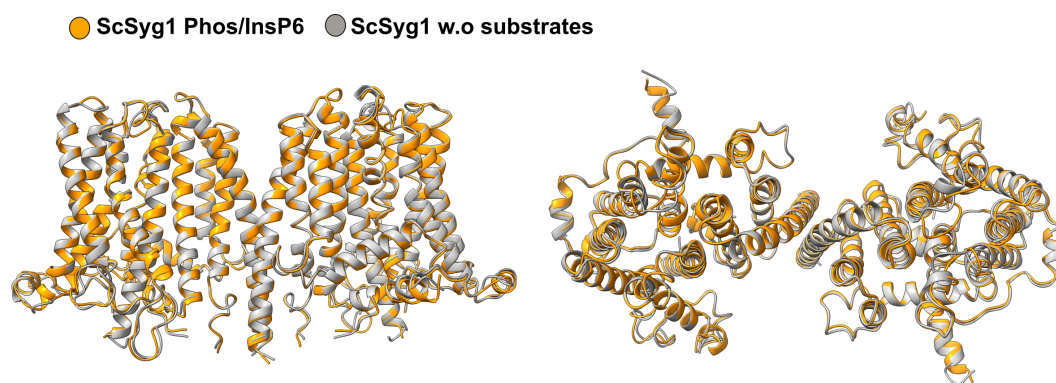


Figure 31: Comparison of ScSyt1 in presence and absence of substrates. ScSyt1 in the absence (grey) and presence (orange) of substrates show no major differences in the TM domain. All helices of both models match nearly perfectly and loop regions show only minor deviations.

of the transmembrane part only can be found in the Supplement (Figure S2). Superposition of both structures reveals small differences in the loop regions, while differences in the TM helices are negligible (Figure 31). Also the SPX loop, which winds around the TM domain, is in the same position in both structures. The map with well-defined density for the SPX domain enabled rigid-body fitting of SPX domain crystal structures or AlphaFold predictions (Figure 32). The density fitted the three-helix bundle of the SPX domain well and also showed density for the two small N-terminal helices ($\alpha 1$ and $\alpha 2$).

3.2.7 Phosphate binding

Although the overall structures of the TM domain of ScSyt1 appeared to be highly similar, additional densities are present within the putative translocation pathway of the substrate-bound ScSyt1 structure. Two prominent density blobs were modelled as phosphate ions as they are well coordinated by highly conserved residues (Figure 33). Additional weak densities within the pathway are likely all water molecules, as they were also observable in the absence of phosphate and do not show pronounced coordination by multiple sidechains. The phosphate molecule (P1), which is located near the cytoplasmic end is coordinated by sidechains of Glu236, Arg633, His643 and Asn646. The second phosphate (P2) is coordinated by sidechains of Ser564, Arg745, Glu772, Arg775 and Arg776 (Figure 33A). The phosphate molecule P1, located at the cytoplasmic end of the translocation pathway, is coordinated by Glu236, which is part of the SPX loop that closes the translocation pathway from the cytoplasmic side. All other coordinating residues are conserved residues within the translocation pathway. Phosphate P2 is located above the narrowed stretch within the pathway and the coordinating residues belonging to TM5, TM9 and TM10 are all highly conserved.

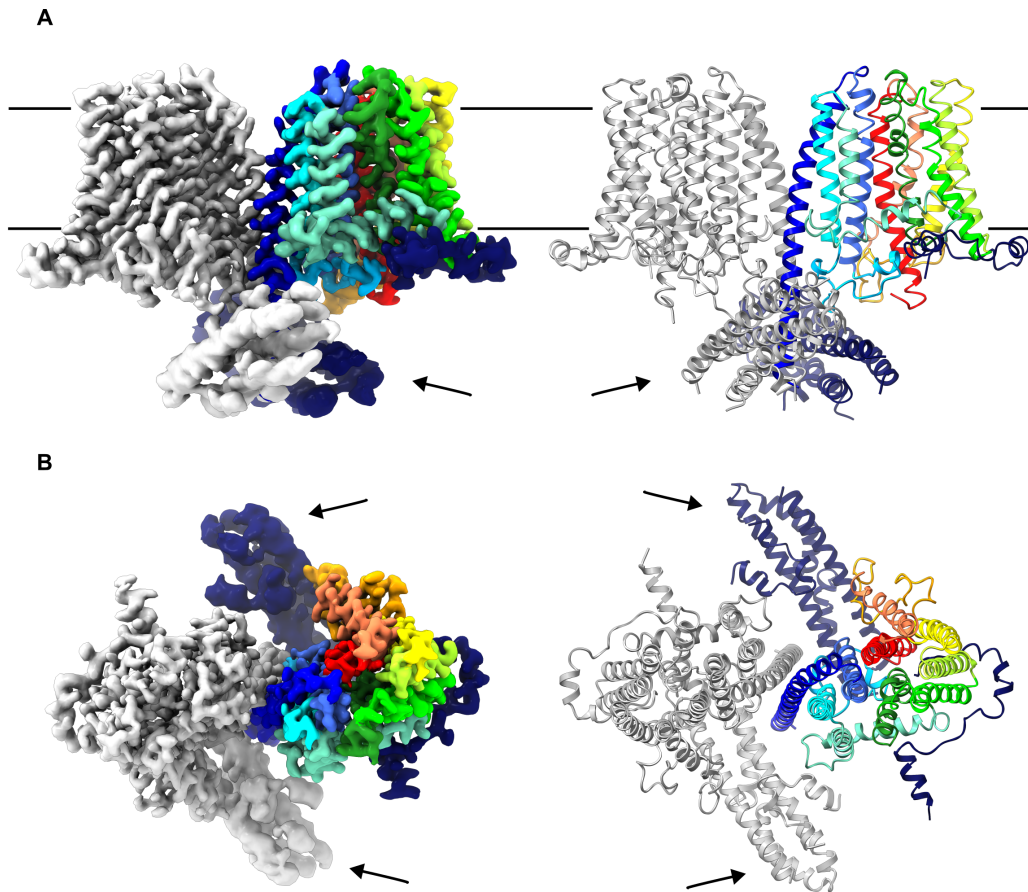


Figure 32: Structure of ScSyg1 in the presence of phosphate and InsP₆. (A) Side views of the map (left) and model (right) of ScSyg1 in the presence of substrates. One protomer is colored in grey while the other one is colored by individual transmembrane helices and the SPX domain. Densities and models of the SPX domain are indicated by black arrows. The membrane plane is indicated by black lines. (B) Top views of the map (left) and the corresponding model (right). Both are turned by 90° in relation to (A).

Closer inspection of the putative translocation pathway shows that extracellular loop 5 (ECL5) adopts two different conformations within the same substrate-bound map (Figure 34). The stretch between Pro755 and Val763 is located at the extracellular end of the translocation pathway and is present in a "retracted" and an "extended" conformation. In the retracted conformation, the pathway is open towards the extracellular side since the loop protrudes away from the membrane plane. This conformation is also observed in the substrate-free structure. In the extended conformation the loop protrudes into the translocation pathway and thus closes it towards the extracellular side.

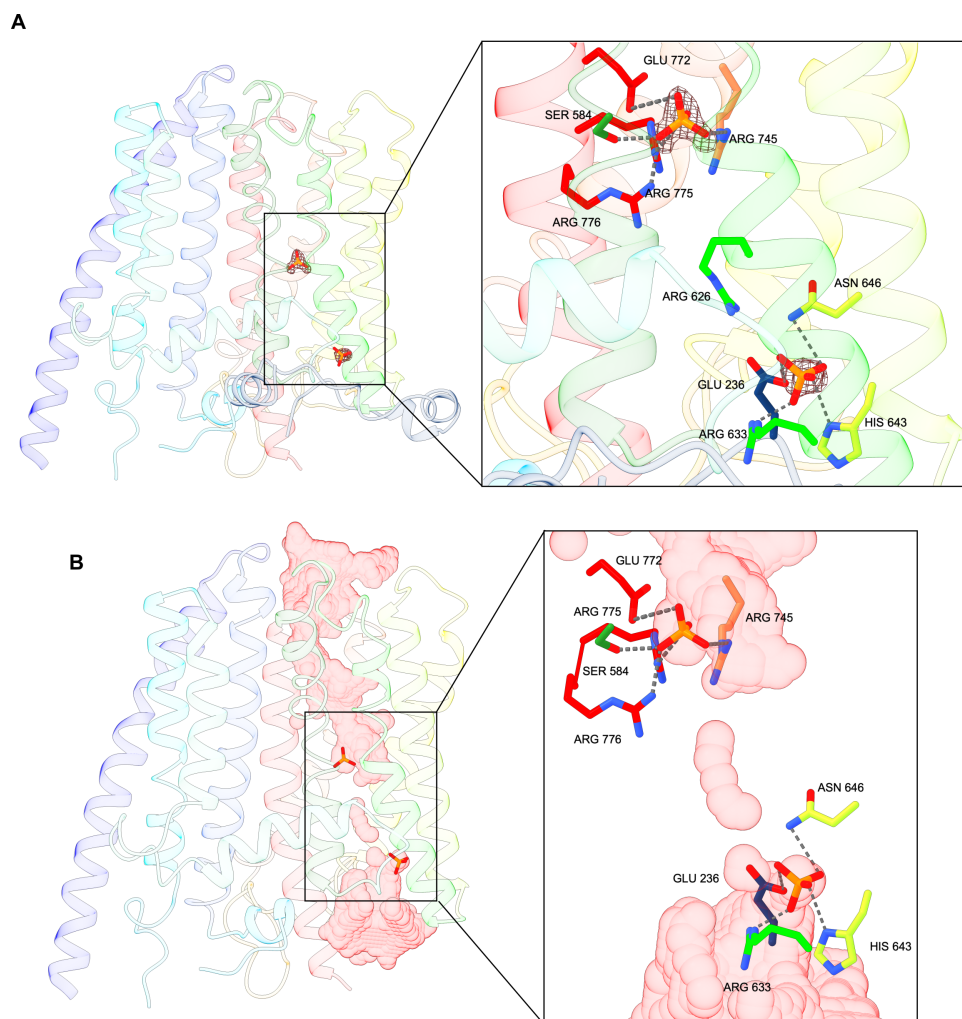


Figure 33: Putative phosphate binding sites. (A) In the presence of substrates, two additional densities were observed in the putative translocation pathway of Sc-Syg1. When modelling phosphate into both densities, each phosphate ion is coordinated by several conserved sidechains: lower P_i (Glu236, Arg633, His643, Asn646), upper P_i (Ser564, Arg745, Glu772, Arg775, Arg776). (B) The lower phosphate ion is located right at the entry of the putative translocation pathway, while the upper phosphate sits right above the narrowed stretch (SPX loop is not shown).

3.2.8 The SPX domain of ScSyg1

While the overall structure of the TM part is very similar in the absence and presence of substrate, the SPX domains show clear differences between both states (Figure 35). In the absence of substrates, the SPX domain is only partially resolved, while in the presence of substrates most of the SPX helix bundle is resolved and therefore an atomic model building could be built (Figure 36A). One end of the SPX helix bundle is located below the transmembrane part of ScSyg1, while the other end lies outside of the TM part radius (Figure 36A). The bundle is not entirely parallel to the membrane plane but tilted

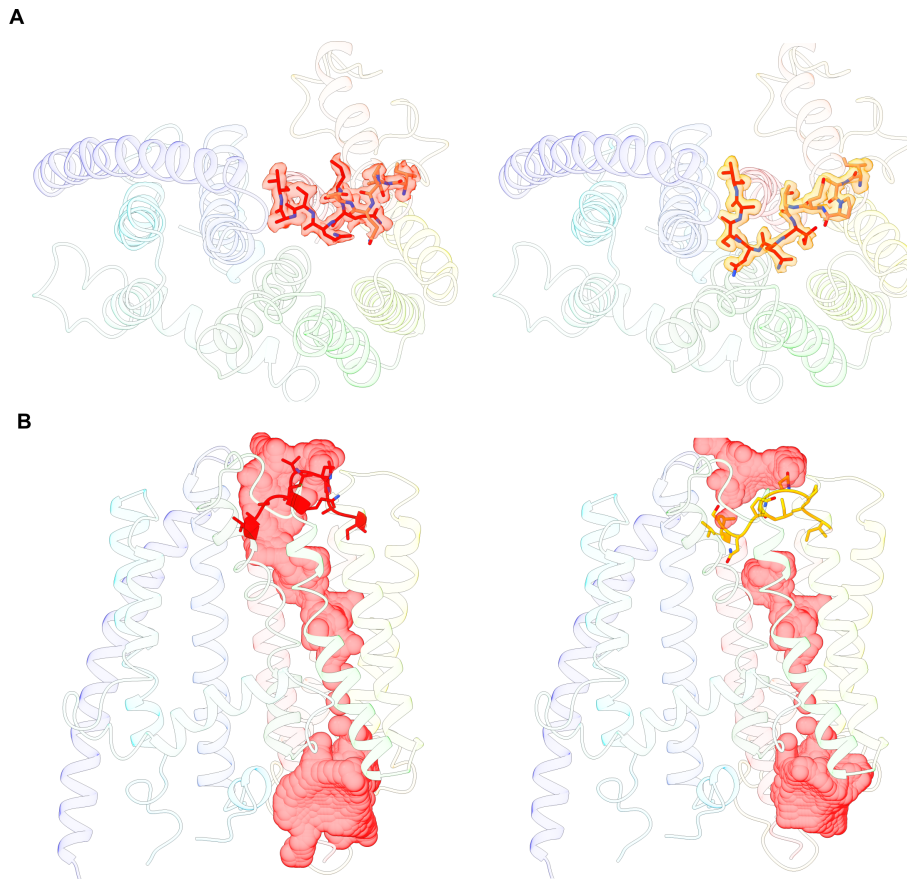


Figure 34: Different conformations of the ScSyt1 extracellular loop 5 (ECL5). (A) The ScSyt1 map with bound substrates shows ECL5 in two different conformations. The retracted conformation (left) matches the conformation observed in the absence of substrate, while the extended (right) conformation is only observed in the presence of substrates. (B) With ECL5 in the retracted conformation, the putative substrate pathway is open towards the extracellular side. In the extended conformation the loop closes the pathway towards the extracellular side.

by about 15° . This tilting results in the SPX end below the TM part being further away from the membrane plane while the other end is closer to the hypothetical membrane plane. The loops between the individual bundle helices are not resolved outside of the stretch that wraps around the transmembrane part (Leu198 - Ala239). Also the stretch that connects the SPX domain and TM1 (Leu365 - Thr376) is not resolved and therefore it is not clear which SPX domain is connected to which transmembrane part.

The N-terminal small helices ($\alpha 1$ and $\alpha 2$) of the SPX domain are located above the end of the helix bundle that is closer to the hypothetical membrane plane and not located beneath the TM part. An additional weak density was observed near the N-terminus (Figure 36B), which corresponds to the binding site for InsP_6 , as observed in the SPX domain crystal structures (Wild et al., 2016). Modelling InsP_6 into this density, it is coor-

minated within a cluster of five conserved lysine residues (Lys2, Lys26, Lys284, Lys287, Lys288) that are in close proximity.

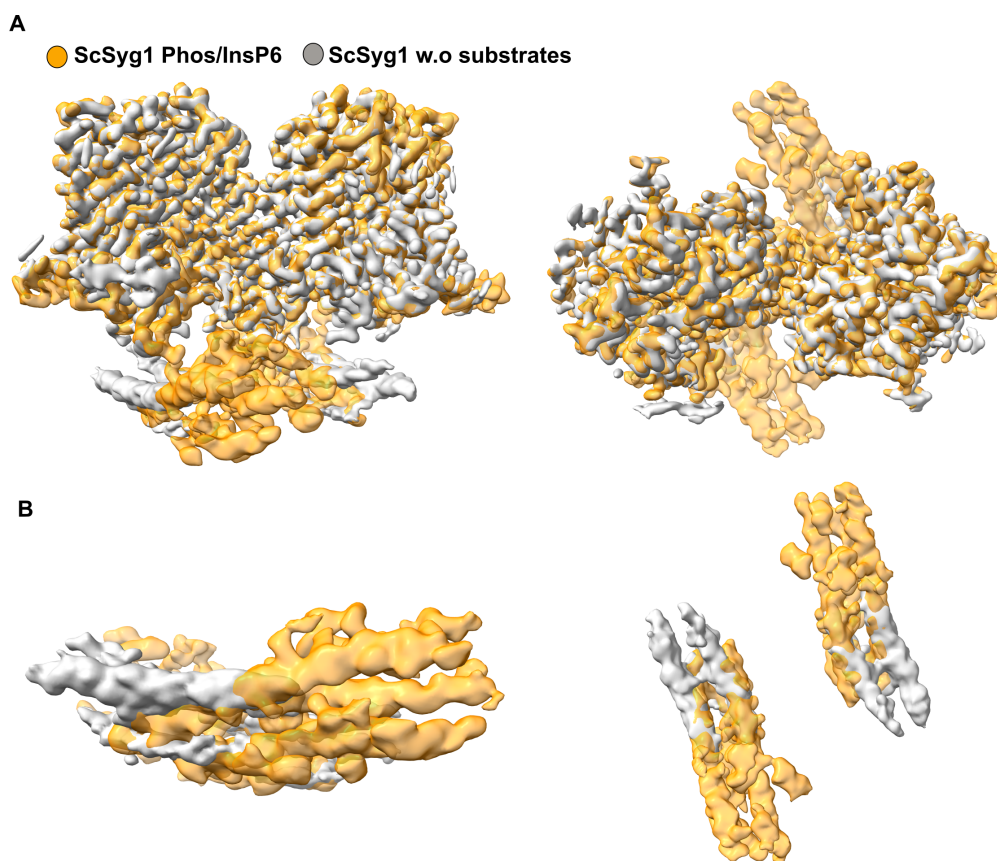


Figure 35: Comparison of SPX domains in the presence and absence of substrates. (A) While ScSyg1 shows no major differences in the TM domain, the SPX domain differs depending on the presence (orange) or absence (grey) of substrates. In the substrate bound structure density for nearly the complete SPX helix bundle is resolved whereas in the substrate-free map it is only partially covered. (B) Side and top views of overlaid SPX domain densities.

The SPX domain interacts with the TM domain at the cytoplasmic end of helix TM1 (Figure 37A). This cytoplasmic end of TM1 (His377 - Thr383) is not resolved in the absence of substrates, but is in the substrate-bound structure. Here, mainly hydrophobic interactions are found between sidechains of TM1 and sidechains of the SPX helix bundle. An additional density is present between the two TM1 helices, which is in close proximity to four conserved lysine residues (Lys378, Lys381 from each monomer). The motif of a conserved basic patch and the size of the density indicate that this may potentially be an additional binding site for InsP₆. Another contact site between SPX and TM domains is found between intracellular loop 4 (ICL4) and the SPX helix bundle (Figure 37B). At

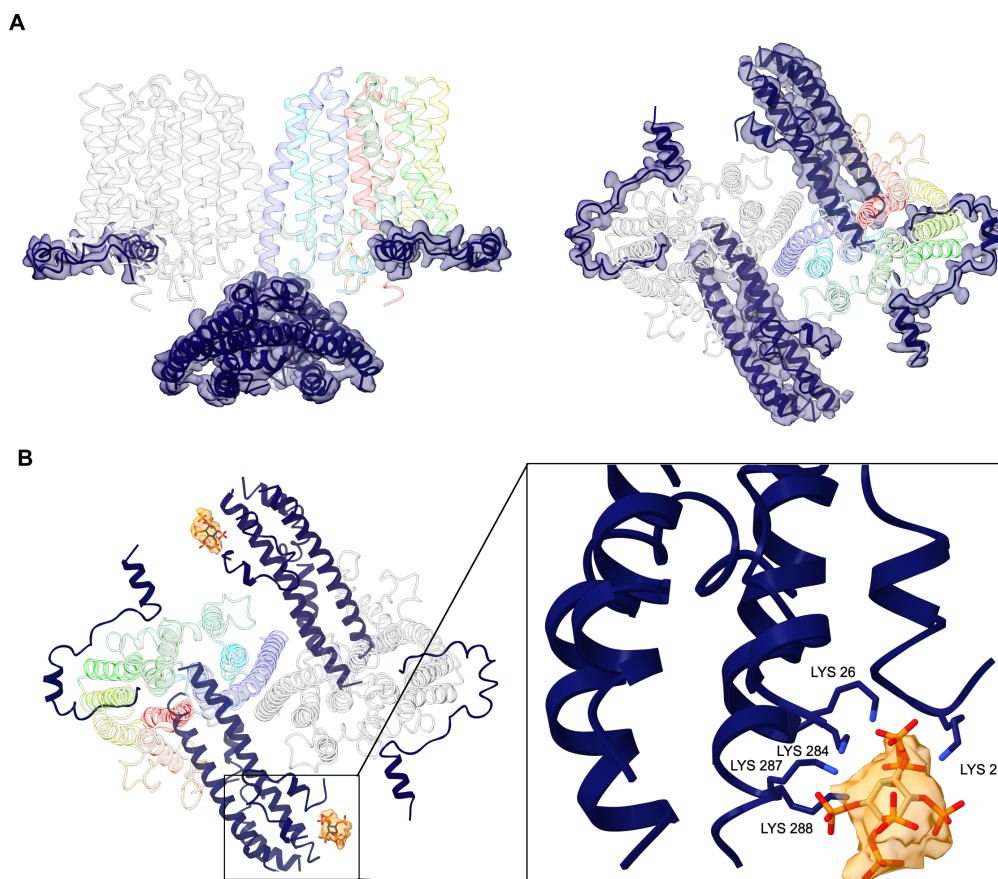


Figure 36: SPX domain structure and InsP₆ binding site. (A) Overview of the SPX domain model and the corresponding density. The initial model was generated using AlphaFold. (B) Additional density (orange) was observed at the predicted InsP₆ binding side. InsP₆ was modelled into the density and is likely coordinated by five lysine residues (Lys2, Lys26, Lys284, Lys287, Lys288).

this contact site, one tryptophan residue (Trp721) from ICL4 is wedged between two hydrophobic residues (Phe111 and Trp114) of SPX helix α 3. This interaction is not observed in the absence of substrates, since the SPX domain is not resolved in this area.

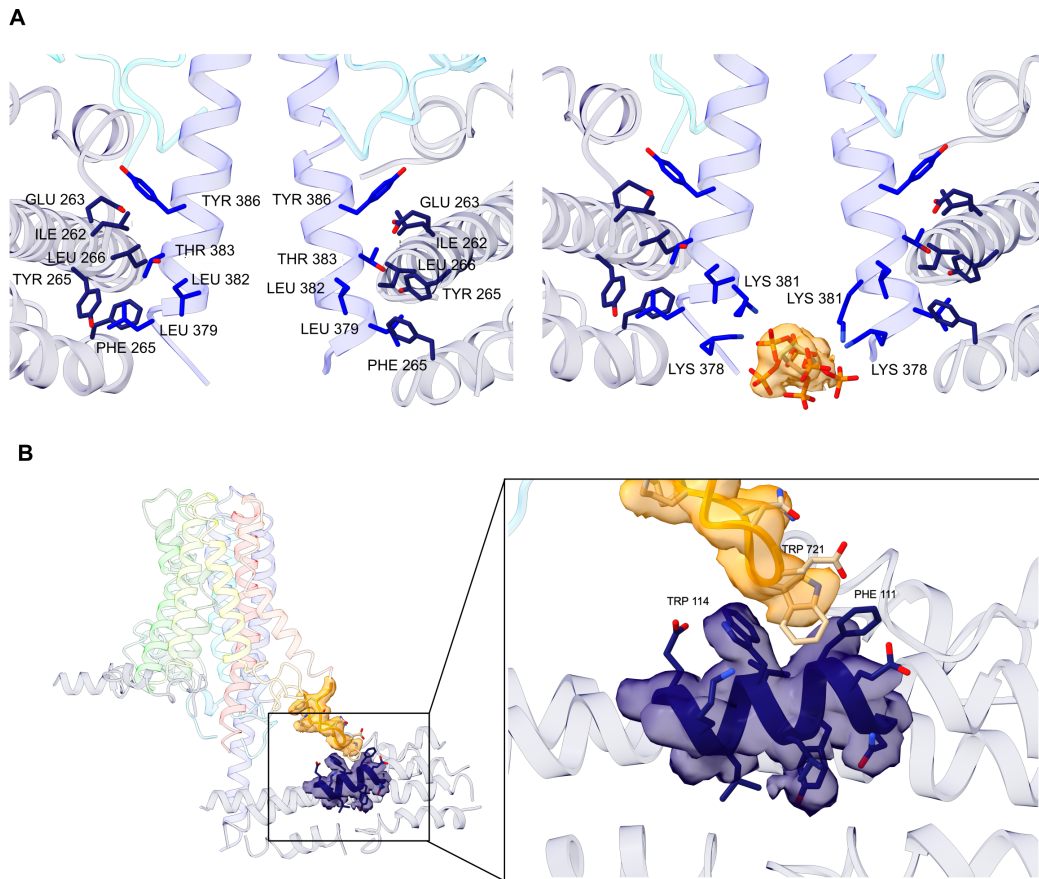


Figure 37: Contacts between TM and SPX domain and a putative additional InsP_6 binding site. (A) The SPX domain and TM1 interact mainly via hydrophobic sidechain interactions. An additional non-protein density was observed between the cytoplasmic ends of opposite TM1s at the dimer interface. Based on the size of the density and the proximity of conserved lysine residues (Lys378, Lys381) from both TM1s, InsP_6 was modelled into the density. (B) Contacts between SPX domain and ICL4. Trp721 of ICL4 is wedged between Trp114 and Phe111 of the SPX domain.

3.2.9 Expression and purification of HsXpr1

In addition to Syg1 proteins from different yeast species, also the human phosphate exporter Xpr1 was heterologously expressed in *S. cerevisiae*. Although HsXpr1 was successfully expressed, the protein was unstable during purification under different tested conditions, resulting in protein aggregation and disassembly of the putative dimeric assembly. To overcome this problem, the protein was homologously expressed in HEK293 GnTI- cells using the BacMam system.

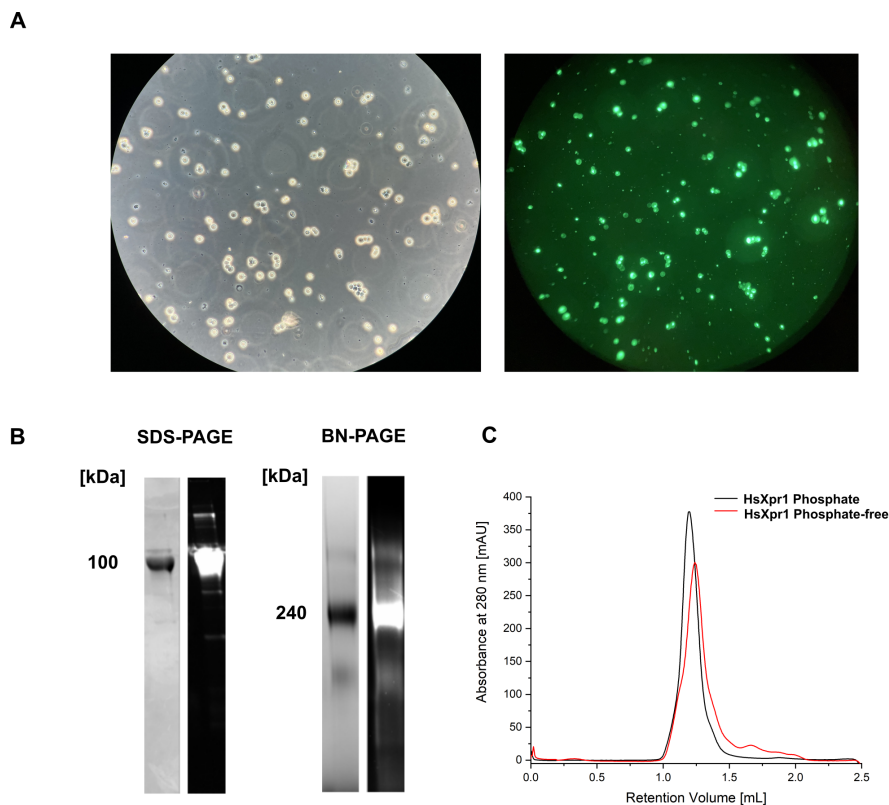


Figure 38: Expression and purification of HsXpr1 from HEK293 GnTI- cells.(A) HEK cells 72 h after induction, as seen in the bright field (left) and fluorescence channel (right). (B) SDS-PAGE and BN-PAGE analysis of purified HsXpr1. Dark bands on white background are Coomassie-stained gels and bright bands on black background are visualized by in-gel GFP fluorescence. (C) SEC profiles of HsXpr1 purified in the presence and absence of phosphate. Elution peaks around 1.25 mL correspond to dimeric HsXpr1.

HsXpr1 was expressed as C-terminal GFP fusion protein to quickly assess expression levels. Fluorescence microscopy images of HEK cells, 72h after induction, confirmed high protein expression levels (Figure 38A). Different detergents were tested for their solubilization efficiency and their effect on protein stability, as described for Pho90 and Syg1. HsXpr1 purified in DDM/CHS was pure, monodisperse and dimeric, but showed

massive preferential orientation and aggregation on vitrified cryo-EM grids. Therefore, DDM/CHS was replaced by LMNG/CHS in the final steps of protein purification for cryo-EM, which resolved the problem of preferred orientation and aggregation during vitrification. The purified protein samples showed a single band around 100 kDa on a SDS-PAGE gel, corresponding to the molecular weight of HsXpr1-GFP (108 kDa) and a monodisperse peak in the SEC profile, both in the presence and absence of phosphate (Figure 38). BN-PAGE analysis revealed that HsXpr1 forms dimers in solution as seen for homologous ScSyg1.

Purified HsXpr1 was analyzed by negative-stain EM and showed uniformly sized particles, confirming good sample quality. Different sample vitrification conditions were tested and cryo-EM grid quality was assessed by recording small datasets using a Glacios microscope, operating at 200 kV and equipped with a Falcon 3 camera. An initial small dataset was recorded and processed, resulting in 2D classes and 3D reconstructions that are reminiscent of ScSyg1 classes and show a dimeric arrangement with recognizable secondary structure features (Figure S3).

3.2.10 High-resolution cryo-EM data acquisition of HsXpr1

HsXpr1 datasets were recorded in the absence and presence of phosphate on a 300 kV Titan Krios G4i microscope. In total, 15,329 movies were recorded in the presence of phosphate and 21,128 movies in the absence of phosphate, with a total electron dose of $65 \text{ e}^- / \text{Å}^2$ and a defocus range of $-0.8 - -2.3 \text{ μm}$ (Table 9, Material and Methods). The datasets were processed in CryoSPARC (Figure 39 and Figure 40). First, the recorded movies were motion-corrected and Ctf-estimated. Particle picking was performed using multiple picking strategies (CryoSPARC's blob picker and pretrained template picker as well as Topaz). After extraction, the particle stacks were cleaned by multiple rounds of 2D classification. The 2D classes show different angular views of the protein with clear secondary structure elements and resembled the observed classes of ScSyg1. *Ab initio* 3D reconstruction of multiple independent classes and subsequent heterogeneous refinement further removed broken particles. Non-uniform refinements of phosphate-bound HsXpr1 resulted in a map with an overall resolution of 3.45 Å. For phosphate-free HsXpr1, an additional round of 3D classification (3 classes) was performed and subsequent non-uniform refinement yielded a map with an overall resolution of 3.01 Å. Both maps were sharpened using DeepEMenhancer. The final maps revealed the transmembrane part in detail, but no well-defined density for the SPX domain was present in either map.

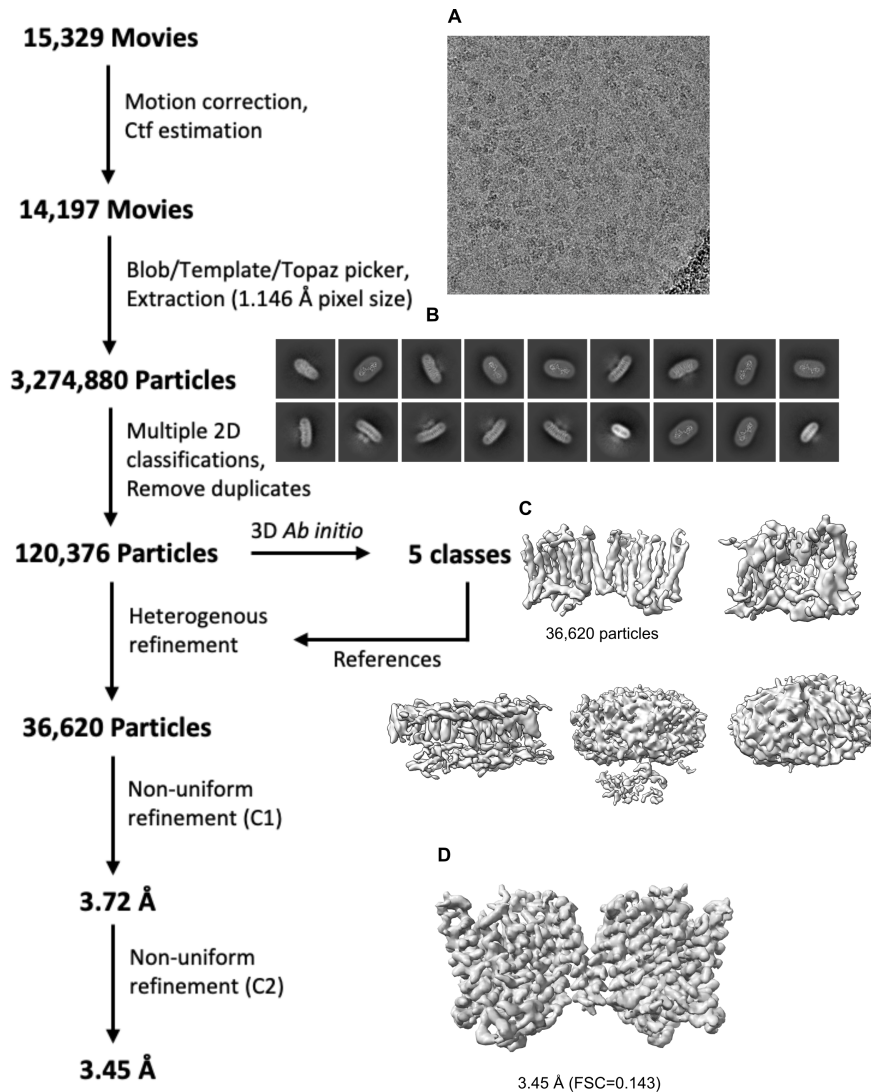


Figure 39: Processing scheme of HsXpr1 in the presence of phosphate. The cryo-EM processing pipeline to obtain 3D reconstructions of HsXpr1 is shown on the left. A representative micrograph (A), final 2D classes (B) and all *ab initio* models (C) are displayed. The final map (D) after non-uniform refinement with C2-symmetry applied is shown at the bottom.

3.2.11 Structures of HsXpr1

The overall fold of HsXpr1 resembled the fold of ScSyg1 (Figure 41). The dimer dimensions are 110 x 50 x 40 Å (in the phosphate-bound structure) and each monomer consists of 10 transmembrane helices. The phosphate-bound structure is a C2-symmetric dimer and both monomers are tilted slightly, by approximately 10° in relation to the theoretical membrane plane.

The dimer interface is formed exclusively by helix TM1, as seen for the homologous

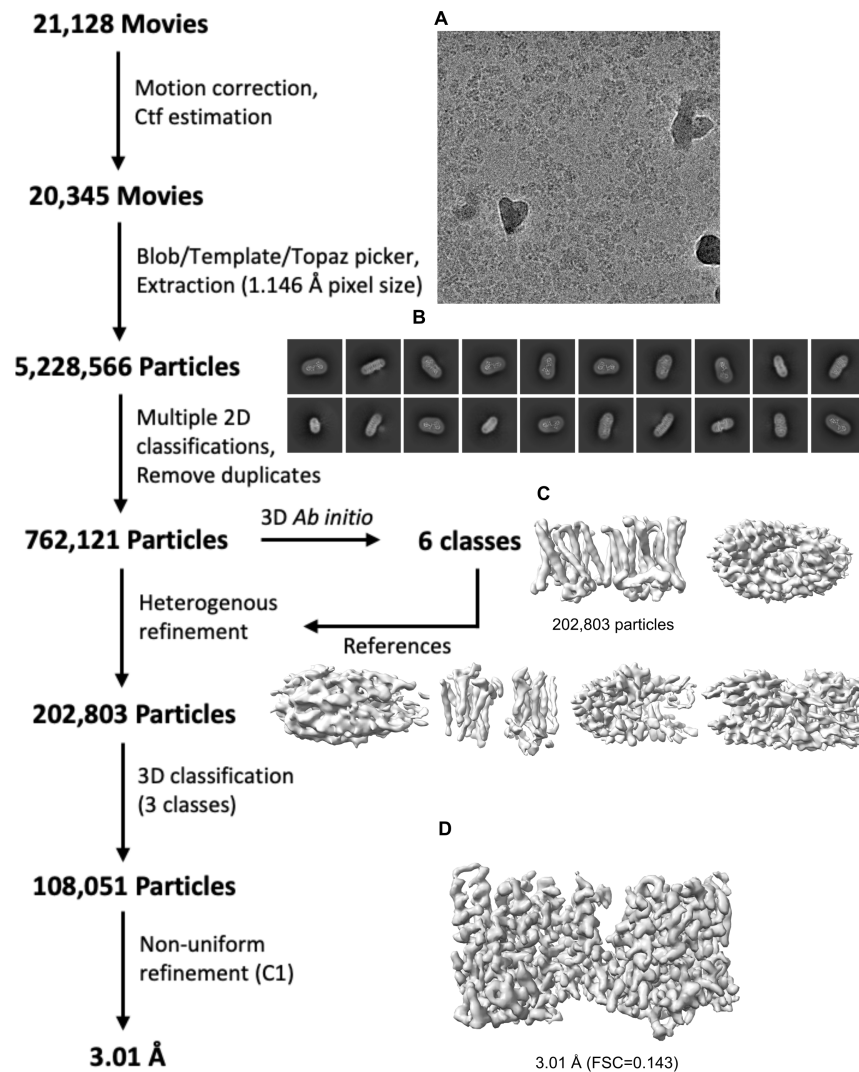


Figure 40: Processing scheme of HsXpr1 in the absence of phosphate. The cryo-EM processing pipeline to obtain 3D reconstructions of HsXpr1 is shown on the left. A representative micrograph (A), final 2D classes (B) and all *ab initio* models (C) are displayed. The final asymmetric map (D) after non-uniform refinement is shown at the bottom.

ScSyg1. Helices TM2-TM5 also form a hydrophobic pocket at the inner leaflet of the membrane. Helices TM5-TM10 are organized into a six-helix bundle, forming the putative phosphate translocation pathway. In the absence of phosphate, the HsXpr1 dimer adopts an asymmetric conformation with one protomer being rotated approximately 40° along the molecule axis that is perpendicular to the membrane plane. Interestingly, the rotation does not occur at the dimer interface of TM1, but TM2-TM10 are rotated while TM1 is in a similar position as in the symmetric dimer in the presence of phosphate. Overall, the individual monomers have almost identical structures as the symmetric phosphate-bound monomers (RMSD of 0.95 Å and 1.15 Å (TM2-TM10), respectively),

only their orientation to each other has changed. The asymmetric dimer is not tilted in relation to the membrane plane as seen for the phosphate-bound dimer, but sits planar within the membrane plane.

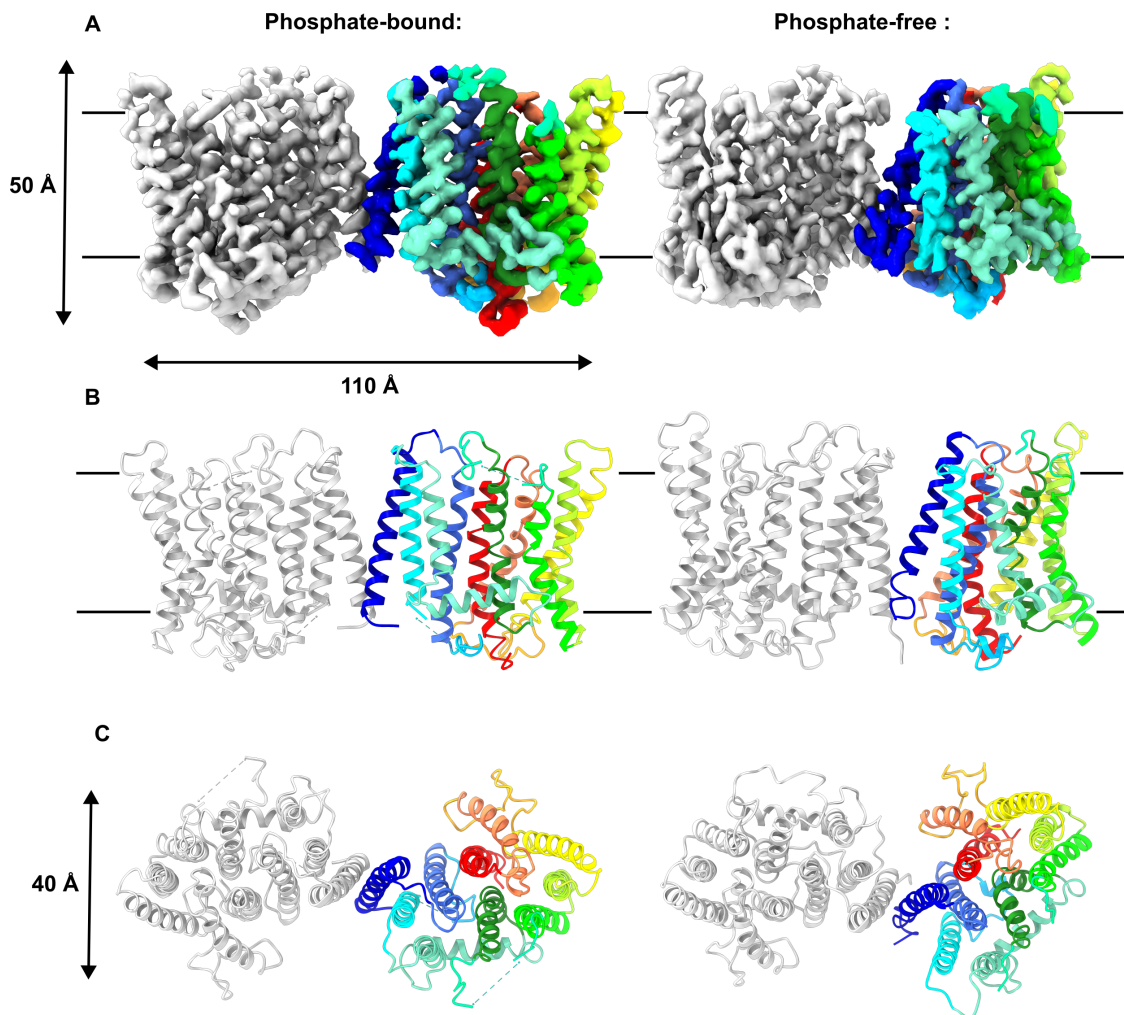


Figure 41: Overall structure of HsXpr1. (A) Side views of HsXpr1 maps in the presence (left) and absence (right) of phosphate. One protomer is colored in grey while the other one is colored by individual transmembrane helices (same coloring as for ScSyg1). (B) Corresponding models of HsXpr1. Individual transmembrane helices are numbered. Phosphate-bound HsXpr1 adopts a symmetric dimeric assembly, while in the phosphate-free structure one monomer adopts a different orientation leading to an asymmetric dimer. (C) Top views of models. Both are turned by 90° in relation to (B).

Superposition of both HsXpr1 dimers illustrates the change in orientation of monomer, depending on the presence of phosphate (Figure 42). When comparing the structures of phosphate-bound HsXpr1 and ScSyg1, differences in dimer orientation, but also within the superimposed monomers are observed. The difference in the dimer orientation is mainly due to the tilted arrangement of HsXpr1 protomers in relation to the membrane

plane, while ScSyg1 sits planar within the membrane plane. Variations in the monomer architecture are mainly observed within loops and in the outer leaflet parts of helices TM1 and TM7-9.

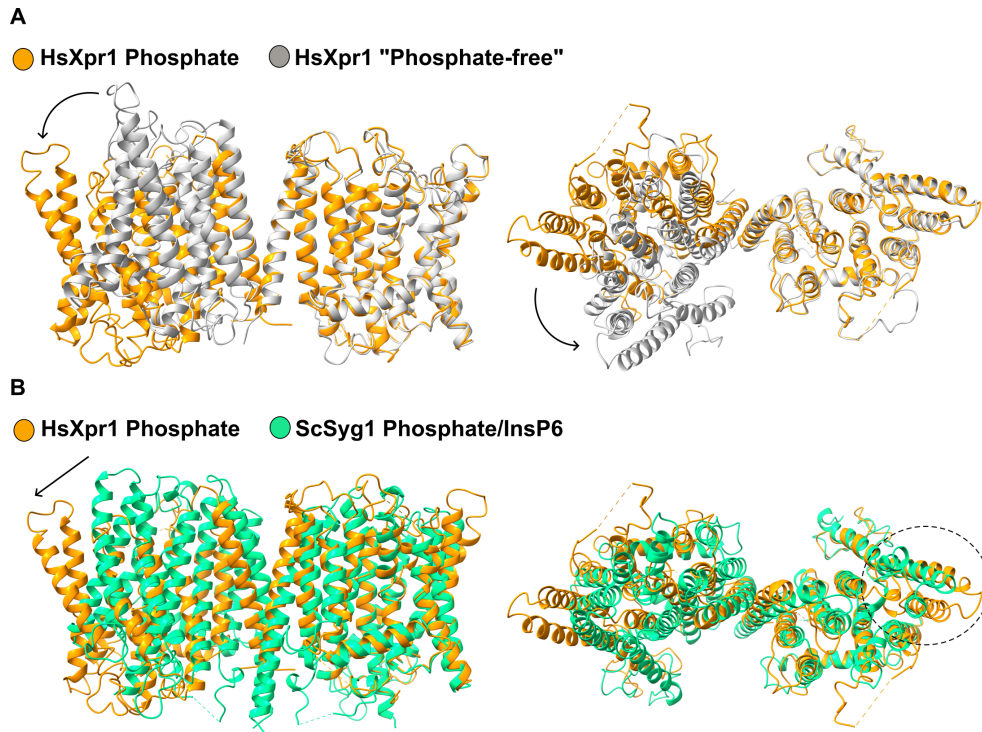


Figure 42: Comparisons of HsXpr1 structures. (A) Comparison of HsXpr1 structures in the presence and absence of phosphate. (B) Comparison of HsXpr1 and ScSyg1 structures in the presence of phosphate and phosphate/InsP₆. Structural differences are indicated by black arrows or circles.

3.2.12 Structural details of HsXpr1 and comparison to ScSyg1

Although orientations of monomers vary between the two HsXpr1 structures and are also different compared to ScSyg1, the dimer interfaces formed by TM1 are comparable (Figure 43). Especially, the sites of direct helix contact are conserved both in sequence and structure. In HsXpr1, Gly238 (Gly407 in ScSyg1) and Gly242 (Gly411 in ScSyg1) allow for very close helix packing and hydrophobic interactions of the surrounding hydrophobic sidechains in a glycine-zipper like fashion.

HsXpr1 also forms a hydrophobic pocket within the inner leaflet of the membrane, which is accessible from the cytoplasm and also has a lateral opening above the lateral helix TM4a (Figure 43C). This pocket is formed by helices TM2-5 and density for a lipid

3.2. The eukaryotic phosphate exporters Syg1 and Xpr1

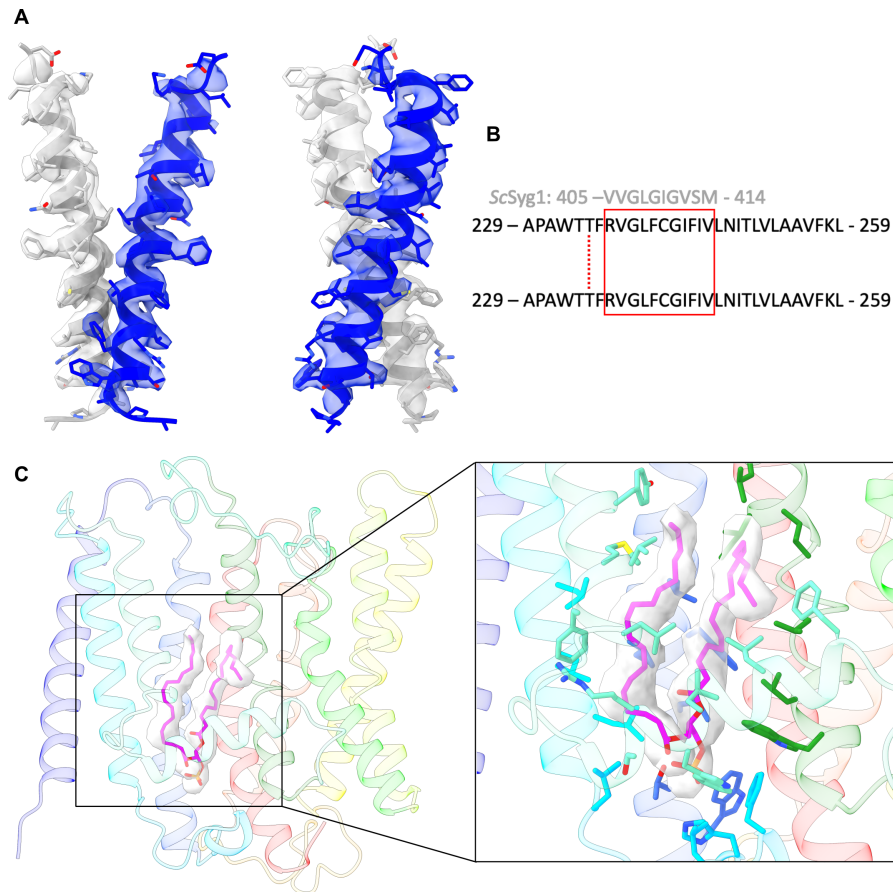


Figure 43: HsXpr1 dimerization interface and lipid binding pocket. (A) The HsXpr1 dimer interface between TM1s from opposing protomers, colored in grey and blue, is restricted to a small area. The right representation is turned by 90° in relation to the left one. (B) Sequence of TM1 that is involved in the dimer interaction in a glycine-zipper like fashion (red box) compared to the same motif in ScSyg1. Thr234 sidechains also show direct contacts (dotted red line). (C) Overview of the HsXpr1 lipid binding pocket (left). The pocket is formed by helices TM2-5 within the inner leaflet of the membrane. Cryo-EM density for the lipid is shown in grey. A close-up view shows interactions between the lipid and HsXpr1 residues (right).

molecule was observed within the pocket. As in ScSyg1, the hydrophobic tails of the lipid protrude into this pocket and interact with several hydrophobic residues. However, no basic sidechains are present to coordinate the phosphate group as seen in ScSyg1, since none of these basic sidechains are conserved in HsXpr1 or in other eukaryotic phosphate exporters. TLC analysis of co-purified lipids did not identify any specific lipids. Also, the density for the lipid headgroup is not resolved well enough to identify a specific class of phospholipids. Thus, PA was modelled into the lipid density as an default lipid molecule.

As in ScSyg1, helices TM5-10 of HsXpr1 form a six-helix bundle with the putative substrate translocation pathway in its center (Figure 44). This pathway is accessible from

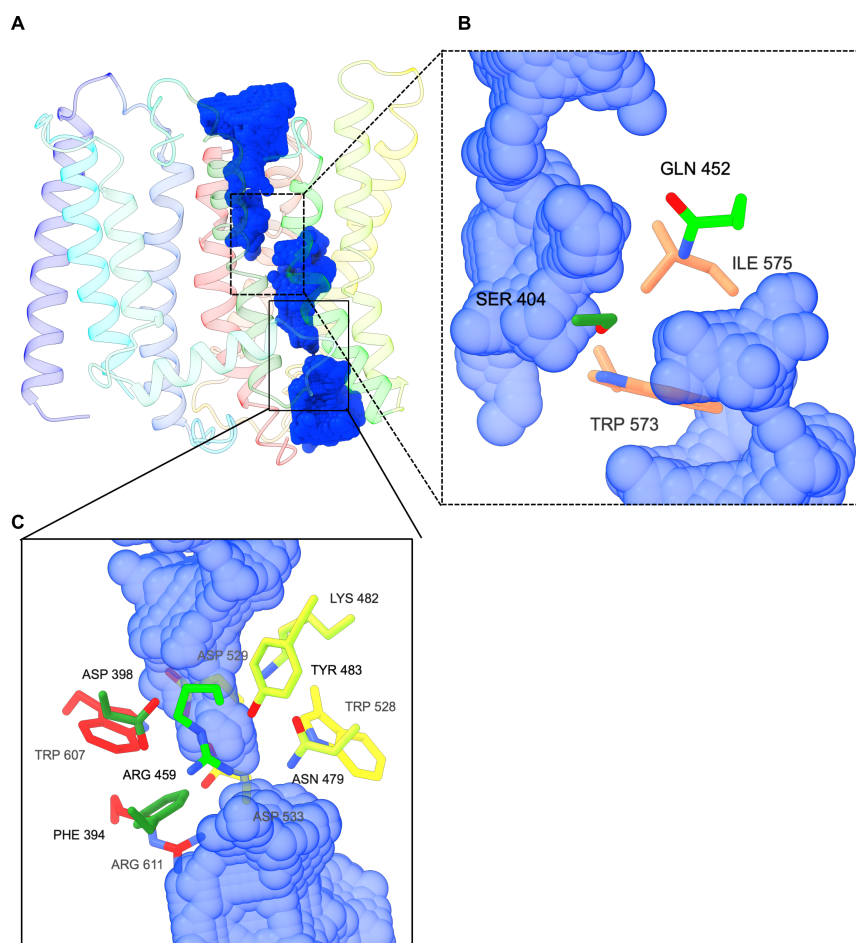


Figure 44: Putative phosphate translocation pathway in HsXpr1. (A) Overview of the putative translocation pathway, spanning the transmembrane part of HsXpr1. The interior pathway surface was calculated using Hollow-1.3 (blue surface). (B) The pathway is interrupted by Trp573 and Ile575 of TM9 within the center of the helix bundle. (C) The translocation pathway shows a narrow stretch close to the cytoplasmic exit. Charged and bulky sidechains point towards the interior of the pathway leading to its narrowing.

both sides of the membrane, but has a constriction close to the cytoplasmic end and is interrupted in proximity to the extracellular side. At the constriction site bulky (Phe394, Tyr483, Trp528, Trp607) and polar/charged (Asp398, Arg459, Asn479, Lys482, Asp529, Asp533, Arg611) residues are in close proximity leading to a narrowing of the translocation pathway at this position. As in ScSyg1 two conserved aspartate and one asparagine residues (Asp398, Asn479, Asp533) are present at the narrowest stretch of the pathway and come into close contact (Asn479-Asp533: 5.7 Å, Asp398-Asp533: 5.6 Å). While in ScSyg1 the translocation pathway is not accessible from the cytoplasmic side due to the closure by the SPX loop, it is accessible in HsXpr1 since no large SPX loops are present in HsXpr1. Also in contrast to ScSyg1, where the translocation pathway is continuous

3.2. The eukaryotic phosphate exporters Syg1 and Xpr1

from the phosphate binding sites to the extracellular side, it is blocked in the middle of the HsXpr1 pathway. The interruption of the translocation pathway in HsXpr1 is clearly different from the ScSyg1 structures. Here, Trp573 (and Ile575) of TM9 in particular are located directly within the putative translocation pathway, leading to its interruption. This is due to a missing kink in TM9 of HsXpr1 compared to ScSyg1 where the upper part of this helix is pointing away from the translocation pathway (Figure 45). Instead, TM9 of HsXpr1 extends into the center of the helix bundle, resulting in the positioning of Trp573 and Ile575 within the pathway. A comparison of these residues to the corresponding ones in ScSyg1 (Trp748 and Val750) shows that they are located outside of the translocation pathway in ScSyg1. Along with this change in TM9 conformation, helices TM7 and TM8 of HsXpr1 are shifted outwards compared to these helices in ScSyg1. This outward movement is likely necessary for TM9 to assume its new position.

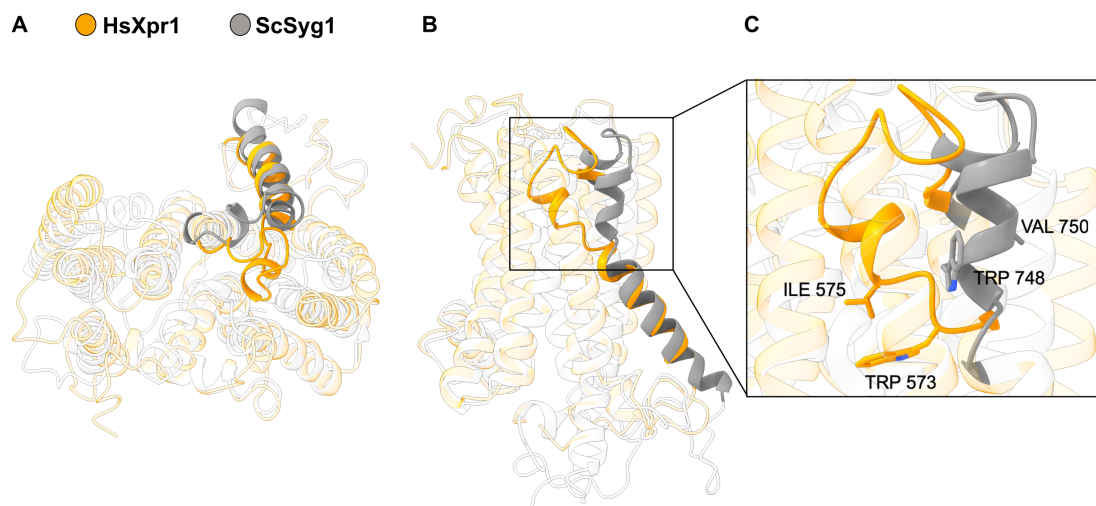


Figure 45: Different conformations of TM9 in HsXpr1 and ScSyg1. (A) Comparison of HsXpr1 (orange) and ScSyg1 (grey) monomers with highlighted helix TM9 and ECL5, as seen from the extracellular side. (B) Same as (A) but rotated by 90° and seen along the membrane plane. While TM9 adopts a kinked conformation in ScSyg1, it does not in HsXpr1. (C) Due to the missing kink in TM9 Trp573 and Ile575 occupy a position within the translocation pathway. Homologous residues in ScSyg1 (Trp748 and Val 750) are located outside the translocation pathway.

In the presence of phosphate, some additional weak density is present in the middle of the translocation pathway (Figure 46). This density is interpreted as a phosphate ion, which is coordinated by the conserved residues Asp529, Lys482, Arg570 and Arg603. The binding site is located just above the narrow constriction site and the coordinating residues belong to helices TM7-10. Interestingly, only this one phosphate ion was identified, whereas in substrate-bound ScSyg1 two phosphate ions are present within

the translocation pathway. When comparing the binding sites, it becomes clear that the binding site in HsXpr1 is different from the ones observed in ScSyg1. Arg570 and Arg603 (Arg745 and Arg775 in ScSyg1) are the only residues that are involved in phosphate coordination in both exporters. However, the positions of the coordinated phosphate ions in HsXpr1 and ScSyg1 are approximately 4 Å apart, with the phosphate ion in ScSyg1 (P2) located closer to the extracellular end of the translocation pathway. While several additional small densities are observed in the ScSyg1 maps that can be interpreted as water molecules, no such densities are present in HsXpr1 maps due to the lower overall resolution.

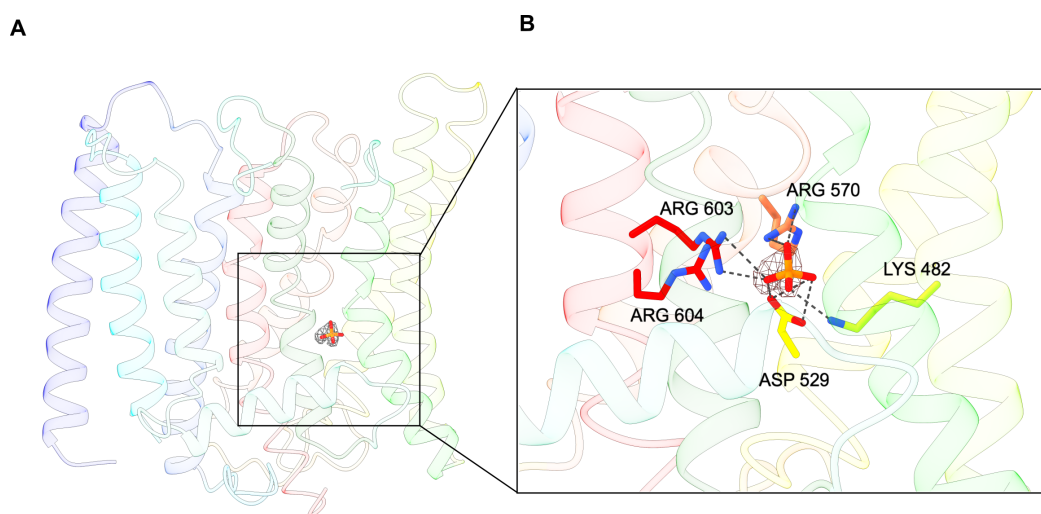


Figure 46: Phosphate binding site in HsXpr1. (A) Overview of the phosphate binding site within the translocation pathway of HsXpr1. Cryo-EM density around the phosphate is shown as grey mesh. (B) Close-up view of the phosphate binding site as indicated by a black box in (A). Charged sidechains of Lys482, Asp529, Arg570 and Arg603 are coordinating the phosphate ion.

3.2.13 The SPX domain of HsXpr1

The soluble SPX domain is not well-resolved in the two HsXpr1 maps. However, at lower threshold levels, some additional density appears at the cytoplasmic side of phosphate-bound HsXpr1 (Figure 47). Yet, this density does not resemble the overall fold of the SPX domain as observed in the ScSyg1 structure or in crystal structures of the SPX domain from HsXpr1. The poorly resolved SPX domain density is likely caused by its intrinsic flexibility relative to the rigid TM part. The same can be observed in all maps of the phosphate importer ScPho90 and to a lesser degree in the map of substrate-free ScSyg1. Since the addition of InsP₆ improved the resolution of the SPX domain of ScSyg1, the same was attempted for HsXpr1. However, HsXpr1 did not behave well in the pres-

ence of InsP_6 in vitrified ice and showed aggregation, preferential orientation and low abundance in the grid holes. So far, these problems have not been resolved, impeding structural elucidation of InsP_6 -bound HsXpr1 by cryo-EM.

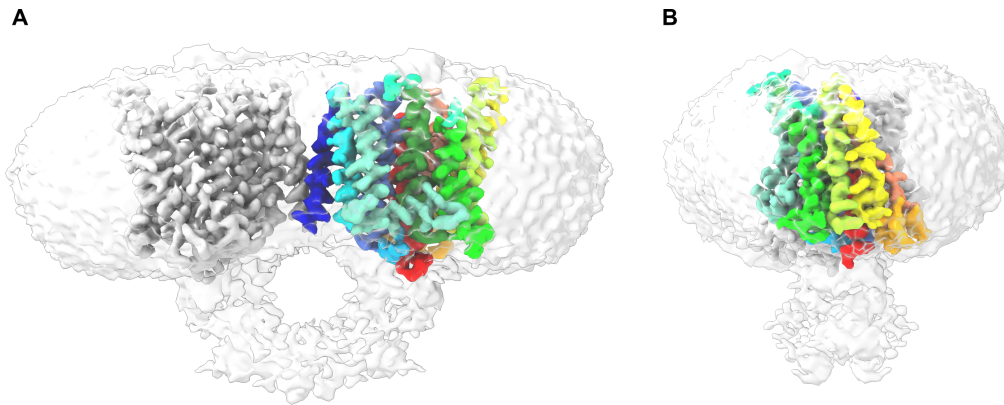


Figure 47: SPX density of HsXpr1. (A) Cryo-EM density of phosphate-bound HsXpr1 at high (grey/rainbow) and low (transparent grey) threshold levels. Density for the soluble SPX domain is visible at a low threshold level below the detergent micelle. (B) Same map representation turned by 90° in relation to (A).

3.2.14 The HsXpr1 dimer with inverted monomers

During data processing of the phosphate-free HsXpr1 dataset, an additional class of particles was identified. At first glance, 2D classes differed significantly from the usual 2D classes of HsXpr1. They indicate a putative transmembrane protein with C2-symmetry and 10 TM helices, which are organized into two helix bundles without direct contact between them (Figure 48A). Further refinement resulted in a final C2-symmetric map with an overall resolution of 4.0 Å. Since the individual ten-helix assemblies showed high similarity to HsXpr1 monomers, HsXpr1 was fitted into each one and matched almost perfectly. Surprisingly, however, one of the monomers is inverted in its topology compared to the other one, meaning that it was flipped by 180° within the membrane plane (Figure 48B). Whether this HsXpr1 assembly has a physiological relevance is not clear, but membrane proteins with inverted topology are very uncommon. Therefore, this assembly might have formed during solubilization and purification and does not represent a physiological state of the protein, thus analysis of the structure was not prioritized.

3.2.15 Phosphate transport mediated by HsXpr1 and ScSyg1

To evaluate the phosphate transport activity of phosphate exporters ScSyg1 and HsXpr1, both proteins were reconstituted into liposomes. Preformed liposomes (40 % POPC, 30 % DOPE, 30 % POPG + 10 % Cholesterol (w/w)) were destabilized by Triton-X-100

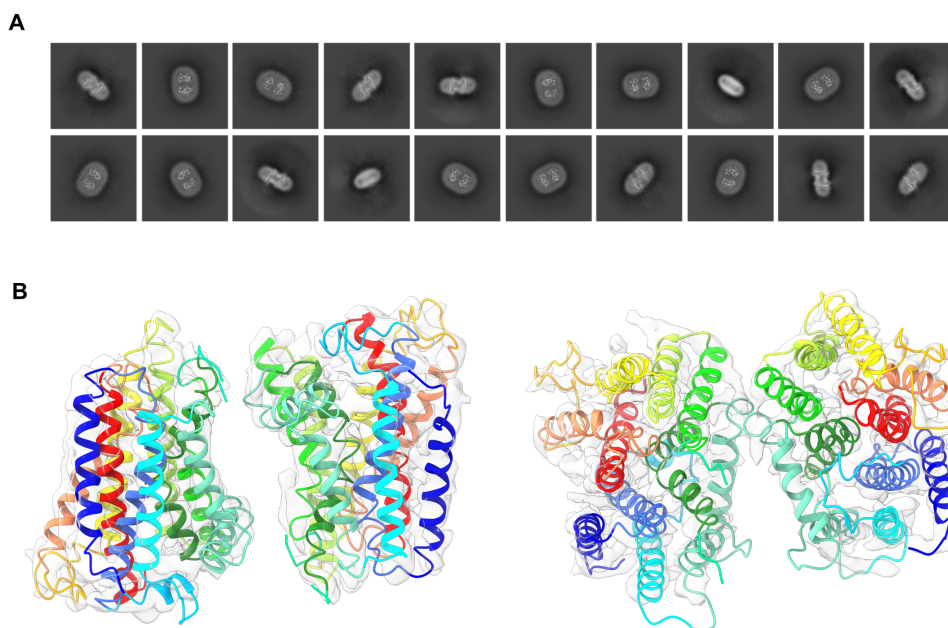


Figure 48: Alternative conformation of HsXpr1 dimer with inverted topologies. (A) 2D classes of HsXpr1 in the absence of phosphate with a divergent fold. (B) Final map (transparent grey) and fitted HsXpr1 models (rainbow). One of the HsXpr1 monomers is inverted in its topology compared to the other one and monomers are not in direct contact.

addition and incubated with the protein samples, before the detergent was removed using Bio-beads. For transport measurements ^{33}P -labeled phosphate was used as reporter molecule.

Empty liposomes without reconstituted protein show no detectable phosphate transport activity with or without the addition of InsP_6 . In contrast, both ScSyg1- and HsXpr1-reconstituted liposomes show phosphate transport activity (Figure 49). The addition of InsP_6 during transport measurements results in a substantially increased transport activity for both transporters. The transport rates for both ScSyg1 and HsXpr1 are low in the absence of InsP_6 and are almost linear over the whole reaction time (60 min). Under these conditions ScSyg1 and HsXpr1 show comparable transport rates of 0.11 ± 0.02 and $0.07 \pm 0.03 \text{ nmol} * \text{mg}^{-1}\text{protein} * \text{min}^{-1}$, respectively. Through the addition of InsP_6 the overall transport activity and the initial transport rates increase clearly. The initial transport rates are linear for about 20 min and amount to $0.51 \pm 0.19 \text{ nmol} * \text{mg}^{-1}\text{protein} * \text{min}^{-1}$ for ScSyg1 and $0.28 \pm 0.09 \text{ nmol} * \text{mg}^{-1}\text{protein} * \text{min}^{-1}$ for HsXpr1.

3.2. The eukaryotic phosphate exporters Syg1 and Xpr1

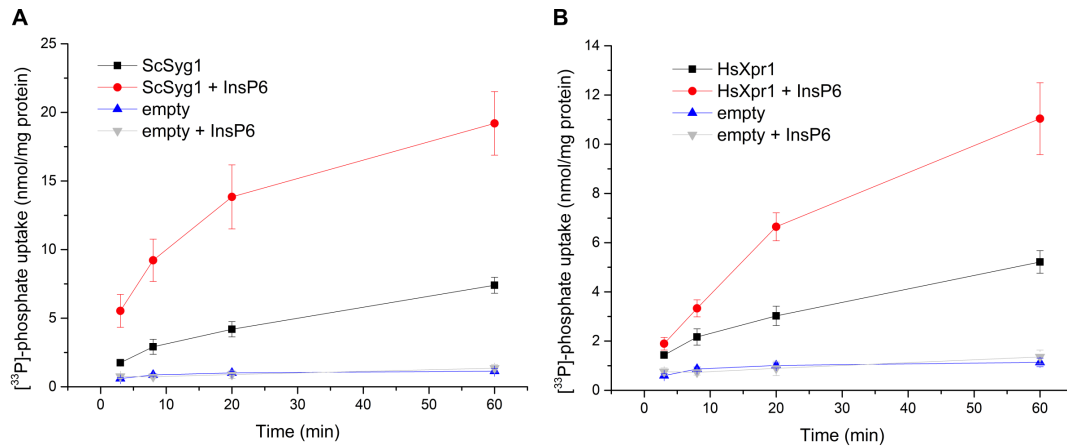


Figure 49: Functional characterization of HsXpr1 and ScSyg1. Uptake of ^{33}P -phosphate by ScSyg1 (A) and HsXpr1 (B) into reconstituted liposomes. Control transport experiments were performed with empty liposomes. The addition of InsP_6 leads to an increased transport activity of ScSyg1 and HsXpr1. Mean values and standard deviations are shown ($n=3$).

4 Discussion

This discussion chapter is divided into four parts. In the first part, the acquired and analyzed cryo-EM data is discussed in the light of recent developments in the field of cryo-EM. The second and third parts discuss the respective results obtained for the low-affinity phosphate importer Pho90 and the phosphate exporters Syg1 and Xpr1 in a biological context. In the last chapter, the findings are summarized and future directions are discussed in a brief outlook.

4.1 Electron cryo-microscopy in structural biology of membrane proteins

Thanks to recent hardware and software developments in the field of cryo-EM, both the number of protein structures and their resolution have increased over the last several years (Callaway, 2020). These improvements also aided in the structural determination of small membrane proteins, which have long been difficult targets for structural studies. In this thesis, structures of small membrane proteins have been determined by cryo-EM up to a resolution of 2.2 Å due to these recent improvements. All high-resolution datasets were recorded using a Titan Krios G4i microscope, in which several new hardware improvements have been implemented. It is equipped with a cold-FEG electron source, which emits electrons with high spatial and temporal coherence. This increases the signal-to-noise ratio (SNR) at high spatial frequencies, leading to more high-resolution information within recorded micrographs (Nakane et al., 2020). These advantages mainly make a difference for resolutions better than 2 Å (Nakane et al., 2020), but have also shown improvements in map quality of reconstructions with lower nominal resolutions.

The microscope also features a new Selectris energy filter, which is very stable over prolonged data acquisition times, allowing narrow slit widths (Kahl et al., 2019). This allows for efficient filtering of inelastically scattered electrons, which contribute to background noise. Especially for small proteins decreased noise levels are beneficial, since they are difficult to identify in low contrast cryo-EM images (Wu et al., 2020). The improved

image contrast also enables the acquisition of images with lower defocus values, as the image contrast in cryo-EM depends also on the defocus. Although higher defocus values improve image contrast, they also lead to an attenuation of high frequency information, which in turn limits the resolution. Therefore, recording images at lower defoci due to the improved SNR by efficiently removing inelastically scattered electrons, is directly beneficial for the resolution of small membrane proteins. The defocus values used in the acquired datasets were as low as $-0.5\ \mu\text{m}$, which is very low for small membrane proteins. Nevertheless, automated particle picking successfully picked particles even from low defocus micrographs and these particles likely aided in achieving resolutions up to $2.2\ \text{\AA}$.

Additionally, the microscope is equipped with a new Falcon 4 camera. With an increased frame rate of 284 Hz and an improved counting algorithm, the camera is able to detect electron events at sub-pixel accuracy using short exposure times (Nakane et al., 2020). The acquired videos are stored in an electron-event representation (EER) format, allowing for flexible dose fractionation during data processing. Taken together, this detector enables the acquisition of top-quality images with high throughput. Using the Falcon 4 camera together with aberration-free image shift (AFIS), datasets were recorded at a speed of approximately 400 movies per hour in EER format. This resulted in large datasets of high-quality images which was one of the main reasons for high-resolution reconstructions.

Besides new hardware technology, advances in data processing software have also helped to resolve cryo-EM structures of challenging proteins. Especially for small, flexible and locally disordered proteins, new algorithms have helped in determining their 3D structure. CryoSPARC's non-uniform refinement accounts for spatial variability, as in detergent micelles, to improve the resolution of ordered protein features within the micelles (Punjani et al., 2020). This refinement algorithm proved to be the best for all structures elucidated here and was used to refine the final maps of each protein. Other new algorithms helped in dealing with the intrinsic flexibility of proteins or individual domains (Punjani et al., 2021). 3D variability analysis in CryoSPARC was used either to separate different states of the ScPho90 transport domain or to select ScSyt1 particles with well-ordered SPX domains to subsequently improve the resolution of this domain. Other processing strategies to cope with particle heterogeneity, such as RELION's 3D classification (Scheres, 2016) with or without alignments were also tried, but proved to be less successful for the datasets presented here. In general, multiple processing strategies should be tested, as each individual dataset might benefit from different approaches.

The recent advances in the field of cryo-EM listed here have aided in the structure determination of difficult biological specimen like small membrane proteins. However, the major limiting factor in both the number of structures and the reported resolution for difficult target proteins remains sample preparation (Weissenberger et al., 2021). Excessive screening of expression, purification and freezing parameters is necessary to obtain high-quality samples, which can be used for structure determination. Here, all proteins were optimized and analyzed by SEC, SDS-PAGE, BN-PAGE and negative-stain EM as well as the screening of multiple grids in our 200 kV Glacios microscope. This resulted in optimized specimens that were the basis for all the high-resolution structures in this thesis.

Using optimized protein samples and a state-of-the-art electron microscope, what is limiting the resolution? One main limiting factor, even though optimized for structure determination remains the protein sample itself. Most proteins exist in different conformational states or contain domains with inherent flexibility, which limits the achievable resolution of these parts of the protein (Chari et al., 2023). For example, the SPX domain of ScPho90 only attained a modest resolution most likely due to its high conformational flexibility. Strategies to overcome this flexibility include, but are not limited to, the addition of binding partners that might stabilize discrete states or the deletion of flexible linkers to increase overall rigidity. The addition of InsP₆ increased the rigidity of the SPX domain of ScSyt1 and thereby facilitated its structure elucidation. InsP₆ was used as it is a stable and commercially available derivative of InsPPs and has also been shown to bind to SPX domains (Wild et al., 2016). An additional factor limiting sample quality is the interaction of the specimen with the air-water interface which can lead to protein denaturation (D'Imprima et al., 2019). Although not many "broken" particles were observed in the 2D classes of all datasets, it can be difficult to detect classes of partially denatured small membrane proteins, since they are often difficult to align. For example, in the 2D classes of HsXpr1 datasets, many particles appeared blurred and only a small subset of particles showed high-resolution features and ended up in the final reconstructions. Besides the interaction with the air-water interface, low protein stability may have led to the loss of structural integrity of many particles. In general, the low number of well-defined particles is likely the main factor limiting the resolution of HsXpr1 to 3.0 Å. Continuous support films have been successfully used to overcome air-water interface interactions, but also have disadvantages especially for small proteins, as they increase background noise and reduce contrast (Grassucci et al., 2007; Pantelic et al., 2012). Hence, continuous support films were not the strategy of choice in this project.

Another known effect limiting resolution in cryo-EM is beam-induced motion, as the incident electron beam releases mechanical strains in the vitreous ice (Brilot et al., 2012). Recently, the development of ultrastable gold grids (HexAuFoil) was shown to limit specimen movement to less than 1 Å, resulting in nearly motion-free imaging (Naydenova et al., 2020). All cryo-EM datasets in this thesis were acquired using standard copper C-Flat grids. Even though modern motion correction programs can correct for most particle movement, initial frames with the most high frequency information due to the lowest radiation damage are down-weighted, because the largest particle motions occur in these frames. Therefore, motion-free imaging using newly developed HexAuFoil grids might be a promising strategy to improve the resolution of the presented structures further.

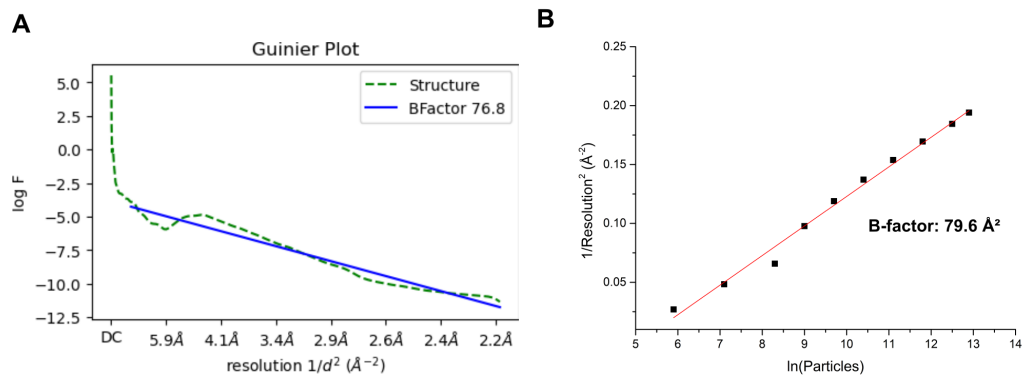


Figure 50: Determination of B-factors. B-factors for the ScSyt1 (phosphate/InsP₆) reconstructions. In the final NU refinement in CryoSPARC a B-factor of 76.8 Å was determined as seen in the Guinier plot (left). A B-factor plot using fractions of the same particle stack was prepared as comparison and the B-factor was estimated from the fitted slope (right).

A "brute-force" strategy to improve the resolution is to simply increase the number of particles by acquiring more data. The number of particles needed to obtain a respective resolution is described by an experimental B-factor (Rosenthal et al., 2003). The B-factor is an overall measure for the quality of the data and the lower it is, the less particles are needed to obtain a given resolution. The correlation between particle number and resolution becomes linear when plotting the logarithmic particle number against the reciprocal square of the resolution. As an example, the B-factor plot for the ScSyt1 (phosphate/InsP₆) map is shown in Figure 50. The slope of this linear plot corresponds to the B-factor and was 79.6 Å² which is close the B-factor calculated by CryoSPARC in the final NU refinement of this map which was 76.8 Å². Extrapolating from this plot,

approximately 3.6 million final particles would be required to improve the resolution up to 2 Å. Assuming a similar particles-per-micrograph number this would require roughly 120,000 micrographs which in turn would occupy a lot of microscope time and computer storage. Hence, improving data quality rather than increasing data quantity is the better strategy in improving the resolution of the cryo-EM structures reported in this thesis.

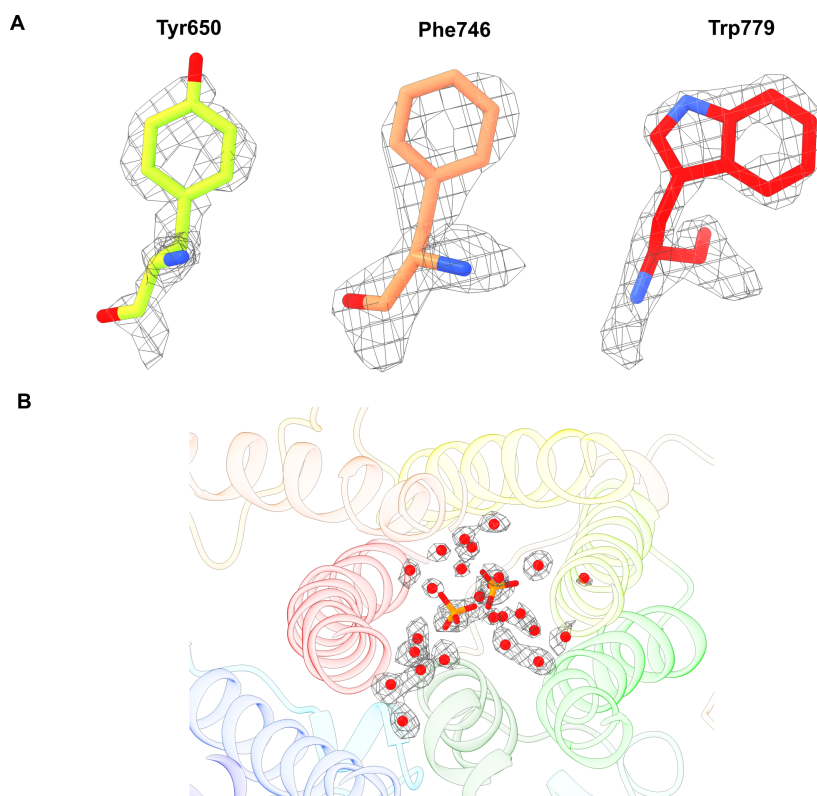


Figure 51: High resolution features of cryo-EM maps. Structural details of the final ScSyg1 (phosphate/InsP₆) map at 2.2 Å resolution. (A) Holes in the density of selected aromatic sidechains are visible. (B) In the putative substrate translocation pathway density for multiple water molecules is visible.

With the continuously improving resolution in cryo-EM, the question arises which resolution is required to answer specific biological questions. While at a resolution of approximately 5 Å or better secondary structures and the overall fold of the protein can be modelled confidently, resolutions of roughly 3.5 Å or better are needed to model sidechains and to recognize small bound ligands (Chari et al., 2023). The spatial arrangement of sidechains and ligands are very important to understand the function of a protein and its specific biological properties. At resolutions better than 3 Å, small sidechains and specific rotamers of larger sidechains can be modelled with higher confidence and at resolutions around 2.5 Å densities for solvent water molecules become visible and interpretable. The visualization of water molecules is very interesting, as they play important

roles in protein-catalyzed enzymatic reactions or in the transport of substrates. Resolutions of 1.5 Å and higher are necessary to visualize individual atoms, which is essential for the visualization of hydrogen-bonding networks or specific charge states of individual residues. The cryo-EM maps presented in this thesis have resolutions between 3.4 Å and 2.2 Å, which all allow for confident secondary structure and sidechain modelling. The highest resolution maps of ScPho90 and ScSyz1 (2.3 Å and 2.2 Å, respectively) show typical holes in the density of aromatic residues at high resolution and also many non-protein densities that can be interpreted as water molecules (Figure 51).

To address the questions of the underlying mechanisms of eukaryotic phosphate transport, the achieved resolutions are sufficient, since nearly all sidechains of the TM domains have been modelled with high confidence and bound substrates have been identified. Improving the resolution could help in resolving substrate protein interactions in more detail, visualize hydrogen-bonding networks or identifying alternative sidechains conformations. However, instead of improving the maximum resolution of individual maps, it would be more beneficial for the understanding of eukaryotic phosphate translocation mechanisms to elucidate different conformations of the proteins or to improve the resolution in highly flexible parts of the protein (such as the SPX domains). Furthermore, in addition to high-resolution structural data, also detailed functional analysis of proteins are important to interpret structural findings and to pinpoint underlying biochemical principles of the transport mechanisms.

4.2 The eukaryotic low-affinity phosphate importer

Pho90

4.2.1 Overall structure

Sequence alignments of low-affinity phosphate transporters with sequences of known protein structures using HHpred (MPI Bioinformatics Toolkit), revealed that they show the highest similarity to structures of the DASS family (Zimmermann et al., 2017). So far, structures of this transporter family are only available from tricarboxylate or dicarboxylate transporter like CitS, HsNaCT (SLC13A5) or LaINDY and VcINDY (Mancusso et al., 2012; Sauer et al., 2021; Wöhlert et al., 2015; Sauer et al., 2020). The cryo-EM structures of ScPho90 are the first of a phosphate transporter with a similar overall fold. A comparison of these different transporters is shown in Figure 52. The overall organization of the TM helices is very similar in all five structures, especially LaINDY, VcINDY and HsNaCT show a highly conserved fold in comparison to ScPho90. SeCitS shows a similar domain architecture, but the position of individual helices deviates from those of the other structures. Interestingly, nearly all published structures of NaCT and INDY are in a symmetric inward-open conformation, with both transport domains shifted towards the cytoplasm. The only published structure in a symmetric outward-open conformation is LaINDY (Sauer et al., 2020). Conversely, the ScPho90 structures presented in this thesis are in a symmetric outward-open conformation and a asymmetric conformation with one transport domain shifted towards the cytoplasm and one towards the extracellular side. The scaffold domain of both INDY proteins and HsNaCT superimpose nearly perfectly with the ScPho90 scaffold domain and the hydrophobic dimer interactions are also very similar in all three structures. The π -stacking interaction of opposing Trp721 (ScPho90) are also present in LaINDY (Trp339), VcINDY (Trp320) and HsNaCT (Trp408) while the other π -stacking interaction of opposing Trp498 (ScPho90) is not conserved. The helix bundle of the transport domain of the inward facing monomer in the asymmetric ScPho90 structure superimposes well with the inward-open structures of VcINDY and HsNaCT. The overall RMSD of the monomers are 3.29 Å (VcINDY) and 3.82 Å (NaCT) with the largest deviations in different loop conformations. When comparing the outward-open monomer of ScPho90 with VcINDY and HsNaCT, the transport domains do not match, since the helix bundle is shifted by 11 Å towards the extracellular side. This results in RMSD values of 8.62 Å (VcINDY) and 9.13 Å (NaCT) for the compared monomers. Comparing the outward-open monomer of ScPho90 with the LaINDY monomer shows that the helix bundles superimpose well and the positioning of all helical elements is conserved (Figure 52F). The overall RMSD is 4.34 Å with the largest deviations in different

loops. The structural similarity of ScPho90 with transporters of the DASS family suggests a similar substrate translocation mechanism, which is discussed in the following sections.

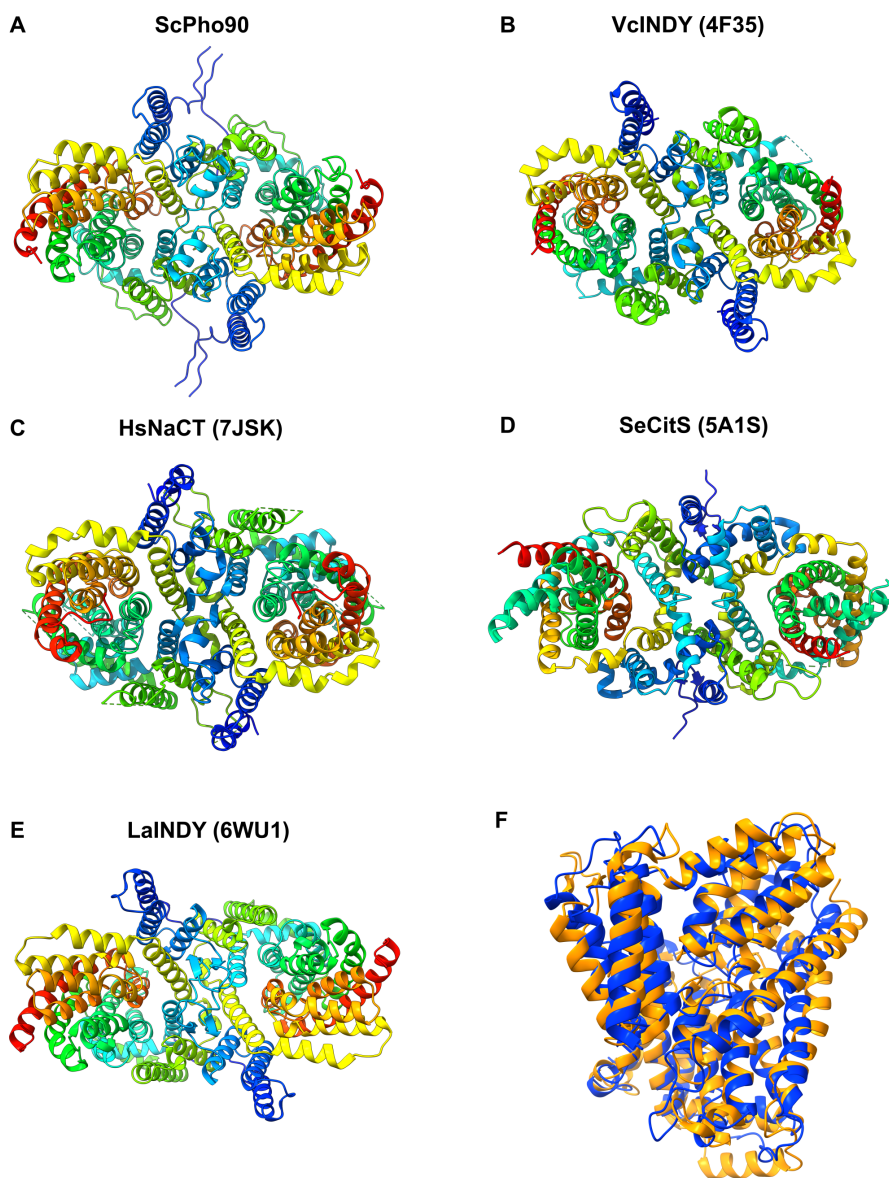


Figure 52: Comparison of ScPho90 with known homologous structures. (A-E) All proteins are represented as their biological dimeric assembly and each monomer is rainbow-colored from blue (N-terminus) to red (C-terminus). All structures show an overall conserved fold. Structures of VcINDY, HsNaCT, SeCitS and LaINDY were obtained from the PDB. (F) Comparison of outward-open monomers of ScPho90 (blue) and LaINDY (orange), turned by 90° in relation to (A-E).

Sequence alignment with other eukaryotic transporters also revealed that ScPho90 shares high homology with mammalian sodium sulfate symporters NaS1 (SLC13A1) and NaS2

(SLC13A4). Based on the sequence homology and chemical similarity of phosphate and sulfate, ScPho90 may serve as a model for NaS1/NaS2-mediated human sulfate transport. Using AlphaFold (multimer) (Evans et al., 2022) the dimeric structures of HsNaS1 and HsNaS2 were predicted and compared with the ScPho90 structure (Figure 53). As expected, the overall fold of NaS1/NaS2 and ScPho90 are nearly identical. Both NaS1 and NaS2 dimers are predicted to be in a symmetric inward-open conformation. This is likely due to the fact that most homologous proteins in the PDB (VcINDY, HsNaCT), which are used for AlphaFold structure prediction, are in this conformation. The main differences in the overall structures are long cytoplasmic protrusions of helices TM5b and TM6 in both NaS1 and NaS2 (not shown in Figure 53). The function of these protrusions has not been studied. Comparing the inward-open monomer of ScPho90 with NaS1 and NaS2 predicted monomers, showed that all TM helices match well with the largest deviations in helices TM6 and TM11b. The RMSD values (calculated without the cytoplasmic protrusions of NaS1 and NaS2) reflect the overall structural similarity with values of 3.98 Å (NaS1) and 4.21 Å (NaS2).

4.2.2 Phosphate binding and comparison with known phosphate transporter structures

The structure of ScPho90 in the presence of phosphate revealed substrate density within the outward-open binding pocket. Two sodium ions and one phosphate ion were assigned to these densities. The density for the phosphate ion within the binding pockets is weak. In general, cryo-EM density for negatively charged ions or residues has been found to be weak. This phenomenon has been examined in detail for glutamate and aspartate sidechains but also applies to non-protein residues (Allegretti et al., 2014; Fromm et al., 2015). Two effects have been described that contribute to the weak cryo-EM density of negatively charged residues: On the one hand a higher susceptibility to radiation damage (shown for glutamate and aspartate sidechains) results in signal loss over the exposure time, and on the other hand negative electron scattering factors of the negatively charged oxygen atoms result in generally weaker density for these atoms (Kühlbrandt et al., 1994; Yonekura et al., 2018). All datasets were recorded at pH 8 at which free phosphate ions are predominantly divalent negatively charged. This divalent negative charge results in weaker densities for phosphate ions, making their discrimination from water molecules based on the observed density more difficult.

So far, only two structures of phosphate transporters have been deposited in the PDB: TmPiT from the thermophilic bacterium *Thermotoga maritima*, which is a homologue of

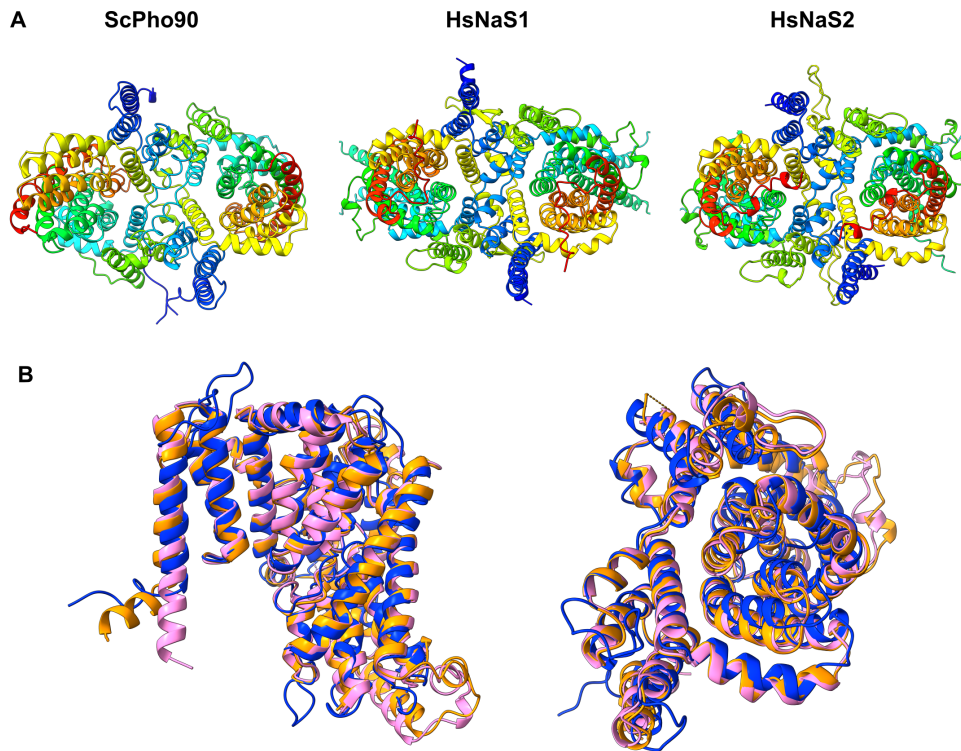


Figure 53: Comparison of ScPho90 with human sulfate transporters. Dimeric structures of HsNaS1 and HsNaS2 were predicted using AlphaFold. (A) All proteins are represented as their biological dimeric assembly and each monomer is rainbow-colored from blue (N-terminus) to red (C-terminus). (B) Comparison of ScPho90 (blue), HsNaS1 (orange) and HsNaS2 (pink) monomers in the inward-open state.

mammalian SLC20 phosphate transporters and the yeast high-affinity phosphate transporter Pho89 (Tsai et al., 2020) and PiPT from the fungus *Piriformospora indica*, a homologue of SLC22 and yeast high-affinity phosphate transporter Pho84 (Pedersen et al., 2013). Comparing the phosphate coordination in ScPho90 with coordination motifs in PiPT and TmPiT, shows clear differences (Figure 54). In all three structures the phosphate ion is coordinated by different polar residues, but in both PiPT and TmPiT, it is also coordinated by aspartate residues that were shown to be essential for binding and transport function (Pedersen et al., 2013; Tsai et al., 2020). In contrast, no potentially negatively charged residues are present in the binding pocket of ScPho90. While PiPT is a proton/phosphate symporter and Asp324 within its binding pocket is likely protonated and deprotonated during the transport cycle, TmPiT is also a sodium/phosphate symporter. In TmPiT both sodium ions are 4.5 Å away from the phosphate. So, as in ScPho90 they are not in direct contact with the phosphate ion, but are coordinated by aspartate residues. In addition, three histidine residues are in the vicinity of the binding

site, but do not coordinate the phosphate ion directly as seen for ScPho90. One could speculate that the absence of charged residues in the binding pocket of ScPho90 might reduce the affinity for phosphate compared to the high-affinity transporters. However, additional biochemical analysis is necessary to find out whether this is true.

The phosphate coordinating residues in ScPho90 are conserved throughout yeast low-affinity phosphate transporters (Figure S4). Mutation of coordinating residues Asn566 or Ser815 to alanine was shown to significantly diminish ScPho90-mediated phosphate uptake, highlighting their importance. Sequence alignment of ScPho90 with HsNaS1 and HsNaS2 shows that Asn566 and Ser815 are also conserved in human sodium sulfate symporters (Figure S5). Of the other coordinating residues, Gln605 is substituted by a threonine and His779 is substituted by an asparagine in both HsNaS1 and HsNaS2. These differences might explain the selectivity for sulfate over phosphate in these transporters. Since sulfate has a slightly larger ionic radius than phosphate (Jenkins et al., 1979), replacing Gln605 and His779 with smaller residues like threonine and asparagine might favor sulfate coordination. To verify this hypothesis, mutation of coordinating residues of ScPho90 and of the human sulfate transporters and subsequent determination of phosphate and sulfate affinities would be necessary.

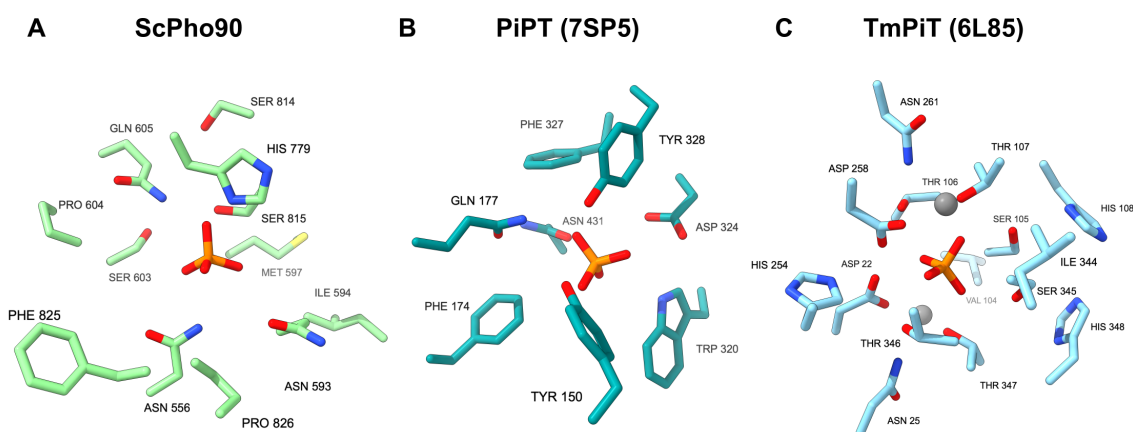


Figure 54: Comparison of phosphate coordination in phosphate transporters. Residues within a distance of 5 Å to the phosphate molecules are shown. Structures of PiPT (7SP5) and TmPiT (6L85) were obtained from the PDB.

The overall arrangement of the substrates within the binding pocket matches the one observed in the substrate-bound structures of homologues HsNaCT and VcINDY (Mancusso et al., 2012; Sauer et al., 2021). The phosphate ion is located within the center of the binding pocket and flanked by the two sodium ions, which are not in direct contact with phosphate. The distances between sodium and phosphate ions were 5.7 and

8.7 Å, respectively. The distances between sodium ions and citrate (HsNaCT) and succinate (VcINDY) were shorter, ranging between 4.5 and 6.0 Å, as citrate and succinate are larger molecules compared to phosphate. The similar arrangement of substrates is interesting, since substrate bound structures of HsNaCT and VcINDY are in inward-open conformations, while the substrate bound structure of ScPho90 is in an outward-open conformation. This indicates that no major structural rearrangements in substrate coordination take place during the transition from outward- to inward-open conformation in these transporters. To verify this hypothesis substrate-bound structures of the same protein in complementary conformations would be of interest.

4.2.3 Pho90 phosphate translocation mechanism

In the absence of phosphate, ScPho90 was elucidated in two different conformations - a symmetric outward-open conformation and an asymmetric state with one protomer in the inward-open conformation. These distinct conformations reveal aspects of the substrate translocation mechanism. Between both conformations, the transport domain rotates approximately 30° and shifts 11 Å (His779) from the exterior side to the cytoplasmic side, while the scaffold domain remains static. This movement results in the accessibility of the substrate binding pocket from opposite sides of the membrane in the distinct conformations enabling substrate binding on the extracellular side and release into the cytoplasm. The type of movement is reminiscent of an "elevator-type" mechanism, which has been described for several other transporters (Lee et al., 2013; Reyes et al., 2009; Wöhlert et al., 2015). Although individual elevator-type mechanisms differ slightly, the basic mechanism comprises a fixed scaffold domain and a moving transporter domain which slides as a rigid body through the lipid bilayer thereby alternating between outward- and inward-open states (Garaeva et al., 2020).

Based on the structures of ScPho90 presented here and the knowledge of elevator-type transport mechanisms of other transporters, a transport mechanism for low-affinity type phosphate transporter is proposed (Figure 55). Substrates bind to the transporter in the outward-open conformation, with the binding pocket being accessible from the extracellular site. Upon binding of sodium and phosphate ions, the transport domain moves towards the cytoplasm relatively to the rest of the protein in an elevator-like motion. This conformational change is driven by the sodium gradient, which was also shown in the transport assay, as in the absence of a gradient, transport was nearly abolished. The general energy barrier for this transition is likely not very high, since the interactions between scaffold and transport domain in both conformations consist mainly of unspecific hydrophobic interactions across a similar contact surface area. The sole broken salt

bridge (E455-R480) is compensated by the formation of a new one (E688-K614) in the inward-open conformation. In the inward-open conformation, the binding pocket is accessible from the cytoplasm and substrates can be released. The overall arrangement of sidechains in the binding pocket is comparable to the outward-open conformation with only minor sidechain differences. It is not clear, whether these subtle changes decrease substrate affinity or whether the lower cytoplasmic sodium ion concentration facilitates substrate release into the cytoplasm. After substrate release, the substrate-free protomer then transitions back to the outward-open state.

Like many elevator-type transporters, ScPho90 forms a homodimer. The significance of this oligomerization and the role of dimeric assembly in cooperativity of transport between individual protomers have been discussed recently (Holzhüter et al., 2020). In the recorded datasets no particles were observed with both protomers in an inward-open conformation, which would be a sign for positive cooperativity, since the transition of one protomer may facilitate the transition of the other. However, this is likely due to the fact that the outward-open conformation is energetically more favorable and in the absence of a sodium gradient only few protomers adopt an inward-open conformation (one protomer in approximately 15 % of particles in the phosphate-free dataset). In addition, induced membrane deformations in the vicinity of the transporter have been proposed as a mechanistic basis for cooperativity of elevator-type transporters, as this could alter the energy landscape of the opposing protomer (Zhou et al., 2019). In the asymmetric map of ScPho90, the surrounding micelle was not found to be significantly deformed in the vicinity of either protomer but since detergent micelles do not exactly mimic the natural membrane environment this could be different in native membranes. Hence, structural elucidation within a lipid bilayer and in presence of a sodium gradient may shed further light on the cooperativity of these transporters. However, this is technically challenging, especially for small proteins, since proteins need to be imaged directly within membrane vesicles or by tomography *in situ*.

A unique feature of low-affinity phosphate transporters compared to other elevator-type transporters and high-affinity phosphate transporters is the presence of the regulatory SPX domain. How this cytoplasmic domain regulates phosphate translocation by the TM part is not well understood (Secco et al., 2012b). The SPX domain is not well resolved in the determined cryo-EM maps and no atomic model has been built. The low resolution is likely caused by high structural flexibility, which is in line with structure predictions, predicting a large flexible linker between the SPX domain and the TM part. Fitting the AlphaFold model into the density maps revealed that the SPX domain does

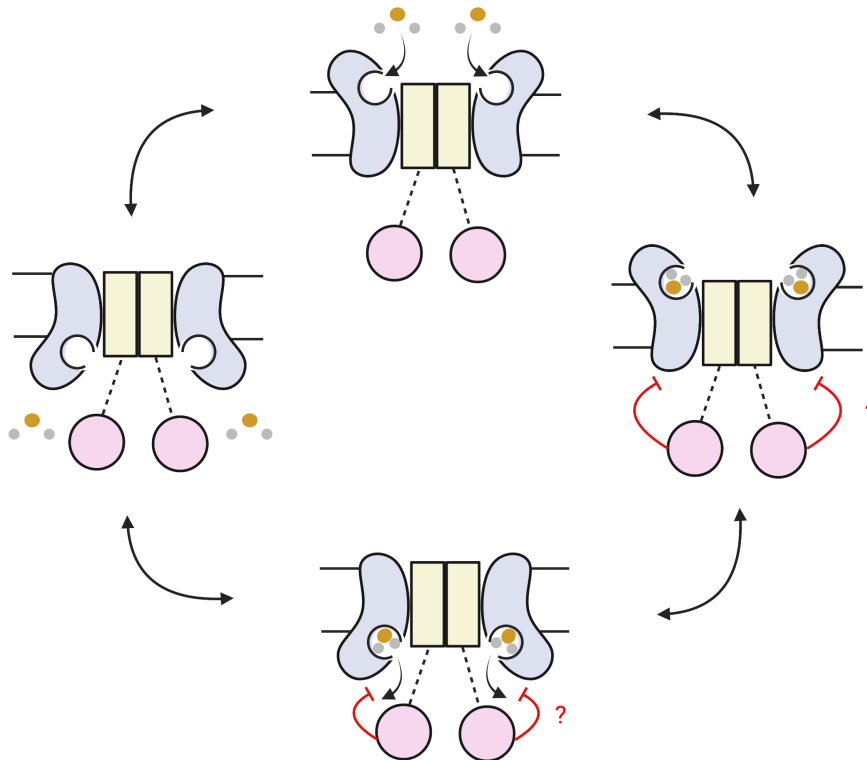


Figure 55: Putative phosphate translocation mechanism by low-affinity phosphate transporters. In the outward-open conformation, phosphate and sodium ions can access the binding pocket from the extracellular side. Upon substrate binding and driven by the sodium gradient, the transport domain shifts towards the cytoplasm, resulting in the accessibility of the binding pocket from the cytoplasm, thus inducing an inward-open conformation. Substrates are released into the cytoplasm, which in turn triggers the transition of the transport domain back into an outward-open conformation. The SPX domain executes its regulatory function by either inhibiting the conformational change of the transporter or by preventing substrate release.

not completely match the observed density (Figure S6). This is probably due to the fact that the density represents an average of all spatial orientations of the flexible SPX domain, while AlphaFold predicts a single conformation of it. Using 3D classification and 3D variability analysis discrete states of the SPX domain could not be determined. Therefore, it remains speculative how the SPX domain regulates ScPho90-mediated phosphate transport. Deletion of the SPX domain in the transport assays showed no drastic effect on phosphate transport *in vitro*. However, previous *in vivo* studies have demonstrated an inhibitory effect of the SPX domain on phosphate transport (Hürlimann et al., 2009). These differences are probably due to lacking factors in the *in vitro* reconstitutions that influence the regulatory function of the SPX domain. SPX domains are known to bind InsPPs and it has been shown that the SPX domain of ScPho90 interacts with soluble proteins such as Spl2 that might influence transport activity (Hürlimann et al., 2009; Wild

et al., 2016). It can be speculated that upon interaction with these additional partners the SPX domain can, by an unknown mechanism, inhibit either the conformational change of the transporter or the substrate release, thereby reducing phosphate transport activity. However, further structural and functional investigations are required to evaluate the regulatory mechanism of SPX domains on ScPho90-mediated phosphate transport.

4.3 The eukaryotic phosphate exporters Syg1 and Xpr1

4.3.1 Overall structure of ScSyg1/HsXpr1

In the framework of these studies, the structure of an eukaryotic phosphate exporter of the SLC53 family has been determined for the first time. Comparison of TM domain models of ScSyg1 and HsXpr1 with the PDB database (PDBeFold) showed no structural similarity to any deposited structure. Also sequence homology analysis using the HHpred server revealed no known homologous structure (Zimmermann et al., 2017). Furthermore, the protein has not been described to form dimers so far, but the structures as well as BN-gel analysis of ScSyg1 and HsXpr1 show that they mainly form dimers in solution. The number of 10 TM helices in individual monomers is uncommon in polytopic TM proteins, which mostly have 4, 7 or 12 TM helices (Dobson et al., 2015).

Although the overall fold of ScSyg1 and HsXpr1 is nearly identical, dimer orientations in ScSyg1 and HsXpr1 differ. While both ScSyg1 structures have the same elongated and planar dimer orientation, the phosphate-bound HsXpr1 dimer is tilted by 10° in relation to the membrane plane. It is known that proteins can bend membranes locally but whether the observed bending is physiologically relevant cannot be judged based on the structure alone. A tilted dimer structure has also been reported for other membrane proteins, as for example, the bacterial potassium transporter KimA. It has been speculated that the loss of lipids at the dimer interface led to this tilted conformation in KimA (Tascón et al., 2020). Although elongated densities at the dimer interface indicate the presence of co-purified lipids, it is likely that most of the lipids are lost during purification. This could be an explanation for the observed tilted dimer assembly. The phosphate-free HsXpr1 dimer displayed an asymmetric structure, with one monomer rotated by approximately 40° within the membrane plane. Whether this symmetry break and the rotation of one protomer is physiologically relevant, is not certain at present. Since the structures of the two protomers are nearly identical, a direct effect on phosphate transport activity is unlikely. The dimer reorientation might just be an effect of an intrinsic instability of purified HsXpr1, since dimers with one monomer in an inverted orientation were also found in the absence of phosphate. This arrangement can be excluded to occur under physiological conditions. It might arise from dimer disassembly during purification and inverted reassembly during protein concentration or detergent removal.

4.3.2 Dimerization interface of phosphate exporters

The TM dimer interface in eukaryotic phosphate exporters is only formed by interactions between TM1 helices of both protomers. This interaction is both in sequence and in structure reminiscent of a so-called glycine zipper (Kim et al., 2005). Transmembrane glycine zipper motifs are typical interaction motifs, often found in interfaces between transmembrane α -helices (Lemmon et al., 1992). The sequence of the interacting stretch in TM1 has the typical GxxxG motif of glycine zippers. Gly407 and Gly411 (ScSyg1, Gly238 and Gly242 in HsXpr1) are located at the direct helix interface and are separated by one helix turn to allow for tight helix packing of the crossing helices. This allows surrounding hydrophobic residues to interact closely with the opposing hydrophobic residues. Despite this very small dimer interface, ScSyg1 dimers appear to be relatively stable, as monomeric ScSyg1 was hardly detected by BN-gel analysis. Also during cryo-EM analysis, no classes for monomeric ScSyg1 were obtained. In contrast, HsXpr1 dimers were less stable in solution and were susceptible to disassembly into monomers during purification, especially when heterologously expressed in yeast. In the phosphate-free dataset of HsXpr1 many particles with disrupted TM1 dimer interactions were observed, resulting in a non-native dimeric arrangement, in which one of the HsXpr1 monomers is flipped within the membrane.

When comparing the dimer interface to known structures, very similar dimer interactions are observed in dimeric NMR structures of receptor tyrosine kinase (RTK) transmembrane helices like ErbB2 (Figure 56) (Bocharov et al., 2008). The TM helices of RTKs also have glycine zipper motifs, which are located at the helix dimer contact sites. However, RTKs also contain large extracellular domains that bind signalling molecules and play an important role in their dimerization. Interestingly, RTKs dimerize only transiently when activated and must dissociate again to terminate signalling. Whether eukaryotic phosphate exporters also form dimers only transiently *in vivo* and if this has a physiological relevance needs to be further investigated.

The individual SPX domains in the substrate-bound ScSyg1 dimer show no direct interactions that might confer protein dimerization. But due to an unresolved linker region between the SPX domain and TM1 (Leu365 - Thr376), it is unclear if each SPX domain sits beneath the TM part of the same protomer or if SPX domains are swapped and interact with the TM part of the opposite dimer. The unresolved 12 amino acid linker in theory would be sufficient to allow both domain organizations. Such a "domain-swapped" dimer would further stabilize the dimer formation through interactions of the SPX domain with the TM part of the opposing dimer.

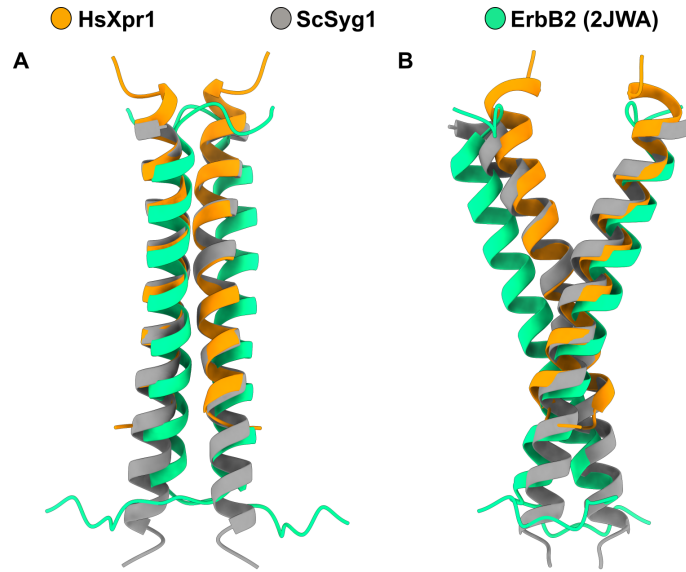


Figure 56: Comparison of dimer interfaces. (A) Comparison of dimer interfaces of HsXpr1, ScSyg1 and ErbB2. All 3 dimers contain glycine zipper motifs that allow for tight helix packing. (B) Same as in (A) but rotated by 90° along the theoretical membrane plane. The angle of the crossing helices is slightly different in ErbB2 compared to HsXpr1 and ScSyg1.

4.3.3 Effect of bound lipids

The hydrophobic binding pocket constituted by helices TM2-5 in both ScSyg1 and HsXpr1, was found to contain a phospholipid. Lipids have been shown to modulate the activity of multiple ion channels and transporters by direct interactions with the protein (Cheng et al., 2022; Martens et al., 2016; Neumann et al., 2017). Thus, binding of specific lipids in the hydrophobic pockets of ScSyg1 and HsXpr1 might also have an allosteric effect on their phosphate transport activities. Whether this is true for eukaryotic phosphate exporters needs to be investigated by further functional experiments. It is also possible that bound lipids are only responsible for stabilizing the tertiary structure of phosphate exporters, as this assembly may have led to an improvement in protein stability at some point in evolution (Corradi et al., 2019).

TLC analysis of co-purified ScSyg1 lipids revealed that mainly PC and PE (in LMNG-purified samples) are bound to the protein and the modelled PE matches the observed density well. TLC analysis of purified HsXpr1 did not identify specific lipids and the headgroup density was not well resolved. Thus, PA as default lipid molecule was modelled into its hydrophobic pocket. The plasma membrane of eukaryotic organisms is asymmetric in its lipid composition, with PC mainly located in the outer leaflet and other phospholipids (PE, PS, PI) predominantly in the inner leaflet (Ikeda et al., 2006).

Therefore, binding of PE over PC into the pocket located at the inner leaflet of the membrane would biologically make sense. Lipid-like densities are also observed at the protein surface, thus PC co-purified with ScSyg1 is likely to bind there. It is also possible that no specific type of lipid binds within the hydrophobic pocket, but a mixture of different phospholipids. In the structure of ScSyg1 only the phosphate of the lipid headgroup was found to be coordinated by basic sidechains, while in HsXpr1 no specific headgroup coordination was observed. This may be an indication that the binding of lipids into the hydrophobic pocket in phosphate exporters is unspecific for lipid headgroups.

4.3.4 Substrate translocation pathway

Helices TM5-10 of ScSyg1 and HsXpr1 form a six-helix bundle with a putative substrate translocation pathway at its center. Analyzing the characteristic of this pathway provides valuable insights into the translocation mechanism. The overall architecture of the helix bundle is very similar between ScSyg1 and HsXpr1 (RMSD: 2.8 Å), with main differences in the outer leaflet portions of helices TM7-9. The inner radius of the translocation pathway was analyzed with MOLEonline (Pravda et al., 2018) and ranged between 1.3 and 3 Å in ScSyg1, with the most narrowly constricted part between Asp580 and Asp695 at the cytoplasmic end of the translocation pathway. The constriction of the pore radius to 1.3 Å prevents water molecules (radius of 1.4 Å) from freely diffusing through the pathway (Sehnal et al., 2013). Parts of the pathway that are wider than 1.4 Å are hydrated due to many sidechains, enabling hydrogen bonding networks. This can be seen in the high resolution maps of ScSyg1, where non-protein density within the translocation pathway are mainly water molecules.

In HsXpr1, the pore radius in proximity to the conserved aspartate residues is larger with a pore radius of 1.8 Å. However, the translocation pathway is completely blocked at the non-kinked end of TM9 through the insertion of Trp573 into the center of the helix bundle. This non-kinked conformation of TM9 is enabled by an outward movement of TM7 and TM8 to allow for TM9 to extend into the translocation pathway. This insertion likely prevents phosphate from transversing the protein in this conformation and most likely constitutes an extracellular gate in HsXpr1. While Trp573 is highly conserved throughout eukaryotes, it is not located inside the translocation pathway in the ScSyg1 structures, where TM9 was kinked outwards. The structures of the helix bundle in presence and absence of substrates are nearly identical for HsXpr1 and ScSyg1, respectively. Thus, no conformational changes were observed in the translocation pathway under these different conditions, which would provide valuable insights into the phosphate translocation mechanism. However, since different conformations of the

highly conserved helix bundle are present in HsXpr1 and ScSyg1, these differences possibly highlight different states of a conserved translocation mechanism. Supporting this hypothesis, AlphaFold predicts TM9 of HsXpr1 to adopt a kinked conformation, as seen for ScSyg1 (Figure S7). Therefore, kinking of TM9 might be a conserved mechanism in eukaryotic phosphate exporters to change between outward-occluded and outward-open conformations. Still, it is possible that mechanistic differences between ScSyg1- and HsXpr1-mediated phosphate export exist. For example, in the presence of phosphate and InsP_6 two alternative conformations of extracellular loop 5 (ECL5) were observed in ScSyg1, one where the loop is inserted into the translocation pathway blocking it from the extracellular side. This could represent an additional strategy to form an extracellular gate in ScSyg1, compared to the straightening of TM9 in HsXpr1. Further functional characterization of TM9 and ECL5 of ScSyg1 would help to decipher their role in the phosphate export mechanism.

While the translocation pathway is accessible from the cytoplasmic side in HsXpr1 structures, it is closed by a long SPX loop in ScSyg1. This non-conserved loop most likely functions as a cytoplasmic gate of yeast phosphate exporters, as its closing of the translocation pathway leads to an inward-occluded conformation of ScSyg1. Because HsXpr1 does not contain this SPX loop, a similar mechanism in the human phosphate exporter can be excluded. Furthermore, no other structural elements were observed at the cytoplasmic end of HsXpr1 that would function as a cytoplasmic gate. Thus, how HsXpr1 can adopt an inward-occluded conformation remains an open question. Since the cytoplasmic SPX domain of HsXpr1 is not well resolved, it is possible that it could play a role in the inward occlusion of HsXpr1. Elucidating the complete HsXpr1-SPX structure would provide valuable information.

4.3.5 Phosphate binding

Within the substrate translocation pathway of ScSyg1 several non-protein densities are present. In contrast, only very few additional densities are observed in HsXpr1 maps. The main reason for this is the higher resolution of ScSyg1 maps (2.3 Å), while resolutions of HsXpr1 maps do not exceed 3 Å. Therefore, multiple water molecules are modelled in the water filled translocation pathway of ScSyg1, but not in HsXpr1. In the phosphate-bound ScSyg1 structures, two of the non-protein densities within the pathway were interpreted as phosphate ions, while all other densities were interpreted as water molecules. The interpretation as phosphate ions is mainly based on their coordination by several polar or charged residues within the translocation pathway (P1:

Glu236, Arg633, His643, Asn646; P2: Ser564, Arg745, Glu772, Arg775, Arg776). Densities that were interpreted as water molecules show less pronounced sidechain coordination, which is typical for water molecules. In addition, almost all of the phosphate coordinating sidechains are highly conserved. The weak density for phosphate ions may be related to their double negative charge which leads to negative scattering factors in cryo-EM (see 4.2.2).

In the absence of substrates, the ScSyg1 map also reveals several non-protein densities in the translocation pathway. These densities can all be interpreted as water molecules due to the absence of substrates, however it is also possible that bound phosphate was co-purified. As of now, no binding affinity of phosphate to Syg1 (or Xpr1) proteins has been reported, making it difficult to judge how tight phosphate binds to the protein and whether it might co-purify from the host. Comparing the densities within the translocation pathways of both maps reveals a high degree of similarity. This might indicate that the translocation pathway in the "substrate-free" ScSyg1 structure is at least still partially occupied by bound phosphate. Therefore, to obtain a true apo structure of the protein, a different purification strategy might be necessary to dispose bound phosphate completely.

In the map of phosphate-bound HsXpr1, the only observed non-protein density within the translocation pathway was interpreted as a phosphate ion, since it is coordinated by the highly conserved residues Lys482, Asp529, Arg570 and Arg603. This additional density is not present in the phosphate-free HsXpr1 map, further indicating that it likely represents a bound phosphate ion. Compared to the ScSyg1 model with two phosphate ions in the translocation pathway, the bound phosphate ion in HsXpr1 is not in the same position (Figure 57). Since the phosphate ion (P1) at the cytoplasmic end of ScSyg1 is also coordinated by Glu236 of the non-conserved SPX loop, this phosphate binding site might be unique to yeast phosphate exporters. Phosphate P2 in ScSyg1 and the coordinated phosphate in HsXpr1 have two corresponding coordinating sidechains (Arg570 and Arg603 in HsXpr1, Arg745 and Arg775 in ScSyg1), but P2 of ScSyg1 is located 4 Å further towards the extracellular side within the translocation pathway. In HsXpr1, binding of phosphate at this position is prevented by Trp573, which occupies this potential binding site. Outward kinking of TM9 (as seen in ScSyg1) would make this binding site accessible. Kinking of TM9 would also create a continuous pathway from the binding site to the extracellular space, thus enabling phosphate export.

A comparison of the phosphate binding sites of ScSyg1 and HsXpr1 with known phos-

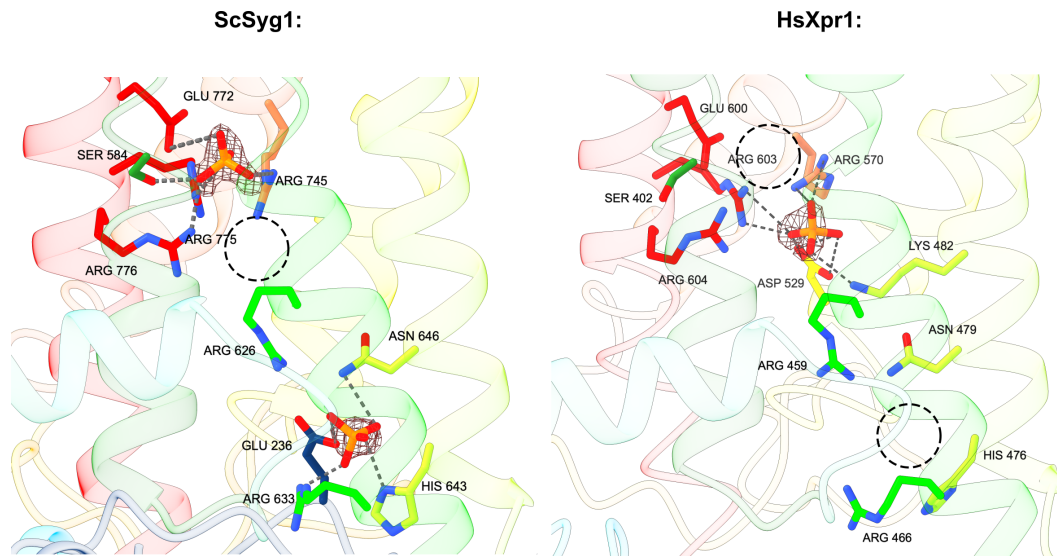


Figure 57: Comparison of phosphate coordination in ScSyg1 and HsXpr1. In the translocation pathway of ScSyg1 two densities were interpreted as phosphate ions (left), while in HsXpr1 a phosphate ion was assigned to the only obtained non-protein density (right). Dashed circles indicate the position of bound phosphate ions in the other phosphate exporter, respectively. The bound phosphate in HsXpr1 is coordinated by two equivalent arginines as the upper phosphate in ScSyg1 (Arg570 and Arg603; Arg745 and Arg775), but is located 4 Å further down within the translocation pathway. The upper binding position is not accessible in HsXpr1, since it is occupied by Trp573 of TM9 (not shown).

phosphate transporters (Pedersen et al., 2013; Tsai et al., 2020) shows that the phosphate exporters have a unique phosphate coordination pattern (see Figure 54). Many basic residues (mainly lysine and arginine) are involved in phosphate coordination in Syg1/Xpr1, which are not present in other phosphate transporters. The reason for that might be that the other known phosphate transporters are sodium/phosphate (ScPho90, TmPiT) or proton/phosphate (PiPT) symporters, where the cationic co-substrates compensate the negative charge of the phosphate ion (Pedersen et al., 2013; Tsai et al., 2020). Syg1/Xpr1 is not known to be a secondary active transporter and the phosphate coordination might indicate that no cation is co-transported. Furthermore, no sodium or proton gradient was necessary to drive Syg1/Xpr1-mediated phosphate transport in the *in vitro* transport assays.

4.3.6 Regulatory role of the SPX domain

In the structures of ScSyg1 and HsXpr1, the soluble SPX domain is less well resolved likely due to its flexibility in relation to the TM domain. However, through the addition of the SPX domain substrate InsP₆, it was possible to isolate a subset of ScSyg1 particles

(using 3D variability analysis) with a well-resolved SPX domain density. Binding of InsP_6 presumably favors the SPX domain to adopt a certain conformation in relation to the TM domain, aiding in structure determination. The SPX domain of ScSyg1 shows the same overall fold as isolated SPX domains solved by X-ray crystallography (Wild et al., 2016). However, ScSyg1 is only the second structure of a full-length SPX domain-containing protein, after the recent structure of the yeast VTC complex (Guan et al., 2023).

Superimposing the crystal structures of SPX domains from HsXpr1 (5IJH) and CtGde1 (5IJJ) illustrates the conserved three-helix bundle motif (Figure 58). The bundle consists of the long helices α_3 and α_4 as well as the two small helices α_5 and α_6 . The α_6 helix is in the same position as α_6 of CtGde1, while this helix points away from the helix bundle in the crystal structure of HsXpr1 SPX. The N-terminus of the ScSyg1 SPX domain adopts the same helical hairpin fold (α_1 and α_2) as in both crystal structures.

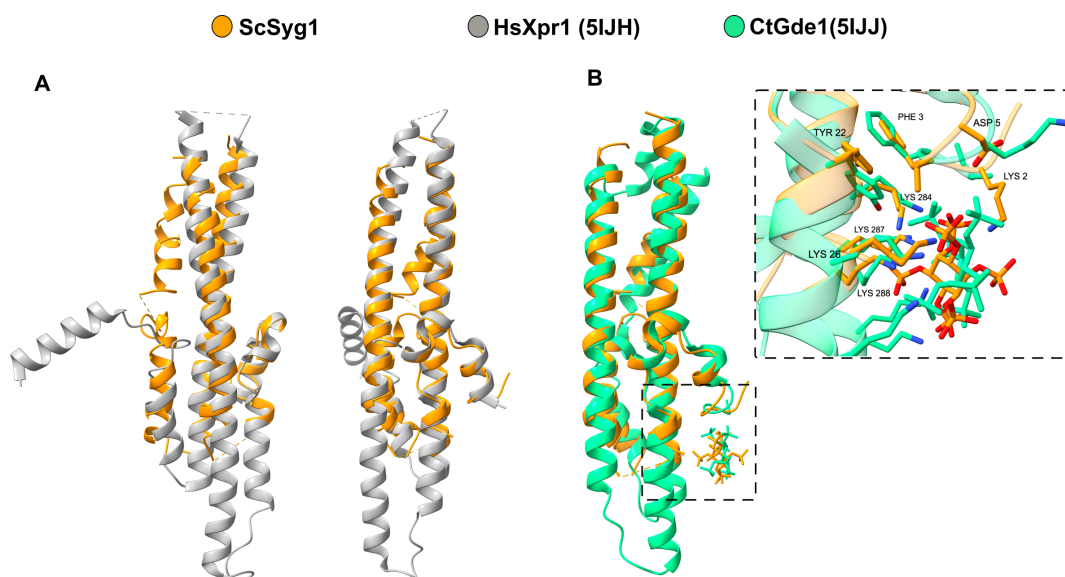


Figure 58: Structural comparison of SPX domains. (A) Comparison of the SPX domain of ScSyg1 determined here and the crystal structure of the SPX domain from HsXpr1 (5IJH). The main difference is the alternative orientation of the α_6 helix. (B) Comparison of the ScSyg1 SPX domain with the substrate-bound SPX domain from CtGde1 (5IJJ) reveals identical InsP_6 binding sites.

In the SPX crystal structures, two very basic surface clusters were identified, termed phosphate binding cluster (PBC) and lysine surface cluster (KSC), which are involved in InsP_6 binding (Wild et al., 2016). All residues of these clusters (mainly lysine) are highly conserved in all known SPX domains. Comparing InsP_6 -bound ScSyg1 with InsP_6 -bound CtGde1 reveals that the binding mode of InsP_6 is almost identical. Nearly all residues from the PBC and KSC (Lys2, Tyr22, Lys26, Lys284, Lys287 and Lys288 of ScSyg1) are

4.3. The eukaryotic phosphate exporters Syg1 and Xpr1

present at the InsP₆ binding site. Only Lys30 (not conserved in ScSytg1) and Lys132 (Lys291 in ScSytg1) of the KSC are not present as the density is not well resolved in this part.

The additional potential InsP₆ binding site in ScSytg1 between the cytoplasmic ends of TM1 is also close to a basic surface cluster (Lys378, Lys380 of both protomers). This basic surface cluster at the beginning of TM1 is conserved in homologues from plants and animals, where it shows a KAMK sequence motif. Together with the observation that this stretch of TM1 is unresolved in the absence of InsP₆, this suggests an additional InsP₆ binding site outside of the SPX domain that is unique to eukaryotic phosphate exporters. Further investigations are needed to determine the physiological function of this putative additional InsP₆ binding site.

The crystal structures of isolated SPX domains have elucidated their overall fold and binding mode of InsP₆ and InsPPs. However, it remains unclear how InsP₆/InsPP binding to this domain regulates the activity of multiple different phosphate transporters, enzymes and transcription factors. In the absence of substrates, the SPX domain of ScSytg1 is less well resolved, likely due to an increased flexibility. Based on the cryo-EM density, an interaction between the SPX domain and helix TM1 can be assumed, but no further interactions are seen in the absence of InsP₆. In contrast, in the InsP₆-bound structure a contact between SPX helix α 3 and intracellular loop 4 (ICL4) is present, apart from interactions between SPX domain and helix TM1. This is enabled by a "swing-like" motion of the SPX helix bundle towards ICL4. This different conformation of the SPX domain is likely induced through binding of InsP₆. The additional contact site is interesting, as it might induce changes within the translocation pathway, since ICL4 is directly connected to helix TM9. However, no major differences are found in the TM domain between substrate-bound and substrate-free structures and also TM9 shows the same kinked conformation in both ScSytg1 structures. Only extracellular loop 5 (which is connected to ICL4 through helix TM9) assumes two different conformations in the substrate-bound structure. Whether this is caused by the observed ICL4 - SPX interaction is not clear and must be further investigated.

An important difference in the SPX domains of ScSytg1 and HsXpr1 is the presence of long unstructured loops between individual SPX helices of ScSytg1. These long loops are also found in homologues from plants but are not conserved in sequence. The resolved loop between α 3- and α 4-helices of the ScSytg1 SPX domain (Leu198 - Ala239) occludes the translocation pathway mainly through Glu236 and Phe238, which are lo-

cated directly in the entrance of the pathway. This conformation of the loop is observed in both ScSyg1 structures and Glu236 is even involved in phosphate coordination in the translocation pathway. The similar conformations could be due to co-purified phosphate within the translocation pathway also in the "substrate-free" structure. Due to its role in closing of the translocation pathway, this loop might function as a gate on the cytoplasmic side of ScSyg1. Based on its additional involvement in phosphate coordination, this loop might also play an important role in the regulation of Syg1 in yeast and plants. However, its absence in metazoans implies that this is not a conserved mechanism in eukaryotic phosphate export. It is tempting to speculate that due to the limited P_i availability to plants and fungi, this might present an additional regulatory mechanism to limit unwanted phosphate efflux (Hou et al., 2020). Yet, in the *in vitro* transport assays, basal phosphate transport in the absence of InsP_6 was observed for both HsXpr1 and ScSyg1. Additional functional characterization would help in identifying the specific role of this loop in the regulation of phosphate export in yeast.

4.3.7 Proposed mechanism of phosphate export in eukaryotes

The presented structures of eukaryotic phosphate exporters ScSyg1 and HsXpr1 allow for the proposal of a phosphate translocation mechanism by this conserved protein family. Since there are no other structures of proteins with a homologous translocation pathway, it is possible that the translocation mechanism differs from known substrate transport mechanisms. Based on the conserved overall fold between ScSyg1 and HsXpr1 and the high conservation of sidechains within the translocation pathway, a consistent mechanism for eukaryotic phosphate export is likely. However, slight differences observed in the structures might also indicate subtle mechanistic differences.

Although Xpr1 was first described as a phosphate exporter 10 years ago, it is still not known whether it functions as an active or passive transporter or even as a channel (Giovannini et al., 2013). The overall fold of ScSyg1 and HsXpr1 is not reminiscent of typical ion channels, in which multiple subunits form a central ion conducting pore. However, in recent years structures of atypical ion channels were reported. For example the CLC family of chloride transporters and channels has several members that are homologous both in structure and sequence but function as either chloride channels or proton/chloride antiporters (Accardi et al., 2004; Park et al., 2018). This emphasizes that distinguishing transporters and channels solely based on their structures is difficult. Transport assays showed phosphate transport activity of both ScSyg1 and HsXpr1 in the absence of additional ion gradients, suggesting that they do not function as secondary-active transporter. However, the measured initial transport rates are quite slow and

linear over a longer period of time (approximately 20 min) which favours a transporter-like mechanism over the faster ion conductance of a channel.

Transporters and channels can also be discriminated based on the presence of one or two gates and the consequence that channels can be open to both sides of the membrane at once, while transporters are only accessible from one side at a time (Gadsby, 2009). The ScSyg1 structures are in an inward-occluded state and HsXpr1 structures are in an outward-occluded state, with neither protein showing a continuously open translocation pathway. In HsXpr1, TM9 functions as an extracellular gate that occludes the translocation pathway towards the exterior. In ScSyg1, the SPX loop occludes the pathway from the cytoplasmic side, thereby functioning as a cytoplasmic gate. Assuming that both proteins can also adopt the respective other conformation, the following transport mechanism is proposed (Figure 59). In the inward-open (outward-occluded) conformation, phosphate enters the translocation pathway from the cytoplasm. Upon phosphate binding, a cytoplasmic gate (X) closes to occlude the translocation pathway towards the cytoplasm. In ScSyg1, the SPX loop likely functions as the cytoplasmic gate. After closure of the cytoplasmic gate, TM9 kinks and the pathway adopts an outward-open (inward-occluded) conformation, allowing phosphate to exit into the extracellular space. Phosphate dissociation then enables the protein to revert to the inward-open conformation by straightening of TM9 and opening of the cytoplasmic gate for a new translocation cycle.

The regulatory role of the SPX domain in this translocation cycle remains elusive. It is clear that upon binding of $\text{InsP}_6/\text{InsPPs}$ to the SPX domain, phosphate export activity is increased, as also shown in the phosphate transport assays. How $\text{InsP}_6/\text{InsPPs}$ binding increases phosphate export on a mechanistic level remains open to speculation. The interaction of the $\text{InsP}_6/\text{InsPPs}$ -bound SPX domain with intracellular loop 4 might facilitate conformational changes in adjacent TM9 and thereby increase phosphate export. A simultaneous effect on the cytoplasmic gate is conceivable, since in ScSyg1 it is part of the SPX domain. Nevertheless, further structural and functional studies are needed to pinpoint the regulatory mechanism of the SPX domain in eukaryotic phosphate export.

4.3.8 Conserved function of EXS domain proteins

The sequences comprising helices TM6-10 of eukaryotic phosphate exporters that make up most of the phosphate translocation pathway, are annotated as EXS domain (PS51380). The domain is named after its presence in Erd1, Xpr1 and Syg1. Erd1 was named after and identified due to defects in ER protein retention when it is knocked out (Pelham et

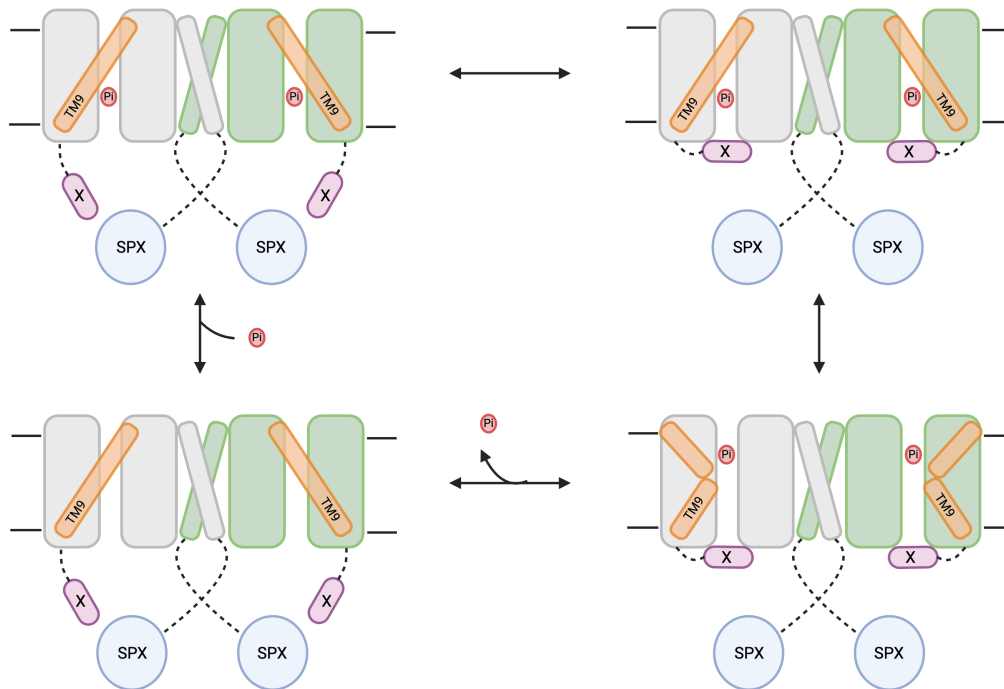


Figure 59: Proposed model of eukaryotic phosphate export. Phosphate can enter the translocation pathway from the cytoplasm in an inward-open conformation and induces the putative cytoplasmic gate to close. Thereby, kinking of TM9 is induced, resulting in an outward-open conformation of the translocation pathway. In this conformation phosphate is released into the extracellular medium which enables the protein to revert into an inward-open conformation. Starting from this conformation a new export cycle can take place.

al., 1988). Recently, it has been shown that Erd1 plays a major role in glycosyltransferase recycling from the Golgi apparatus and was suggested to function as a Golgi phosphate exporter (Hsieh et al., 2023; Sardana et al., 2021). Interestingly, in contrast to Syg1 and Xpr1, Erd1 does not have a regulatory SPX domain. Comparing ScSyg1 and HsXpr1 structures with the AlphaFold prediction of yeast Erd1 shows a conserved overall fold and phosphate translocation pathway (Figure 60A). Strikingly, Erd1 is predicted to have only 9 TM helices, with TM1 from Syg1/Xpr1 missing. One may speculate that the absence of TM1 indicates that Erd1 does not dimerize, as is the case for ScSyg1 and HsXpr1. The absence of the first TM helix might also lead to an inversion of the overall topology of Erd1 compared to Syg1/Xpr1. This would be consistent with a reversed phosphate transport direction from the Golgi into the cytoplasm (compared to the export from the cytoplasm by Syg1/Xpr1). However, it is also possible that Erd1 adopts the same topology as Syg1/Xpr1 (only without TM1), but can still transport phosphate from the Golgi

are only present in fungi and plants but not in multicellular animals. Because animals are mobile and heterotrophic organisms, obtain nutrients from the digestion of other organisms that are rich in phosphate, they rarely have high P_i demands (Penido et al., 2012). On the other hand, plants and microorganisms often live in environments with limited P_i availability (Ågren et al., 2012). Therefore, Erd1 might be responsible for phosphate recycling from the Golgi in these organisms to limit phosphate loss. Animals which have a surplus P_i can tolerate phosphate loss by exocytosis and therefore do not depend on phosphate recycling by Erd1 proteins.

Since protein domains are defined as distinct structural or functional units of a protein (Wetlaufer, 1973), it would make sense to extend the definition of the EXS domain to also cover TM5 of Syg1 and Xpr1 and TM4 of Erd1. This would result in the EXS domain being the six-helix bundle, forming the translocation pathway in eukaryotic phosphate export proteins.

4.3.9 Sequence conservation and disease mutations in HsXpr1

The structures of phosphate exporters ScSyg1 and HsXpr1 show that their tertiary structure is highly conserved. Multiple sequence alignment of homologous proteins from different eukaryotes reveals that also the primary structures are highly conserved (Figure 61). In particular, sequences within the SPX domain and within the translocation pathway (EXS domain) are identical or very similar. In the SPX domain this mainly involves residues that participate in $InsP_6/InsPP$ binding or in SPX helix contacts. In the EXS domain nearly all highly conserved residues line the inside of the translocation pathway.

Studies investigating mutations within the *Xpr1* gene of PFBC patients have shown that most disease-linked mutations also occur within the SPX and EXS domains (Anheim et al., 2016; Legati et al., 2015; López-Sánchez et al., 2019; Ramos et al., 2018; Tang et al., 2021). These mutations can be mapped onto the obtained HsXpr1 structure and onto the homologous SPX domain structure of ScSyg1, since the SPX domain of HsXpr1 was not resolved (Figure 62). The most frequently observed mutation L145P (V271 in ScSyg1) and mutation L87P (L129 in ScSyg1) are both located at conserved hydrophobic SPX helix contact sites. The mutations to proline likely disrupt helix formation and would lead to misfolding of the SPX domain. The L145P has also been described to lead to impaired phosphate export and loss of plasma membrane localization (Legati et al., 2015), which might be due to protein misfolding. The other SPX domain mutants S136N (I262 in ScSyg1), L140D (L266 in ScSyg1) and L218S (L379 in ScSyg1) are located at the interface of

4.3. The eukaryotic phosphate exporters Syg1 and Xpr1

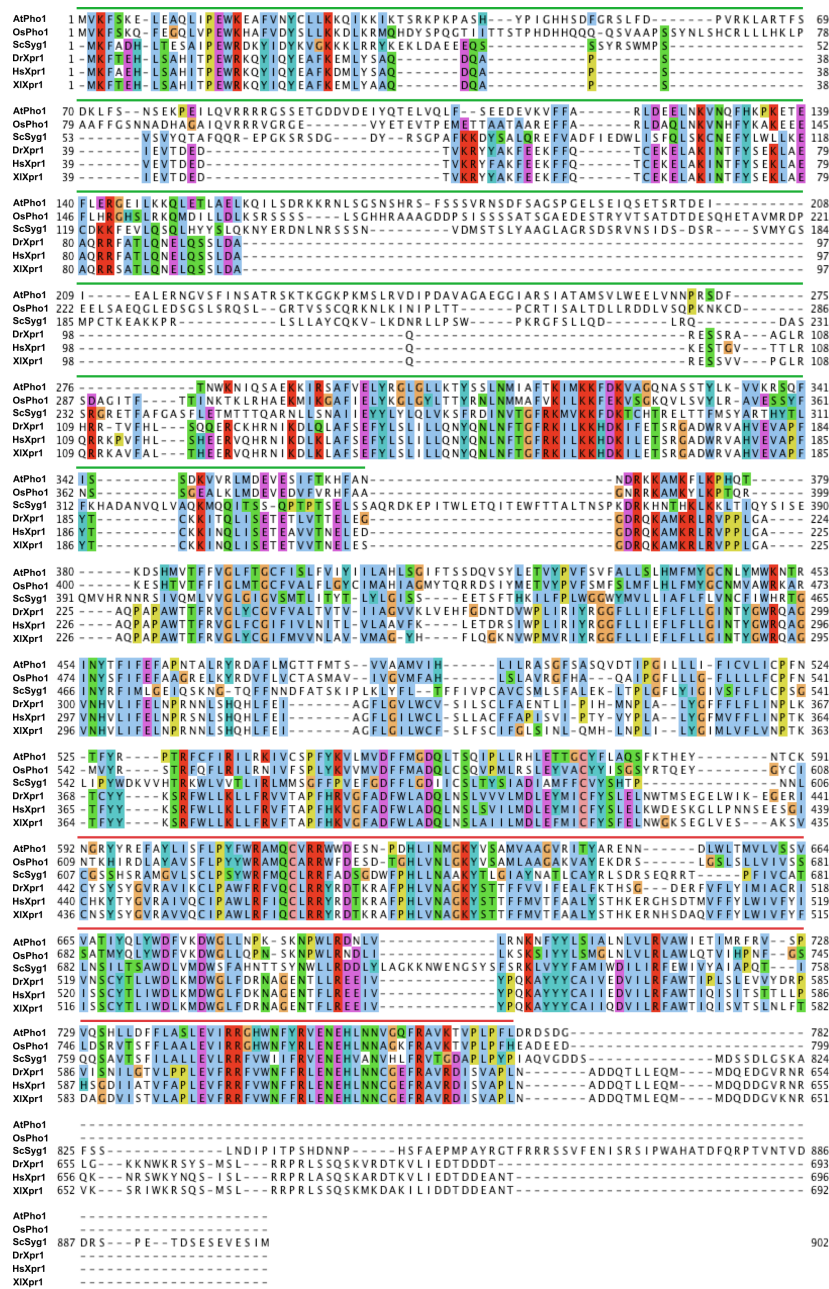


Figure 61: Multiple sequence alignment of eukaryotic phosphate exporters. Sequences of *AtPho1* (*A. thaliana*), *OsPho1* (*O. sativa*), *ScSyg1* (*S. cerevisiae*), *DrXpr1* (*D. rerio*), *HsXpr1* (*H. sapiens*) and *XIXpr1* (*X. laevis*) are aligned. Sequences are colored according to the Clustal X color scheme and gaps are shown as minus (-) symbols. SPX (green lines) and EXS (red lines) domains are highlighted. Sequences were aligned using Clustal Omega (Madeira et al., 2022).

TM1 and the SPX domain. All three mutants have been shown to have impaired phosphate export function *in vivo* (Legati et al., 2015), which might be caused by an impaired coupling of SPX regulation to the TM domain. Further functional analysis of these mutants are necessary to confirm this hypothesis.

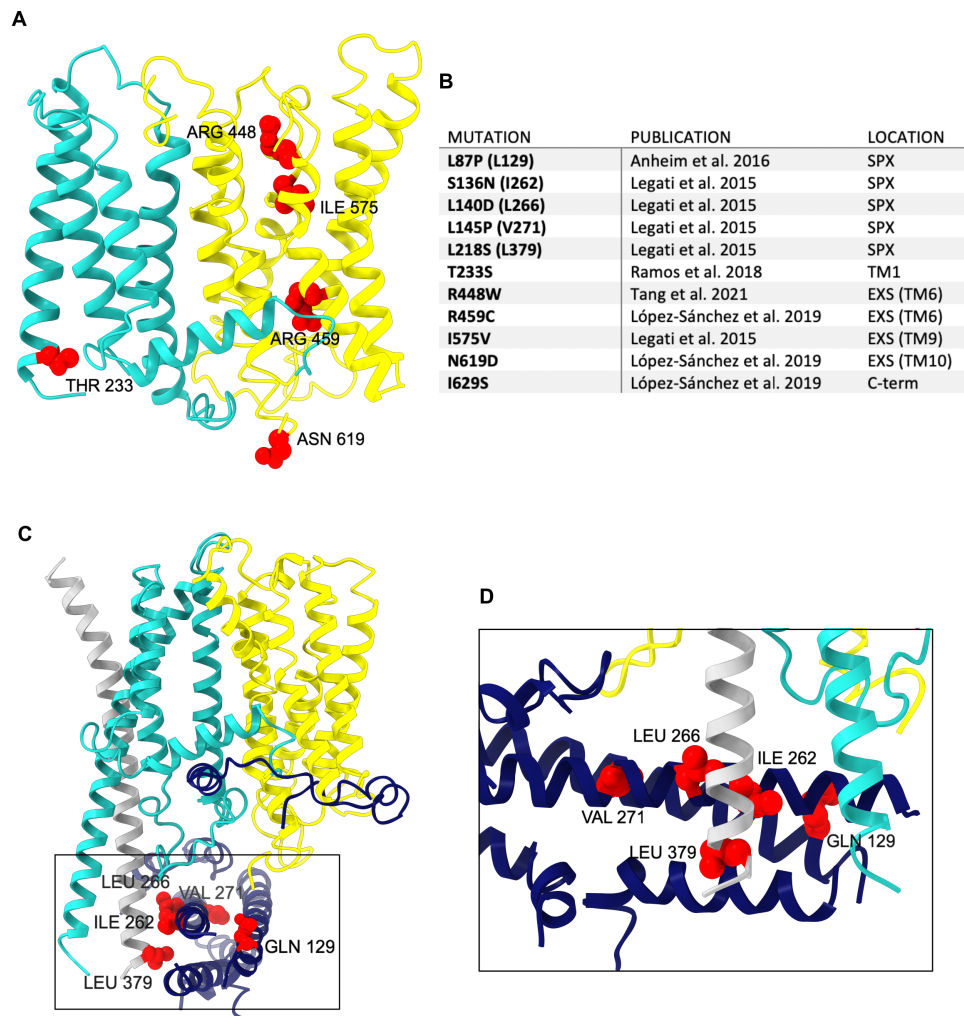


Figure 62: Mapping of PFBC-linked mutations onto HsXpr1 and ScSyg1. (A) Overview of PFBC-linked mutations in the TM part of HsXpr1. Residues affected by mutations are shown as red spheres. Helices TM1-4 are turquoise and helices TM5-10 (EXS domain) are yellow. (B) List of PFBC-linked mutations and their locations. Corresponding residues of ScSyg1 to mutations in the HsXpr1 SPX domain are listed in parentheses. (C) Overview of PFBC-linked mutations in the SPX domain of HsXpr1 mapped to the ScSyg1 structure. Residues affected by mutations are shown as red spheres. Helices TM1-4 are turquoise and helices TM5-10 (EXS domain) are yellow. TM1 of the opposing protomer is grey. (D) Enlarged view of mutations within the SPX domain, rotated by 90° in relation to (C).

In the EXS domain, disease-linked mutations can directly be mapped onto the structure of HsXpr1. The R448W mutation is located at the extracellular end of helix TM6 right at the end of the translocation pathway. This arginine is conserved only in metazoans but not in fungi and plants. Its location indicates a function in substrate translocation, but no functional studies have been conducted with this mutant yet (Tang et al., 2021).

Another arginine mutation R459C is also located in helix TM6 and protrudes into the translocation pathway. This residue is highly conserved and is located in the center of the translocation pathway. The mutation was shown to lead to a decreased phosphate export activity (López-Sánchez et al., 2019), which is likely due to defective phosphate binding or transport. Another disease-linked mutation of a highly conserved residue is N619D. This asparagine is located at the cytoplasmic end of TM10, just at the entrance of the translocation pathway and is therefore likely to play a role in substrate translocation. *In vivo* phosphate transport of this mutant has been shown to be impaired (López-Sánchez et al., 2019). Additionally, the mutant I629S has been found in PFBC patients and was shown to have a decreased phosphate export activity (López-Sánchez et al., 2019). This residue is located in the C-terminal cytoplasmic stretch that is not resolved in any of the cryo-EM maps. Therefore, no role for this disease-linked mutation can be analyzed based on the structures presented here.

Mapping the known disease-linked mutations of HsXpr1 onto the structures of HsXpr1 and ScSyg1 helps to understand the pathogenic mechanism behind individual mutations. While the phenotype of most mutants is impaired or decreased phosphate export, their causes are distinct. Mutants in the SPX domain likely lead to improper regulation of the transporter, either by misfolding or impaired regulatory coupling to the TM part. Other mutations located in the EXS domain directly impair substrate binding or substrate translocation. Understanding these differences can help in treating HsXpr1-linked diseases by developing specialized therapeutic agents.

4.3.10 Physiological impact

Apart from its critical role in PFBC, Xpr1 plays a crucial role in human phosphate homeostasis in general, being the only known phosphate exporter. Phosphate export is critical, since elevated cellular P_i levels have a variety of detrimental effects, including cardiovascular complications, impaired bone mineralization and chronic kidney diseases (Kendrick et al., 2011; Penido et al., 2012; Vervloet et al., 2017). Moreover, Xpr1 was also found to be overexpressed in various types of cancer and was suggested as a potential biomarker or immunotherapy target (Akasu-Nagayoshi et al., 2022; Bondeson et al., 2022; Chen et al., 2019; Wang et al., 2022). In modern society, excessive P_i levels become an increasing problem due to high-phosphate diets, since modern highly processed food often contains high amounts of added phosphate as preservative or flavour enhancers (Calvo et al., 2023). Hence, regulation of P_i levels at the cellular and organismal level become increasingly more important for healthcare. Therefore, understanding the action

and regulation of human phosphate export is key in developing therapeutic strategies to deal with health issues caused by an imbalance in cellular P_i levels.

For example, structure-based drug design is a powerful method to rationally design new pharmacological compounds based on a protein structure (Anderson, 2003). Obviously the prerequisite for successful structure-based drug design are well-resolved protein structures. The reported structures of HsXpr1 (and with limitations also the ScSyg1 structures) are therefore likely to help in developing new compounds, which can alter HsXpr1-mediated phosphate export activity, thereby affecting cellular phosphate homeostasis. Besides the direct use in drug design, protein structures also provide valuable insights into the molecular mechanism of proteins. Understanding the mechanism of HsXpr1-mediated phosphate export is also crucial in developing therapeutic strategies to combat HsXpr1 malfunctions. For example, inositol pyrophosphate mimicking substances might theoretically be used to treat patients with chronically high cellular P_i levels. However, if mutations within the SPX domain or within important residues involved in transmitting the regulatory function towards the translocation pathway occur, this strategy is likely unsuccessful. The same is true vice versa, if compounds targeting the export pathway are developed but the reason for dysfunctional phosphate homeostasis is associated with misregulation by the SPX domain. Therefore, a detailed knowledge of the phosphate export mechanism is essential to combat human diseases associated with phosphate homeostasis. The here presented results provide a basis for understanding the mechanism of eukaryotic phosphate export and will be valuable in future research of eukaryotic phosphate homeostasis.

4.4 Concluding remarks and outlook

In this thesis, the first structures of a yeast low-affinity phosphate importer and of eukaryotic phosphate exporters from yeast and humans are presented, providing insights into their function at a molecular level.

Inward- and outward-open structures of the low-affinity phosphate transporter ScPho90 reveal its conserved overall fold with DASS-family transporters and provide insights into phosphate translocation by an "elevator-type" mechanism. The function of its regulatory SPX remains speculative, due to its low-resolution density. High-resolution information of the SPX domain in a full-length structure of ScPho90 would add substantially to understanding its regulatory role. Attempts to increase the rigidity of the SPX domain were not successful in this work, but testing different binding partners or identifying conformation-specific nanobodies might enable structure determination by trapping the SPX domain in a rigid conformation. In addition, more comprehensive and sophisticated functional characterization are needed to uncover mechanistic details of low-affinity phosphate import in eukaryotes.

The cryo-EM structures of ScSyt1 and HsXpr1 reveal a conserved dimeric fold of eukaryotic phosphate exporters, in which EXS domains form the phosphate translocation pathway. Based on the structures and the observed differences in the phosphate translocation pathway of ScSyt1 and HsXpr1, a phosphate export mechanism is proposed. In addition, the structure of the substrate-bound SPX domain of ScSyt1 reveals its orientation relative to the TM part and allows speculation on its regulatory mechanism. To confirm the proposed mechanism for eukaryotic phosphate exporters further structural and functional investigations are required. Functional studies built on the ^{33}P -phosphate transport assays presented here should analyze the effect of mutations in putative important residues for phosphate translocation. This includes residues involved in phosphate binding and in opening and closing of the translocation pathway. This will provide valuable insights to understand the eukaryotic phosphate export mechanism further. In addition, molecular dynamics (MD) simulations using the structures reported here as input will shed light on the dynamics of eukaryotic phosphate exporters and provide additional insights into the transport mechanism. Further structural investigations will aim to elucidate structures of HsXpr1 and ScSyt1 (or other eukaryotic phosphate exporters) in complementary conformations to confirm a conserved mechanism. Also, elucidating structures of HsXpr1 with well-resolved SPX domains would aid in deciphering its regulatory mechanism.

Bibliography

- Abbe, E. (1873). "Beiträge zur Theorie des Mikroskops und der mikroskopischen Wahrnehmung". In: *Archiv für mikroskopische Anatomie* 9.1, pp. 418–440.
- Accardi, A. and C. Miller (2004). "Secondary active transport mediated by a prokaryotic homologue of ClC Cl⁻ channels". In: *Nature* 427.6977, pp. 803–807.
- Adams, P. D., P. V. Afonine, G. Bunkóczi, V. B. Chen, I. W. Davis, N. Echols, J. J. Headd, L. W. Hung, G. J. Kapral, R. W. Grosse-Kunstleve, A. J. McCoy, N. W. Moriarty, R. Oeffner, R. J. Read, D. C. Richardson, J. S. Richardson, T. C. Terwilliger, and P. H. Zwart (2010). "PHENIX: A comprehensive Python-based system for macromolecular structure solution". In: *Acta Crystallographica Section D: Biological Crystallography* 66.2, pp. 213–221.
- Agre, P., G. M. Preston, B. L. Smith, Jin Sup Jung, S. Raina, C. Moon, W. B. Guggino, and S. Nielsen (1993). "Aquaporin CHIP: The archetypal molecular water channel". In: *American Journal of Physiology - Renal Fluid and Electrolyte Physiology* 265.4 34-4.
- Ågren, G. I., M. Wetterstedt, and M. F. K. Billberger (2012). "Nutrient limitation on terrestrial plant growth – modeling the interaction between nitrogen and phosphorus". In: *New Phytologist* 194.4, pp. 953–960.
- Akasu-Nagayoshi, Y., T. Hayashi, A. Kawabata, N. Shimizu, A. Yamada, N. Yokota, R. Nakato, K. Shirahige, A. Okamoto, and T. Akiyama (2022). "PHOSPHATE exporter XPR1/SLC53A1 is required for the tumorigenicity of epithelial ovarian cancer". In: *Cancer Science* March, pp. 2034–2043.
- Allegretti, M., D. J. Mills, G. McMullan, W. Kühlbrandt, and J. Vonck (2014). "Atomic model of the F420-reducing [NiFe] hydrogenase by electron cryo-microscopy using a direct electron detector". In: *eLife* 3, pp. 1–20.
- Anderson, A. C. (2003). "The Process of Structure-Based Drug Design". In: *Chemistry & Biology*.
- Anheim, M., U. López-Sánchez, D. Giovannini, A. C. Richard, J. Touhami, L. N'Guyen, G. Rudolf, A. Thibault-Stoll, T. Frebourg, D. Hannequin, D. Campion, J. L. Battini, M. Sitbon, and G. Nicolas (2016). "XPR1 mutations are a rare cause of primary familial brain calcification". In: *Journal of Neurology* 263.8, pp. 1559–1564.

- Ansermet, C., M. B. Moor, G. Centeno, M. Auberson, D. Z. Hu, R. Baron, S. Nikolaeva, B. Haenzi, N. Katanaeva, I. Gautschi, V. Katanaev, S. Rotman, R. Koesters, L. Schild, S. Pradervand, O. Bonny, and D. Firsov (2017). “Renal fanconi syndrome and hypophosphatemic rickets in the absence of xenotropic and polytropic retroviral receptor in the nephron”. In: *Journal of the American Society of Nephrology* 28.4, pp. 1073–1078.
- Ardito, F., M. Giuliani, D. Perrone, G. Troiano, and L. L. Muzio (2017). “The crucial role of protein phosphorylation in cell signaling and its use as targeted therapy (Review)”. In: *International Journal of Molecular Medicine* 40.2, pp. 271–280.
- Austin, S. and A. Mayer (2020). “Phosphate Homeostasis – A Vital Metabolic Equilibrium Maintained Through the INPHORS Signaling Pathway”. In: *Frontiers in Microbiology* 11, July, pp. 1–21.
- Azevedo, C. and A. Saiardi (2017). “Eukaryotic Phosphate Homeostasis: The Inositol Pyrophosphate Perspective”. In: *Trends in Biochemical Sciences* 42.3, pp. 219–231.
- Baker, L. A. and J. L. Rubinstein (2010). “Radiation Damage in Electron Cryomicroscopy”. In: *Methods in Enzymology* 481.10.
- Battini, J. L., J. E. J. Rasko, and A. D. Miller (1999). “A human cell-surface receptor for xenotropic and polytropic murine leukemia viruses : Possible role in G protein-coupled signal transduction”. In: 96, February, pp. 1385–1390.
- Bepler, T., A. Morin, M. Rapp, J. Brasch, L. Shapiro, A. J. Noble, and B. Berger (2019). “Positive-unlabeled convolutional neural networks for particle picking in cryo-electron micrographs”. In: *Nature Methods* 16.11, pp. 1153–1160. arXiv: 1803.08207.
- Bergeron, M. J., B. Cl emen on, M. A. Hediger, and D. Markovich (2013). “Molecular Aspects of Medicine SLC13 family of Na⁺-coupled di- and tri-carboxylate / sulfate”. In: *Molecular Aspects of Medicine* 34.2-3, pp. 299–312.
- Bergwitz, C. and J. Harald (2010). “Regulation of Phosphate Homeostasis by PTH , Vitamin D , and FGF23”. In.
- Blaustein, M. P., W. J. Lederer, and L. Annunziato (2008). “Sodium / Calcium Exchange : Its Physiological Implications”. In: *Society* 79.3, pp. 763–854.
- Bocharov, E. V., K. S. Mineev, P. E. Volynsky, Y. S. Ermolyuk, E. N. Tkach, A. G. Sobol, V. V. Chupin, M. P. Kirpichnikov, R. G. Efremov, and A. S. Arseniev (2008). “Spatial structure of the dimeric transmembrane domain of the growth factor receptor ErbB2 presumably corresponding to the receptor active state”. In: *Journal of Biological Chemistry* 283.11, pp. 6950–6956.
- Bondeson, D. P., B. R. Paoletta, A. Asfaw, M. V. Rothberg, T. A. Skipper, C. Langan, G. Mesa, A. Gonzalez, L. E. Surface, K. Ito, M. Kazachkova, W. N. Colgan, A. Warren, J. M. Dempster, J. M. Krill-Burger, M. Ericsson, A. A. Tang, I. Fung, E. S. Chambers, M. Abdusamad, N. Dumont, J. G. Doench, F. Piccioni, D. E. Root, J. Boehm, W. C.

- Hahn, M. Mannstadt, J. M. McFarland, F. Vazquez, and T. R. Golub (2022). “Phosphate dysregulation via the XPR1–KIDINS220 protein complex is a therapeutic vulnerability in ovarian cancer”. In: *Nature Cancer* 3.6, pp. 681–695.
- Bradford, M. M. (1976). “A Rapid and Sensitive Method for the Quantitation of Microgram Quantities of Protein Utilizing the Principle of Protein-Dye Binding”. In: *Analytical Biochemistry* 5.5, pp. 407–415.
- Brilot, A. F., J. Z. Chen, A. Cheng, J. Pan, S. C. Harrison, C. S. Potter, B. Carragher, R. Henderson, N. Grigorieff, and H.-r. Em (2012). “Beam-induced motion of vitrified specimen on holey carbon film”. In: *Journal of Structural Biology* 177.3, pp. 630–637.
- Brown, R. B. and M. S. Razzaque (2018). “Phosphate toxicity and tumorigenesis”. In: *Biochimica et Biophysica Acta - Reviews on Cancer* 1869.2, pp. 303–309.
- Callaway, E. (2020). “Revolutionary cryo-EM is taking over structural biology”. In: *Nature* 578.7794, p. 201.
- Calvo, M. S., E. K. Dunford, and J. Uribarri (2023). “Industrial Use of Phosphate Food Additives: A Mechanism Linking Ultra-Processed Food Intake to Cardiorenal Disease Risk?” In: *Nutrients* 15.16.
- Chari, A. and H. Stark (2023). “Prospects and Limitations of High-Resolution Single-Particle Cryo-Electron Microscopy”. In: *Annual Review of Biophysics*.
- Chen, B. V. Chen, W. B. Arendall, J. J. Headd, D. A. Keedy, R. M. Immormino, G. J. Kapral, L. W. Murray, J. S. Richardson, and D. C. Richardson (2010). “MolProbity: All-atom structure validation for macromolecular crystallography”. In: *Acta Crystallographica Section D: Biological Crystallography* 66.1, pp. 12–21.
- Chen, W. Chen, Q.-l. Li, Q. Pan, H.-y. Zhang, X.-y. Fu, F. Yao, J.-n. Wang, and A.-k. Yang (2019). “Xenotropic and polytropic retrovirus receptor 1 (XPR1) promotes progression of tongue squamous cell carcinoma (TSCC) via activation of NF- κ B signaling”. In: *Journal of Experimental & Clinical Cancer Research* 6, pp. 1–12.
- Cheng, W. W. Cheng, M. J. Arcario, and J. T. Petroff (2022). “Druggable Lipid Binding Sites in Pentameric Ligand-Gated Ion Channels and Transient Receptor Potential Channels”. In: *Frontiers in Physiology* 12.January.
- Cheng, Y. Cheng, N. Grigorieff, P. A. Penczek, and T. Walz (2015). “A Primer to Single-Particle Cryo-Electron Microscopy”. In: *Cell* 161.3, pp. 438–449.
- Chua, E. Y. D., J. H. Mendez, M. Rapp, S. L. Ilca, Y. Z. Tan, K. Maruthi, H. Kuang, C. M. Zimanyi, A. Cheng, E. T. Eng, A. J. Noble, C. S. Potter, and B. Carragher (2022). “Better, Faster, Cheaper: Recent Advances in Cryo-Electron Microscopy”. In: *Annual Review of Biochemistry*.
- Collins, J. F., L. Bai, and F. K. Ghishan (2004). “The SLC20 family of proteins : dual functions as sodium-phosphate cotransporters and viral receptors”. In: pp. 647–652.

- Corradi, V., B. I. Sejdiu, H. Mesa-Galoso, H. Abdizadeh, S. Y. Noskov, S. J. Marrink, and D. P. Tieleman (2019). “Emerging Diversity in Lipid-Protein Interactions”. In: *Chemical Reviews* 119.9, pp. 5775–5848.
- Cridland, C. and G. Gillaspay (2020). “Inositol pyrophosphate pathways and mechanisms: What can we learn from plants?” In: *Molecules* 25.12.
- D’Imprima, E., D. Floris, M. Joppe, R. Sánchez, M. Grininger, and W. Kühlbrandt (2019). “Protein denaturation at the air-water interface and how to prevent it”. In: *eLife* 8, pp. 1–18.
- Dawson, P. A., L. Beck, and D. Markovich (2003). “Hyposulfatemia , growth retardation , reduced fertility , and seizures in mice lacking a functional NaS i -1 gene”. In: 100.23.
- Deng, D., C. Xu, P. Sun, J. Wu, C. Yan, M. Hu, and N. Yan (2014). “Crystal structure of the human glucose transporter GLUT1”. In: *Nature* 510.7503, pp. 121–125.
- Denisov, I. G., Y. V. Grinkova, A. A. Lazarides, and S. G. Sligar (2004). “Directed Self-Assembly of Monodisperse Phospholipid Bilayer Nanodiscs with Controlled Size”. In: *Journal of the American Chemical Society* 126.11, pp. 3477–3487.
- Dietz, K. J., N. Tavakoli, C. Kluge, T. Mimura, S. S. Sharma, G. C. Harris, A. N. Chardonens, and D. Gollack (2001). “Significance of the V-type ATPase for the adaptation to stressful growth conditions and its regulation on the molecular and biochemical level”. In: *Journal of Experimental Botany* 52.363, pp. 1969–1980.
- Dobson, L., I. Reményi, and G. E. Tusnády (2015). “The human transmembrane proteome”. In: *Biology Direct* 10.1, pp. 1–18.
- Dubochet, J., M. Adrian, J.-J. Chang, J.-C. Homo, J. Lepault, A. W. McDowell, and P. Schultz (1988). *Cryo-electron microscopy of vitrified specimens*.
- Emsley, P. and K. Cowtan (2004). “Coot: Model-building tools for molecular graphics”. In: *Acta Crystallographica Section D: Biological Crystallography* 60.12 I, pp. 2126–2132.
- Evans, R., M. O’Neill, A. Pritzel, N. Antropova, A. Senior, T. Green, A. Zidek, R. Bates, S. Blackwell, J. Yim, E. Clancy, R. Jain, P. Kohli, J. Jumper, and D. Hassabis (2022). “Protein complex prediction with AlphaFold-Multimer”. In: *bioRxiv*.
- Farrow, E. G. and K. E. White (2011). “Recent Advances in Renal Phosphate Handling”. In: *Nature Reviews Nephrology* 6.4, pp. 207–217.
- Finkelstein, A. (1976). “Water and nonelectrolyte permeability of lipid bilayer membranes”. In: *Journal of General Physiology* 68.2, pp. 127–135.
- Forster, I. C., N. Hernando, J. Biber, and H. Murer (2013). “Phosphate transporters of the SLC20 and SLC34 families”. In: 34, pp. 386–395.
- Frank, J. (2006). “Three-Dimensional Electron Microscopy of Macromolecular Assemblies: Visualization of Biological Molecules in Their Native State”. In: *Oxford University Press*.

- Frank, J. (2017). “Advances in the field of single-particle cryo-electron microscopy over the last decade”. In: *Nature Protocols* 12.2, pp. 25–35.
- Frauenfeld, J., R. Löving, J. P. Armache, A. F. Sonnen, F. Guettou, P. Moberg, L. Zhu, C. Jegerschöld, A. Flayhan, J. A. Briggs, H. Garoff, C. Löw, Y. Cheng, and P. Nordlund (2016). “A saposin-lipoprotein nanoparticle system for membrane proteins”. In: *Nature Methods* 13.4, pp. 345–351.
- Fromm, S. A., T. A. Bharat, A. J. Jakobi, W. J. Hagen, and C. Sachse (2015). “Seeing tobacco mosaic virus through direct electron detectors”. In: *Journal of Structural Biology* 189.2, pp. 87–97.
- Gadsby, D. C. (2009). “Ion channels versus ion pumps: The principal difference, in principle”. In: *Nature Reviews Molecular Cell Biology* 10.5, pp. 344–352.
- Garaeva, A. A. and D. J. Slotboom (2020). “Elevator-type mechanisms of membrane transport”. In: *Biochemical Society Transactions* 0.March.
- Ghillebert, R., E. Swinnen, P. De Snijder, B. Smets, and J. Winderickx (2011). “Differential roles for the low-affinity phosphate transporters Pho87 and Pho90 in *Saccharomyces cerevisiae*”. In: *Biochemical Journal* 434.2, pp. 243–251.
- Gietz, R. D. and R. H. Schiestl (2007). “High-efficiency yeast transformation using the LiAc/SS carrier DNA/PEG method”. In: *Nature Protocols* 2.1, pp. 31–34.
- Giots, F., M. C. V. Donaton, and J. M. Thevelein (2003). “Inorganic phosphate is sensed by specific phosphate carriers and acts in concert with glucose as a nutrient signal for activation of the protein kinase A pathway in the yeast *Saccharomyces cerevisiae*”. In: 47, pp. 1163–1181.
- Giovannini, D., J. Touhami, P. Charnet, M. Sitbon, and J. L. Battini (2013). “Inorganic Phosphate Export by the Retrovirus Receptor XPR1 in Metazoans”. In: *Cell Reports* 3.6, pp. 1866–1873.
- Glaeser, R. M. (1971). “Limitations to significant information in biological electron microscopy as a result of radiation damage”. In: *Journal of Ultrastructure Research* 36.3-4, pp. 466–482.
- Goddard, T. D., C. C. Huang, E. C. Meng, E. F. Pettersen, G. S. Couch, J. H. Morris, and T. E. Ferrin (2018). “UCSF ChimeraX: Meeting modern challenges in visualization and analysis”. In: *Protein Science* 27.1, pp. 14–25.
- Grassucci, R. A., D. J. Taylor, and J. Frank (2007). “Preparation of macromolecular complexes for cryo-electron microscopy”. In: *Nature Protocols* 2.12, pp. 3239–3246.
- Gu, C., H. N. Nguyen, A. Hofer, H. J. Jessen, X. Dai, H. Wang, and S. B. Shears (2017). “The significance of the bifunctional kinase/phosphatase activities of diphosphoinositol pentakisphosphate kinases (PPIP5Ks) for coupling inositol pyrophosphate cell sig-

- ning to cellular phosphate homeostasis”. In: *Journal of Biological Chemistry* 292.11, pp. 4544–4555.
- Guan, Z., J. Chen, R. Liu, Y. Chen, Q. Xing, Z. Du, M. Cheng, J. Hu, W. Zhang, W. Mei, B. Wan, Q. Wang, J. Zhang, P. Cheng, H. Cai, J. Cao, D. Zhang, J. Yan, P. Yin, M. Hothorn, and Z. Liu (2023). “The cytoplasmic synthesis and coupled membrane translocation of eukaryotic polyphosphate by signal-activated VTC complex”. In: *Nature Communications* 14.1, pp. 1–12.
- Hamburger, D., E. Rezzonico, J. M.-c. Petétot, C. Somerville, and Y. Poirier (2002). “Identification and Characterization of the Arabidopsis PHO1 Gene Involved in Phosphate Loading to the Xylem”. In: 14.April, pp. 889–902.
- He, P., O. Mann-collura, J. Fling, N. Edara, R. Hetz, and M. S. Razzaque (2020). “High phosphate actively induces cytotoxicity by rewiring pro-survival and pro-apoptotic signaling networks in HEK293 and HeLa cells”. In: April, pp. 1–21.
- Hediger, M. A., B. Clémenton, R. E. Burrier, and E. A. Bruford (2013). “The ABCs of membrane transporters in health and disease (SLC series): Introduction”. In: *Molecular Aspects of Medicine* 34.2-3, pp. 95–107.
- Helenius, A. and K. Simons (1975). “Solubilization of membranes by detergents”. In: *Biochimica et biophysica acta* 415, pp. 29–79.
- Henderson, R. (2018). “From Electron Crystallography to Single Particle CryoEM (Nobel Lecture)”. In: *Angewandte Chemie - International Edition* 57.34, pp. 10804–10825.
- Ho, B. K. and F. Gruswitz (2008). “HOLLOW: Generating accurate representations of channel and interior surfaces in molecular structures”. In: *BMC Structural Biology* 8, pp. 1–6.
- Holzhüter, K. and E. R. Geertsma (2020). “Functional (un)cooperativity in elevator transport proteins”. In: *Biochemical Society Transactions* 48.3, pp. 1047–1055.
- Hou, E., Y. Luo, Y. Kuang, C. Chen, X. Lu, L. Jiang, X. Luo, and D. Wen (2020). “Global meta-analysis shows pervasive phosphorus limitation of aboveground plant production in natural terrestrial ecosystems”. In: *Nature Communications* 11.1, pp. 1–9.
- Hsieh, Y.-f., D. Suslov, L. Espen, M. Schiavone, C. Rautengarten, A. Griess-osowski, C. Voiniciuc, and Y. Poirier (2023). “cis -Golgi phosphate transporters harboring an EXS domain are essential for plant growth and development”. In: *Plant Physiology* 192.2, pp. 1000–1015.
- Hürlimann, H. C., B. Pinson, M. Stadler-Waibel, S. C. Zeeman, and F. M. Freimoser (2009). “The SPX domain of the yeast low-affinity phosphate transporter Pho90 regulates transport activity”. In: *EMBO Reports* 10.9, pp. 1003–1008.
- Hürlimann, H. C., M. Stadler-Waibel, T. P. Werner, and F. M. Freimoser (2007). “Pho91 Is a Vacuolar Phosphate Transporter That Regulates Phosphate and Polyphosphate

- Metabolism in *Saccharomyces cerevisiae*". In: *Molecular Biology of the Cell* 18.November, pp. 3250–3263.
- Ikeda, M., A. Kihara, and Y. Igarashi (2006). "Lipid asymmetry of the eukaryotic plasma membrane: Functions and related enzymes". In: *Biological and Pharmaceutical Bulletin* 29.8, pp. 1542–1546.
- Jenkins, H. D. and K. P. Thakur (1979). "Reappraisal of thermochemical radii for complex ions". In: *Journal of Chemical Education* 56.9, pp. 576–577.
- Jorgensen, P. L., K. O. Håkansson, and S. J. Karlish (2003). "Structure and Mechanism of Na,K-ATPase: Functional Sites and Their Interactions". In: *Annual Review of Physiology* 65, pp. 817–849.
- Joyeux, L. and P. A. Penczek (2002). "Efficiency of 2D alignment methods". In: *Ultramicroscopy* 92, pp. 33–46.
- Jumper, J., R. Evans, A. Pritzel, T. Green, M. Figurnov, O. Ronneberger, K. Tunyasuvunakool, R. Bates, A. Židek, A. Potapenko, A. Bridgland, C. Meyer, S. A. Kohl, A. J. Ballard, A. Cowie, B. Romera-Paredes, S. Nikolov, R. Jain, J. Adler, T. Back, S. Petersen, D. Reiman, E. Clancy, M. Zielinski, M. Steinegger, M. Pacholska, T. Berghammer, S. Bodenstein, D. Silver, O. Vinyals, A. W. Senior, K. Kavukcuoglu, P. Kohli, and D. Hassabis (2021). "Highly accurate protein structure prediction with AlphaFold". In: *Nature* 596.7873, pp. 583–589.
- Kahl, F., V. Gerheim, M. Linck, H. Müller, R. Schillinger, and S. Uhlemann (2019). *Test and characterization of a new post-column imaging energy filter*. Vol. 212. Elsevier Inc., pp. 35–70.
- Kalantar-Zadeh, K., L. Gutekunst, R. Mehrotra, C. P. Kovesdy, R. Bross, C. S. Shinaberger, N. Noori, R. Hirschberg, D. Benner, A. R. Nissenson, and J. D. Kopple (2010). "Understanding sources of dietary phosphorus in the treatment of patients with chronic kidney disease". In: *Clinical Journal of the American Society of Nephrology* 5.3, pp. 519–530.
- Kendrick, J., B. Kestenbaum, and M. Chonchol (2011). "Phosphate and Cardiovascular Disease". In: *Adv Chronic Kidney Disease* 18.2, pp. 113–119.
- Kim, S., T. J. Jeon, A. Oberai, D. Yang, J. J. Schmidt, and J. U. Bowie (2005). "Transmembrane glycine zippers: Physiological and pathological roles in membrane proteins". In: *Proceedings of the National Academy of Sciences of the United States of America* 102.40, pp. 14278–14283.
- Knowles, T. J., R. Finka, C. Smith, Y. P. Lin, T. Dafforn, and M. Overduin (2009). "Membrane proteins solubilized intact in lipid containing nanoparticles bounded by styrene maleic acid copolymer". In: *Journal of the American Chemical Society* 131.22, pp. 7484–7485.

- Komaba, H. and M. Fukagawa (2016). “Phosphate—a poison for humans?” In: *Kidney International* 90.4, pp. 753–763.
- Kühlbrandt, W. (2004). “Biology, structure and mechanism of P-type ATPases”. In: *Nature Reviews Molecular Cell Biology* 5.4, pp. 282–295.
- Kühlbrandt, W. (2014). “The resolution revolution”. In: *Science* 343.6178, pp. 1443–1444.
- Kühlbrandt, W. (2019). “Structure and Mechanisms of F-Type ATP Synthases”. In: *Annual Review of Biochemistry* 88.7, pp. 515–549.
- Kühlbrandt, W., D.-N. Wang, and Y. Fujiyoshi (1994). “Atomic model of plant light-harvesting complex by electron crystallography”. In: *Nature* 264. February, pp. 1105–1111.
- Laemmli, U. K. (1970). “Cleavage of Structural Proteins during the Assembly of the Head of Bacteriophage T4”. In: *Nature* 227, pp. 680–685.
- Lee, C. Lee, H. J. Kang, C. Von Ballmoos, S. Newstead, P. Uzdavinyas, D. L. Dotson, S. Iwata, O. Beckstein, A. D. Cameron, and D. Drew (2013). “A two-domain elevator mechanism for sodium/proton antiport”. In: *Nature* 501.7468, pp. 573–577.
- Lee, S. Lee, P. A. Dawson, A. K. Hewavitharana, P. N. Shaw, and D. Markovich (2006). “Disruption of NaS1 Sulfate Transport Function in Mice Leads to Enhanced Acetaminophen-Induced Hepatotoxicity”. In: 3, pp. 1241–1247.
- Legati, A., D. Giovannini, G. Nicolas, U. López-Sánchez, B. Quintáns, J. R. Oliveira, R. L. Sears, E. M. Ramos, E. Spiteri, M. J. Sobrido, Á. Carracedo, C. Castro-Fernández, S. Cubizolle, B. L. Fogel, C. Goizet, J. C. Jen, S. Kirdlar, A. E. Lang, Z. Miedzybrodzka, W. Mitarnun, M. Paucar, H. Paulson, J. Pariente, A. C. Richard, N. S. Salins, S. A. Simpson, P. Striano, P. Svenningsson, F. Tison, V. K. Unni, O. Vanakker, M. W. Wessels, S. Wetchaphanphesat, M. Yang, F. Boller, D. Champion, D. Hannequin, M. Sitbon, D. H. Geschwind, J. L. Battini, and G. Coppola (2015). “Mutations in XPR1 cause primary familial brain calcification associated with altered phosphate export”. In: *Nature Genetics* 47.6, pp. 579–581.
- Lemmon, M. A., J. M. Flanagan, H. R. Treutlein, J. Zhang, and D. M. Engelman (1992). “Sequence Specificity in the Dimerization of Transmembrane α -Helices”. In: *Biochemistry* 31.51, pp. 12719–12725.
- Levin, E., T. Bendory, N. Boumal, J. Kileel, and A. Singer (2017). “3D ab initio modelling in cryo-EM by autocorrelation analysis”. In: *arXiv*. arXiv: arXiv:1710.08076v2.
- Levy, S., M. Kafri, M. Carmi, and N. Barkai (2011). “The Competitive Advantage of a Dual-Transporter System”. In: 1408.2011.
- Li, X., C. Gu, S. Hostachy, S. Sahu, C. Wittwer, H. J. Jessen, D. Fiedler, H. Wang, and S. B. Shears (2020). “Control of XPR1-dependent cellular phosphate efflux by InsP8 is an

- exemplar for functionally-exclusive inositol pyrophosphate signaling”. In: *Proceedings of the National Academy of Sciences of the United States of America* 117.7, pp. 3568–3574.
- Locher, K. P. (2009). “Structure and mechanism of ATP-binding cassette transporters”. In: *Philosophical Transactions of the Royal Society B: Biological Sciences* 364.1514, pp. 239–245.
- López-Sánchez, U., G. Nicolas, A. C. Richard, D. Maltête, M. Charif, X. Ayrignac, C. Goizet, J. Touhami, G. Labesse, J. L. Battini, and M. Sitbon (2019). “Characterization of XPR1/SLC53A1 variants located outside of the SPX domain in patients with primary familial brain calcification”. In: *Scientific Reports* 9.1, pp. 1–9.
- Madeira, F., M. Pearce, A. R. Tivey, P. Basutkar, J. Lee, O. Edbali, N. Madhusoodanan, A. Kolesnikov, and R. Lopez (2022). “Search and sequence analysis tools services from EMBL-EBI in 2022”. In: *Nucleic Acids Research* 50.W1, W276–W279.
- Mancini, F. R., A. Affret, C. Dow, B. Balkau, F. Clavel-Chapelon, F. Bonnet, M. C. Boutron-Ruault, and G. Fagherazzi (2018). “High dietary phosphorus intake is associated with an increased risk of type 2 diabetes in the large prospective E3N cohort study”. In: *Clinical Nutrition* 37.5, pp. 1625–1630.
- Mancusso, R., G. G. Gregorio, Q. Liu, and D.-N. Wang (2012). “Structure and mechanism of a bacterial sodium-dependent dicarboxylate transporter”. In: *Nature* 491.7425, pp. 622–626.
- Martens, C., R. A. Stein, M. Masureel, A. Roth, S. Mishra, R. Dawaliby, A. Konijnenberg, F. Sobott, C. Govaerts, and H. S. McHaourab (2016). “Lipids modulate the conformational dynamics of a secondary multidrug transporter”. In: *Nature Structural and Molecular Biology* 23.8, pp. 744–751.
- McDowall, A. W., J.-J. Chang, R. Freeman, J. Lepault, C. A. Walter, and J. Dubochet (1983). “Electron microscopy of frozen hydrated sections of vitreous ice and vitrified biological samples”. In: *Journal of Microscopy* 131, pp. 1–9.
- Mulugu, S., W. Bai, P. C. Fridy, R. J. Bastidas, J. C. Otto, D. E. Dollins, T. a. Haystead, A. a. Ribeiro, and J. D. York (2007). “A Conserved Family of Enzymes That Phosphorylate Inositol Hexakisphosphate”. In: *Science* 106.2007, pp. 106–109.
- Müthing, J. and M. Radloff (1998). “Nanogram detection of phospholipids on thin-layer chromatograms”. In: *Analytical Biochemistry* 257.1, pp. 67–70.
- Nakane, T., A. Kotecha, A. Sente, G. McMullan, S. Masiulis, P. M. Brown, I. T. Grigoras, L. Malinauskaite, T. Malinauskas, J. Miehl, T. Uchański, L. Yu, D. Karia, E. V. Pechnikova, E. de Jong, J. Keizer, M. Bischoff, J. McCormack, P. Tiemeijer, S. W. Hardwick, D. Y. Chirgadze, G. Murshudov, A. R. Aricescu, and S. H. Scheres (2020). “Single-particle cryo-EM at atomic resolution”. In: *Nature* 587.7832, pp. 152–156.

- Naydenova, K., P. Jia, and C. J. Russo (2020). “Cryo-EM with sub-1 Å specimen movement”. In: *Science* 370.6513, pp. 223–226.
- Neumann, J., D. Rose-Sperling, and U. A. Hellmich (2017). “Diverse relations between ABC transporters and lipids: An overview”. In: *Biochimica et Biophysica Acta - Biomembranes* 1859.4, pp. 605–618.
- Nogales, E. and S. H. Scheres (2015). “Cryo-EM: A Unique Tool for the Visualization of Macromolecular Complexity”. In: *Molecular Cell* 58.4, pp. 677–689.
- Ogawa, N., J. DeRisi, and P. O. Brown (2000). “New components of a system for phosphate accumulation and polyphosphate metabolism in *Saccharomyces cerevisiae* revealed by genomic expression analysis”. In: *Molecular Biology of the Cell* 11.12, pp. 4309–4321.
- Ohi, M., Y. Li, Y. Cheng, and T. Walz (2004). “Negative Staining and Image Classification – Powerful Tools in Modern Electron Microscopy”. In: *Biological Procedures Online* 6.1, pp. 23–34.
- Orlova, E. V. and H. R. Saibil (2011). “Structural Analysis of Macromolecular Assemblies by Electron Microscopy”. In: *Chemical Reviews*.
- Pantelic, R. S., J. C. Meyer, U. Kaiser, and H. Stahlberg (2012). “The application of graphene as a sample support in transmission electron microscopy”. In: *Solid State Communications* 152.15, pp. 1375–1382. arXiv: 1204.6647.
- Park, E. and R. Mackinnon (2018). “Structure of the CLC-1 chloride channel from homo sapiens”. In: *eLife* 7, pp. 1–24.
- Parker, J. L. and S. Newstead (2014). “Method to increase the yield of eukaryotic membrane protein expression in *saccharomyces cerevisiae* for structural and functional studies”. In: *Protein Science* 23.9, pp. 1309–1314.
- Pattison-Granberg, J. and B. L. Persson (2000). “Regulation of Cation-Coupled High-Affinity Phosphate Uptake in the Yeast *Saccharomyces cerevisiae*”. In: 182.17, pp. 5017–5019.
- Pedersen, B. P., H. Kumar, A. B. Waight, A. J. Risenmay, Z. Roe-zurz, B. H. Chau, A. Schlessinger, M. Bonomi, W. Harries, A. Sali, A. K. Johri, and R. M. Stroud (2013). “Crystal structure of a eukaryotic phosphate transporter”. In: *Nature* 496.7446, pp. 533–536.
- Pelham, H. R., K. G. Hardwick, and M. J. Lewis (1988). “Sorting of soluble ER proteins in yeast.” In: *The EMBO journal* 7.6, pp. 1757–1762.
- Penczek, P. A. (2010). “Image Restoration in Cryo-electron Microscopy Pawel”. In: *Methods in Enzymology* 482.1, pp. 35–72. arXiv: NIHMS150003.
- Penido, M. G. M. G. and U. S. Alon (2012). “Phosphate homeostasis and its role in bone health”. In: pp. 2039–2048.

- Persson, B. L., A. Berhe, U. Fristedt, P. Martinez, J. Pattison, J. Petersson, and R. Weinander (1998). "Phosphate permeases of *Saccharomyces cerevisiae*". In: 1365, pp. 23–30.
- Persson, B. L., J. O. Lagerstedt, J. R. Pratt, J. Pattison-Granberg, K. Lundh, S. Shokrollahzadeh, and F. Lundh (2003). "Regulation of phosphate acquisition in *Saccharomyces cerevisiae*". In: *Current Genetics* 43.4, pp. 225–244.
- Pettersen, E. F., T. D. Goddard, C. C. Huang, G. S. Couch, D. M. Greenblatt, E. C. Meng, and T. E. Ferrin (2004). "UCSF Chimera - A visualization system for exploratory research and analysis". In: *Journal of Computational Chemistry* 25.13, pp. 1605–1612.
- Popova, Y., P. Thayumanavan, E. Lonati, M. Agrochão, and J. M. Thevelein (2009). "Transport and signaling through the phosphate-binding site of the yeast Pho84 phosphate transceptor". In.
- Pravda, L., D. Sehnal, D. Toušek, V. Navrátilová, V. Bazgier, K. Berka, R. S. Vařeková, J. Koča, and M. Otyepka (2018). "MOLEonline: A web-based tool for analyzing channels, tunnels and pores (2018 update)". In: *Nucleic Acids Research* 46.W1, W368–W373.
- Punjani, A. and D. J. Fleet (2021). "3D variability analysis : Resolving continuous flexibility and discrete heterogeneity from single particle cryo-EM". In: *Journal of Structural Biology* 213.2, p. 107702.
- Punjani, A., J. L. Rubinstein, D. J. Fleet, and M. A. Brubaker (2017). "cryoSPARC : algorithms for rapid unsupervised cryo-EM structure determination". In: *Nature Methods* 14.3.
- Punjani, A., H. Zhang, and D. J. Fleet (2020). "Non-uniform refinement: adaptive regularization improves single-particle cryo-EM reconstruction". In: *Nature Methods* 17.12, pp. 1214–1221.
- Ramos, E. M., M. Carecchio, R. Lemos, J. Ferreira, A. Legati, R. L. Sears, S. C. Hsu, C. Panteghini, L. Magistrelli, E. Salsano, S. Esposito, F. Taroni, A. C. Richard, C. Tranchant, M. Anheim, X. Ayrignac, C. Goizet, M. Vidailhet, D. Maltete, D. Wallon, T. Frebourg, L. Pimentel, D. H. Geschwind, O. Vanakker, D. Galasko, B. L. Fogel, A. M. Innes, A. Ross, W. B. Dobyns, D. Alcantara, M. O'Driscoll, D. Hannequin, D. Campion, J. R. Oliveira, B. Garavaglia, G. Coppola, and G. Nicolas (2018). "Primary brain calcification: an international study reporting novel variants and associated phenotypes". In: *European Journal of Human Genetics* 26.10, pp. 1462–1477.
- Reisinger, V. and L. A. Eichacker (2006). "Analysis of membrane protein complexes by blue native PAGE". In: *Proteomics* 1.1-2 SUPPL. Pp. 6–15.
- Reyes, N., C. Ginter, and O. Boudker (2009). "Transport mechanism of a bacterial homologue of glutamate transporters". In: *Nature* 462.7275, pp. 880–885.
- Rohou, A. and N. Grigorieff (2015). "CTFFIND4 : Fast and accurate defocus estimation from electron micrographs". In: *Journal of Structural Biology* 192.2, pp. 216–221.

- Rosenthal, P. B. and R. Henderson (2003). “Optimal Determination of Particle Orientation, Absolute Hand, and Contrast Loss in Single-particle Electron Cryomicroscopy”. In: *Journal of Molecular Biology*, pp. 721–745.
- Sanchez-Garcia, R., J. Gomez-Blanco, A. Cuervo, J. M. Carazo, C. O. S. Sorzano, and J. Vargas (2021). “DeepEMhancer: a deep learning solution for cryo-EM volume post-processing”. In: *Nature Communications Biology* 4.1, pp. 1–8.
- Sardana, R., C. M. Highland, B. E. Straight, C. F. Chavez, J. C. Fromme, and S. D. Emr (2021). “Golgi membrane protein Erd1 is essential for recycling a subset of Golgi glycosyltransferases”. In: *eLife* 10, pp. 1–16.
- Sauer, D. B., J. Song, B. Wang, J. K. Hilton, N. K. Karpowich, J. A. Mindell, W. J. Rice, and D.-n. Wang (2021). “Structure and inhibition mechanism of the human citrate transporter NaCT”. In: *Nature* 591. September 2020.
- Sauer, D. B., N. Trebesch, J. J. Marden, N. Cocco, J. Song, A. Koide, S. Koide, E. Tajkhorshid, and D. N. Wang (2020). “Structural basis for the reaction cycle of DASS dicarboxylate transporters”. In: *eLife* 9, pp. 1–74.
- Scheres, S. H. W. (2012). “RELION : Implementation of a Bayesian approach to cryo-EM structure determination”. In: *Journal of Structural Biology* 180.3, pp. 519–530.
- Scheres, S. H. W. (2015). “Semi-automated selection of cryo-EM particles in RELION-1.3”. In: *Journal of Structural Biology* 189.2, pp. 114–122.
- Scheres, S. H. W. (2016). “Processing of Structurally Heterogeneous Cryo-EM Data in RELION”. In: *Methods in Enzymology* 579, pp. 125–157.
- Scheres, S. H. W. and S. Chen (2012). “Prevention of overfitting in cryo-EM structure determination”. In: *Nature Methods* 9.9, pp. 853–854.
- Schröder, R. R., W. Hofmann, and J. F. Ménéret (1990). “Zero-loss energy filtering as improved imaging mode in cryoelectronmicroscopy of frozen-hydrated specimens”. In: *Journal of Structural Biology* 105.1-3, pp. 28–34.
- Secco, D., C. Wang, B. A. Arpat, Z. Wang, Y. Poirier, S. D. Tyerman, P. Wu, H. Shou, and J. Whelan (2012a). “The emerging importance of the SPX domain-containing proteins in phosphate homeostasis”. In: *New Phytologist* 193.4, pp. 842–851.
- Secco, D., C. Wang, H. Shou, and J. Whelan (2012b). “Phosphate homeostasis in the yeast *Saccharomyces cerevisiae*, the key role of the SPX domain-containing proteins”. In: *FEBS Letters* 586.4, pp. 289–295.
- Sehnal, D., R. S. Vařeková, K. Berka, L. Pravda, V. Navrátilová, P. Banáš, C. M. Ionescu, M. Otyepka, and J. Koča (2013). “MOLE 2.0: Advanced approach for analysis of biomacromolecular channels”. In: *Journal of Cheminformatics* 5.8, pp. 1–13.

- Shears, S. B. (2018). “Intimate connections: Inositol pyrophosphates at the interface of metabolic regulation and cell signaling”. In: *Journal of Cellular Physiology* 233.3, pp. 1897–1912.
- Spain, B. H., D. Koo, M. Ramakrishnan, B. Dzudzor, and J. Colicelli (1995). “Truncated Forms of a Novel Yeast Protein Suppress the Lethality of a G Protein α Subunit Deficiency by Interacting with the β Subunit γ ”. In: *Journal of Biological Chemistry* 270.43, pp. 25435–25444.
- Tang, L. O., B. H. Hou, X. N. Zhang, Z. Y. Xi, C. X. Li, and L. Xu (2021). “Biallelic XPR1 mutation associated with primary familial brain calcification presenting as paroxysmal kinesigenic dyskinesia with infantile convulsions”. In: *Brain and Development* 43.2, pp. 331–336.
- Tascón, I., J. S. Sousa, R. A. Corey, D. J. Mills, D. Griwatz, N. Aumüller, V. Mikusevic, P. J. Stansfeld, J. Vonck, and I. Hänel (2020). “Structural basis of proton-coupled potassium transport in the KUP family”. In: *Nature Communications* 11.1, pp. 1–10.
- Terwilliger, T. C., S. J. Ludtke, R. J. Read, P. D. Adams, and P. V. Afonine (2020). “Improvement of cryo-EM maps by density modification”. In: *Nature Methods* 17. September.
- Thompson, R. F., M. Walker, C. A. Siebert, S. P. Muench, and N. A. Ranson (2016). “An introduction to sample preparation and imaging by cryo-electron microscopy for structural biology”. In: *METHODS* 2016.
- Tonelli, M., F. Sacks, M. Pfeffer, Z. Gao, and G. Curhan (2005). “Relation between serum phosphate level and cardiovascular event rate in people with coronary disease”. In: *Circulation* 112.17, pp. 2627–2633.
- Tsai, J. Y., C. H. Chu, M. G. Lin, Y. H. Chou, R. Y. Hong, C. Y. Yen, C. D. Hsiao, and Y. J. Sun (2020). “Structure of the sodium-dependent phosphate transporter reveals insights into human solute carrier SLC20”. In: *Science Advances* 6.32, pp. 1–10.
- Vaughan, A. E., R. Mendoza, R. Aranda, J.-I. Battini, and A. D. Miller (2012). “Xpr1 Is an Atypical G-Protein-Coupled Receptor That Mediates Xenotropic and Polytropic Murine Retrovirus Neurotoxicity”. In: pp. 1661–1669.
- Vervloet, M. G., S. Sezer, Z. A. Massy, L. Johansson, M. Cozzolino, and D. Fouque (2017). “The role of phosphate in kidney disease”. In: *Nature Reviews Nephrology* 13.1, pp. 27–38.
- Vicent, I., A. Navarro, J. M. Mulet, S. Sharma, and R. Serrano (2015). “Uptake of inorganic phosphate is a limiting factor for *Saccharomyces cerevisiae* during growth at low temperatures”. In: *FEMS Yeast Research* 15.3, pp. 1–13.
- Wagner, T., F. Merino, M. Stabrin, T. Moriya, C. Antoni, A. Apelbaum, P. Hagel, O. Sitsel, T. Raisch, D. Prumbaum, D. Quentin, D. Roderer, S. Tacke, B. Siebolds, E. Schubert, T. R. Shaikh, P. Lill, C. Gatsogiannis, and S. Raunser (2019). “SPHIRE-crYOLO is a fast

- and accurate fully automated particle picker for cryo-EM”. In: *Nature Communications Biology* 2019, pp. 1–13.
- Wang and L. Wang (2022). “Bioinformatics analyses proposed xenotropic and polytropic retrovirus receptor 1 as a potential diagnostic and prognostic biomarker and immunotherapeutic target in head and neck squamous cell carcinoma”. In: *Auris Nasus Larynx* 50.1, pp. 134–150.
- Wang, Y. Wang, C. Ribot, E. Rezzonico, and Y. Poirier (2004). “Structure and Expression Profile of the Arabidopsis PHO1 Gene Family Indicates a Broad Role in Inorganic Phosphate Homeostasis 1”. In: *Plant Physiology* 135.May, pp. 400–411.
- Wege, S., G. A. Khan, J. Y. Jung, E. Vogiatzaki, S. Pradervand, I. Aller, A. J. Meyer, and Y. Poirier (2016). “The EXS Domain of PHO1 participates in the response of shoots to phosphate deficiency via a root-to-shoot signal1[OPEN]”. In: *Plant Physiology* 170.1, pp. 385–400.
- Weissenberger, G., R. J. Henderikx, and P. J. Peters (2021). “Understanding the invisible hands of sample preparation for cryo-EM”. In: *Nature Methods* 18.5, pp. 463–471.
- Wetlaufer, D. B. (1973). “Nucleation, rapid folding, and globular intrachain regions in proteins.” In: *Proceedings of the National Academy of Sciences* 70.3, pp. 697–701.
- Wild, R., R. Gerasimaite, J. Y. Jung, V. Truffault, I. Pavlovic, A. Schmidt, A. Saiardi, H. Jacob Jessen, Y. Poirier, M. Hothorn, and A. Mayer (2016). “Control of eukaryotic phosphate homeostasis by inositol polyphosphate sensor domains”. In: *Science* 352.6288, pp. 986–990.
- Wilson, M. S., H. J. Jessen, and A. Saiardi (2019). “The inositol hexakisphosphate kinases IP6K1 and -2 regulate human cellular phosphate homeostasis, including XPR1-mediated phosphate export”. In: *Journal of Biological Chemistry* 294.30, pp. 11597–11608.
- Wöhlert, D., M. J. Grötzinger, W. Kühlbrandt, and Ö. Yildiz (2015). “Mechanism of Na⁺-dependent citrate transport from the structure of an asymmetrical CitS dimer”. In: *eLife*, pp. 1–18.
- Wu, M. and G. C. Lander (2020). “How low can we go? Structure determination of small biological complexes using single-particle cryo-EM”. In: *Current Opinion in Structural Biology* 64, pp. 9–16.
- Wykoff, D. D. and E. K. O’Shea (2001). “Phosphate transport and sensing in *Saccharomyces cerevisiae*”. In: *Genetics* 159.4, pp. 1491–1499.
- Wykoff, D. D., A. H. Rizvi, J. M. Raser, B. Margolin, and E. K. O’Shea (2007). “Positive Feedback Regulates Switching of Phosphate Transporters in *S. cerevisiae*”. In: *Molecular Cell* 27.6, pp. 1005–1013.

- Yamada, S., M. Tokumoto, N. Tatsumoto, M. Taniguchi, H. Noguchi, T. Nakano, K. Masutani, H. Ooboshi, K. Tsuruya, and T. Kitazono (2014). "Phosphate overload directly induces systemic inflammation and malnutrition as well as vascular calcification in uremia". In: *American Journal of Physiology - Renal Physiology* 306.12, pp. 1418–1428.
- Yang, N. J. and M. J. Hinner (2015). "Getting Across the Cell Membrane: An Overview for Small Molecules, Peptides, and Proteins". In: *Methods in Molecular Biology*, pp. 1–267.
- Yonekura, K., R. Matsuoka, Y. Yamashita, T. Yamane, M. Ikeguchi, A. Kidera, and S. Maki-Yonekura (2018). "Ionic scattering factors of atoms that compose biological molecules". In: *IUCrj* 5, pp. 348–353.
- Zhang, K. (2016). "Gctf : Real-time CTF determination and correction". In: *Journal of Structural Biology* 193.1, pp. 1–12.
- Zheng, S. Q., E. Palovcak, J.-p. Armache, K. A. Verba, and D. A. Agard (2017). "Motion-Cor2 - anisotropic correction of beam-induced motion for improved cryo-electron microscopy". In: *Nature Methods* 14.4, pp. 331–332.
- Zhou, W., G. Fiorin, C. Anselmi, H. A. Karimi-Varzaneh, H. Poblete, L. R. Forrest, and J. D. Faraldo-Gómez (2019). "Large-scale state-dependent membrane remodeling by a transporter protein". In: *eLife* 8, pp. 1–20.
- Zimmermann, L., A. Stephens, S. Z. Nam, D. Rau, J. Kübler, M. Lozajic, F. Gabler, J. Söding, A. N. Lupas, and V. Alva (2017). "A Completely Reimplemented MPI Bioinformatics Toolkit with a New HHpred Server at its Core". In: *Journal of Molecular Biology* 430.15, pp. 2237–2243.
- Zivanov, J., T. Nakane, and S. H. W. Scheres (2019). "A Bayesian approach to beam-induced motion correction in cryo-EM single-particle analysis". In: *IUCrj*, pp. 5–17.

Supplement

Table S1: Processing and refinement statistics of ScPho90 datasets.

Parameters	ScPho90 phos- phate	ScPho90 phosphate- free sym.	ScPho90 phosphate- free asym.
Data processing			
Movies	4,942	13,845	
Initial particles	476,290	1,857,014	
Final particles	192,548	304,932	33,833
Symmetry	C2	C2	C1
Map resolution (Å)	2.62	2.29	3.15
FSC threshold	0.143		
Map sharpening B factor (Å)	106.8	79.7	92.0
Model composition			
Non-hydrogen atoms	7,762	8,066	7,150
Protein residues	970	978	953
Ligands	14	8	0
B factors			
Protein	57.32	39.34	49.83
Ligands	52.00	43.40	
R.m.s deviations			
Bond lengths (Å)	0.003	0.003	0.003
Bond angles	0.647	0.556	0.536
Ramachandran plot			
Favored (%)	97.71	98.04	97.57
Allowed (%)	2.29	1.96	2.43
Disallowed (%)	0	0	0
Validation			
MolProbity Score	1.77	1.73	1.47
Clashscore	7.54	8.05	6.85
Poor rotamers (%)	2.41	2.39	0.39

Table S2: Processing and refinement statistics of ScSyt1 datasets.

Parameters	ScSyt1 phosphate- free	ScSyt1 phosphate/InsP₆	ScSyt1 phosphate/InsP₆ SPX
Data processing			
Movies	16,970	13,902	
Initial particles	2,796,653	2,212,011	
Final particles	219,125	383,541	110,211
Symmetry	C2		
Map resolution (Å)	2.33	2.19	2.44
FSC threshold	0.143		
Map sharpening B factor (Å)	82.1	76.8	74.8
Model composition			
Non-hydrogen atoms	7520	7506	10300
Protein residues	888	884	1202
Ligands	2	6	6
B factors			
Protein	50.05	41.48	63.65
Ligands	20.00	42.59	42.91
R.m.s deviations			
Bond lengths (Å)	0.009	0.003	0.003
Bond angles	0.984	0.513	0.586
Ramachandran plot			
Favored (%)	97.83	98.39	97.61
Allowed (%)	2.05	1.61	2.39
Disallowed (%)	0.11	0	0
Validation			
MolProbity Score	1.78	1.63	1.98
Clashscore	12.84	6.24	8.58
Poor rotamers (%)	1.52	2.41	3.78

Table S3: Processing and refinement statistics of HsXpr1 datasets.

Parameters	HsXpr1 phos- phate	HsXpr1 phosphate- free	HsXpr1 (yeast)
Data processing			
Movies	15,329	21,128	15,249
Initial particles	3,274,880	5,228,566	2,377,606
Final particles	36,620	108,051	34,951
Symmetry	C2	C1	C2
Map resolution (Å)	3.45	3.01	6.34
FSC threshold	0.143		
Map sharpening B factor (Å)	87.4	80.4	518.7
Model composition			
Non-hydrogen atoms	6270	6494	
Protein residues	748	766	
Ligands	2	2	
B factors			
Protein	86.84	54.68	
Ligands	98.90	40.31	
R.m.s deviations			
Bond lengths (Å)	0.003	0.004	
Bond angles	0.669	0.696	
Ramachandran plot			
Favored (%)	94.02	94.08	
Allowed (%)	5.98	5.79	
Disallowed (%)	0	0.13	
Validation			
MolProbity Score	2.09	2.14	
Clashscore	15.26	17.59	
Poor rotamers (%)	0.60	0.15	

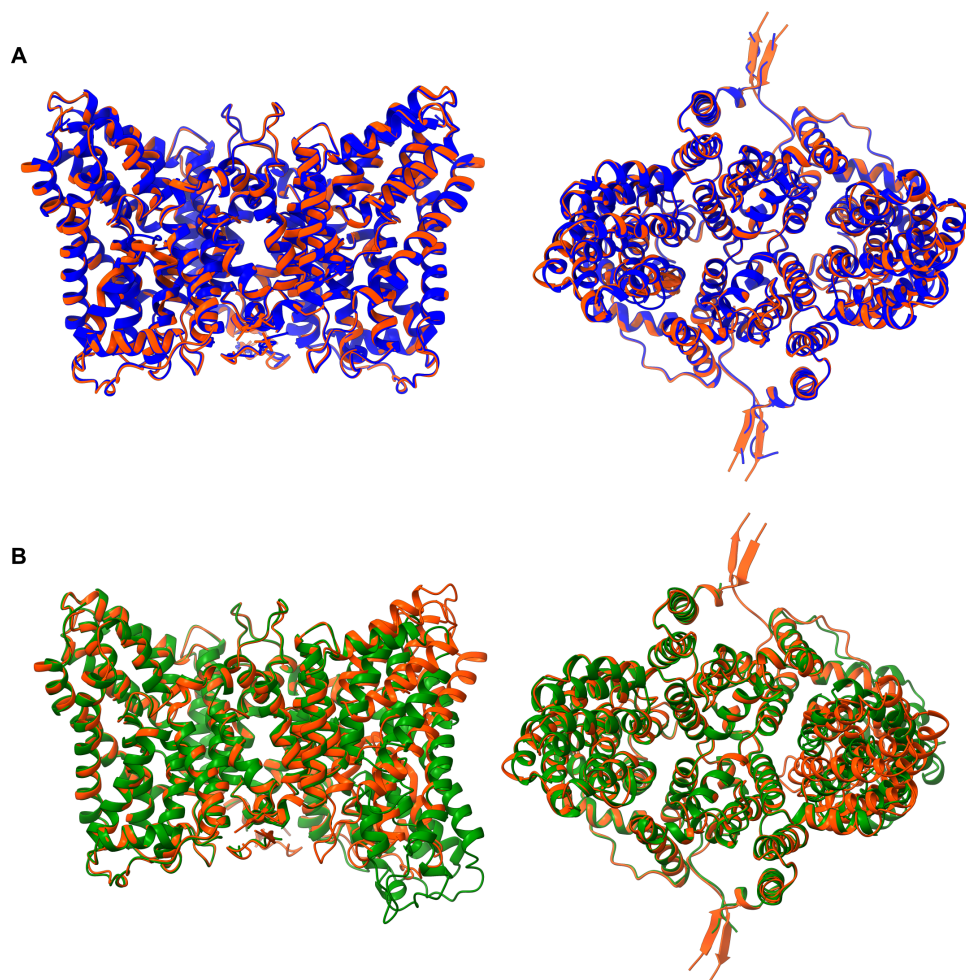


Figure S1: Comparison of ScPho90 models. (A) Comparison of symmetric ScPho90 models in the presence (blue) and absence (orange) of phosphate seen along the membrane plane (left) and from the cytoplasm (right). (B) Comparison of the symmetric (orange) and asymmetric (green) models of ScPho90 in the absence of phosphate seen along the membrane plane (left) and from the cytoplasm (right).

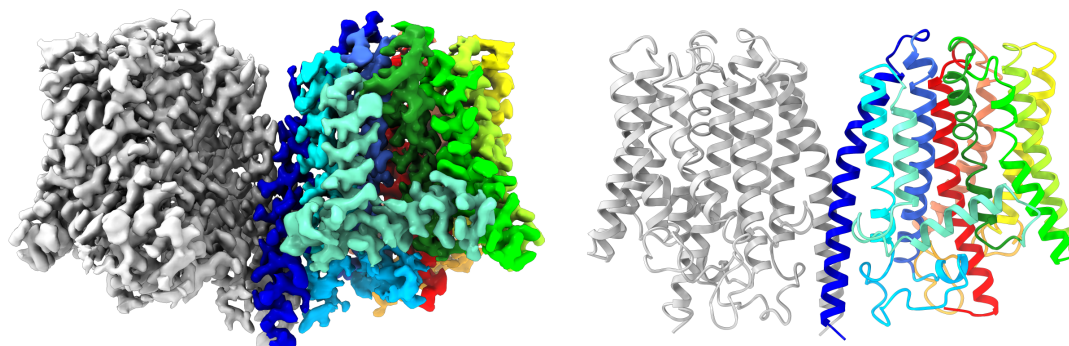


Figure S2: Map and model of the TM part of ScSyg1 in the presence of phosphate/InsP₆. One protomer of the ScSyg1 map (left) and model (right) is colored in grey while the other one is colored by individual transmembrane helices.

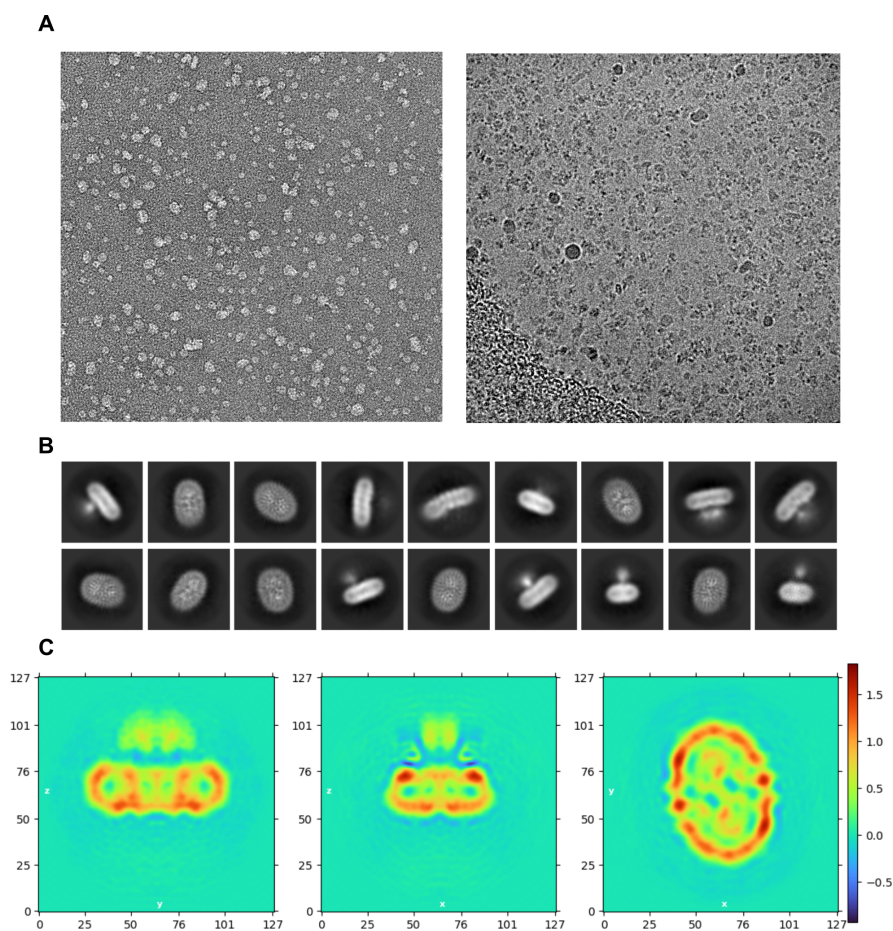


Figure S3: HsXpr1 sample screening by electron microscopy. (A) Images of purified HsXpr1 either stained with uranyl formate (left) or embedded in a thin layer of vitreous ice (right). Both images show homogeneously sized particles and good particle distributions. (B) 2D classes of HsXpr1. 2D classes show both top and side views. In top views the helix organisation can be seen as well as the twofold symmetry of dimeric Sc-Syg1 particles. (C) Unidirectional views of a HsXpr1 3D reconstruction with an overall resolution of approximately 12 Å.

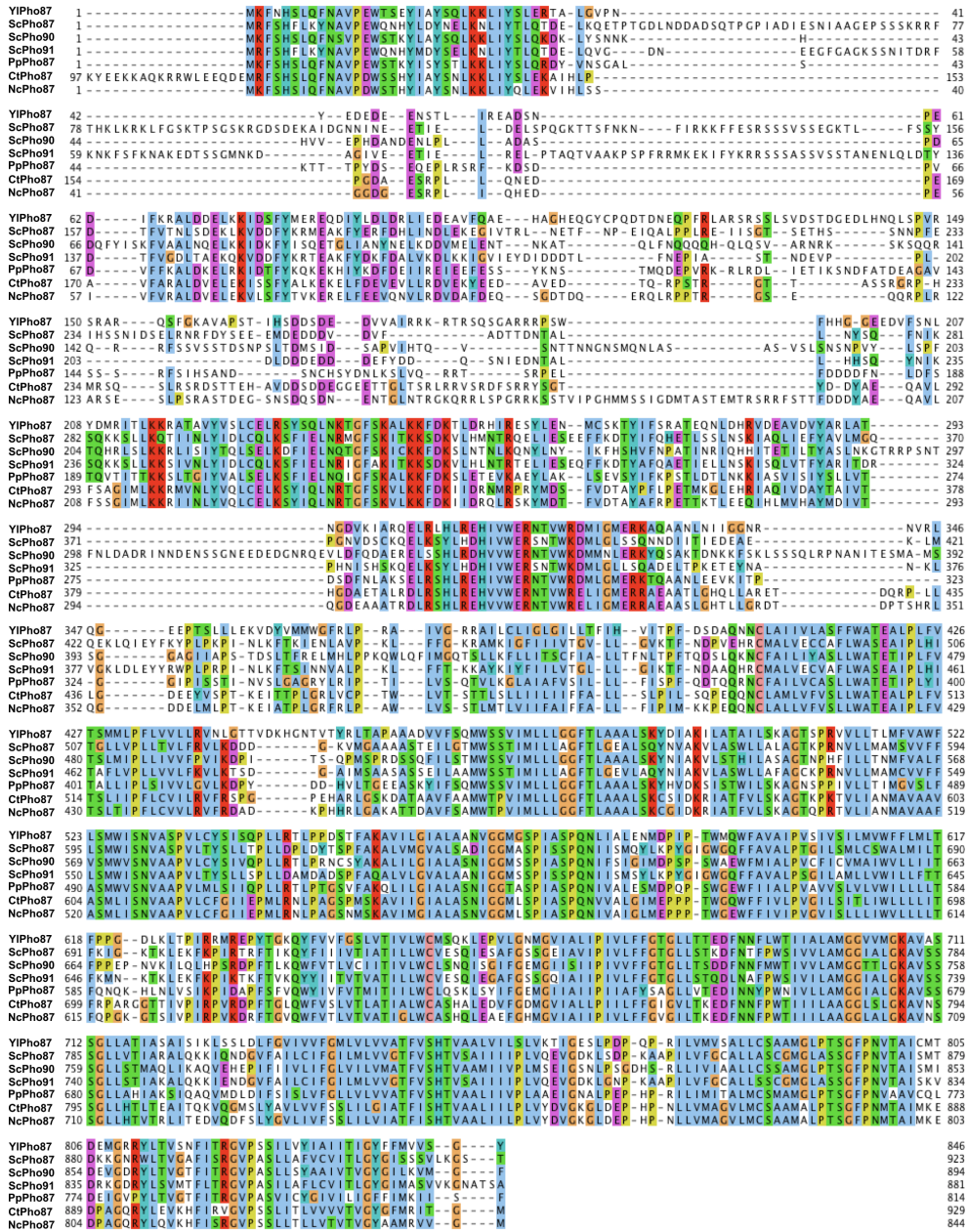


Figure S4: Alignment of yeast low-affinity phosphate transporter. Sequences of YlPho87 (*Y. lipolytica*), ScPho87, ScPho90, ScPho91 (*S. cerevisiae*), PpPho87 (*P. pastoris*), CtPho87 (*C. thermophilum*) and NcPho87 (*N. crassa*) are aligned. Sequences are colored according to the Clustal X color scheme and gaps are shown as minus (-) symbols. Sequences were aligned using Clustal Omega (Madeira et al., 2022).


```

ScPho87 429 YFKYLP LKPK I NLKFTK I ENLAVPKLFFGK R A M I G F I I V T G V L L G V K T F N D V E H R C M A L V E C C A F L W A S E A I P L 504
ScPho90 384 Y Y R W P L P R P I N L K F T S I N N V A L P K L F F T K K A Y I Y F I I L V T G L L L G I K T F N D A A Q H R C M A L V E C V A F L W A S E A I P L 459
HsNas1 8 ----- L V Y R R F L F V V F T V L V L L P L P I V L H T K A E C A Y T L F V V A T F W L T E A L P L 55
HsNas2 8 ----- L R V R K L L L V V C V P L L L L P L P V L H P S S A S C A Y V L I V T A V Y V W S E A V P L 55

ScPho87 505 H I T C L L V P L L T V L F R V L K D D D G K V M G A A A S T E I L G T M W S S T I M I L L A G F T L G E A L S Q Y N V A V L A S W L L A L A G T K 580
ScPho90 460 H I T A F L V P L L V V L F K V L K T S D G A I M S A A S A S S E I L A A M W S S T I M I L L A G F T L G E V L A Q Y N I A V L A S W L L A F A G C K 535
HsNas1 56 S V T A L L P S L M L P M F G I M P S ----- K K V A S A Y F K D F L L L L G V I C L A T S I I E K W N L H R I A L K M V M M V G N 119
HsNas2 56 G A A L V P A F L Y P F F G V L R S ----- N V A A E Y F K N T L L L V G V I C V A A A V E K W N L H R I A L R M V L M A G A R 119

ScPho87 581 P R N V L L M A M S V V F F L S M W I S N V A S P V L T Y S L L T P L L D P L ----- 619
ScPho90 536 P R N V L L M A M C V V F F L S M W I S N V A A P V L T Y S L L S P L L D A M ----- 574
HsNas1 120 P A W L T L G F M S S T A F L S M W L S N T S T A A M V M P I A E A V V Q Q I I N A E A E V E A ----- T Q M T Y F 173
HsNas2 120 P G M L L L C F M C C T T L L S M W L S N T S T T A M V M P I V E A V L Q E L V S A E D E Q L V A G N S N T E E A E P I S L D V K N S Q P S L E L I F V 195

ScPho87 620 ----- D Y T S P F A K A L V 630
ScPho90 575 ----- D A D S P F A Q A L V 585
HsNas1 174 N G S T N H G L E I D E S V N G H E I N E R K E K T K P P G Y N N D T G K I S S K V E L ----- E K N S G M R T K Y R T K K H V T R L T C 241
HsNas2 196 N E E S N A D L - T T L M H N E N L G V P S I T N P I K T A N Q H Q G K Q H P S Q E K P Q V L T P S P R K Q K L N R K Y R S H H D M I C K C L S 269

ScPho87 631 M G V A L S A D I C G M A P I S S P O N I I S M Q Y L K ----- P Y G I G W C Q F F A V A L P T C I L S M L C S W A L M I L T F ----- 692
ScPho90 586 G V A L A A N I C G M S P I S S P O N I I S M S Y L K ----- P Y G I G W C Q F F A V A L P S G I L A M L L V W I L L F T T F ----- 647
HsNas1 242 L C I A Y S S T I C G L T T I T C T S T N L I F A E Y F N T R Y P D C R C L N F G S W F T F S F P A A L I I L L S W I W L Q W L F L G F N F E M F 317
HsNas2 270 L S I S Y S A T I G G L T T I I G T S T S L I F L E H F N N Q Y P A A E V N F G T W F L S F P I S L I M L V V S W F W M H W L L G C N F K E T C S 345

ScPho87 693 I G K T R ----- L E R F K P I R T R F T I K Q Y F I I V T I A T I L L W C V E S ----- - Q I E S A F G S G E I 742
ScPho90 648 M N K T R ----- L E R F K P I K T F T V K Q Y I I T V I V A T I L L W C V E S ----- - Q I E G A F G S G Q I 697
HsNas1 318 C G K I T Y Q Q K A C A - E V I K Q E Y Q K L G P I R Y Q E I V T L V L F I M A --- L L W F S R D P G F V P C W S A L F S E Y P G F A I D S T V 388
HsNas2 346 L S K K I K T K R E Q L S E K R I Q E E Y E K L G D I S Y P E M V T G F F I L M T --- V L W F T R E P G F V P C W D S F F - E K K G Y R I D A T V 416

ScPho87 743 A V I P I ----- V L F F G T G L L S T K D F N T - F P W S I V V L A M G G I A L G K A V S S S G L L V T I A R 793
ScPho90 698 A I I P I ----- V L F F G T G L L S T Q D L N A - F P W S I V I L A M G G I A L G K A V S S S G L L S T I A K 748
HsNas1 389 A L L I G L L F F L I P A K T L T K T T - P T G E - I V A F D Y S P L I T W K E F Q S F M P W D I A I L V G G F A L A D G C E E S G L S K W I G N 460
HsNas2 417 Y V F L G F L L F L I P A K K P - C F G K K N D G E N Q I H S L G T E P I I T W K D F Q K T M P W E I V I L V G G Y A L A S G K S G L S T W I G N 491

ScPho87 794 A L Q K K I Q N D V F A I L C I F G I L M L V V G T F V S H T V S A I I I I P L V Q E V G D K L S - D P K A A P I L V F G C A L L A S C M G L A S S 868
ScPho90 749 A L Q K K I E N D V F A I L C I F G I L M L V V G T F V S H T V S A I I I I P L V Q E V G D K L G - N P K A A P I L V F G C A L L S C M G L A S S 823
HsNas1 461 K L S - P L G S L P A W L I L I S S L M V T S L T E V A S N P A T I T L F L P I L S P L A E A I H V N P L Y I L I P --- S T L C T S F A F L L P V A 532
HsNas2 492 Q M L - S L S S L P P A V T L L A C I L L V S I V T E F V S N P A T I T I F L P I L C S L S E T L H I N P L Y T L I P --- V T M C I S F A V M L P V G 563

ScPho87 869 C F P N V T A I S M T D K K G N R W L T V G A F I S R G V P A S L L A F V C V I T L --- C Y G I ----- S S V L K E S --- T 923
ScPho90 824 C F P N V T A I S K V D R K G D R Y L S V M T F L T R G V P A S I L A F L C V I T L --- C Y G I ----- M A S V V K G N A T S A 881
HsNas1 533 N P P N A I V F S Y G H ----- L K V I D M V K A G L G V N I V G A V V - M L G I C T W I V P M F D L Y T Y P S W A P A M S N E T M - P 595
HsNas2 564 N P P N A I V F S Y G H ----- C Q I K D M V K A G L G V N I G L V I V - M M A I N T W G V S L F H L D T Y P A W A R - V S N I T D Q A 626

```

Figure S5: Alignment of yeast Pho87/90 and human Nas1/2. Sequences of the transmembrane region of ScPho87, ScPho90 (*S. cerevisiae*) and HsNas1, HsNas2 (*H. sapiens*) are aligned. Sequences are colored according to the Clustal X color scheme and gaps are shown as minus (-) symbols. Sequences were aligned using Clustal Omega (Madeira et al., 2022).

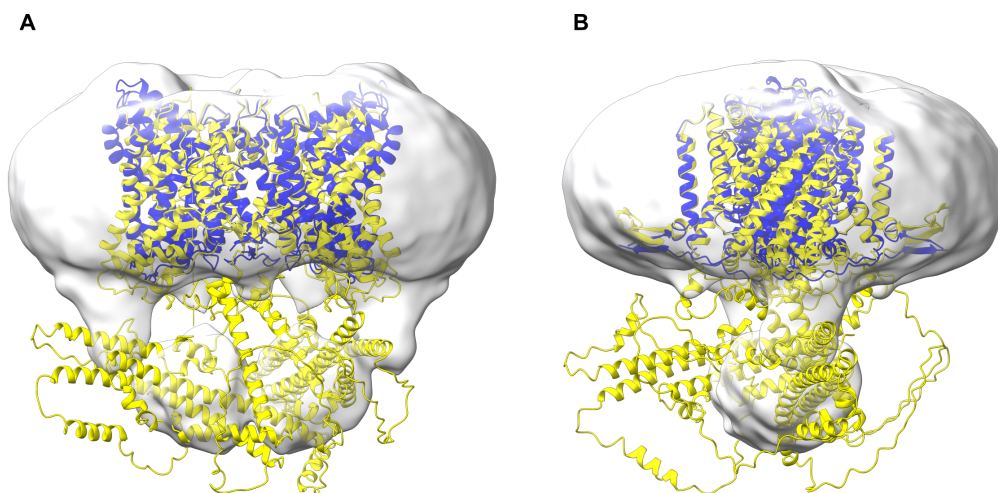


Figure S6: Comparison of experimental and AlphaFold predicted ScPho90 structures. (A) The predicted AlphaFold model of ScPho90 (yellow) and the experimentally determined symmetric structure (blue) are superimposed. The corresponding map at a low threshold is shown in grey. In the predicted AlphaFold model both protomers adopt an inward-open conformation. (B) Same as in A but turned by 90° within the membrane plane. The predicted SPX domain only partially matches the ScPho90 map with several helices located outside of the cryo-EM density.

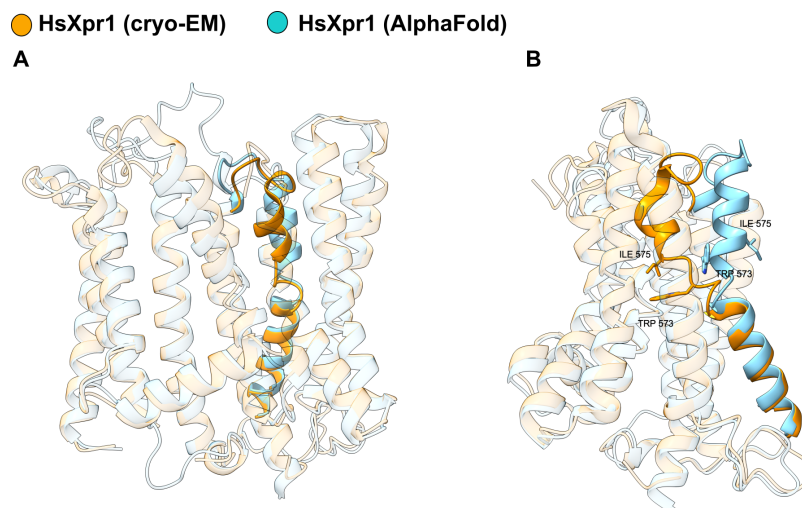


Figure S7: Comparison of experimental and AlphaFold predicted HsXpr1 structures. (A) Superposition of the cryo-EM (orange) and AlphaFold predicted (light blue) structure of HsXpr1. The different conformations of helix TM9 are highlighted. (B) Same as in A but turned by 90° within the membrane plane. The kinked conformation of TM9 in the AlphaFold model and the unkinked conformation in the cryo-EM model of HsXpr1 are highlighted. Residues Trp573 and Ile575 of TM9 are shown as sticks.

Acknowledgements

Additional information

Declaration of scientific collaboration

Except where stated otherwise by reference or acknowledgement, the work presented was generated by myself under the supervision of my advisors during my doctoral studies. All contributions from colleagues are referenced in the thesis and below:

Sabine Häder (technical assistant) assisted in the expression of HsXpr1 in HEK293 GnTI-cells. She was involved in cell culture cultivation, baculovirus production, screening of expression conditions, large-scale expressions and membrane isolations.

Julian Schneider (intern) assisted in the purification of HsXpr1 from HEK293 membranes. He was involved in the determination of suitable purification conditions, sample preparation for cryo-EM, cryo-EM grid screening and data collection.

Dr. Özkan Yildiz (supervisor) assisted in model building and refinement of the atomic models presented in this thesis.

Permission rights for figures, tables and illustrations

All figures and tables in this work were prepared by myself. Whenever a figure, table or text is identical to a previous publication, it is stated explicitly that copyright permission and/or co-author agreement has been obtained.

The results of the Pho90 part (Chapter 3.1 and 4.2) have been submitted for publication but have not been published as of the submission of this thesis. A manuscript, reporting results for the Syg1/Xpr1 part (Chapter 3.2 and 4.3) has been prepared but has also not been published yet.

Figure 2 was obtained from Austin et al., 2020. This article was published in *Frontiers*

in Microbiology and is an open-access article distributed under the terms of the Creative Commons Attribution License (CC-BY) (<https://creativecommons.org/licenses/by/4.0/>).


Figures 1, 5, 6 and 7 were generated using BioRender.com with a subscription including publishing rights.

The atomic models not generated in this work were obtained from the PDB under accession codes 4F35, 7JSK, 5A1S, 7SP5, 6L85, 2JWA, 5IJH, 5IJJ, 6WU1.

AlphaFold models were generated according to Jumper et al., 2021.

Eidesstaatliche Erklärung

Hiermit versichere ich, dass ich die vorliegende Arbeit selbstständig angefertigt habe und keine anderen als die angegebenen Hilfsmittel und Quellen verwendet habe.



Simon J. R. Schneider

Frankfurt am Main, den 08.01.24

Curriculum vitae